AD-A097 341 ENVIRONMENTAL RESEARCH INST OF MICHIGAN ANN ARBOR RA--ETC F/G 17/9
DETERMINATION OF BACKSCATTER CHARACTERISTICS OF SEA ICE USING S--ETC(U)
MAR 81 R W LARSON, J D LYDEN, R A SHUCHMAN N00014-79-C-0690
UNCLASSIFIED ERIM-142600-1-F NL

1 OF 3
AD
A097341

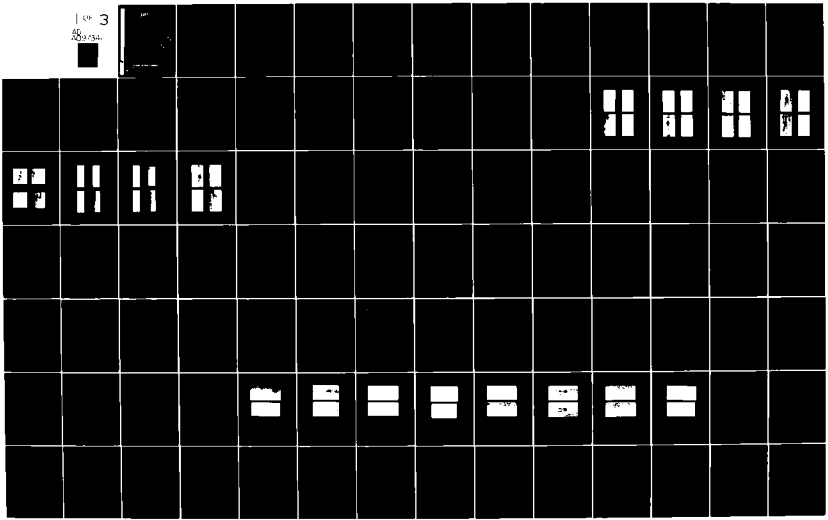

12

142600-1-F

Final Report

DETERMINATION OF BACKSCATTER CHARACTERISTICS OF SEA ICE USING SYNTHETIC APERTURE RADAR DATA

R.W. LARSON, J.D. LYDEN, and R.A. SHUCHMAN
Radar and Optics Division

R.T. LOWRY
INTERA Environmental Consultants, Ltd.

MARCH 1981

Office of Naval Research
Arctic Sciences Program (Code 461)
800 N. Quincy Street
Arlington, Virginia
Contract No. N00014-79-C-0690
Technical Monitor: Dr. Charles Luther

ENVIRONMENTAL
RESEARCH INSTITUTE OF MICHIGAN
BOX 8618 • ANN ARBOR • MICHIGAN 48107

81 4 6 228

TECHNICAL REPORT STANDARD TITLE PAGE

1. Report No.	2. Government Accession No. AD-A097341	3. Recipient's Catalog No.
4. Title and Subtitle Determination of Backscatter Characteristics of Sea Ice Using Synthetic Aperture Radar Data.		5. Report Date (11) March ~~1981~~
		6. Performing Organization Code
7. Author(s) R.W. Larson, J.D. Lyden, R.A. Shuchman, R.T. Lowry		8. Performing Organization Report No. (14) ERIM-142600-1-F
9. Performing Organization Name and Address Radar and Optics Division Environmental Research Institute of Michigan P.O. Box 8618 Ann Arbor, Michigan 49107		10. Work Unit No.
		11. Contract or Grant No. (15) N00014-79-C-0690
12. Sponsoring Agency Name and Address Office of Naval Research Arctic Science Program (Code 461) 800 N. Quincy Street Arlington, Virginia 22217		13. Type of Report and Period Covered (7) Final Report 1 July ~~1979~~ ~~to~~ 31 August ~~1980~~
		14. Sponsoring Agency Code

15. Supplementary Notes

Charles Luther was the ONR technical monitor for these research activities.

16. Abstract

This final report presents results obtained from an analysis of multichannel synthetic aperture radar (SAR) data obtained from imaging flights over areas of sea ice. The SAR system operated simultaneously at 3 cm and 23 cm wavelengths, with two orthagonal-polarization receivers, horizontal and vertical, for each wavelength.

Two SAR data sets were used, one from sea ice test sites in the Beaufort Sea region with data flights conducted during March 1979 as a part of the Canada SURSAT program, and the other data obtained during March 1977 as a part of the Canadian SAR-77 program conducted in Labrador, Newfoundland. Ground truth information was provided by consultants from INTERA, Ottawa, Ontario, Canada, for the Beaufort Sea sites and from REMOTEC, St. John's, Newfoundland, Canada, for the Labrador sites.

The SAR data were converted into digital image format and four basic measurements made on the data from each test site: 1) mean value, 2) standard deviation, 3) histogram, and 4)relative power scans at constant range lines. The results are presented in several formats: 1) cluster plots, 2) variance versus ice type, 3)coefficient of variation, and 4) two measures of the polarization ratio. Relative values of backscatter coefficients for several ice types are compared, but absolute values cannot be obtained.

(Over)

17. Key Words synthetic aperture radar (SAR) remote sensing sea ice X-band, L-band digital and statistical analysis	18. Distribution Statement The distribution of this report is unlimited.

19. Security Classif. (of this report)	20. Security Classif. (of this page)	21. No. of Pages	22. Price
Unclassified	Unclassified		

16. Abstract

Imagery of each of the SAR channels are included along with ground truth reports. Conclusions and recommendations for additional work are also included.

ACKNOWLEDGEMENTS

The work reported herein was performed for the Office of Naval Research (ONR) by the Radar and Optics division of the Environmental Research Institute of Michigan (ERIM). The ONR technical monitor was Charles Luther. Richard Larson and Robert Shuchman served as the co-principal investigators for this program while James Lyden performed the computer and statistical analysis.

Alex Klooster and Abby Liskow of ERIM are acknowledged for generating the digital data used in this program.

Appendices A and B were provided by Ray Lowry of INTERA and Richard Worsfold of REMOTEC, respectively. Special thanks are given to Rene Ramseier of Atmospheric Environment Service for his helpful suggestions and use of the Beaufort Sea ice data collected during the Canadian SURSAT project.

TABLE OF CONTENTS

ACKNOWLEDGEMENTS iii
LIST OF FIGURES vii
LIST OF TABLES ix
1. INTRODUCTION 1
2. SUMMARY 5
3. SYNTHETIC APERTURE RADAR DETERMINATION OF BACKSCATTER CHARACTERISTICS OF SEA ICE 9
   3.1 Data Set 9
   3.2 Sites 14
   3.3 Data Reduction 24
   3.4 Data Analysis Approach 30
4. RESULTS 53
   4.1 Cluster Diagrams 53
   4.2 Standard Deviation-to-Mean Ratios 60
   4.3 Isorange Scans 60
   4.4 Dynamic Range 77
   4.5 Relative Backscatter Values 81
   4.6 Histogram Analysis 81
   4.7 Polarization Ratios 90
   4.8 Signal-to-Clutter Ratios 95
   4.9 Graphic Display 103
5. CONCLUSIONS 105
REFERENCES 109
APPENDIX A: GROUND TRUTH FROM SEA TEST SITES A-1
APPENDIX B: INTERPRETATION OF SAR '77 DIGITIZED ICE DATA B-1
APPENDIX C: HISTOGRAMS FROM BEAUFORT SEA DATA C-1

LIST OF FIGURES

1. Flow Chart of SAR Sea Ice Data Analysis 9
2. Four-channel Imagery of Beaufort Area 1 (Shallow) 16
3. Four-channel Imagery of Beaufort Area 1 (Steep) 17
4. Four-channel Imagery of Beaufort Area 2 (Shallow) 18
5. Four-channel Imagery of Beaufort Area 2 (Steep) 19
6. Four-channel Imagery of Hopedale Area 1 20
7. Four-channel Imagery of Hopedale Area 2 21
8. Additional Four-channel Imagery of Hopedale Area 2 22
9. Four-channel Imagery of Hopedale Areas 3 and 4 23
10. Representative Histogram 25
11. Representative Cluster Plot (L-Band) 26
12. Representative Example of Isorange Transects 29
13. Representative Perspective Plot 31
14. Cluster Plots of Beaufort Area 2 54
15. Cluster Plots of Beaufort Area 1 55
16. Cluster Plots Showing the Effect of Varying Resolution 56
17. Cluster Plots of Hopedale Area 1 57
18. Cluster Plots of Hopedale Areas 3 and 4 58
19. Relative Mean of Received Signal vs. Ice Type, Area B2, X-Band 61
20. Relative Mean of Received Signal vs. Ice Type, Area B2, L-Band 62
21. X-Band (Shallow) Constant-Range Transects of Beaufort Area 1 . . 66
22. X-Band (Steep) Constant-Range Transects of Beaufort Area 1 . . . 67
23. L-Band (Shallow) Constant-Range Transects of Beaufort Area 1 . . 68
24. L-Band (Steep) Constant-Range Transects of Beaufort Area 1 . . . 69
25. X-Band (Shallow) Constant-Range Transects of Beaufort Area 2 . . 70
26. X-Band (Steep) Constant-Range Transects of Beaufort Area 2 . . . 71
27. L-Band (Shallow) Constant-Range Transects of Beaufort Area 2 . . 72
28. L-Band (Steep) Constant-Range Transects of Beaufort Area 2 . . . 73

LIST OF FIGURES (Concluded):

29. Annotated X-Band (Shallow) Constant-Range Transects of Beaufort Area 2 75

30. Annotated X-Band (Steep) Constant-Range Transects of Beaufort Area 2 76

31. Annotated X-Band (Shallow) Constant-Range Transects of Beaufort Area 1 78

32. Annotated X-Band (Steep) Constant-Range Transects of Beaufort Area 1 79

33. Relative Values of Backscatter Cross Section--X_{HH} 83

34. Histogram of Site B2-F X_{HV}(Steep) 86

35. Histogram of Site B2-G X_{HV}(Steep) 87

36. Histogram of Site B1-A X_{HV}(Steep) 88

37. Histogram of Site B1-B X_{HV}(Steep) 89

38. Polarization Ratio of Coefficient of Deviation vs. Ice Type, Area B2, X-Band 92

39. Polarization Ratio of Coefficient of Deviation vs. Ice Type, Area B2, L-Band 93

40. Probability of Detection vs. Signal-to-Noise Ratio 96

41. X-Band (HH) Perspective Plots of Ship and Iceberg Location 97

42. X-Band (HV) Perspective Plots of Ship and Iceberg Location 100

43. L-Band (HH) Perspective Plots of Ship and Iceberg Location 101

44. L-Band (HV) Perspective Plots of Ship and Iceberg Location 102

LIST OF TABLES

1. Beaufort Sea Ice Characterization 12
2. Hopedale Area Ice Characterization 15
3. Summary of Data Measurements for Site B1-A 32
4. Summary of Data Measurements for Site B1-B 33
5. Summary of Data Measurements for Site B1-C 34
6. Summary of Data Measurements for Site B1-D 35
7. Summary of Data Measurements for Site B1-E 36
8. Summary of Data Measurements for Site B1-F 37
9. Summary of Data Measurements for Site B2-A 38
10. Summary of Data Measurements for Site B2-B 39
11. Summary of Data Measurements for Site B2-C 40
12. Summary of Data Measurements for Site B2-D 41
13. Summary of Data Measurements for Site B2-E 42
14. Summary of Data Measurements for Site B2-F 43
15. Summary of Data Measurements for Site B2-G 44
16. Summary of Data Measurements for Site B2-H 45
17. Summary of Data Measurements for Site B2-I 46
18. Summary of Data Measurements for Sites H1-A and H1-B 47
19. Summary of Data Measurements for Site H1-C 48
20. Summary of Data Measurements for Sites H2-A, H2-B, and H2-C . . 49
21. Summary of Data Measurements for Sites H3-A, H3-B, and H3-C . . 50
22. Coefficient of Deviation for Four Ice Types from Area B2 . . . 63
23. Coefficient of Deviation for Four Ice Types from Area B1 (Shallow Incidence Angle) 64
24. Summary Table of Comparisons between Measured Values 65
25. Dynamic Range of Received Signal (in dB) for Beaufort Test Sites 80
26. Relative Values of Backscatter for Various Beaufort Sites . . . 82
27. Polarization Ratios for Four Sites in Area B2 91

LIST OF TABLES (Concluded):

28. Values of the Polarization Ratio for the Coefficient of Deviation for Area B1 94
29. Signal-to-Clutter (Surrounding Ice) Ratio Table (Values in dB) 98
30. Probability of Detection of Ships and Icebergs 99

DETERMINATION OF BACKSCATTER CHARACTERISTICS OF SEA ICE USING SYNTHETIC APERTURE RADAR DATA

1
INTRODUCTION

This final report summarizes research performed for the Office of Naval Research (ONR) Arctic Science Program. The report covers the reporting period of 1 July 1979 to 31 August 1980.

The objectives of this research effort were (1) to determine the backscatter characteristics of sea ice using data obtained from an X- and L-band SAR system and (2) to correlate these backscatter characteristics with various ice types to determine possible signatures for ice classification. Both deterministic and statistical measures were investigated for classification signatures.

The microwave imaging radar system used in this program provides several very desirable capabilities for the remote sensing of ice. These include: (1) very large area coverage, (2) day-night and nearly all-weather operations, (3) multiple operating channels (wavelength and/or polarization selection), (4) near-real-time availability of output imagery, and (5) an illumination source which is a part of the sensor.

For extremely large area coverage, a very wide swathwidth capability is required*. Operation from a spacecraft provides the optimum geometry for wide area coverage; operation from an aircraft can provide coverage over approximately 40 km swaths and, with dual systems, can provide this coverage on both sides of the vehicle; this could also be done in spacecraft systems, providing data link along with sufficient weight and power are available. It is clear from a

---

*Multiple-swath operating techniques have been suggested in various reports by ERIM and others. These techniques include multiple antennas, dual-feed antenna, and multi-frequency operation [1].

consideration of the SAR imaging geometry that the viewing or incidence angle[*] from a radar system in space will be very steep ($15^\circ \leq \theta_{inc} \leq 45^\circ$). On the other hand, for a radar system in an aircraft, wide swath operation will require imaging at shallow incidence angles, say $30^\circ \leq \theta_{inc} < 85^\circ$.

For both aircraft and spacecraft applications, information is required with which to determine the best operating wavelength, polarization, and angle of incidence for the classification of various ice types. Also, an optimum single frequency must be selected for best discrimination, in both steep and shallow incidence angle operation. Finally, a decision must be made regarding the selection and advantages (in terms of discrimination capability) of multi-channel radar systems. The data set utilized in this initial study had advantages in that four channels of radar imagery are available (3 cm and 23 cm, both HH and HV polarization). Some comparisons can be made with data obtained from other microwave sensors (such as scatterometers) in order (1) to predict the performance at wavelengths different from those used in operating imaging radars and (2) to calibrate the radar data.

The important SAR system operating parameters are the wavelength, incidence or depression angle, polarization, and resolution. It would be very desirable to have a multi-channel SAR that has absolute calibration capability for demonstration experiments such as those considered here. The data utilized in this study are not calibrated. Relative comparisons of backscatter values between channels cannot be made due to unknown system constants (such as system response, antenna gain, and processor variations). Comparison on a single channel can be made, as described later, by selecting test areas at constant depression angles.

---

[*] Incidence angle is defined (in the usual manner) as the angle between the vertical and the direction of the incident radiation.

It is hoped that this report can be used as a SAR data handbook of ice signatures for use by the ICESEX and ICE-RADARSAT Science Working Groups.

2
SUMMARY

Two multi-channel SAR data sets obtained from imaging flights over two different sea-ice areas were analyzed. Each data set included four SAR channels: 3 cm and 23 cm wavelengths were transmitted with horizontal polarization; both horizontal and vertical receiving channels were provided for each wavelength, giving a total of four data channels. The data flights were conducted in the Beaufort Sea area during March 1979 as a part of the Canadian SURSAT project and off the coast of Labrador in February 1977 as a part of the SAR-77 C-CORE Canadian East Coast ice project. Each data set was studied with the aid of consultants who were involved in ground measurements during the two projects. Test sites were selected so as to include several different ice types; 15 sites from the Beaufort Sea area and 10 sites from the Labrador area were selected. Ice types included medium multi-year floes, multi-year pieces, new ice, and first-year ice; the latter two were both with and without snow cover. In addition, SAR data of icebergs and ships were used.

The data reduction steps used were as follows: First, four-channel data from each test site were digitized. Then, four basic measurements were made to characterize the data: (a) mean value of each signal, (b) standard deviation, (c) histogram of each channel, and (d) constant-range transects of the test sites. Measurements were made for three values of spatial resolution (6, 18, and 30 m [2]) and incidence angle values between 40° and 83°.

Using results from the basic measurements, data are presented in five formats: (1) cluster plots of like versus orthogonal polarizations for each wavelength, (2) standard deviation versus ice types, (3) coefficient of deviation (standard deviation divided by mean), (4) polarization ratio (HH mean divided by HV mean), and (5) polarization ratio (HH coefficient of deviation divided by HV coefficient of deviation).

Analysis of the cluster diagram showed that, for the limited samples available, the X_{HV} channel discriminated the multi-year ice best, particularly for steep incidence angles. Other ice types did not appear to cluster; this is particularly true for L-band. As expected, standard deviation values decreased with increasing resolution for each data set. In general, for 6-m resolution, the standard deviation and mean value increased with increasingly rough ice areas at X-band. The presence of ice ridges tended to increase the mean and standard deviation. The coefficient of deviation for both X_{HH} and L_{HH} was larger for both first-year ridged areas and multi-year ridged areas, compared with that from similar areas without ridges. Wet snow-covered ice (Labrador data) showed less signal return at L-band than at X-band.

The dynamic range of signal values was greatest (16 dB) for X_{HV} from the multi-year site, while the minimum dynamic range was 3 dB for X_{HH}, H_{HV}, and L_{HV} from Site 1 (first year). Comparison of the relative value of backscatter power from different ice types derived from SAR data with corresponding σ_0 values obtained from both ground and airborne scatterometer data indicates very similar results. The comparisons were made for first-year versus multi-year at both steep (40°) and shallow (83°) incidence angles; here, SAR and scatterometer relative values agreed within about 1 dB. Similar results were obtained from new and first-year ice sites. Since the SAR data were not calibrated, absolute comparisons could not be made.

Mean values for X_{HH} progressively increased from (1) first-year to (2) first-year with ridges to (3) multi-year to (4) multi-year with ridges. The polarization ratio decreased for this ordering of ice types. Measurements of signal-to-clutter ratio were made for icebergs in pack ice and for ships in ice and in open water. These data are used to determine probability of detection.

The above results were obtained using only a few (one, in some cases) samples of a given ice type. It is recommended that (1) the data set be used for measurement from additional sites containing similar ice types to verify the observations, (2) this data set be utilized further by comparing relative backscatter values for large incidence angles ($40^\circ < \theta < 83^\circ$) in order to extend the values obtained with the airborne scatterometer, (3) multivariant analysis techniques be applied to these data sets, and (4) if data are available, sea ice imaging be analyzed using all digitally recorded and processed SAR signals.

3
SYNTHETIC APERTURE RADAR DETERMINATION OF BACKSCATTER CHARACTERISTICS OF SEA ICE

A summary of the complete data handling approach is given in Figure 1. The first steps are the selection of data, correlation with ground truth, and digitization (as indicated at the top of the figure); these give the selected data in CCT format. Using the digital data, three analyses are then conducted: (1) measurements of selected parameters to characterize data, (2) constant radar range scans, and (3) ship and iceberg detection. The results from each analysis "path" are summarized in "conclusions." These conclusions then serve as inputs for: (1) understanding the SAR imaging mechanism of sea ice, (2) the design of SAR systems for ice surveillance, and (3) single- or multi-channel classification algorithms using SAR data.

3.1 DATA SET

The multi-channel SAR data set included imagery obtained from two experiments conducted in Canada and supported by the Canadian government with joint support/participation by the U.S. government. The first data set considered comes from the Surveillance Satellite (SURSAT) SAR experiment conducted in the Beaufort Sea during March 1979. This experiment was a part of the extensive SURSAT microwave program conducted by Canada during the period Fall 1977 to June 1979. Data from a total of 15 areas were selected from this data set.

In addition, data were utilized from the SAR-77 ice program, jointly sponsored by Canada and the U.S. through the Centre for Cold Oceans Resources Engineering (C-CORE), Memorial University (Newfoundland). This experiment was conducted during the winter of 1977 off the coast of Labrador, Newfoundland; data from ten areas were selected for analysis. Selections were based on (1) the variety of

FIGURE 1. FLOW CHART OF SAR SEA ICE DATA ANALYSIS.

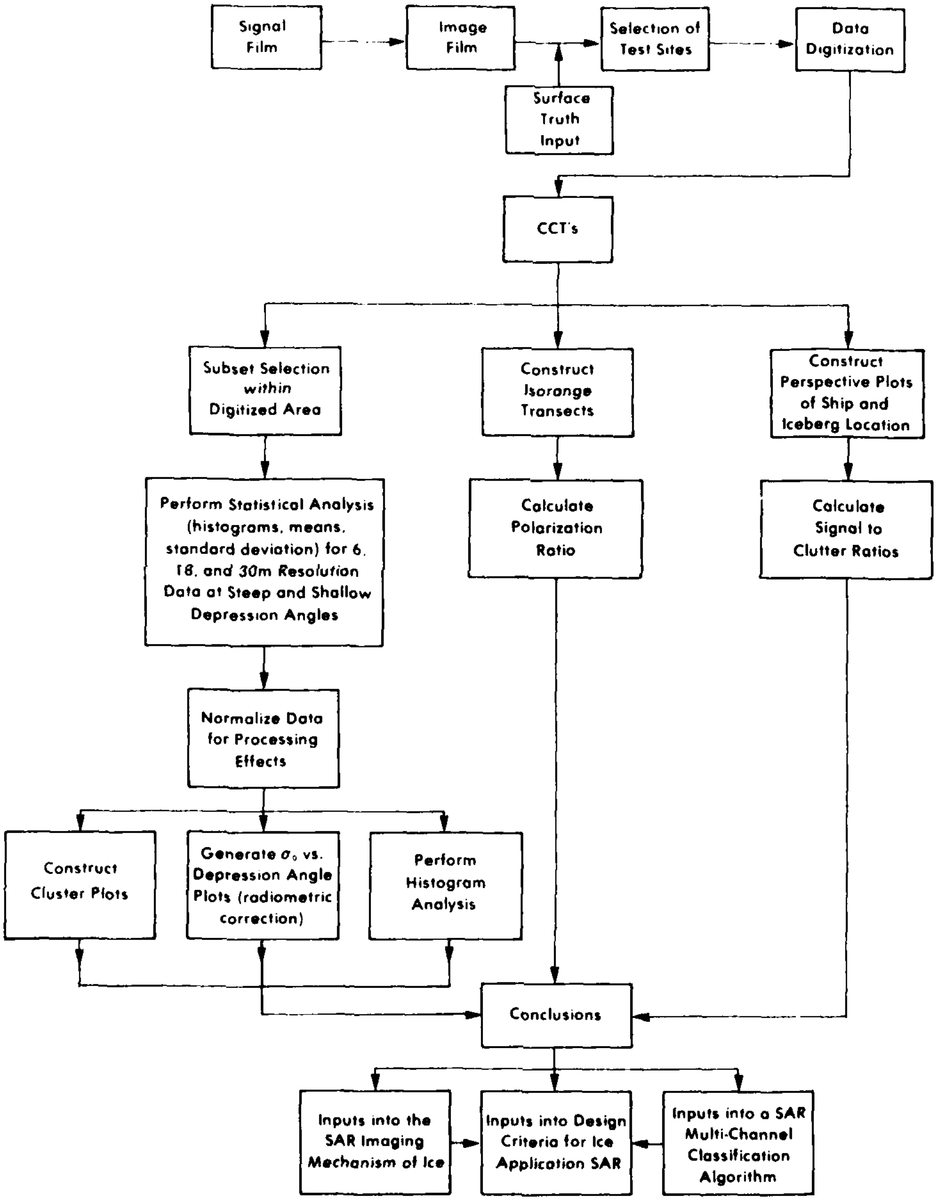

ice types, (2) the ground truth data available, and (3) the quality of the SAR data.

The various ground truth teams selected several sites for extensive ground measurements. Particular SAR data sets, which included four-channel signal records of those sites, were selected with the help of a consultant from INTERA, who was a member of one of the ground truth teams. Data from two SAR flights were selected; during one of these flights, the SAR operating parameters were adjusted so that SAR imagery at steep incidence was obtained; this flight were conducted on 16 March 1979. Data obtained on 18 March 1979 was imaged at shallow incidence angles.

The selected imagery from each test site was converted to CCT digital format using the ERIM image dissector facilities [3]. Analysis was then conducted on the CCT image data using the ERIM digital computer facilities.

Most of the test sites selected are located in the Beaufort Sea area. Site 1 is a nearshore site having shorefast ice, while Site 2 is located 200 nmi north and includes multi-year ice. A summary of the ice types identified at each site is given in Table 1. A detailed discussion of the ice characteristics and classification is given in the ground truth report provided by the INTERA consultants and included as Appendix A.

The test areas used from Site 2* were selected so as to be at a nearly constant depression angle in order to normalize out corrections due to range and antenna gain. This provided two data sets, one at a steep incidence angle of approximately 40° and the other at a shallow incidence angle of approximately 80°. Four data sets were selected from the nearshore site (B1), two at each incidence angle and range.

---

*Site 2 is so designated by the Beaufort analysis team. This site is referred to as B2 in this report.

TABLE 1. BEAUFORT SEA ICE CHARACTERIZATION

Area	Classification	Thickness	Ridging Present	Ridging Age	Ridging Height	Snow Present	Snow Age	Snow Depth	Remarks
B2-A	Multi-year ice	>3 m	Yes	Multi-year	3-5 m	Yes	Present throughout season	3-5 cm	
B2-B	Thick first-year ice	1-2 m	No			Yes	Present throughout season	3-5 cm	
B2-C	Thick first-year ice	1-2 m	No			Yes	Present throughout season	3-5 cm	May be contaminated by multi-year pieces
B2-D	Thick first-year ice	1-2 m	Yes	Not new	1-2 m	Yes	Present throughout season	3-5 cm	
B2-E	Multi-year pieces with hummocks	>3 m	Yes	Mainly multi-year	3-5 m	Yes	Present throughout season	3-5 cm	
B2-F	Multi-year ice	>3 m	Yes	Multi-year	3-5 m	Yes	Present throughout season	3-5 cm	Site contained by large floe
B2-G	Thick first-year ice	1-2 m	No			Yes	Present throughout season	3-5 cm	
B2-H	Thick first-year ice	1-2 m	Yes	Not new	1-2 m	Yes	Present throughout season	3-5 cm	May be contaminated by multi-year pieces
B2-I	Multi-year ice with some thick first-year pieces	>3 m	Yes	First-year and multi-year	1-5 m	Yes	Present throughout season	3-5 cm	

TABLE 1. BEAUFORT SEA ICE CHARACTERIZATION (Concluded)

			Ridging			Snow			
Site	Classification	Thickness	Present	Age	Height	Present	Age	Depth	Remarks
B1-A	Medium first-year ice	~1 m	Yes	Not new	>1 m	Yes	Not new	3-5 cm	Area becoming shorefast zone
B1-B	Young ice (gray-white)	15-20 cm	Yes	Extremely new	<1 m	No			Ridging and finger rafting occurring
B1-C	Medium first-year ice	~1 m	Yes	Not new	>1 m	Yes	Not new	3-5 cm	Area becoming shorefast zone
B1-D	Medium first-year ice	~1 m	Yes	Not new	>1 m	Yes	Not new	3-5 cm	Area becoming shorefast zone
B1-E	Medium first-year ice	~1 m	Very little	Not new	>1 m	Yes	Not new	3-5 cm	Area becoming shorefast zone
B1-F	Young ice (gray-white)	15-20 cm	Yes	Extremely new	<1 m	No			Ridging and finger rafting occurring

SAR data from several additional sites were selected from the imagery obtained during the SAR-77 program. These data, obtained during February and March 1977 off the Labrador Coast, are for shorefast ice near the town of Hopedale, Labrador. A summary of the ice types identified at the Labrador sites is given in Table 2. A complete description of the test sites is given in the ground truth report provided by consultants of the REMOTEC Corp., St. Johns, Newfoundland and included as Appendix B.

Also collected as part of the SAR-77 program were four-channel data of both a ship and an iceberg in a surrounding ice field. Excellent surface truth was provided from the ship at the time of the overflight.

3.2 SITES

The radar images corresponding to the four-channel data analyzed in this report are shown in Figures 2 through 9. In the Beaufort Sea, data were collected at both steep and shallow incidence angles for the two areas. At Hopedale, only one incidence angle was used at each of the four areas. On each of the images is a large area marked by a dashed line that represents the area digitized for computer applications. The smaller squares within this larger area are where the computer analysis was actually performed. Although care was taken in locating these small areas, some are undoubtedly contaminated by unwanted ice types. Also, it was assumed that the ice did not change during the day between flights over the Beaufort Sea.

Figures 2 and 3 contain the shallow and steep images of Beaufort area 1, respectively. This area is characterized by first-year ice with snow toward the left of the image, and new ice without snow to the right.

Figures 4 and 5 are the images for Beaufort area 2, again for both shallow and steep incidence angles, respectively. This site

TABLE 2. HOPEDALE AREA ICE CHARACTERIZATION

			Ridging			Snow			
Site	Classification	Thickness	Present	Age	Height	Present	Age	Depth	Remarks
H1-A	First-year ice	~1 m	Yes	Not new	N/A	No			Shear zone
H1-B	First-year ice	~1 m	Yes	Not new	N/A	No			Shear zone
H1-C	First-year ice	~1 m	Yes	Not new	N/A	No			Shear zone
H2-A	First-year ice	N/A	No			No			Transition zone, near pack ice
H2-B	Young ice	N/A	No			No			Small lead refrozen, transition zone, near pack ice
H2-C	First-year ice	N/A	No			No			Transition zone, near pack ice
H3-A	First-year ice	~1 m	No			Yes	N/A	10 cm	Fast ice, not rough
H3-B	First-year ice	~1 m	Yes	Not new	<1 m	Yes	N/A	10 cm	Fast ice, slight pressure ridging, pancake ice in area
H4-A	Young ice	~1 m	Yes	New	<1 m	Yes	N/A	10 cm	Shear zone

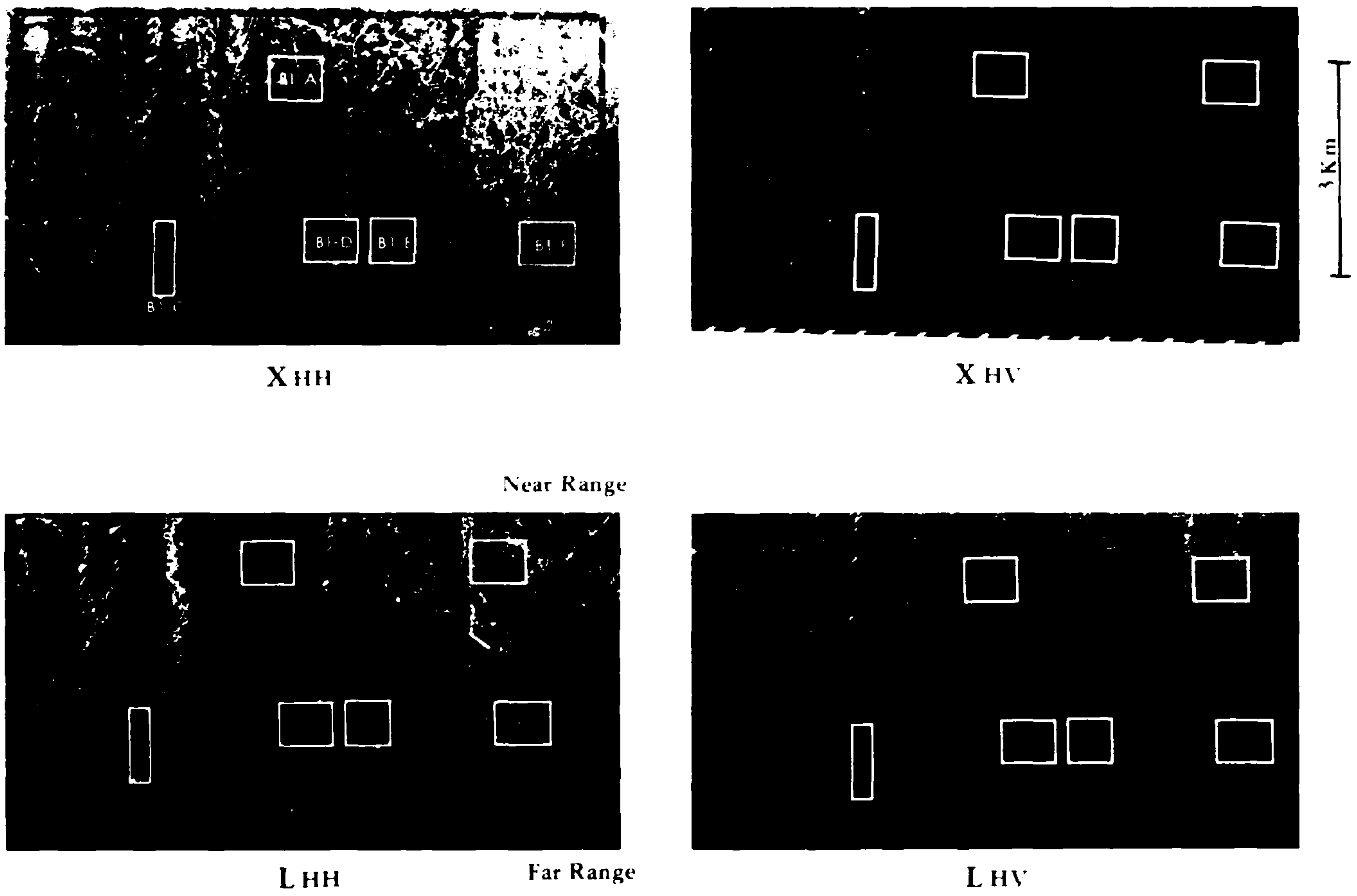

FIGURE 2. FOUR-CHANNEL IMAGERY OF BEAUFORT AREA 1 (SHALLOW).

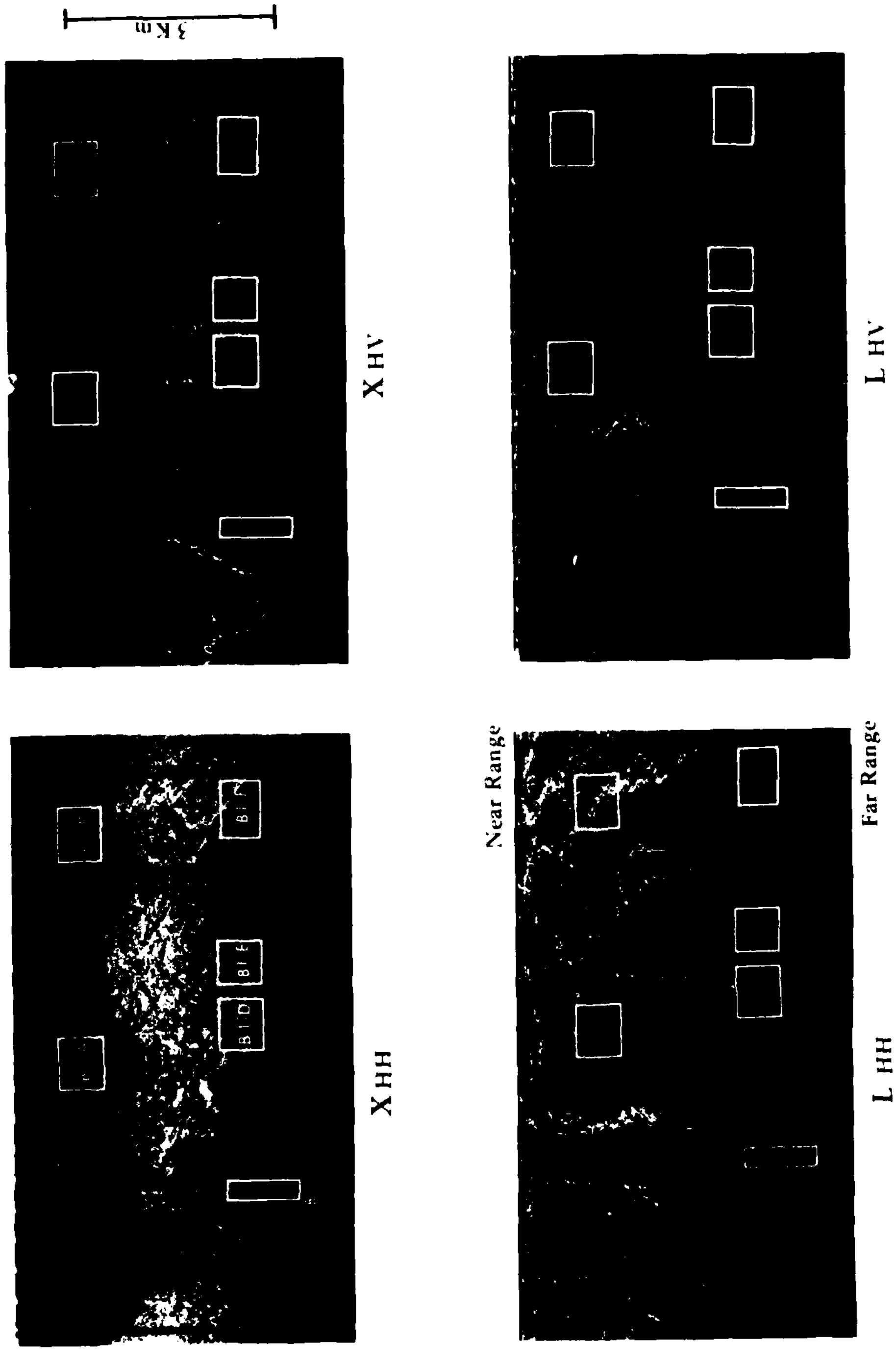

FIGURE 3. FOUR-CHANNEL IMAGERY OF BEAUFORT AREA 1 (STEEP).

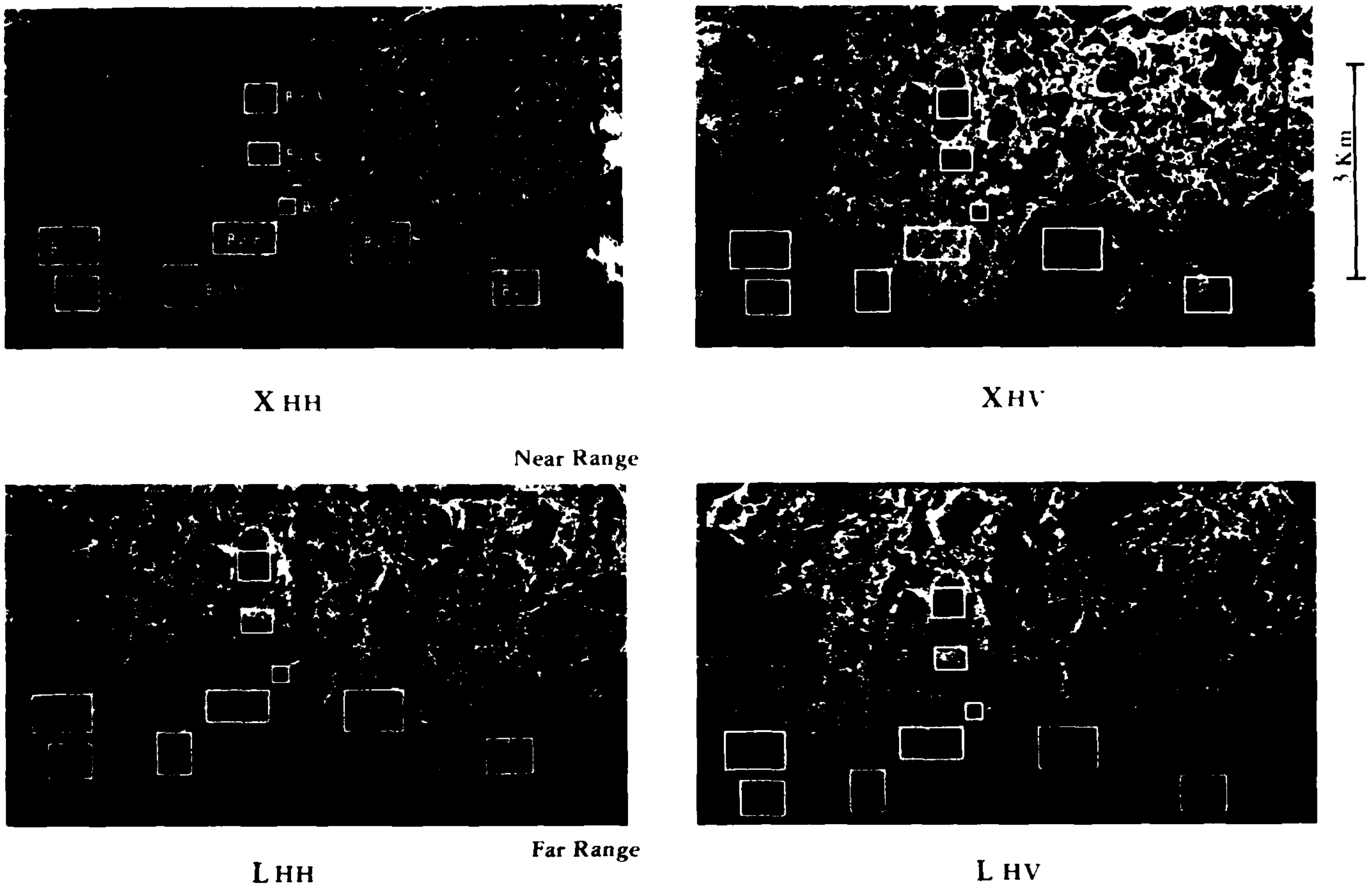

FIGURE 4. FOUR-CHANNEL IMAGERY OF BEAUFORT AREA 2 (SHALLOW).

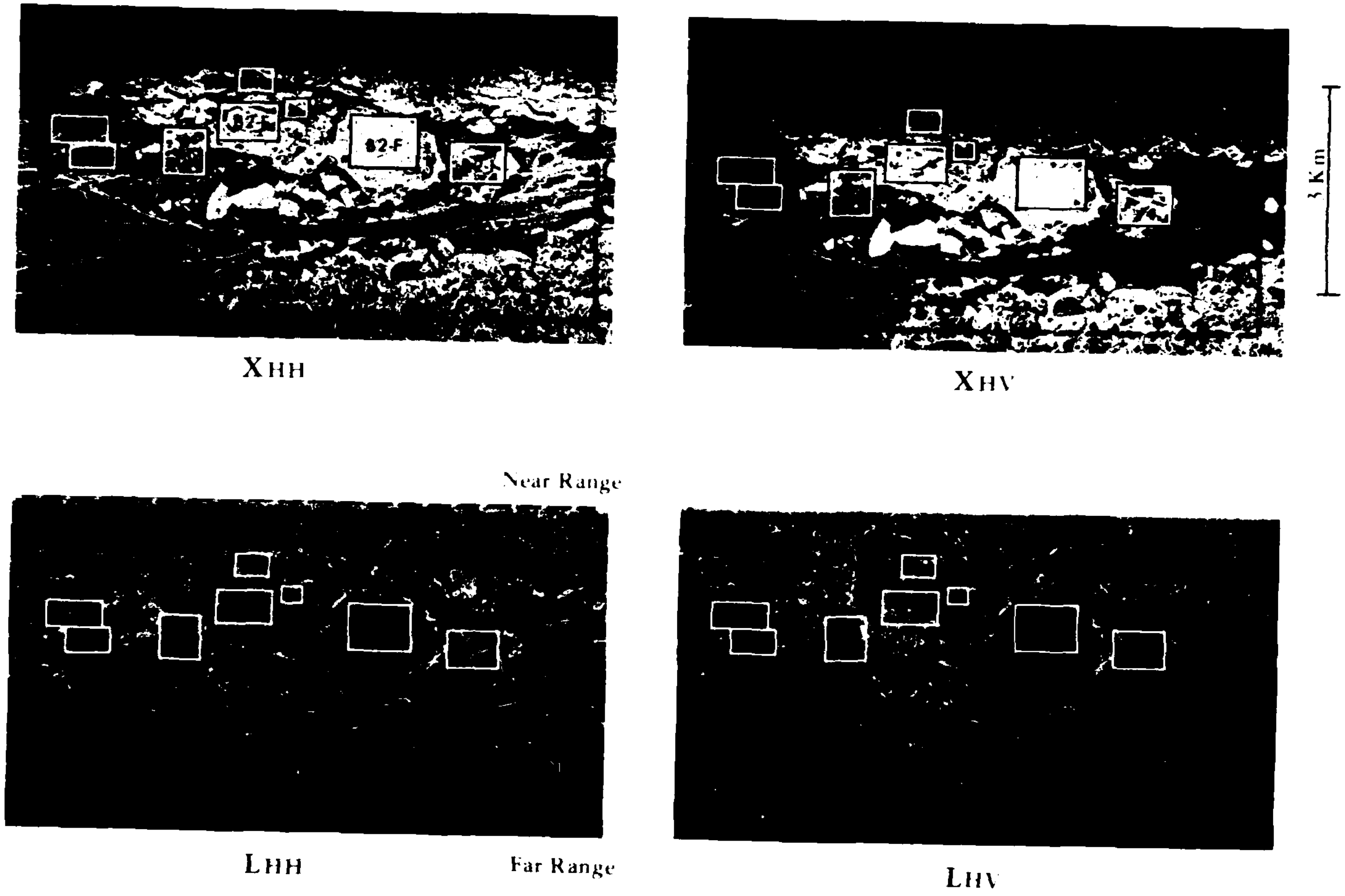

FIGURE 5. FOUR-CHANNEL IMAGERY OF BEAUFORT AREA 2 (STEEP).

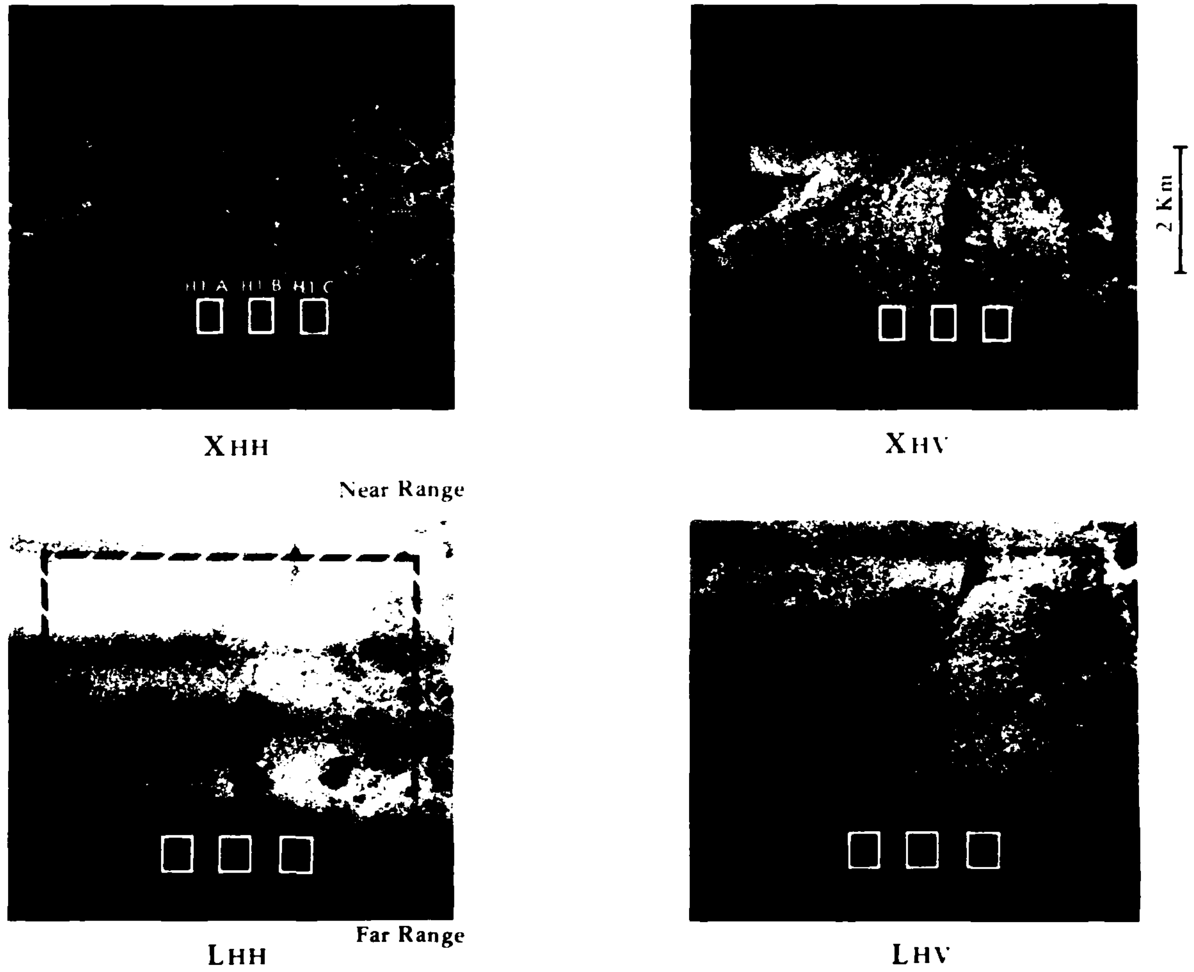

FIGURE 6. FOUR-CHANNEL IMAGERY OF HOPEDALE AREA 1.

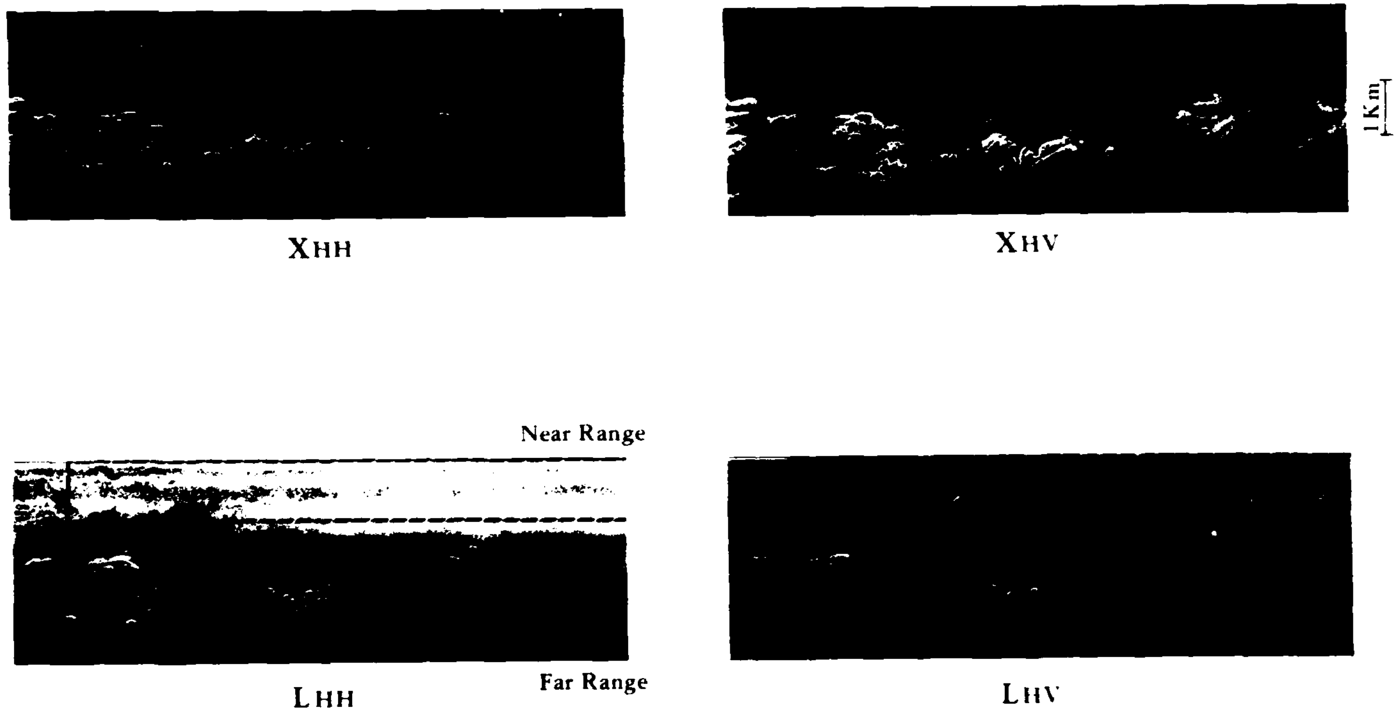

X HH

X HV

L HH

L HV

FIGURE 7. FOUR-CHANNEL IMAGERY OF HOPEDALE AREA 2.

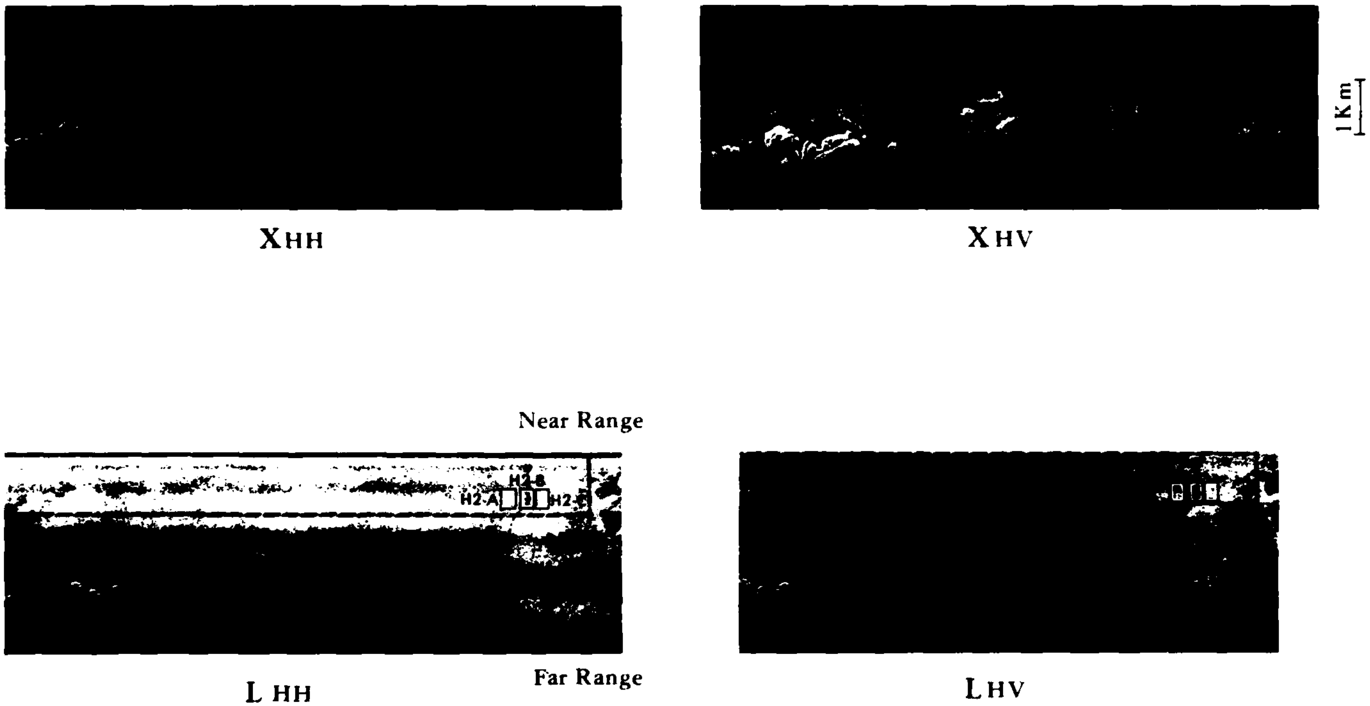

FIGURE 8. ADDITIONAL FOUR-CHANNEL IMAGERY OF HOPEDALE AREA 2.

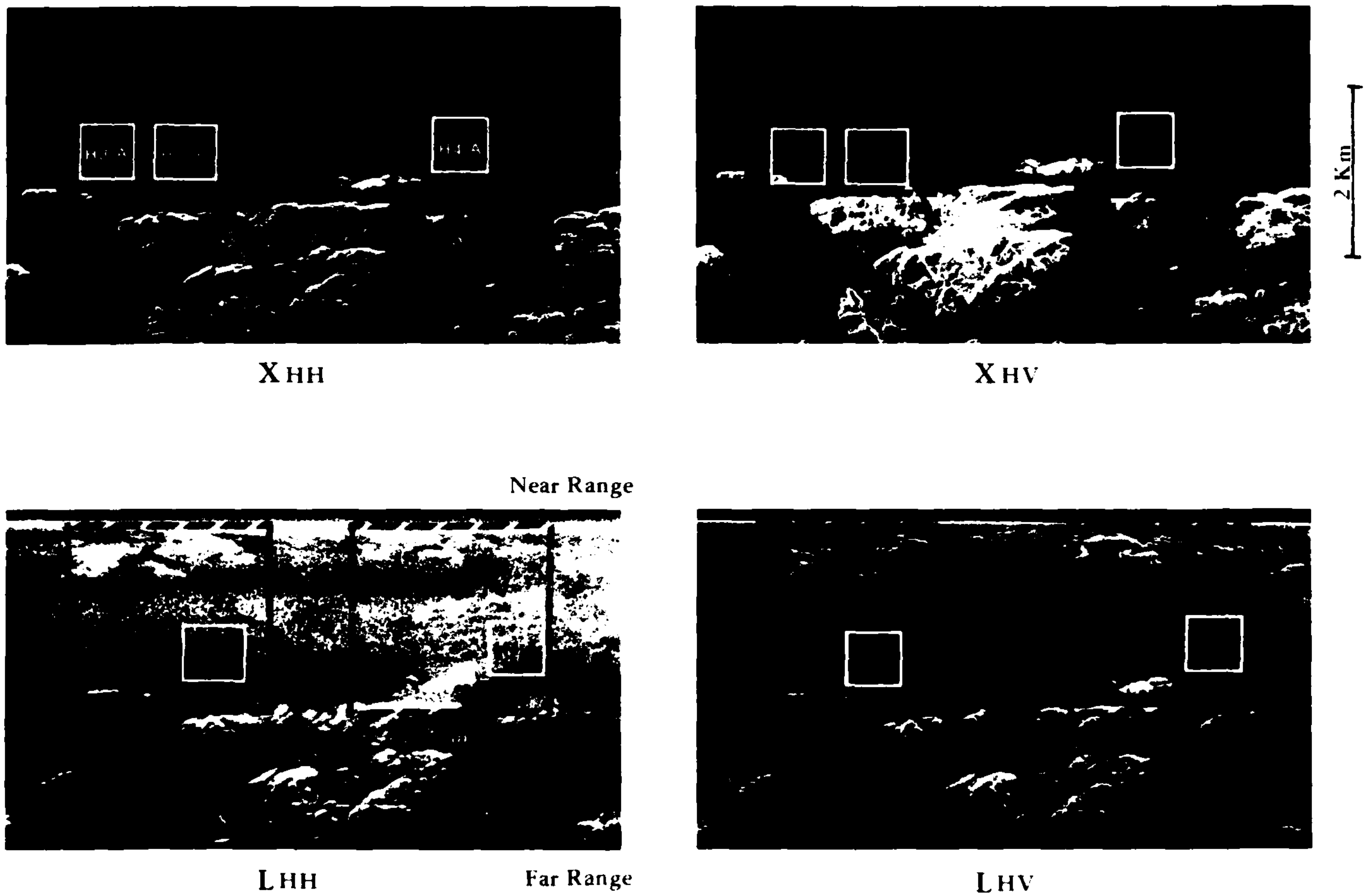

FIGURE 9. FOUR-CHANNEL IMAGERY OF HOPEDALE AREAS 3 AND 4.

contains a wide variety of ice, ranging from young ice to multi-year with ridging. Also note that Site B2-A is not contained in the steep images; this is due to the digitized areas not being exactly coincident.

Figure 6 contains the imagery from Hopedale area 1. Looking from left to right at the three rectangles, the ice goes from first-year to new ice with a shear zone between, which is characterized by rafting.

Figures 7 and 8 show the imagery from Hopedale area 2. Here we attempted to locate a refrozen lead amidst first-year ice. This refrozen lead can be seen in the L-band imagery as H2-B, but cannot be located in the X-band data.

Figure 9 is the imagery for Hopedale areas 3 and 4. This region is basically first-year ice with some ridging and floes. Due to the digitized areas not being exactly coincident, site H3-B could not be located in the L-band data.

3.3 DATA REDUCTION

The large areas outlined in Figures 2 through 9 were digitized at ERIM and computer compatible tapes (CCTs) were produced using the ERIM hybrid optical-digital processor [4]. These digitized areas were then subsetted into specific regions of interest by ice type for statistical and other types of computer analysis performed on the University of Michigan Amdahl system.

The advantages of using a digital computer as opposed to photographic products for image analysis are numerous. Radar sensors frequently operate with a range of return brightnesses spanning 50 dB. Much of this dynamic range can be preserved in radar images using pulse compression techniques implemented by digital or optical processors. However, when a radar image is recorded on photographic emulsion, the dynamic range is compressed. The photographic emulsion

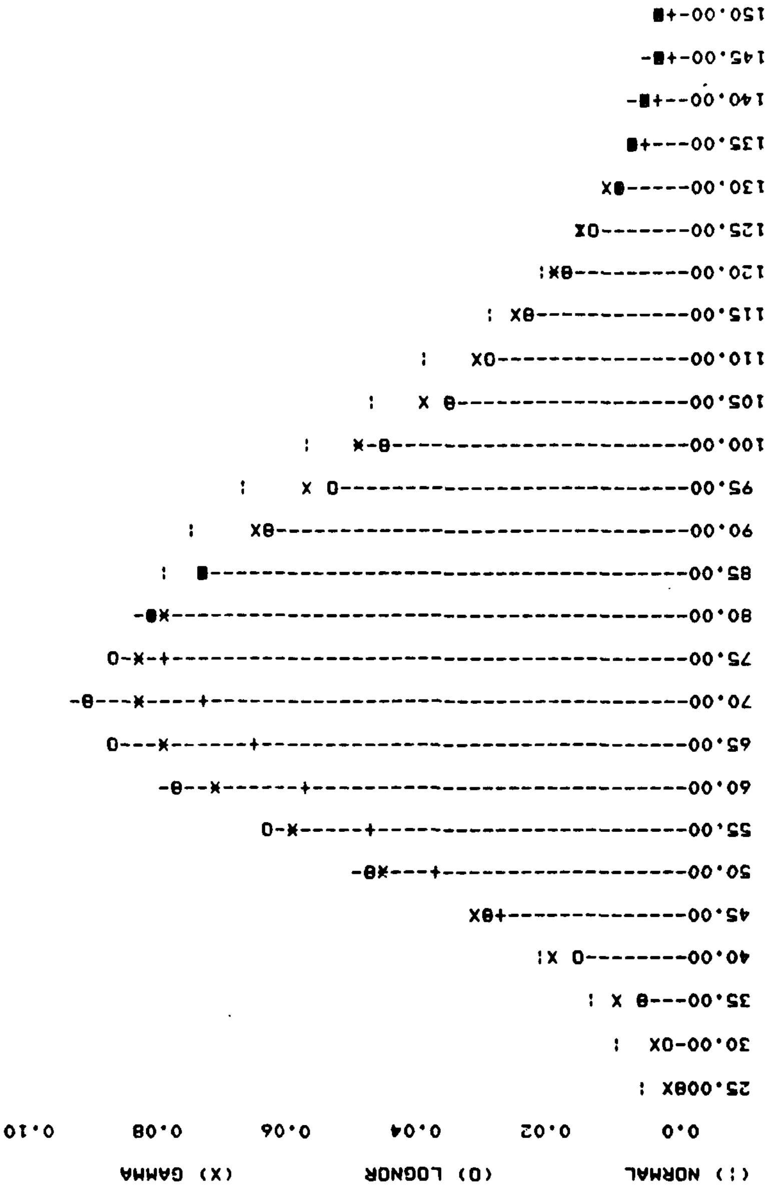

FIGURE 10. REPRESENTATIVE HISTOGRAM.

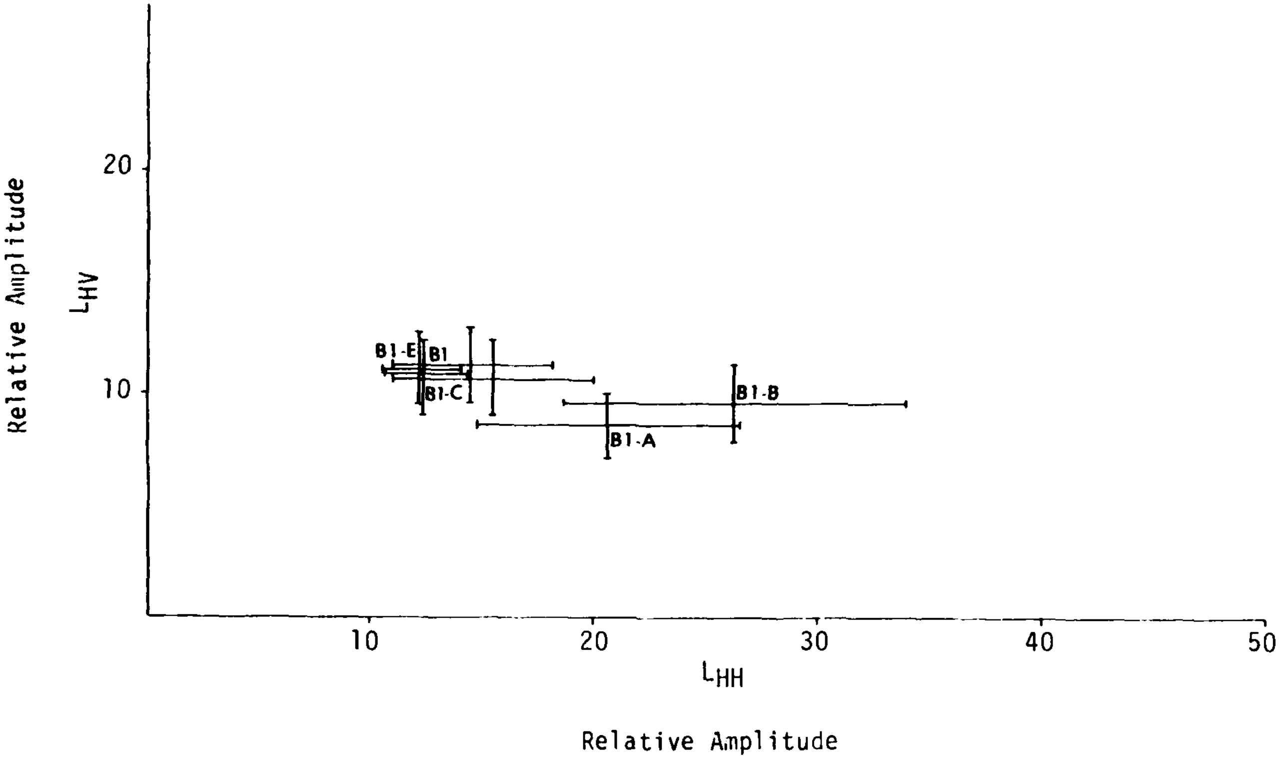

FIGURE 11. REPRESENTATIVE CLUSTER PLOT (L-BAND).

typically provides a 20 dB dynamic range within which only a portion is linear. The resulting brightness compression in radar image photographs may cause many graduational details of radar image intensity to be lost. By going to digital recording, a dynamic range of approximately 40 dB is achievable. This represents a 20 dB improvement over the dynamic range typical of an image recorded directly on film. Digital computers can then be programmed to perform a variety of different measurements. Also, by using the digital approach, much of the subjectiveness of a manual interpretation is removed.

Initial computer processing of the CCTs consisted of subsetting small regions of differing ice types from each of the large digitized areas. Then, for each of these smaller areas, the mean, standard deviation, and number of samples were calculated for 6, 18, and 30 m resolution. Table 4 contains these results and also lists the pertinent processing parameters (e.g., laser power) that were used to normalize the results for more direct comparison.

Also, for each measured mean value and standard deviation, a histogram was drawn. Three other distributions are superimposed on each histogram corresponding to normal, log normal, and gamma. A representative example is shown in Figure 10 with others included as Appendix C.

The measured means and standard deviations produced above were used to form cluster plots, as shown in Figure 11. This is simply a plot of each mean and standard deviation as a function of polarization. It is a very useful tool for deciding which band-polarization combination provides the best discrimination of a specific ice type.

Isorange transects were also taken for the complete length of the digitized areas in the Beaufort Sea. By using a constant-range approach, system effects (e.g., antenna gain, recorder response, power losses, etc.) can be neglected. This process consisted of extracting five adjacent lines of data along constant-range elements;

these were then averaged to form a single line which, in effect, smoothed the data in the range dimension. Next, the data were converted to dB and smoothed using a variable-aperture sliding-window technique. These data were then plotted; an example is shown in Figure 12. It should be noted however, that processing effects (e.g., laser power, etc.) and the effects of differing incidence angles have not been removed at this point; therefore, direct comparisons should only be made between those shown plotted together.

As mentioned previously, four-channel data of a ship and iceberg encompassed by an ice field were collected as part of the SAR-77 program. These data were acquired in digital form, and were processed in order to better understand the ship-ice and iceberg-ice relationships.

Initial digital processing of these data was performed on the ERIM ARIES installation and consisted of:

(1) extracting values of 20-line by 20-point subsets centered on the ship, iceberg, and surrounding clutter (ice),

(2) averaging* these values,

(3) converting to dB, and

(4) calculating signal-to-clutter ratios.

For comparison purposes, this was also done for a ship surrounded by non-frozen water. Also, an attempt was made to graphically portray the ship and iceberg location. This consisted of:

(1) extracting values of 128-line by 128-pixel (192 x 192 m) subsets at the ship and iceberg locations,

(2) averaging these subsets using a 2-line by 2-pixel window, and then

---

*The ship and iceberg averages were defined as the average of the highest 3 dB group of values.

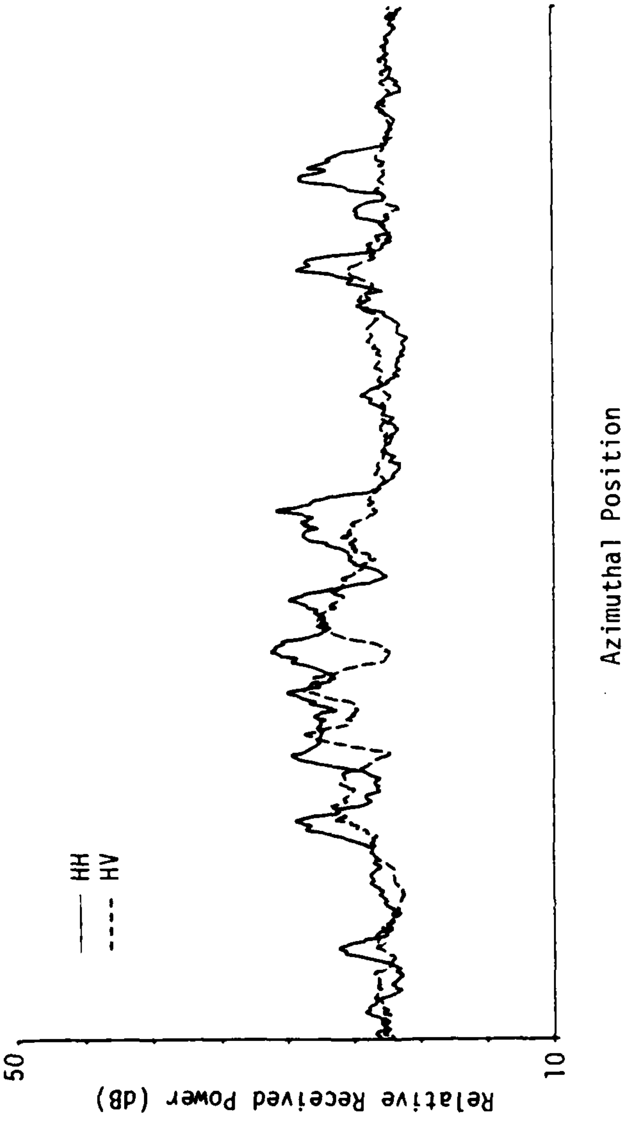

FIGURE 12. REPRESENTATIVE EXAMPLE OF ISORANGE TRANSECTS.

(3) producing plots of alternate lines of these smoothed data using a perspective-view plotting system.

An example of this type of plot is shown in Figure 13.

3.4 DATA ANALYSIS APPROACH

The data from each test area selected are grouped into two sets according to the basic incidence angle. Here, steep incidence angles are defined to be in the range $30^\circ \leq \theta_{inc.} \leq 45^\circ$ while shallow angles fall in the range $76^\circ \leq \theta_{inc.} \leq 83^\circ$. Four basic measurements are made on each of the four channels of data to characterize each set; these are:

(1) mean value (measure of received signal level),

(2) standard deviation (measure of the "roughness" or disorder of the scene),

(3) histogram (distribution of received signal power), and

(4) constant-range-line image scans for relative comparisons of backscatter power (this normalizes for range and antenna response).

Measurements 1-3 were made for all three values of resolution.

These basic measurement results are given in Tables 3 through 21. Values obtained are used in several formats in order to determine trends or signatures to characterize the various ice types included in the data sets. Data formats used are:

(1) cluster plots (mean values of like and cross polarization channels for each wavelength),

(2) standard deviation of backscatter as function of ice type,

(3) coefficient of deviation (standard deviation divided by mean),

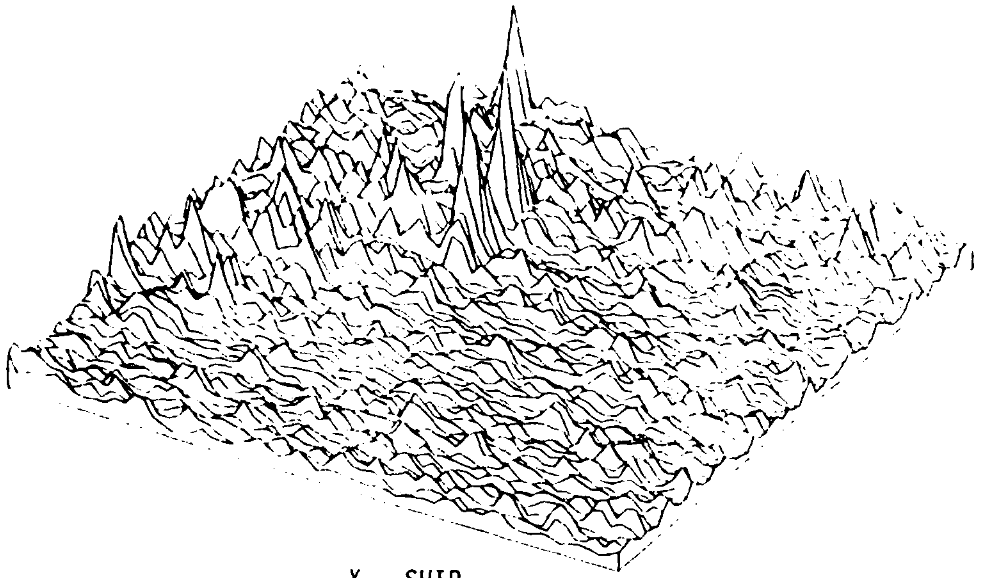

FIGURE 13. REPRESENTATIVE PERSPECTIVE PLOT.

TABLE 3. SUMMARY OF DATA MEASUREMENTS FOR SITE B1-A.

Site[1]	IPL Tape-File	Band (Polarization)	Depression Angle	Resolution (m)	Number of Samples	Measured Mean	Measured Standard Deviation	Laser Power (mW)	Slit Width (μm)	Integration Time (μsec)	Objective Focal Length (mm)	Normalized Mean[2]	Normalized Standard Deviation[2]
B1-A	503-1	X (HH)	12.5°	6	15,000	58.95	20.61	300	20	500	8	41.68	14.57
				18	1,700	58.84	12.42	300	20	500	8	41.61	8.78
				30	600	58.95	9.79	300	20	500	8	41.68	6.92
B1-A	503-2	X (HV)	12.5°	6	15,000	20.68	6.34	300	20	500	8	14.62	4.48
				18	1,700	20.62	3.32	300	20	500	8	14.58	2.35
				30	600	20.68	2.33	300	20	500	8	14.62	1.65
B1-A	508-1	L (HH)	12.5°	6	15,000	20.68	11.80	300	10	500	8	20.68	11.80
				18	1,700	20.64	8.72	300	10	500	8	20.64	8.74
				30	600	20.68	7.16	300	10	500	8	20.68	7.16
B1-A	508-2	L (HV)	12.5°	6	15,000	8.70	2.90	300	10	500	8	8.70	2.90
				18	1,700	8.76	1.68	300	10	500	8	8.76	1.68
				30	600	8.70	1.29	300	10	500	8	8.70	1.29
B1-A	506-1	X (HH)	61.0°	6	15,000	41.48	16.12	300	20	500	8	29.33	11.40
				18	1,700	41.80	12.51	300	20	500	8	29.56	8.85
				30	600	41.48	11.47	300	20	500	8	29.33	8.11
B1-A	506-2	X (HV)	61.0°	6	15,000	18.76	4.57	300	20	500	8	13.27	3.23
				18	1,700	18.79	2.33	300	20	500	8	13.29	1.65
				30	600	18.76	1.78	300	20	500	8	13.27	1.26
B1-A	511-1	L (HH)	61.0°	6	15,000	24.83	8.96	300	10	500	8	24.83	8.96
				18	1,700	24.80	5.68	300	10	500	8	24.80	5.68
				30	600	24.83	4.41	300	10	500	8	24.83	4.41
B1-A	511-2	L (HV)	61.0°	6	15,000	11.27	2.46	300	10	500	8	11.27	2.46
				18	1,700	11.25	1.28	300	10	500	8	11.25	1.28
				30	600	11.27	0.92	300	10	500	8	11.27	0.92

[1] Site 31 was referred to as Site "A" by the SURSAT Beaufort Analysis Team.

[2] Note that the depression angle is simply 90° minus the incidence angle

[3] This normalization only accounted for variations in the digitizing process.

TABLE 4. SUMMARY OF DATA MEASUREMENTS FOR SITE B1-B.

Site	IPL Tape-File	Band (Polarization)	Depression Angle	Resolution (m)	Number of Samples	Measured Mean	Measured Standard Deviation	Laser Power (mW)	Slit Width (μm)	Integration Time (μsec)	Objective Focal Length (mm)	Normalized Mean	Normalized Standard Deviation
B1-B	503-1	X (HH)	12.5°	6	15,000	73.98	27.28	300	20	500	8	52.31	19.29
				18	1,700	73.98	16.44	300	20	500	8	52.31	11.62
				30	600	73.98	12.14	300	20	500	8	52.31	8.58
B1-B	503-2	X (HV)	12.5°	6	15,000	30.25	10.05	300	20	500	8	21.39	7.11
				18	1,700	30.17	5.71	300	20	500	8	21.33	4.04
				30	600	30.25	4.18	300	20	500	8	21.39	2.96
B1-B	508-1	L (HH)	12.5°	6	15,000	26.25	15.22	300	10	500	8	26.25	15.22
				18	1,700	26.26	11.27	300	10	500	8	26.26	11.27
				30	600	26.25	9.06	300	10	500	8	26.25	9.06
B1-B	508-2	L (HV)	12.5°	6	15,000	9.60	3.60	300	10	500	8	9.60	3.60
				18	1,700	9.65	2.18	300	10	500	8	9.65	2.18
				30	600	9.60	1.72	300	10	500	8	9.60	1.72
B1-B	506-1	X (HH)	61.0°	6	15,000	42.96	16.12	300	20	500	8	30.38	11.40
				18	1,700	43.31	12.34	300	20	500	8	30.62	8.73
				30	600	42.96	11.19	300	20	500	8	30.38	7.91
B1-B	506-2	X (HV)	61.0°	6	15,000	19.25	4.72	300	20	500	8	13.61	3.34
				18	1,700	19.27	2.42	300	20	500	8	13.63	1.71
				30	600	19.25	1.78	300	20	500	8	13.61	1.26
B1-B	511-1	L (HH)	61.0°	6	15,000	27.08	10.82	300	10	500	8	27.08	10.82
				18	1,700	27.09	7.46	300	10	500	8	27.09	7.46
				30	600	27.08	6.02	300	10	500	8	27.08	6.02
B1-B	511-2	L (HV)	61.0°	6	15,000	12.38	3.11	300	10	500	8	12.38	3.11
				18	1,700	12.36	1.84	300	10	500	8	12.36	1.84
				30	600	12.38	1.44	300	10	500	8	12.38	1.44

TABLE 5. SUMMARY OF DATA MEASUREMENTS FOR SITE B1-C.

Site	IPL Tape-File	Band (Polarization)	Depression Angle	Resolution (m)	Number of Samples	Measured Mean	Measured Standard Deviation	Laser Power (mW)	Slit Width (μm)	Integration Time (μsec)	Objective Focal Length (mm)	Normalized Mean	Normalized Standard Deviation
B1-C	503-1	X (HH)	7.5°	6	7,875	22.52	8.78	300	20	500	8	15.92	6.21
				18	885	22.61	6.17	300	20	500	8	15.99	4.36
				30	315	22.52	4.74	300	20	500	8	15.92	3.35
B1-C	503-2	X (HV)	7.5°	6	7,875	13.71	3.76	300	20	500	8	9.69	2.66
				18	885	13.71	1.92	300	20	500	8	9.69	1.36
				30	315	13.71	1.41	300	20	500	8	9.69	1.00
B1-C	508-1	L (HH)	7.5°	6	6,750	12.43	3.42	300	10	500	8	12.43	3.42
				18	750	12.43	2.01	300	10	500	8	12.43	2.01
				30	270	12.43	1.53	300	10	500	8	12.43	1.53
B1-C	508-2	L (HV)	7.5°	6	6,750	10.93	3.35	300	10	500	8	10.93	3.35
				18	750	10.93	1.67	300	10	500	8	10.93	1.67
				30	270	10.93	1.13	300	10	500	8	10.93	1.13
B1-C	506-1	X (HH)	41.0°	6	6,750	68.59	21.71	300	20	500	8	48.50	15.35
				18	750	68.59	13.69	300	20	500	8	48.50	9.68
				30	270	68.59	10.39	300	20	500	8	48.50	7.35
B1-C	506-2	X (HV)	41.0°	6	6,750	29.89	7.23	300	20	500	8	21.14	5.11
				18	750	29.89	4.73	300	20	500	8	21.14	3.34
				30	270	29.89	3.74	300	20	500	8	21.14	2.64
B1-C	511-1	L (HH)	41.0°	6	6,750	14.24	9.38	300	10	500	8	14.24	9.38
				18	750	14.24	7.43	300	10	500	8	14.24	7.43
				30	270	14.24	4.99	300	10	500	8	14.24	4.99
B1-C	511-2	L (HV)	41.0°	6	6,750	11.01	2.62	300	10	500	8	11.01	2.62
				18	750	11.01	1.47	300	10	500	8	11.01	1.47
				30	270	11.01	1.10	300	10	500	8	11.01	1.10

TABLE 6. SUMMARY OF DATA MEASUREMENTS FOR SITE B1-D.

Site	IPL Tape-File	Band (Polarization)	Depression Angle	Resolution (m)	Number of Samples	Measured Mean	Measured Standard Deviation	Laser Power (mW)	Slit Width (μm)	Integration Time (μsec)	Objective Focal Length (mm)	Normalized Mean	Normalized Standard Deviation
B1-D	503-1	X (HH)	8.0°	6	15,000	26.06	15.19	300	20	500	8	18.43	10.74
				18	1,700	26.09	11.65	300	20	500	8	18.45	8.24
				30	600	26.06	9.82	300	20	500	8	18.43	6.94
B1-D	503-2	X (HV)	8.0°	6	15,000	14.67	5.69	300	20	500	8	10.37	4.02
				18	1,700	14.68	3.96	300	20	500	8	10.38	2.80
				30	600	14.67	3.11	300	20	500	8	10.37	2.20
B1-D	508-1	L (HH)	8.0°	6	15,000	14.15	7.57	300	10	500	8	14.15	7.57
				18	1,700	14.14	5.78	300	10	500	8	14.14	5.78
				30	600	14.15	4.76	300	10	500	8	14.15	4.76
B1-D	508-2	L (HV)	8.0°	6	15,000	11.15	3.36	300	10	500	8	11.15	3.36
				18	1,700	11.15	1.73	300	10	500	8	11.15	1.73
				30	600	11.15	1.14	300	10	500	8	11.15	1.14
B1-D	506-1	X (HH)	43.0°	6	15,000	78.85	23.57	300	20	500	8	55.76	16.67
				18	1,700	78.79	14.63	300	20	500	8	55.71	10.34
				30	600	78.85	10.90	300	20	500	8	55.76	7.71
B1-D	506-2	X (HV)	43.0°	6	15,000	33.87	10.07	300	20	500	8	23.95	7.12
				18	1,700	33.86	6.43	300	20	500	8	23.94	4.55
				30	600	33.87	5.19	300	20	500	8	23.95	3.67
B1-D	511-1	L (HH)	43.0°	6	15,000	15.66	6.43	300	10	500	8	15.66	6.43
				18	1,700	15.64	4.74	300	10	500	8	15.64	4.74
				30	600	15.66	3.96	300	10	500	8	15.66	3.96
B1-D	511-2	L (HV)	43.0°	6	15,000	10.94	2.76	300	10	500	8	10.94	2.76
				18	1,700	10.95	1.67	300	10	500	8	10.95	1.67
				30	600	10.94	1.32	300	10	500	8	10.94	1.32

TABLE 7. SUMMARY OF DATA MEASUREMENTS FOR SITE B1-E.

Site	IPL Tape-File	Band (Polarization)	Depression Angle	Resolution (m)	Number of Samples	Measured Mean	Measured Standard Deviation	Laser Power (mW)	Slit Width (μm)	Integration Time (μsec)	Objective Focal Length (mm)	Normalized Mean	Normalized Standard Deviation
B1-E	503-1	X (HH)	8.0°	6	13,300	21.96	7.61	300	20	500	8	15.53	5.38
				18	1,530	22.12	6.33	300	20	500	8	15.64	4.48
				30	540	22.01	4.72	300	20	500	8	15.56	3.34
B1-E	503-2	X (HV)	8.0°	6	13,300	13.85	3.69	300	20	500	8	9.79	2.61
				18	1,530	13.84	2.07	300	20	500	8	9.79	1.46
				30	540	13.86	1.50	300	20	500	8	9.80	1.06
B1-E	508-1	L (HH)	8.0°	6	15,000	12.28	3.58	300	10	500	8	12.28	3.58
				18	1,700	12.29	2.45	300	10	500	8	12.29	3.58
				30	600	12.28	1.80	300	10	500	8	12.28	1.80
B1-E	508-2	L (HV)	8.0°	6	15,000	11.15	3.27	300	10	500	8	11.15	3.27
				18	1,700	11.16	1.72	300	10	500	8	11.16	1.72
				30	600	11.15	1.19	300	10	500	8	11.15	1.19
B1-E	506-1	X (HH)	43.0°	6	15,000	78.98	22.91	300	20	500	8	55.85	16.20
				18	1,700	78.96	14.06	300	20	500	8	55.83	9.94
				30	600	78.98	11.08	300	20	500	8	55.85	7.83
B1-E	506-2	X (HV)	43.0°	6	15,000	33.02	8.34	300	20	500	8	23.35	5.90
				18	1,700	33.04	4.78	300	20	500	8	23.36	3.38
				30	600	33.02	3.42	300	20	500	8	23.35	2.42
B1-E	511-1	L (HH)	43.0°	6	13,300	14.44	4.64	300	10	500	8	14.44	4.64
				18	1,530	14.43	3.15	300	10	500	8	14.43	3.15
				30	540	14.44	2.53	300	10	500	8	14.44	2.53
B1-E	511-2	L (HV)	43.0°	6	13,300	10.85	2.65	300	10	500	8	10.85	2.65
				18	1,530	10.85	1.58	300	10	500	8	10.85	1.58
				30	540	10.85	1.24	300	10	500	8	10.85	1.24

TABLE 8. SUMMARY OF DATA MEASUREMENTS FOR SITE B1-F.

Site	IPL Tape-File	Band (Polarization)	Depression Angle	Resolution (m)	Number of Samples	Measured Mean	Measured Standard Deviation	Laser Power (mW)	Slit Width (μm)	Integration Time (μsec)	Objective Focal Length (mm)	Normalized Mean	Normalized Standard Deviation
B1-F	503-1	X (HH)	8.0°	6	15,000	40.95	17.36	300	20	500	8	28.96	12.28
				18	1,700	40.88	12.06	300	20	500	8	28.91	8.53
				30	600	40.95	10.19	300	20	500	8	28.96	7.21
B1-F	503-2	X (HV)	8.0°	6	15,000	15.39	4.27	300	20	500	8	10.88	3.02
				18	1,700	15.37	2.48	300	20	500	8	10.87	1.75
				30	600	15.39	1.91	300	20	500	8	10.88	1.35
B1-F	508-1	L (HH)	8.0°	6	10,000	15.50	8.97	300	10	500	8	15.50	8.97
				18	1,156	15.44	6.36	300	10	500	8	15.44	6.36
				30	400	15.50	5.69	300	10	500	8	15.50	5.69
B1-F	508-2	L (HV)	8.0°	6	10,000	10.77	3.27	300	10	500	8	10.77	3.27
				18	1,156	10.79	1.76	300	10	500	8	10.79	1.76
				30	400	10.77	1.12	300	10	500	8	10.77	1.12
B1-F	506-1	X (HH)	43.0°	6	10,000	84.92	23.38	300	20	500	8	60.05	16.53
				18	1,156	85.03	13.15	300	20	500	8	60.13	9.30
				30	400	84.92	9.66	300	20	500	8	60.05	6.83
B1-F	506-2	X (HV)	43.0°	6	10,000	40.86	10.60	300	20	500	8	28.89	7.50
				18	1,156	40.93	6.09	300	20	500	8	28.94	4.31
				30	400	40.86	4.27	300	20	500	8	28.89	3.02
B1-F	511-1	L (HH)	43.0°	6	10,000	18.98	8.42	300	10	500	8	18.98	8.42
				18	1,156	18.94	6.53	300	10	500	8	18.94	6.53
				30	400	18.98	5.64	300	10	500	8	18.98	5.64
B1-F	511-2	L (HV)	43.0°	6	10,000	11.73	3.03	300	10	500	8	11.73	3.03
				18	1,156	11.72	1.91	300	10	500	8	11.72	1.91
				30	400	11.72	1.56	300	10	500	8	11.72	1.56

TABLE 9. SUMMARY OF DATA MEASUREMENTS FOR SITE B2-A.

Site	IPL Tape-File	Band (Polarization)	Depression Angle	Resolution (m)	Number of Samples	Measured Mean	Measured Standard Deviation	Laser Power (mW)	Slit Width (μm)	Integration Time (μsec)	Objective Focal Length (mm)	Normalized Mean	Normalized Standard Deviation
B2-A	502-1	X (HH)	11.0°	6	6,500	59.11	23.14	300	20	500	8	41.80	16.36
				18	748	59.26	15.57	300	20	500	8	41.90	11.01
				30	260	59.11	11.56	300	20	500	8	41.80	8.17
B2-A	502-2	X (HV)	11.0°	6	6,500	43.16	21.81	300	20	500	8	30.52	15.42
				18	748	43.45	16.91	300	20	500	8	30.72	11.96
				30	260	43.16	14.13	300	20	500	8	30.52	9.99
B2-A	510-1	L (HH)	11.0°	6	6,175	24.07	8.70	300	10	500	8	24.07	8.70
				18	704	24.07	5.67	300	10	500	8	24.07	5.67
				30	247	24.07	4.36	300	10	500	8	24.07	4.36
B2-A	510-2	L (HV)	11.0°	6	6,175	16.54	4.26	300	10	500	8	16.54	4.26
				18	704	16.59	2.91	300	10	500	8	16.59	2.91
				30	247	16.54	1.99	300	10	500	8	16.54	1.99

TABLE 10. SUMMARY OF DATA MEASUREMENTS FOR SITE B2-B.

Site	IPL Tape-File	Band (Polarization)	Depression Angle	Resolution (m)	Number of Samples	Measured Mean	Measured Standard Deviation	Laser Power (mW)	Slit Width (μm)	Integration Time (μsec)	Objective Focal Length (mm)	Normalized Mean	Normalized Standard Deviation
B2-B	502-1	X (HH)	9.0°	6	2,850	34.90	21.02	300	20	500	8	24.68	14.86
				18	325	35.97	19.44	300	20	500	8	25.43	13.75
				30	120	36.85	19.15	300	20	500	8	26.06	13.54
B2-B	502-2	X (HV)	9.0°	6	2,850	23.44	12.38	300	20	500	8	16.57	8.75
				18	325	23.98	10.82	300	20	500	8	16.96	7.65
				30	120	24.43	10.82	300	20	500	8	17.27	7.65
B2-B	510-1	L (HH)	9.0°	6	2,850	24.12	15.31	300	10	500	8	24.12	15.31
				18	325	24.38	13.07	300	10	500	8	24.38	13.07
				30	120	24.65	11.69	300	10	500	8	24.65	11.69
B2-B	510-2	L (HV)	9.0°	6	2,850	16.13	6.70	300	10	500	8	16.13	6.70
				18	325	16.16	5.29	300	10	500	8	16.16	5.29
				30	120	16.18	4.72	300	10	500	8	16.18	4.72
B2-B	505-1	X (HH)	57.0°	6	2,850	71.78	41.55	300	20	500	8	50.76	29.38
				18	325	72.09	35.55	300	20	500	8	50.98	25.14
				30	120	72.41	33.81	300	20	500	8	51.20	23.91
B2-B	505-2	X (HV)	57.0°	6	2,850	36.54	25.51	300	20	500	8	25.84	18.04
				18	325	37.32	23.04	300	20	500	8	26.39	16.29
				30	120	38.18	22.16	300	20	500	8	27.00	15.67
B2-B	513-1	L (HH)	57.0°	6	2,850	27.27	13.51	300	10	500	8	27.27	13.51
				18	325	27.31	10.23	300	10	500	8	27.31	10.23
				30	120	27.30	9.10	300	10	500	8	27.30	9.10
B2-B	513-2	L (HV)	57.0°	6	2,850	16.78	7.50	300	10	500	8	16.78	7.50
				18	325	16.86	5.91	300	10	500	8	16.86	5.91
				30	120	16.93	5.01	300	10	500	8	16.93	5.01

TABLE 11. SUMMARY OF DATA MEASUREMENTS FOR SITE B2-C.

Site	IPL Tape-File	Band (Polarization)	Depression Angle	Resolution (m)	Number of Samples	Measured Mean	Measured Standard Deviation	Laser Power (mW)	Slit Width (μm)	Integration Time (μsec)	Objective Focal Length (mm)	Normalized Mean	Normalized Standard Deviation
B2-C	502-1	X (HH)	8.0°	6	1,125	40.16	26.68	300	20	500	8	28.40	18.87
				18	135	41.10	22.00	300	20	500	8	29.06	15.56
				30	45	40.16	17.40	300	20	500	8	28.40	12.30
B2-C	502-2	X (HV)	8.0°	6	1,125	23.74	15.90	300	20	500	8	16.79	11.24
				18	135	23.79	13.40	300	20	500	8	16.82	9.48
				30	45	23.74	11.15	300	20	500	8	16.79	7.88
B2-C	510-1	L (HH)	8.0°	6	1,125	17.55	5.72	300	10	500	8	17.55	5.72
				18	135	17.81	4.08	300	10	500	8	17.81	4.08
				30	45	17.55	2.85	300	10	500	8	17.55	2.86
B2-C	510-2	L (HV)	8.0°	6	1,125	16.00	6.81	300	10	500	8	16.00	6.81
				18	135	15.92	4.82	300	10	500	8	15.92	4.82
				30	45	16.00	4.38	300	10	500	8	16.00	4.38
B2-C	505-1	X (HH)	52.0°	6	1,125	53.64	25.42	300	20	500	8	37.93	17.97
				18	135	55.04	23.11	300	20	500	8	38.92	16.34
				30	45	53.64	17.78	300	20	500	8	37.93	12.57
B2-C	505-2	X (HV)	52.0°	6	1,125	32.33	17.46	300	20	500	8	22.86	12.35
				18	135	34.14	17.21	300	20	500	8	24.14	12.17
				30	45	32.33	11.85	300	20	500	8	22.86	8.38
B2-C	513-1	L (HH)	52.0°	6	1,125	25.59	11.51	300	10	500	8	25.59	11.51
				18	135	26.29	9.93	300	10	500	8	26.29	9.93
				30	45	25.59	8.19	300	10	500	8	25.59	8.19
B2-C	513-2	L (HV)	52.0°	6	1,125	14.62	4.18	300	10	500	8	14.62	9.18
				18	135	14.93	3.26	300	10	500	8	14.93	3.26
				30	45	14.62	2.09	300	10	500	8	14.62	2.09

TABLE 12. SUMMARY OF DATA MEASUREMENTS FOR SITE B2-D.

Site	IPL Tape-File	Band (Polarization)	Depression Angle	Resolution (m)	Number of Samples	Measured Mean	Measured Standard Deviation	Laser Power (mW)	Slit Width (μm)	Integration Time (μsec)	Objective Focal Length (mm)	Normalized Mean	Normalized Standard Deviation
B2-D	502-1	X (HH)	7.5°	6	13,500	31.44	19.02	300	20	500	8	22.23	13.45
				18	1,500	31.44	13.96	300	20	500	8	22.23	9.87
				30	540	31.44	11.27	300	20	500	8	22.23	7.97
B2-D	502-2	X (HV)	7.5°	6	13,500	16.26	5.11	300	20	500	8	11.50	3.61
				18	1,500	16.26	3.01	300	20	500	8	11.50	2.13
				30	540	16.26	2.29	300	20	500	8	11.50	1.62
B2-D	510-1	L (HH)	7.5°	6	13,500	15.07	7.07	300	10	500	8	15.07	7.07
				18	1,500	15.07	5.04	300	10	500	8	15.07	5.04
				30	540	15.07	4.02	300	10	500	8	15.07	4.02
B2-D	510-2	L (HV)	7.5°	6	13,500	14.05	3.91	300	10	500	8	14.05	3.91
				18	1,500	14.05	2.18	300	10	500	8	14.05	2.18
				30	540	14.05	1.61	300	10	500	8	14.05	1.61
B2-D	505-1	X (HH)	49.0°	6	9,000	79.24	27.50	300	20	500	8	56.03	19.45
				18	1,000	79.24	17.90	300	20	500	8	56.03	12.66
				30	360	79.24	14.00	300	20	500	8	56.03	9.90
B2-D	505-2	X (HV)	49.0°	6	9,000	30.59	12.42	300	20	500	8	21.63	8.78
				18	1,000	30.59	9.02	300	20	500	8	21.63	6.38
				30	360	30.59	7.51	300	20	500	8	21.63	5.31
B2-D	513-1	L (HH)	49.0°	6	9,000	25.34	13.15	300	10	500	8	25.34	13.15
				18	1,000	25.34	9.93	300	10	500	8	25.34	9.93
				30	360	25.34	8.27	300	10	500	8	25.34	8.27
B2-D	513-2	L (HV)	49.0°	6	9,000	13.11	4.75	300	10	500	8	13.11	4.75
				18	1,000	13.11	3.59	300	10	500	8	13.11	3.59
				30	360	13.11	3.13	300	10	500	8	13.11	3.13

TABLE 13. SUMMARY OF DATA MEASUREMENTS FOR SITE B2-E.

Site	IPL Tape-File	Band (Polarization)	Depression Angle	Resolution (m)	Number of Samples	Measured Mean	Measured Standard Deviation	Laser Power (mW)	Slit Width (μm)	Integration Time (μsec)	Objective Focal Length (mm)	Normalized Mean	Normalized Standard Deviation
B2-E	502-1	X (HH)	7.5°	6	12,000	61.61	31.13	300	20	500	8	43.56	22.01
				18	1,350	61.86	21.98	300	20	500	8	43.74	15.54
				30	480	61.68	18.06	300	20	500	8	43.61	12.77
B2-E	502-2	X (HV)	7.5°	6	12,000	44.53	25.43	300	20	500	8	31.49	17.98
				18	1,350	44.72	19.06	300	20	500	8	31.62	13.48
				30	480	44.53	16.18	300	20	500	8	31.49	11.94
B2-E	510-1	L (HH)	7.5°	6	12,000	26.10	13.35	300	10	500	8	26.10	13.35
				18	1,350	26.13	9.29	300	10	500	8	26.13	9.29
				30	480	26.10	7.36	300	10	500	8	26.10	7.36
B2-E	510-2	L (HV)	7.5°	6	12,000	20.72	9.20	300	10	500	8	20.72	9.20
				18	1,350	20.71	6.46	300	10	500	8	20.71	6.46
				30	480	20.72	5.12	300	10	500	8	20.72	5.12
B2-E	505-1	X (HH)	51.0°	6	12,000	97.30	34.06	300	20	500	8	68.80	24.08
				18	1,350	97.31	24.12	300	20	500	8	68.81	17.06
				30	480	97.30	20.38	300	20	500	8	68.80	14.41
B2-E	505-2	X (HV)	51.0°	6	12,000	87.74	36.81	300	20	500	8	62.04	26.03
				18	1,350	87.89	27.69	300	20	500	8	62.15	19.58
				30	480	87.84	23.68	300	20	500	8	62.04	16.74
B2-E	513-1	L (HH)	51.0°	6	12,000	32.34	12.90	300	10	500	8	32.34	12.90
				18	1,350	32.34	9.09	300	10	500	8	32.34	9.09
				30	480	32.34	7.36	300	10	500	8	32.34	7.36
B2-E	513-2	L (HV)	51.0°	6	12,000	21.62	9.38	300	10	500	8	21.62	9.38
				18	1,350	21.60	6.78	300	10	500	8	21.60	6.78
				30	480	21.62	5.56	300	10	500	8	21.62	5.56

TABLE 14. SUMMARY OF DATA MEASUREMENTS FOR SITE B2-F.

Site	IPL Tape-File	Band (Polarization)	Depression Angle	Resolution (m)	Number of Samples	Measured Mean	Measured Standard Deviation	Laser Power (mW)	Slit Width (μm)	Integration Time (μsec)	Objective Focal Length (mm)	Normalized Mean	Normalized Standard Deviation
B2-F	502-1	X (HH)	7.5°	6	15,000	46.84	17.80	300	20	500	8	33.12	12.59
				18	1,700	46.73	11.14	300	20	500	8	33.04	7.88
				30	600	46.84	7.66	300	20	500	8	33.12	5.42
B2-F	502-2	X (HV)	7.5°	6	15,000	21.37	7.60	300	20	500	8	15.11	5.37
				18	1,700	21.36	4.68	300	20	500	8	15.10	3.31
				30	600	21.37	3.09	300	20	500	8	15.11	2.18
B2-F	510-1	L (HH)	7.5°	6	15,000	13.83	3.70	300	10	500	8	13.83	3.70
				18	1,700	13.80	2.25	300	10	500	8	13.80	2.25
				30	600	13.83	1.84	300	10	500	8	13.83	1.84
B2-F	510-2	L (HV)	7.5°	6	15,000	13.63	3.30	300	10	500	8	13.63	3.30
				18	1,700	13.60	1.55	300	10	500	8	13.60	1.55
				30	600	13.63	1.02	300	10	500	8	13.63	1.02
B2-F	505-1	X (HH)	48.0°	6	15,000	94.85	26.83	300	20	500	8	67.07	18.97
				18	1,700	94.74	15.65	300	20	500	8	66.99	11.07
				30	600	94.85	10.60	300	20	500	8	67.07	7.50
B2-F	505-2	X (HV)	48.0°	6	15,000	80.28	24.51	300	20	500	8	56.77	17.33
				18	1,700	80.27	14.67	300	20	500	8	56.76	10.37
				30	600	80.28	9.96	300	20	500	8	56.77	7.04
B2-F	513-1	L (HH)	48.0°	6	15,000	25.33	7.25	300	10	500	8	25.33	7.25
				18	1,700	25.24	4.41	300	10	500	8	25.24	4.41
				30	600	25.33	3.35	300	10	500	8	25.33	3.35
B2-F	513-2	L (HV)	48.0°	6	15,000	12.37	2.71	300	10	500	8	12.37	2.71
				18	1,700	12.39	1.59	300	10	500	8	12.39	1.59
				30	600	12.37	1.28	300	10	500	8	12.37	1.28

TABLE 15. SUMMARY OF DATA MEASUREMENTS FOR SITE B2-G.

Site	IPL Tape-File	Band (Polarization)	Depression Angle	Resolution (m)	Number of Samples	Measured Mean	Measured Standard Deviation	Laser Power (mW)	Slit Width (μm)	Integration Time (μsec)	Objective Focal Length (mm)	Normalized Mean	Normalized Standard Deviation
B2-G	502-1	X (HH)	7.0°	6	9,000	21.13	5.55	300	20	500	8	14.94	3.92
				18	1,000	21.13	2.81	300	20	500	8	14.94	1.99
				30	360	21.13	1.86	300	20	500	8	14.94	1.32
B2-G	502-2	X (HV)	7.0°	6	9,000	14.88	4.57	300	20	500	8	10.52	3.23
				18	1,000	14.88	2.32	300	20	500	8	10.52	1.64
				30	360	14.88	1.70	300	20	500	8	10.52	1.20
B2-G	510-1	L (HH)	7.0°	6	9,000	11.59	2.88	300	10	500	8	11.59	2.88
				18	1,000	11.59	1.38	300	10	500	8	11.59	1.38
				30	360	11.59	0.97	300	10	500	8	11.59	0.97
B2-G	510-2	L (HV)	7.0°	6	9,000	13.49	3.28	300	10	500	8	13.49	3.28
				18	1,000	13.49	1.82	300	10	500	8	13.49	1.82
				30	360	13.49	1.21	300	10	500	8	13.49	1.21
B2-G	505-1	X (HH)	46.0°	6	7,200	76.88	21.40	300	20	500	8	54.36	15.13
				18	800	76.88	13.02	300	20	500	8	54.36	9.21
				30	288	76.88	10.08	300	20	500	8	54.36	7.13
B2-G	505-2	X (HV)	46.0°	6	7,200	26.79	7.44	300	20	500	8	18.94	5.26
				18	800	26.79	4.78	300	20	500	8	18.94	3.38
				30	288	26.79	3.78	300	20	500	8	18.94	2.67
B2-G	513-1	L (HH)	46.0°	6	7,200	16.19	5.56	300	10	500	8	16.19	5.56
				18	800	16.19	4.06	300	10	500	8	16.19	4.06
				30	288	16.19	3.40	300	10	500	8	16.19	3.40
B2-G	513-2	L (HV)	46.0°	6	7,200	11.63	2.51	300	10	500	8	11.63	2.51
				18	800	11.63	1.36	300	10	500	8	11.63	1.36
				30	288	11.63	1.02	300	10	500	8	11.63	1.02

TABLE 16. SUMMARY OF DATA MEASUREMENTS FOR SITE B2-H.

Site	IPL Tape-File	Band (Polarization)	Depression Angle	Resolution (m)	Number of Samples	Measured Mean	Measured Standard Deviation	Laser Power (mW)	Slit Width (μm)	Integration Time (μsec)	Objective Focal Length (mm)	Normalized Mean	Normalized Standard Deviation
B2-H	502-1	X (HH)	7.0°	6	10,000	36.28	22.95	300	20	500	8	25.65	16.32
				18	1,156	36.23	16.90	300	20	500	8	25.62	11.88
				30	400	36.28	13.63	300	20	500	8	25.65	9.64
B2-H	502-2	X (HV)	7.0°	6	10,000	17.58	7.51	300	20	500	8	12.43	5.31
				18	1,156	17.53	5.09	300	20	500	8	12.40	3.60
				30	400	17.58	4.09	300	20	500	8	12.43	2.89
B2-H	510-1	L (HH)	7.0°	6	10,000	15.25	8.12	300	10	500	8	15.25	8.13
				18	1,156	15.19	5.87	300	10	500	8	15.19	5.87
				30	400	15.25	4.64	300	10	500	8	15.25	6.16
B2-H	510-2	L (HV)	7.0°	6	10,000	16.50	6.16	300	10	500	8	16.50	6.16
				18	1,156	16.44	4.33	300	10	500	8	16.44	4.33
				30	400	16.50	3.65	300	10	500	8	16.50	3.65
B2-H	505-1	X (HH)	44.0°	6	5,000	83.85	38.92	300	20	500	8	59.29	27.17
				18	578	84.26	30.58	300	20	500	8	59.58	21.62
				30	200	83.85	25.85	300	20	500	8	59.29	18.28
B2-H	505-2	X (HV)	44.0°	6	5,000	45.39	29.82	300	20	500	8	32.10	21.09
				18	578	45.92	25.43	300	20	500	8	32.47	17.98
				30	200	45.39	21.46	300	20	500	8	32.10	15.17
B2-H	513-1	L (HH)	44.0°	6	10,000	25.21	11.94	300	10	500	8	25.21	11.94
				18	1,156	25.31	9.40	300	10	500	8	25.31	9.40
				30	400	25.21	8.05	300	10	500	8	25.21	8.05
B2-H	513-2	L (HV)	44.0°	6	10,000	16.66	7.94	300	10	500	8	16.66	7.94
				18	1,156	16.76	6.73	300	10	500	8	16.76	6.73
				30	400	16.66	5.47	300	10	500	8	16.66	5.47

TABLE 17. SUMMARY OF DATA MEASUREMENTS FOR SITE B2-I.

Site	IPL Tape-File	Band (Polarization)	Depression Angle	Resolution (m)	Number of Samples	Measured Mean	Measured Standard Deviation	Laser Power (mW)	Slit Width (μm)	Integration Time (usec)	Objective Focal Length (mm)	Normalized Mean	Normalized Standard Deviation
B2-I	502-1	X (HH)	7.0°	6	10,625	40.21	26.59	300	20	500	8	28.43	18.80
				18	1,218	40.18	20.58	300	20	500	8	28.41	14.55
				30	425	40.21	17.72	300	20	500	8	28.43	12.53
B2-I	502-2	X (HV)	7.0°	6	10,625	25.92	18.50	300	20	500	8	18.33	13.08
				18	1,218	26.00	14.51	300	20	500	8	18.38	10.26
				30	425	25.92	12.05	300	20	500	8	18.33	8.52
B2-I	510-1	L (HH)	7.0°	6	10,625	15.63	8.54	300	10	500	8	15.63	8.54
				18	1,218	15.54	6.20	300	10	500	8	15.54	6.20
				30	425	15.63	5.34	300	10	500	8	15.63	5.34
B2-I	510-2	L (HV)	7.0°	6	10,625	15.35	5.66	300	10	500	8	15.35	5.66
				18	1,218	15.35	4.03	300	10	500	8	15.35	4.03
				30	425	15.35	3.38	300	10	500	8	15.35	3.38
B2-I	505-1	X (HH)	48.0°	6	10,625	96.44	38.85	300	20	500	8	68.19	27.47
				18	1,218	96.10	30.10	300	20	500	8	67.95	21.28
				30	425	96.43	25.50	300	20	500	8	68.19	18.03
B2-I	505-2	X (HV)	48.0°	6	10,625	77.90	41.97	300	20	500	8	55.08	29.68
				18	1,218	78.85	35.09	300	20	500	8	55.76	24.81
				30	425	77.90	30.43	300	20	500	8	55.08	21.52
B2-I	513-1	L (HH)	48.0°	6	10,625	24.31	12.38	300	10	500	8	24.31	12.38
				18	1,218	24.15	9.88	300	10	500	8	24.15	9.88
				30	425	24.31	8.64	300	10	500	8	24.31	8.64
B2-I	513-2	L (HV)	48.0°	6	10,625	15.15	6.86	300	10	500	8	15.15	6.86
				18	1,218	15.11	5.44	300	10	500	8	15.11	5.44
				30	425	15.15	4.65	300	10	500	8	15.15	4.65

TABLE 18. SUMMARY OF DATA MEASUREMENTS FOR SITES H1-A AND H1-B.

Site	IPL Tape-File	Band (Polarization)	Depression Angle	Resolution (m)	Number of Samples	Measured Mean	Measured Standard Deviation	Laser Power (mW)	Slit Width (μm)	Integration Time (μsec)	Objective Focal Length (mm)	Normalized Mean	Normalized Standard Deviation
H1-A	426-1	X (HH)	23.0°	6	2,500	26.00	6.62	200	5	900	22.7	11.83	3.01
				18	289	25.92	4.56	200	5	900	22.7	11.79	2.07
				30	100	26.00	3.55	200	5	900	22.7	11.83	1.62
H1-A	426-2	X (HV)	23.0°	6	2,500	14.39	4.49	200	5	900	22.7	6.55	2.04
				18	289	14.29	3.21	200	5	900	22.7	6.50	1.46
				30	100	14.39	2.57	200	5	900	22.7	6.55	1.17
H1-A	418-1	L (HH)	23.0°	6	2,500	20.13	3.87	400	5	900	22.7	6.48	1.25
				18	289	20.13	2.47	400	5	900	22.7	6.48	0.79
				30	100	20.13	1.96	400	5	900	22.7	6.48	0.63
H1-A	418-2	L (HV)	23.0°	6	2,500	27.83	4.89	400	5	900	22.7	8.95	1.57
				18	289	27.78	3.19	400	5	900	22.7	8.94	1.03
				30	100	27.83	2.27	400	5	900	22.7	8.95	0.73
H1-B	426-1	X (HH)	23.0°	6	2,500	20.62	6.59	200	5	900	22.7	9.38	3.00
				18	289	20.50	5.13	200	5	900	22.7	9.33	2.33
				30	100	20.62	4.48	200	5	900	22.7	9.38	2.04
H1-B	426-2	X (HV)	23.0°	6	2,500	10.45	2.36	200	5	900	22.7	4.75	1.07
				18	289	10.42	1.42	200	5	900	22.7	4.74	0.65
				30	100	10.45	1.15	200	5	900	22.7	4.75	0.52
H1-B	418-1	L (HH)	23.0°	6	2,500	15.83	2.56	400	5	900	22.7	5.09	0.82
				18	289	15.85	1.78	400	5	900	22.7	5.10	0.57
				30	100	15.83	1.48	400	5	900	22.7	5.09	0.48
H1-B	418-2	L (HV)	23.0°	6	2,500	23.98	4.10	400	5	900	22.7	7.71	1.32
				18	289	23.92	2.83	400	5	900	22.7	7.70	0.91
				30	100	23.98	2.13	400	5	900	22.7	7.71	0.69

TABLE 19. SUMMARY OF DATA MEASUREMENTS FOR SITE H1-C.

Site	IPL Tape-File	Band (Polarization)	Depression Angle	Resolution (m)	Number of Samples	Measured Mean	Measured Standard Deviation	Laser Power (mW)	Slit Width (μm)	Integration Time (μsec)	Objective Focal Length (mm)	Normalized Mean	Normalized Standard Deviation
H1-C	426-1	X (HH)	23.0°	6	2,500	18.26	4.04	200	5	900	22.7	8.31	1.84
				18	289	18.28	2.70	200	5	900	22.7	8.32	1.27
				30	100	18.26	2.15	200	5	900	22.7	8.31	0.98
H1-C	426-2	X (HV)	23.0°	6	2,500	10.58	2.04	200	5	900	22.7	4.81	0.93
				18	289	10.57	1.16	200	5	900	22.7	4.81	0.53
				30	100	10.58	0.87	200	5	900	22.7	4.81	0.40
H1-C	418-1	L (HH)	23.0°	6	2,500	23.20	3.86	400	5	900	22.7	7.46	1.24
				18	289	23.16	2.69	400	5	900	22.7	7.45	0.87
				30	100	23.20	2.01	400	5	900	22.7	7.46	0.65
H1-C	418-2	L (HV)	23.0°	6	2,500	15.44	2.12	400	5	900	22.7	4.97	0.68
				18	289	15.49	1.38	400	5	900	22.7	4.98	0.44
				30	100	15.44	0.98	400	5	900	22.7	4.97	0.32

TABLE 20. SUMMARY OF DATA MEASUREMENTS FOR SITES H2-A, H2-B, AND H2-C.

Site	IPL Tape-File	Band (Polarization)	Depression Angle	Resolution (m)	Number of Samples	Measured Mean	Measured Standard Deviation	Laser Power (mW)	Slit Width (μm)	Integration Time (μsec)	Objective Focal Length (mm)	Normalized Mean	Normalized Standard Deviation
H2-A	422-1	L (HH)	58.0°	6	500	35.86	10.42	400	5	900	22.7	11.54	3.35
				18	63	35.69	5.92	400	5	900	22.7	11.48	1.90
				30	20	35.86	3.87	400	5	900	22.7	11.54	1.25
H2-A	421-1	L (HV)	58.0°	6	500	31.50	7.20	400	5	900	22.7	10.13	2.32
				18	63	31.92	4.57	400	5	900	22.7	10.27	1.47
				30	20	31.50	3.29	400	5	900	22.7	10.13	1.06
H2-B	422-1	L (HH)	58.0°	6	500	20.56	4.56	400	5	900	22.7	6.61	1.47
				18	63	20.50	2.54	400	5	900	22.7	6.60	0.82
				30	20	20.56	1.55	400	5	900	22.7	6.61	0.50
H2-B	421-1	L (HV)	58.0°	6	500	15.05	3.38	400	5	900	22.7	4.84	1.09
				18	63	14.97	2.47	400	5	900	22.7	4.82	0.79
				30	20	15.05	2.24	400	5	900	22.7	4.84	0.72
H2-C	422-1	L (HH)	58.0°	6	500	34.98	9.02	400	5	900	22.7	11.25	2.90
				18	63	34.87	4.57	400	5	900	22.7	11.22	1.47
				30	20	34.98	2.46	400	5	900	22.7	11.25	0.79
H2-C	421-1	L (HV)	58.0°	6	500	34.61	8.78	400	5	900	22.7	11.13	2.82
				18	63	34.64	5.32	400	5	900	22.7	11.14	1.71
				30	20	34.61	3.71	400	5	900	22.7	11.13	1.19

TABLE 21. SUMMARY OF DATA MEASUREMENTS FOR SITES H3-A, H3-B, AND H4-A.

Site	IPL Tape-File	Band (Polarization)	Depression Angle	Resolution (m)	Number of Samples	Measured Mean	Measured Standard Deviation	Laser Power (mW)	Slit Width (μm)	Integration Time (μsec)	Objective Focal Length (mm)	Normalized Mean	Normalized Standard Deviation
H3-A	424-1	X (HH)	47.0°	6	12,500	26.20	8.50	200	5	900	22.7	11.92	3.87
				18	1,428	26.20	5.09	200	5	900	22.7	11.92	2.32
				30	500	26.20	3.57	200	5	900	22.7	11.92	1.62
H3-A	424-4	X (HV)	47.0°	6	12,500	10.30	3.49	200	5	900	22.7	4.69	1.59
				18	1,428	10.32	2.30	200	5	900	22.7	4.70	1.05
				30	500	10.30	1.80	200	5	900	22.7	4.69	0.82
H3-A	416-4	L (HH)	47.0°	6	12,500	10.09	3.84	25	5	900	22.7	12.98	4.94
				18	1,428	10.01	2.90	25	5	900	22.7	12.88	3.73
				30	500	10.09	2.63	25	5	900	22.7	12.98	3.38
H3-A	416-1	L (HV)	47.0°	6	12,500	14.86	3.26	100	5	900	22.7	9.56	2.10
				18	1,428	14.86	2.03	100	5	900	22.7	9.56	1.31
				30	500	14.86	1.55	100	5	900	22.7	9.56	1.00
H3-B	424-1	X (HH)	47.0°	6	12,500	26.66	10.03	200	5	900	22.7	12.13	4.56
				18	1,428	26.65	6.60	200	5	900	22.7	12.13	3.00
				30	500	26.66	4.72	200	5	900	22.7	12.13	2.15
H3-B	424-4	X (HV)	47.0°	6	12,500	11.04	4.26	200	5	900	22.7	5.02	1.94
				18	1,428	11.03	3.04	200	5	900	22.7	5.02	1.38
				30	500	11.04	2.37	200	5	900	22.7	5.02	1.08
H4-A	424-2	X (HH)	47.0°	6	12,500	24.30	6.65	200	5	900	22.7	11.06	3.03
				18	1,428	24.35	4.03	200	5	900	22.7	11.08	1.83
				30	500	24.30	3.26	200	5	900	22.7	11.06	1.48
H4-A	424-5	X (HV)	47.0°	6	12,500	9.08	2.21	200	5	900	22.7	4.13	1.01
				18	1,428	9.09	1.25	200	5	900	22.7	4.14	0.57
				30	500	9.08	0.99	200	5	900	22.7	4.13	0.45
H4-A	416-5	L (HH)	47.0°	6	12,500	12.84	4.18	25	5	900	22.7	16.52	5.38
				18	1,428	12.76	2.78	25	5	900	22.7	16.42	3.58
				30	500	12.84	2.30	25	5	900	22.7	16.52	2.96
H4-A	416-2	L (HV)	47.0°	6	12,500	16.57	4.02	100	5	900	22.7	10.66	2.59
				18	1,428	16.56	2.77	100	5	900	22.7	10.66	1.78
				30	500	16.57	2.26	100	5	900	22.7	10.66	1.45

(4) polarization ratio (HH mean divided by HV mean),

(5) polarization ratio (HH divided by coefficient of deviation HV coefficient of deviation),

(6) signal-to-clutter ratios for ships and iceberg, and

(7) probability of detection of above ships and iceberg.

Each cluster plot presents the values of received signal return at parallel polarization versus the signal received on the cross (orthogonal) polarization channel for a given wavelength. The two receiver channels on each wavelength (3 cm and 23 cm) are matched in terms of overall transfer function so as to make comparison meaningful. Normalization of all the digital records was carried out to permit the measured digital values of received signal levels to be compared. These normalizations are summarized in Tables 3 through 21. The SAR system does not include absolute calibration; therefore, the measured values from receive channels at different wavelengths cannot be compared. However, the cluster diagrams are given for each operating wavelength to show the grouping or classification of the received signal as a function of ice type. These classifications can be compared to the response or received power level.

The standard deviation and the coefficient of deviation are presented in both tabular and graphical format as a function of ice type. Both of these parameters give measures of the disorder or roughness of the ice area, particularly the coefficient of deviation. Comparison of these parameter values, as a function of ice type, provides a measure of relative roughness. Similarly, the histogram presents a distribution of the range or spread of values of radar cross section included in the areas.

Depolarization is dependent to a large part upon the surface roughness and the dielectric constant of the scattering material (ice). This effect is indicative of the amount of multi-scatter and volume scatter (although depolarization can also occur from single scatter interaction). Using the values of both polarization ratios, these properties are compared as a function of ice type.

4
RESULTS

Discussed in this section are the results produced by the variety of different analyses and measurements performed during this study. These include:

(1) interpretation of cluster diagrams,

(2) standard deviation-to-mean ratios,

(3) isorange scans,

(4) dynamic range measurements,

(5) relative backscatter values,

(6) histogram analysis,

(7) polarization ratios of both means and coefficients of deviation,

(8) signal-to-clutter ratios of both ships and icebergs, and

(9) graphical display of ship and iceberg location.

4.1 CLUSTER DIAGRAMS

Cluster diagrams showing the signal amplitude received on each of the four SAR channels for both steep and shallow incidence angles are given in Figures 14 through 18. All of the results given in these figures are for 6 x 6 m resolution data, except where otherwise indicated. Results obtained from the Beaufort Sea area 2 are given in Figure 14. The multi-year ice areas (B2-E, B2-I and B2-F) are seen to cluster with large signal return on the X_{HV} channel, particularly for steep incidence angle ($\theta_{inc.} = 40°$). Signal returns at X-band from other ice types included in area 2 do not separate. Also, it is clear, from the results shown, that signal returns at L-band for the various ice types in area 2 cluster together for both

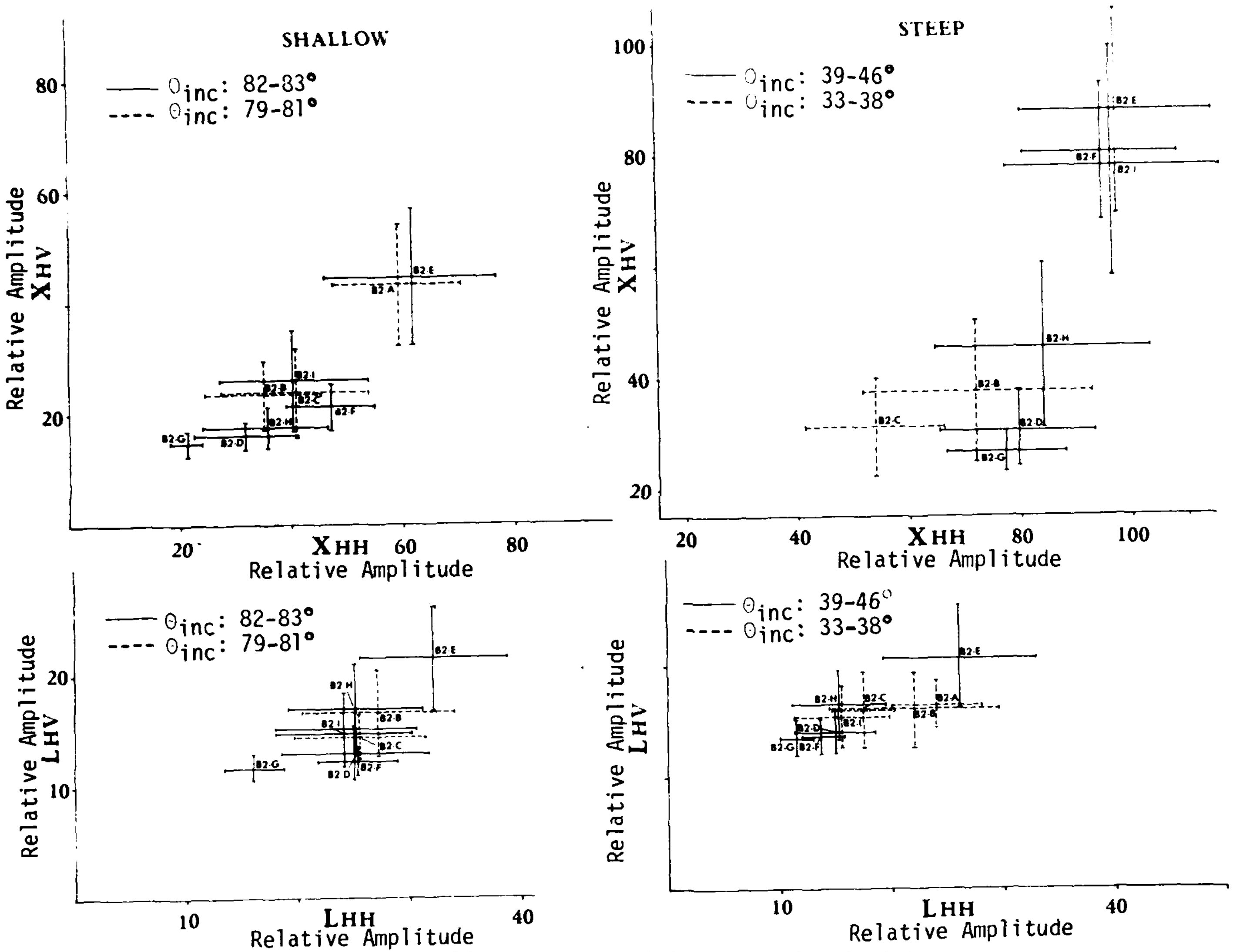

FIGURE 14.. CLUSTER PLOTS OF BEAUFORT AREA 2.

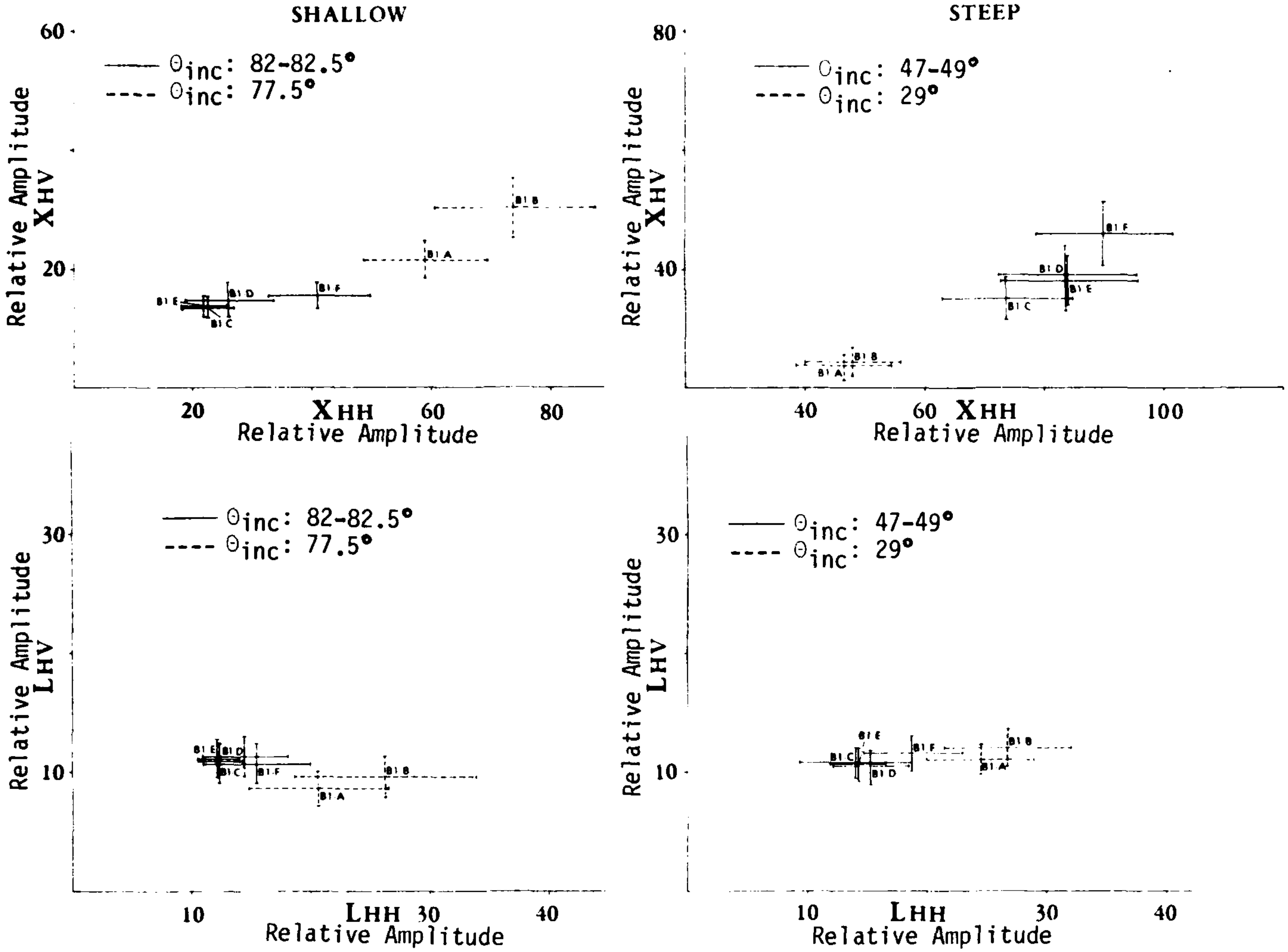

FIGURE 15. CLUSTER PLOTS OF BEAUFORT AREA 1.

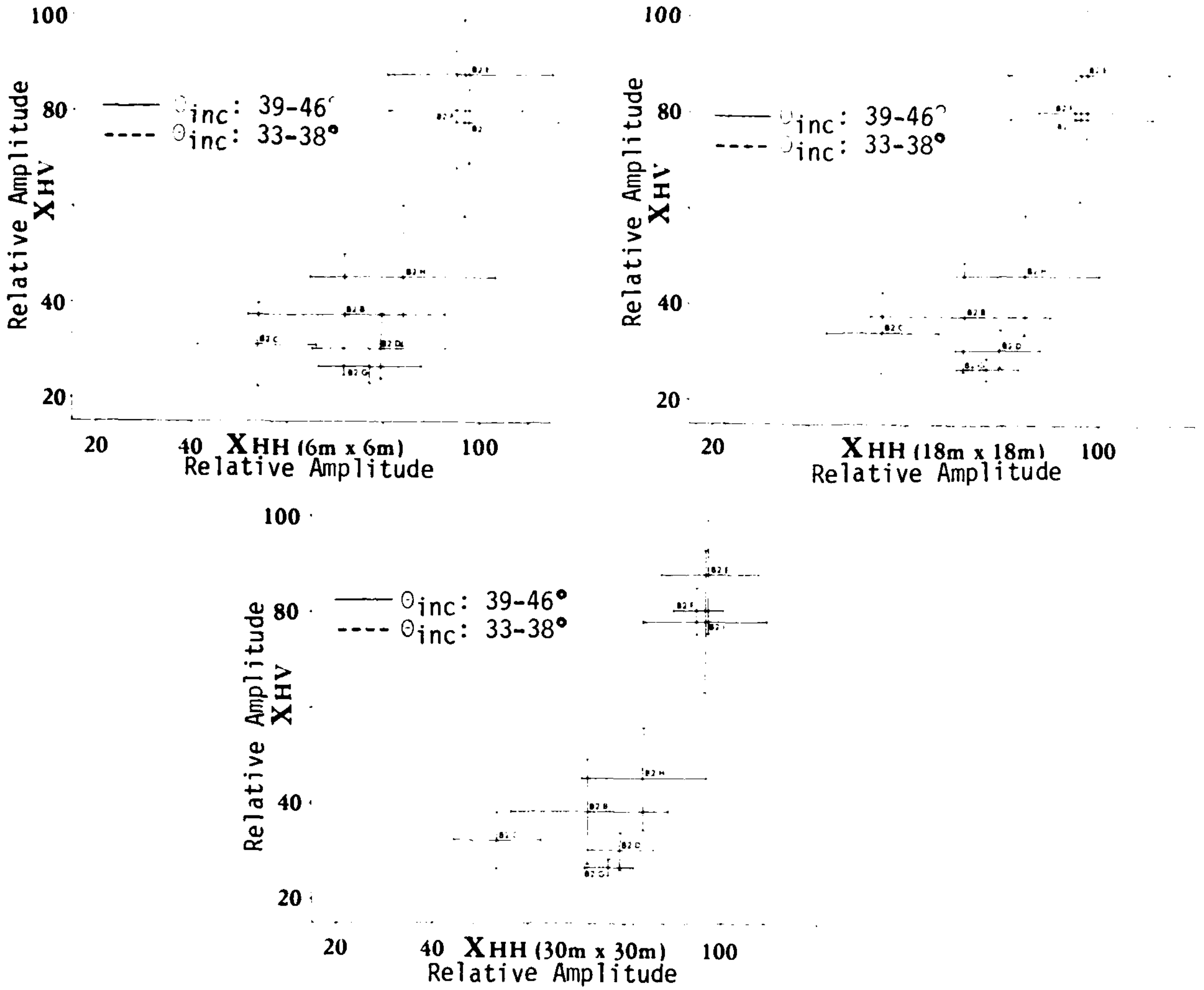

FIGURE 16. CLUSTER PLOTS SHOWING EFFECT OF VARYING RESOLUTION.

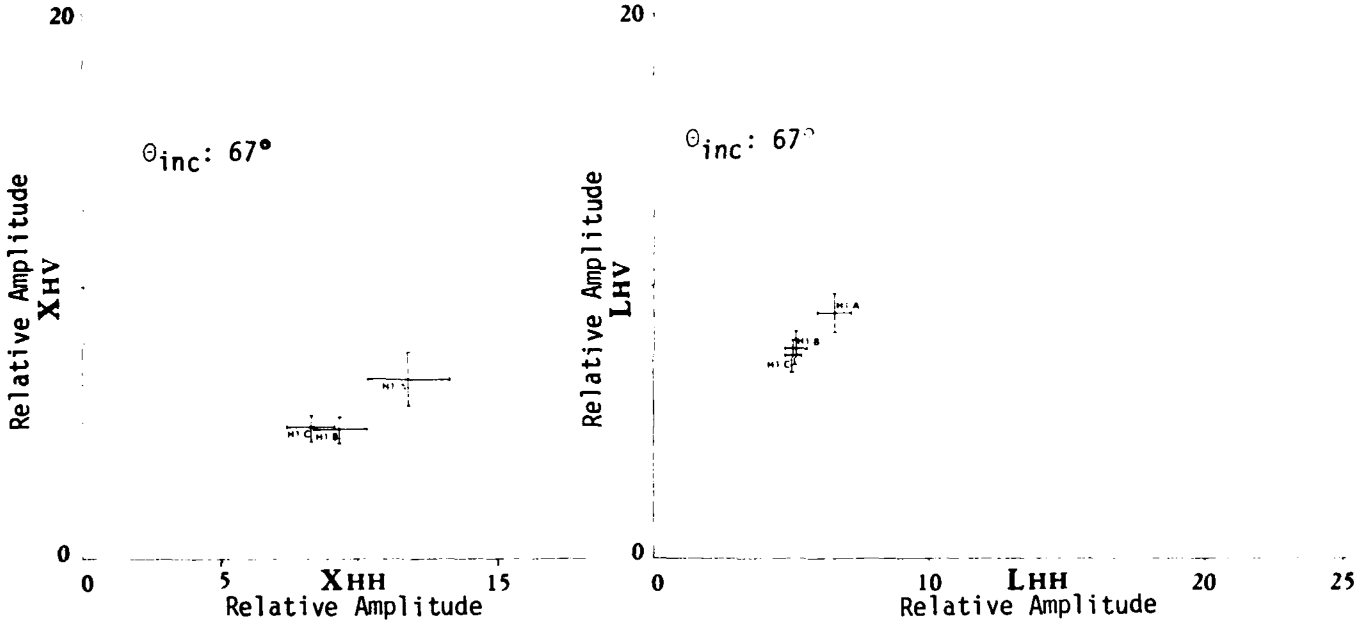

FIGURE 17. CLUSTER PLOTS OF HOPEDALE AREA 1.

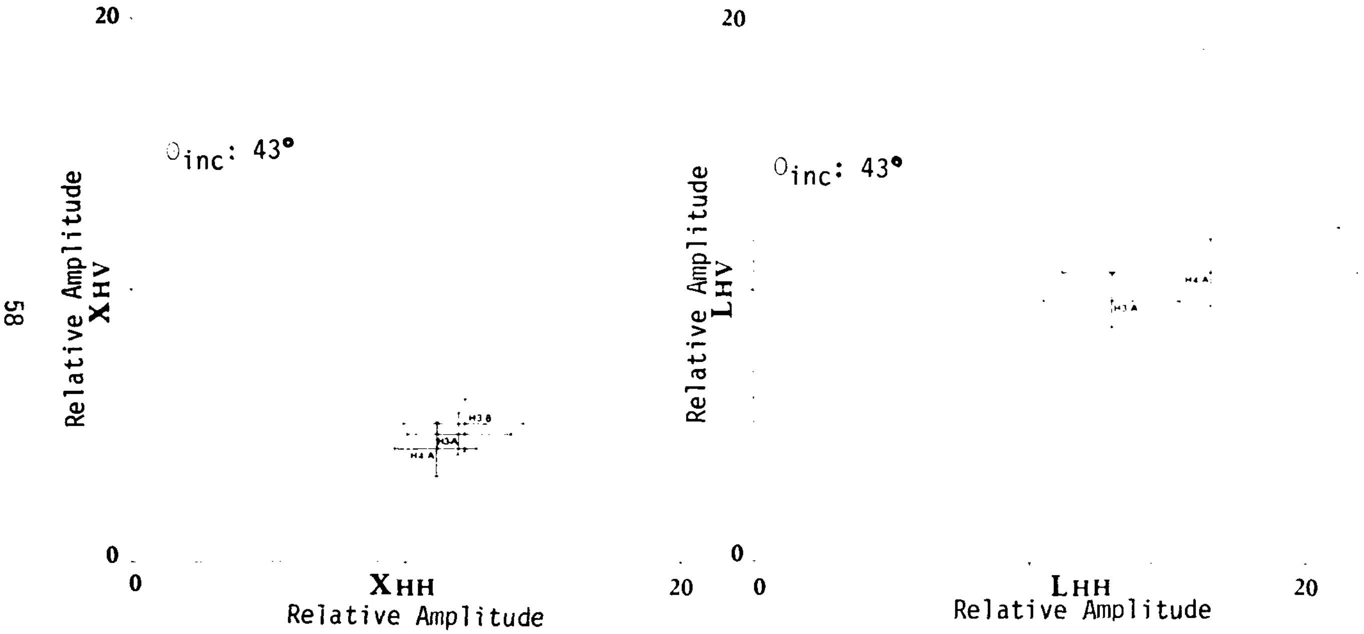

FIGURE 18. CLUSTER PLOTS OF HOPEDALE AREAS 3 AND 4.

steep and shallow incidence angles. Discrimination using L-band SAR data only would appear to be very difficult, if not impossible.

Cluster plots of the received signal amplitude for the near shore site (Figure 15, area 1, Beaufort), show little, if any, characteristic separation as a function of ice type. Similarly, the SAR data obtained from the Hopedale nearshore sites (Figures 17 and 18) cluster together showing little indication of discrimination possibilities.

As discussed previously, the measured standard deviation decreased for increasing resolution. This is illustrated in Figure 16 where cluster diagrams are given for the three values of resolution (6, 18, and 30 meters) for the two X-band channels. These results are to be expected, since larger resolution data are averaged over a greater spectral area; this results in less spread in the variation of radar cross section.

Some general observations can be made about the standard deviation and mean values measured. The mean value tends to increase for increasingly rough ice, particularly for shallow incidence angles. For the HH channel, the standard deviation almost always increases with operating frequency for both shallow and steep incidence angles (standard deviation increases for 10 of 14 cases and decreases for 4 of 14 cases). For the HV channel, the standard deviation increases with frequency for both shallow and steep incidence angles (it increases for 11 of 14 cases and decreases for 3 of 14 cases).

For multi-year classification and based on the variety of ice types for which data were used (Table 1), the X_{HV} channel and a steep incidence angle provide the best discrimination. Also, for multi-year ice, the X_{HH} and X_{HV} channels provide about equal discrimination at shallow incidence angles. There appears to be minimum information available from the L-band channel for classification of the ice types used in this study. A summary of all the measured mean values of received signal amplitude for site 2 is given in Figures 19 and 20 as a function of ice type. The curves are plotted in monotonically-decreasing order of mean value.

4.2 STANDARD DEVIATION-TO-MEAN RATIOS

A coefficient of deviation can be defined as the ratio of standard deviation to mean value, σ/μ. This ratio, dependent upon resolution, presents an indication of the spread in the values of radar cross section of a given scene. Values of the ratio σ/μ calculated for four ice types from area 2 are given in Table 22. The presence of ridges in an ice scene tends to increase the standard deviation of the backscatter values. This is seen by comparing the values given in Table 22 for first-year ice and multi-year ice with and without ridges; for all cases shown, the ratio σ/μ is larger for the ridged areas. Although quantitative measurements of the ice roughness were not made (this should be included in future ice experiments), information obtained from the ground truth data does indicate the ridged areas.

Values of the ratio σ/μ are given in Table 23 for the four test areas as a function of resolution. As stated above, the mean value is constant and the standard deviation decreases with resolution. Table 23 shows that the relative values of the coefficient of deviation for these ice types do not change with resolution. General observations regarding the coefficient of deviation σ/μ are summarized in Table 24.

4.3 ISORANGE SCANS

A line scan at constant range was made through each of the two Beaufort test areas for each SAR channel and for both shallow and steep incidence; these are shown in Figures 21 through 28. These data show the relative received signal level in dB as a function of

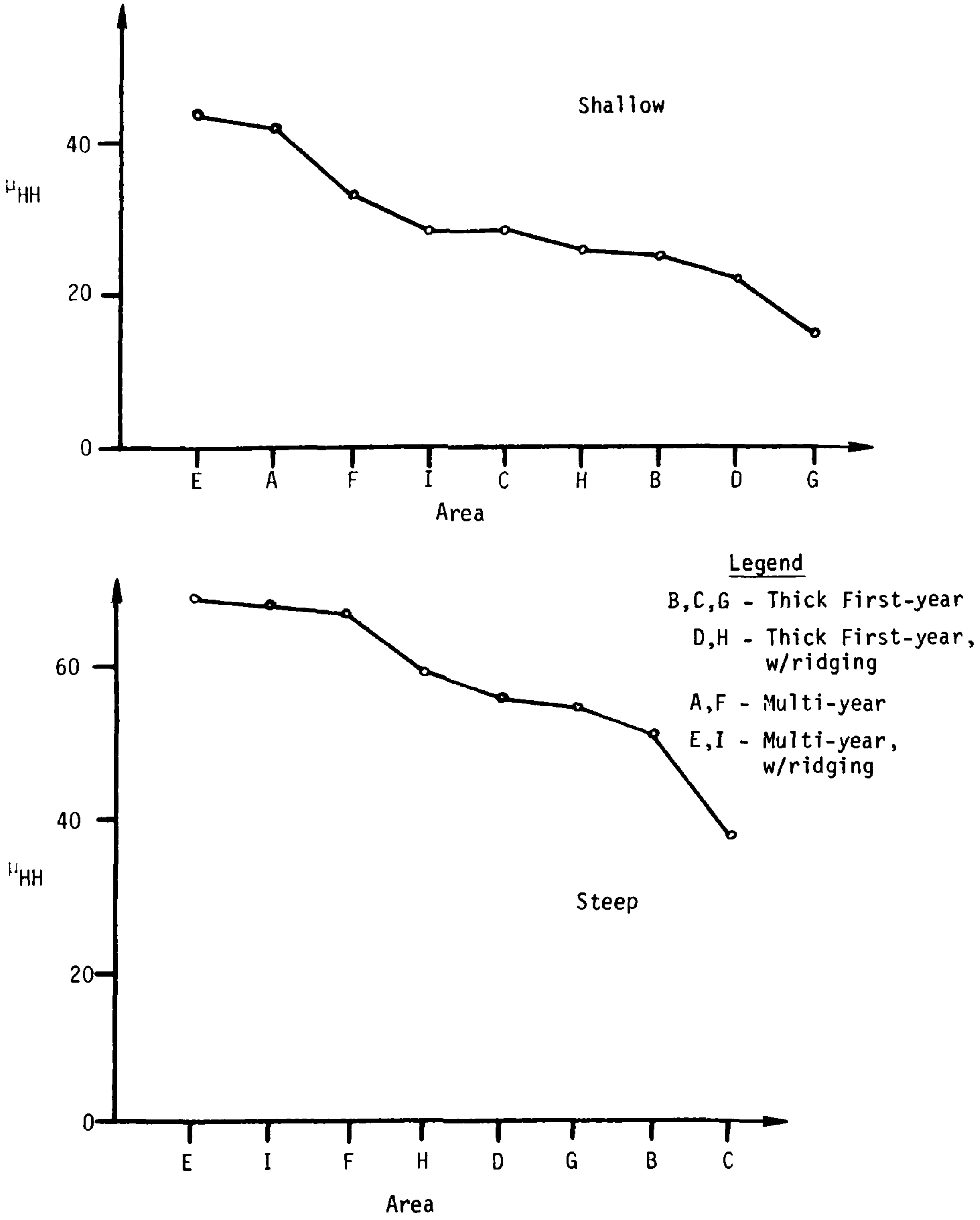

FIGURE 19. RELATIVE MEAN OF RECEIVED SIGNAL VS. ICE TYPE, AREA B2, X-BAND.

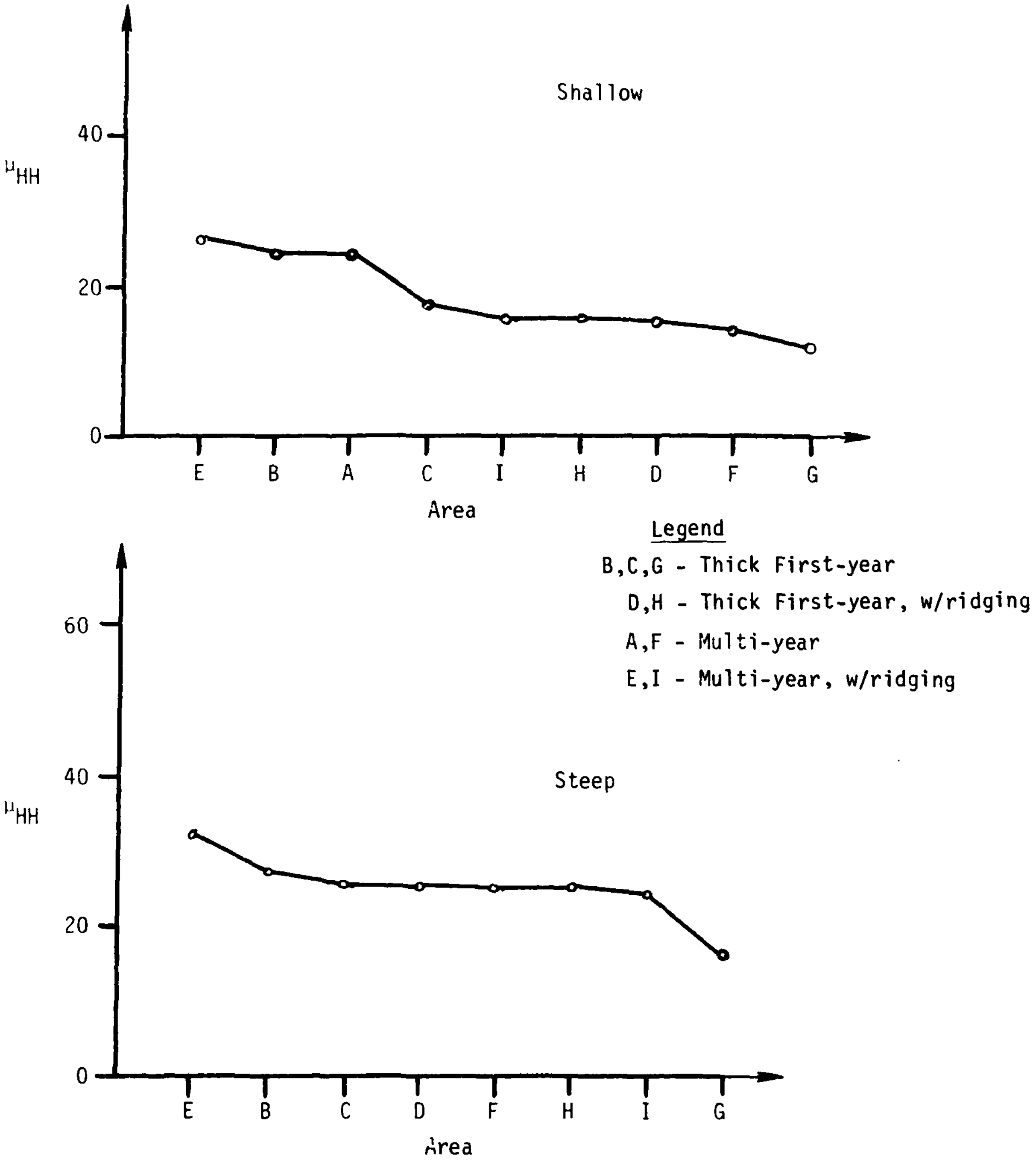

FIGURE 20. RELATIVE MEAN OF RECEIVED SIGNAL VS. ICE TYPE, AREA B2, L-BAND.

TABLE 22
COEFFICIENT OF DEVIATION FOR FOUR ICE TYPES FROM AREA B2

Area	Ice Type	$\frac{\sigma}{\mu}$ for X_{HH}		$\frac{\sigma}{\mu}$ for L_{HH}	
		Steep	Shallow	Steep	Shallow
B2-G	First year	0.28	0.26	0.34	0.25
B2-D	First year with ridges	0.35	0.61	0.52	0.47
B2-F	Multi-year	0.28	0.38	0.29	0.27
B2-E	Multi-year with ridges	0.35	0.51	0.40	0.51

TABLE 23
COEFFICIENT OF DEVIATION FOR FOUR ICE TYPES FROM AREA B1 (SHALLOW INCIDENCE ANGLE)

	RESOLUTION (M)					
	$\overset{\vee}{\wedge}_{HH}$			$\overset{\vee}{\wedge}_{HV}$		
	6	18	30	6	18	30
B1-A	0.35	0.21	0.166	0.31	0.16	0.112
B1-B	0.37	0.22	0.16	0.33	0.189	0.14
B1-D	0.58	0.44	0.37	0.39	0.27	0.21
B1-F	0.35	0.29	0.25	0.28	0.16	0.124

TABLE 24. SUMMARY TABLE OF COMPARISONS BETWEEN MEASURED VALUES*

Beaufort - Area 1

	B1-A	B1-B	B1-C	B1-D	B1-E	B1-F
B1-A		1	2	3, 4	2	1
B1-B	1		2	3, 4	2, 5	1
B1-C	2	2		4	2	2
B1-D	3, 4	3, 4	4		4, 5	3, 4
B1-E	2, 5	2, 5	2	4, 5		2, 5
B1-F	1	1	2	3, 4	2, 5	

Beaufort - Area 2

	B2-A	B2-B	B2-C	B2-D	B2-E	B2-F	B2-G	B2-H	B2-I
B2-A									
B2-B									3
B2-C									2
B2-D									
B2-E								3	3
B2-F							1		
B2-G						1			
B2-H					3				3
B2-I		3	2		3			3	

---

*CODE (for both HH and HV):

1 - Similar for both wavelengths and incidence angles.
2 - Similar for X-band, both incidence angles.
3 - Similar for L-band, both incidence angles.
4 - Similar for X-band, steep incidence angles.
5 - Similar for L-band, steep incidence angles.

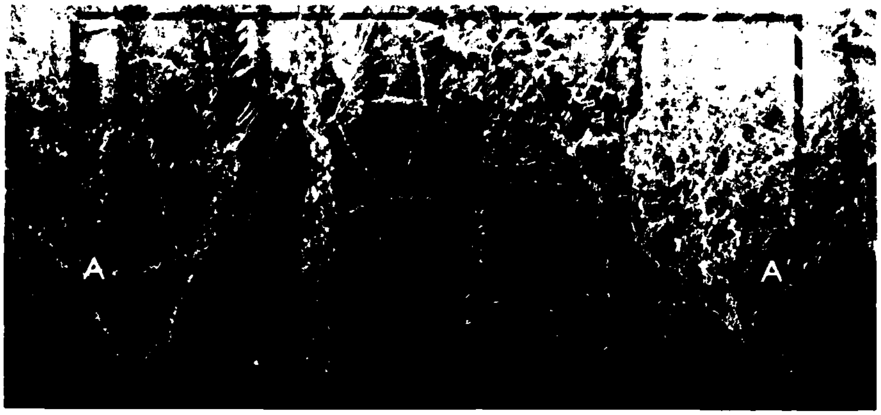

XHH

XHV

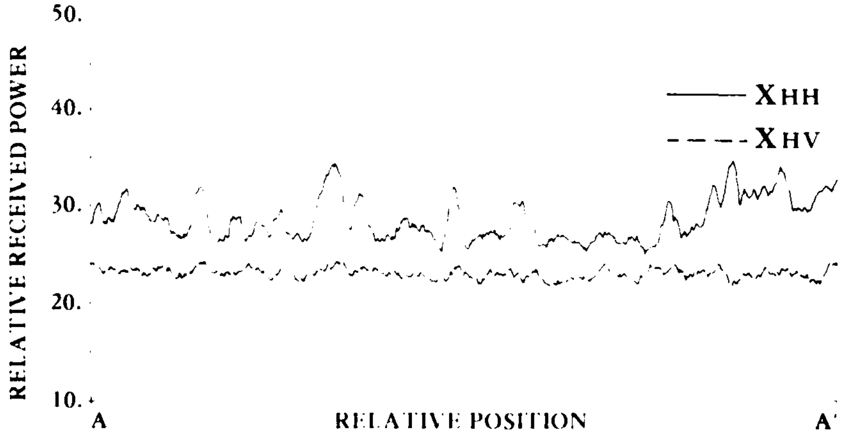

FIGURE 21. X-BAND (SHALLOW) CONSTANT-RANGE TRANSECTS OF BEAUFORT AREA 1.

XHH

XHV

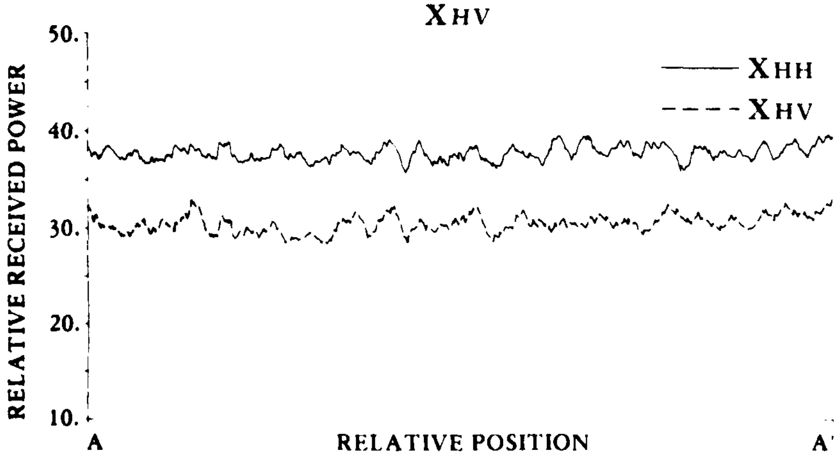

FIGURE 22. X-BAND (STEEP) CONSTANT-RANGE TRANSECTS OF BEAUFORT AREA 1.

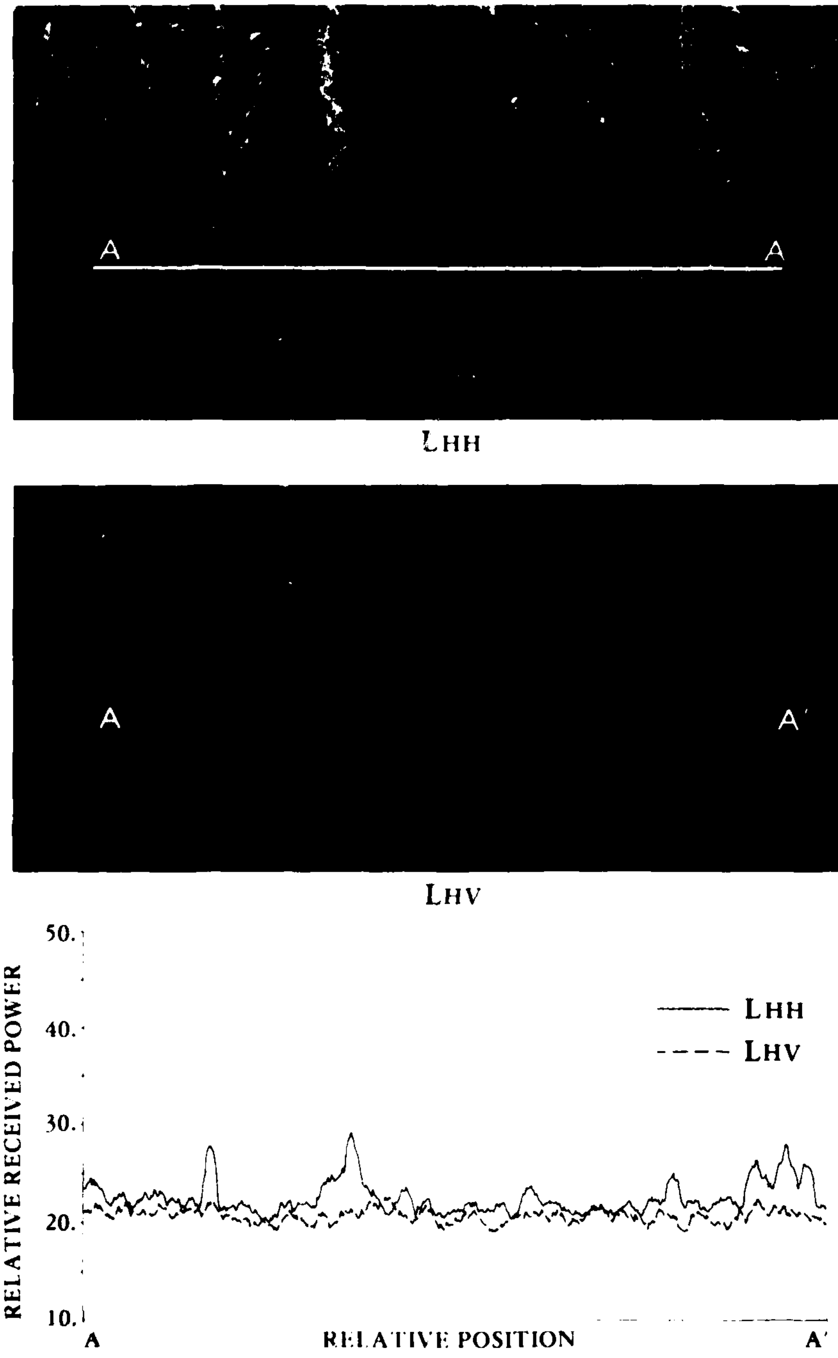

LHH

LHV

FIGURE 23. L-BAND (SHALLOW) CONSTANT RANGE TRANSECTS OF BEAUFORT AREA 1.

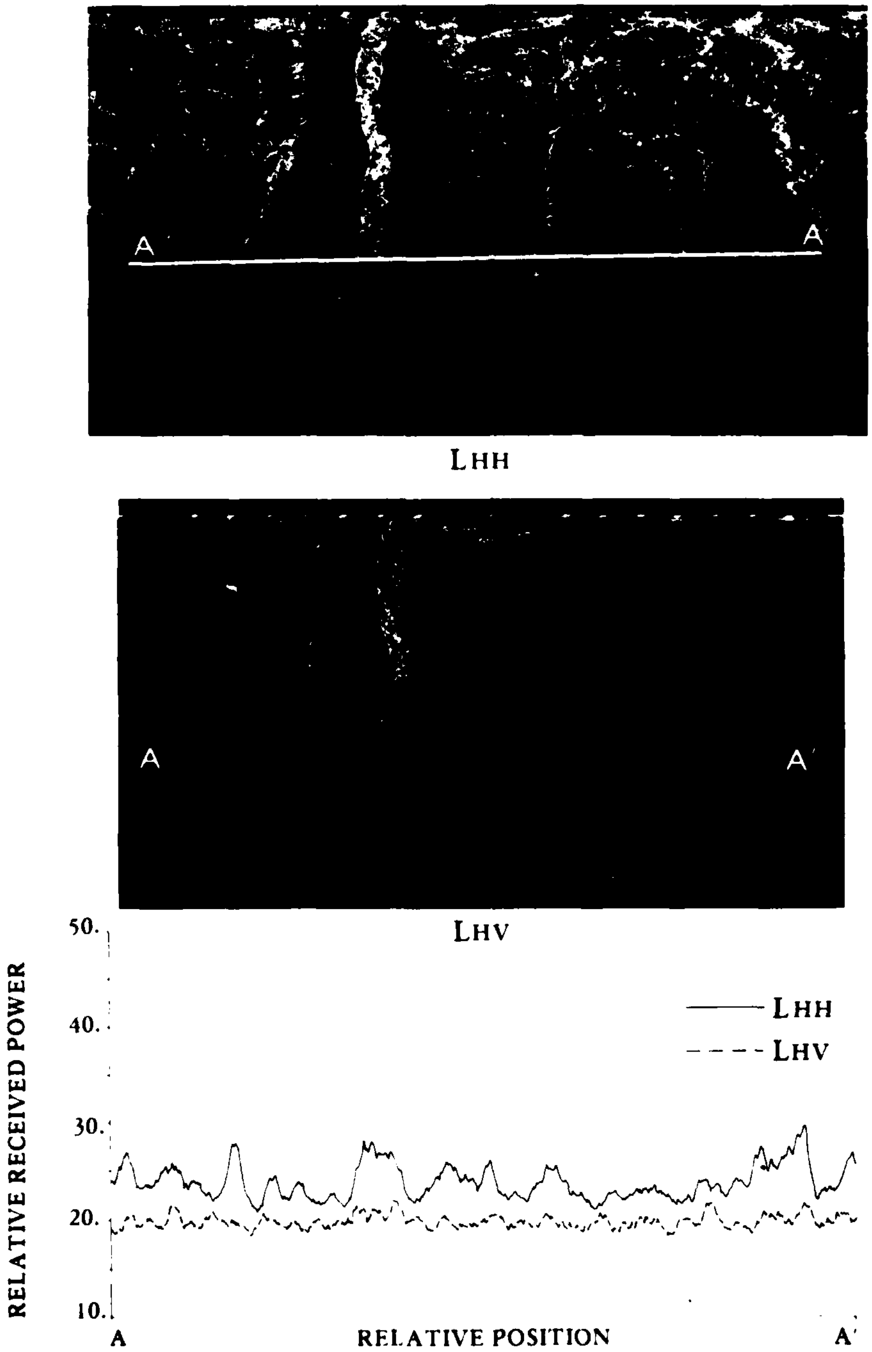

FIGURE 24. L-BAND (STEEP) CONSTANT-RANGE TRANSECTS OF BEAUFORT AREA 1.

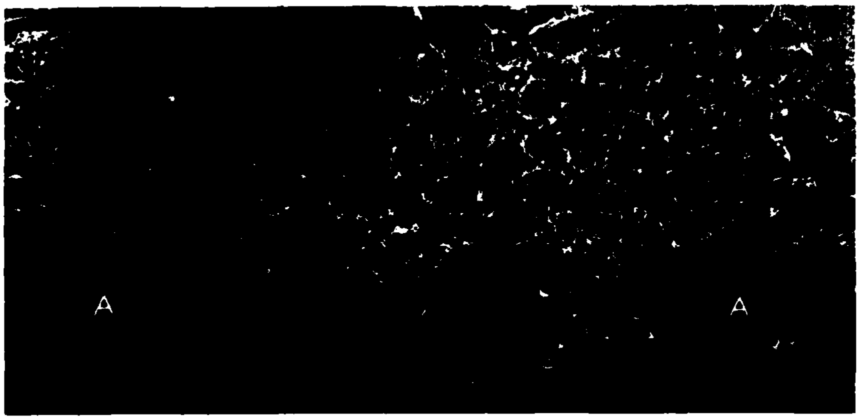

XHH

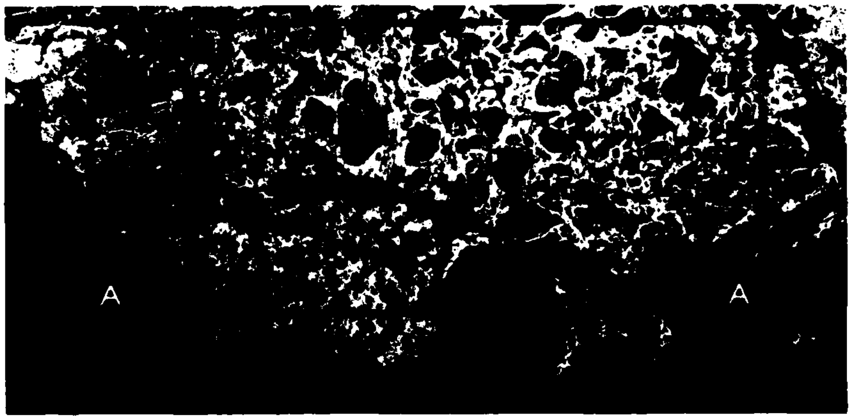

XHV

FIGURE 25. X-BAND (SHALLOW) CONSTANT-RANGE TRANSECTS OF BEAUFORT AREA 2.

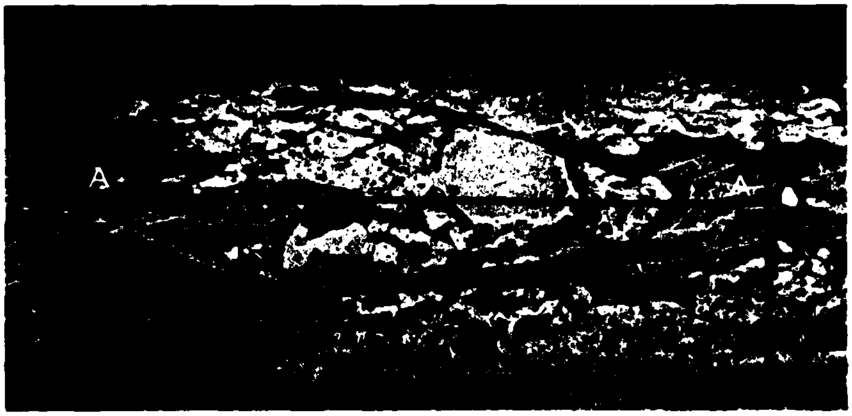

XHH

XHV

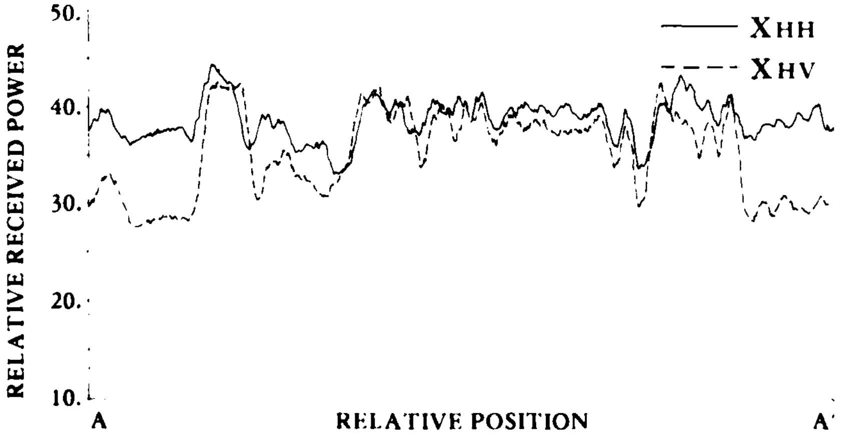

FIGURE 26. X-BAND (STEEP) CONSTANT-RANGE TRANSECTS OF BEAUFORT AREA 2.

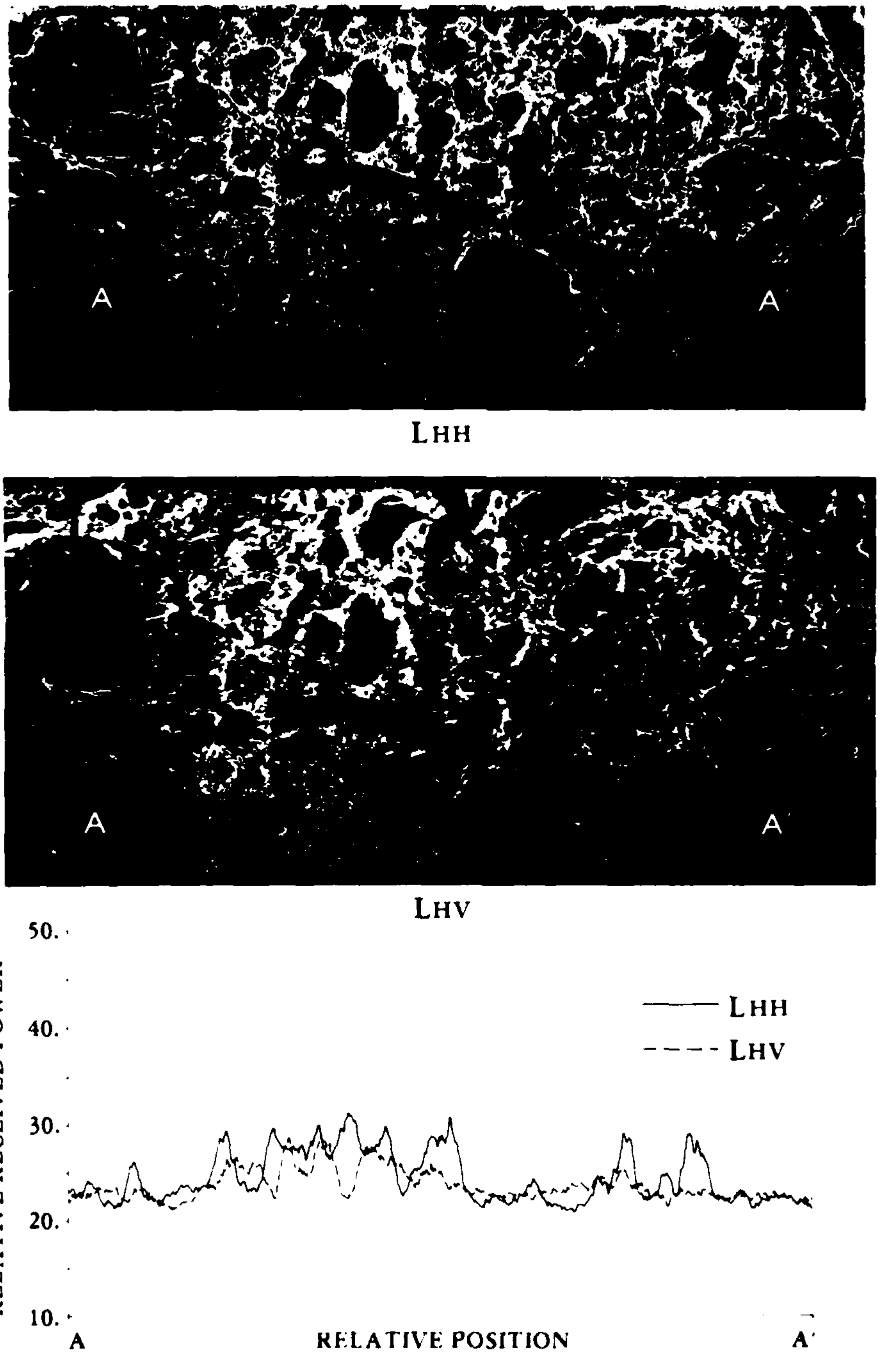

FIGURE 27. L-BAND (SHALLOW) CONSTANT-RANGE TRANSECTS OF BEAUFORT AREA 2.

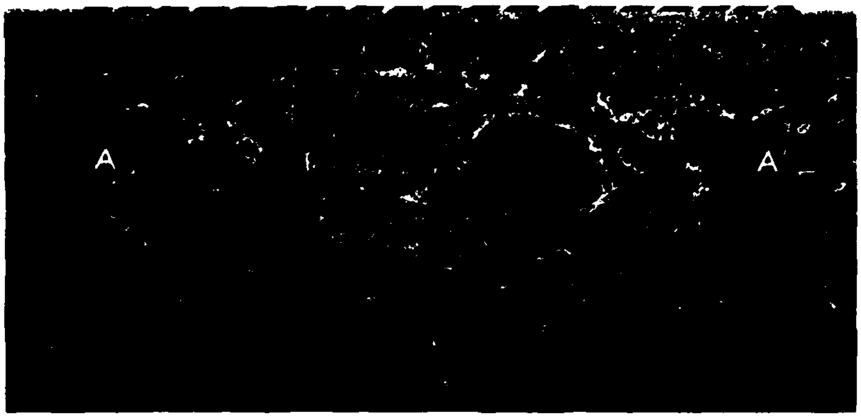

LHH

LHV

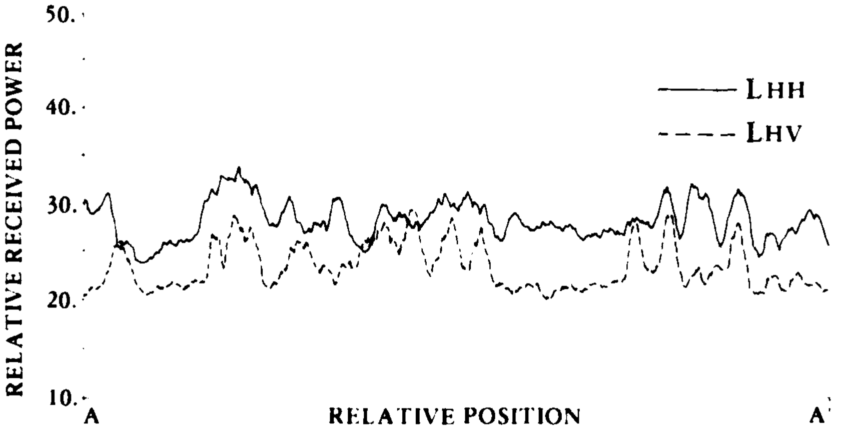

FIGURE 28. L-BAND (STEEP) CONSTANT RANGE TRANSECTS OF BEAUFORT AREA 2.

position along the scan line. (A constant range line is scanned to normalize all variations due to changes in range, incidence angle, and antenna gain. Although range can be determined accurately and corrections for variations in received power as a function of range can be made, variations in antenna response as a function of incidence angle are not at present known to any reasonable degree of accuracy.) These data can be utilized to determine:

(1) the dynamic range of the received signal from each ice scene,

(2) relative values of radar backscatter coefficients, and

(3) comparisons of like and cross polarization for the development of possible discrimination algorithms based on polarization.

The four ice types from the Beaufort Sea area 2, listed in Table 22, are identified on the constant-range transects and given in Figures 29 and 30. Several interesting characteristics of this particular data set and ice types can be seen. In general, received power (radar cross section) is minimum for first-year ice without ridges and maximum for multi-year with ridges. Depolarization is more complete for the multi-year with ridges area near the left-center of the scan than it is for similar areas included elsewhere in the scan. The reason for this is not clear, but perhaps additional detailed ground truth information regarding ridge heights, dielectric constant, and roughness scale would help to explain these effects. Since the depolarization is strongly dependent upon roughness and dielectric constant, the polarization ratio HH mean/HV mean may be a good indicator of these parameters. Also, a recent analysis [5] has suggested that (1) depolarization from surface reflection is independent of depolarization due to volume effects and (2) volume depolarization is only slightly dependent on incidence angle.

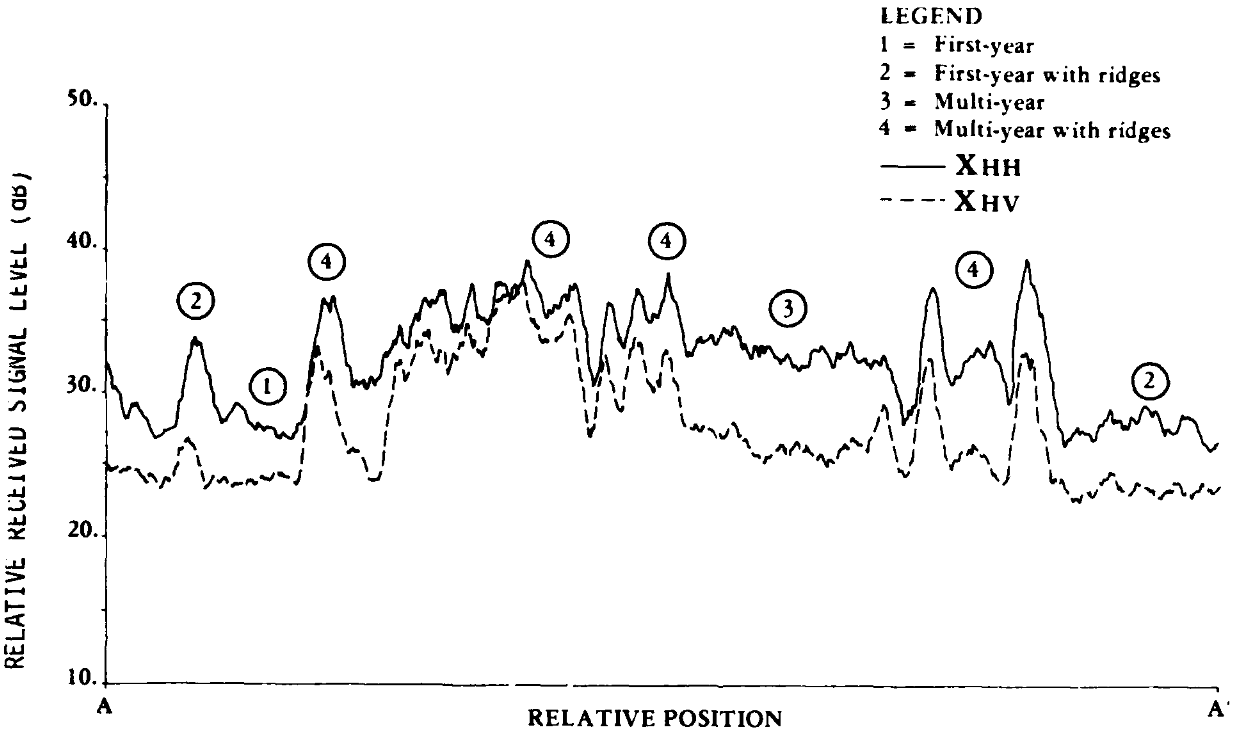

FIGURE 29. ANNOTATED X-BAND (SHALLOW) CONSTANT-RANGE TRANSECTS OF BEAUFORT AREA 2.

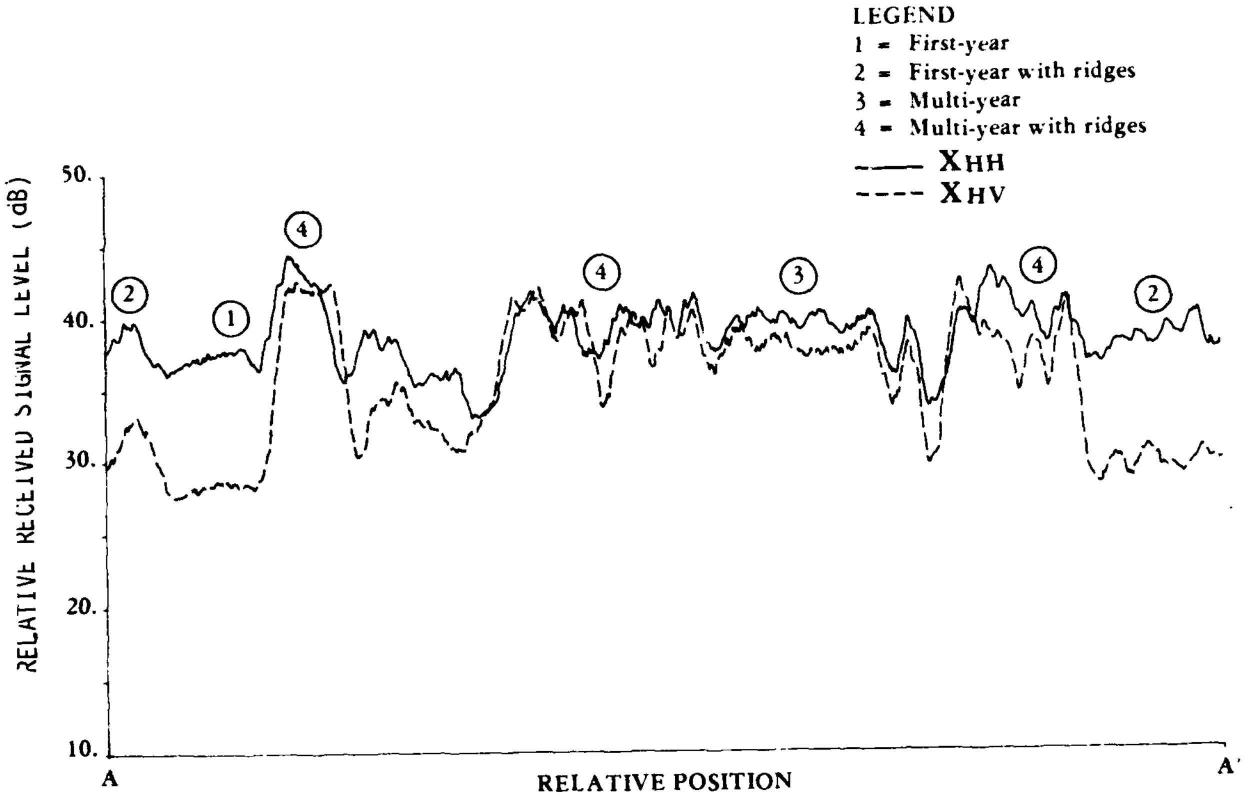

FIGURE 30. ANNOTATED X-BAND (STEEP) CONSTANT-RANGE TRANSECTS OF BEAUFORT AREA 2.

Similar line scans for the Beaufort area 1 are given in Figures 31 and 32 for X-band. The boundary between the 15 cm young ice and a meter of first-year ice covered with snow is indicated by the vertical dotted line. A 4 dB increase in received power (i.e., backscatter cross section) is obtained when traversing from the snow-covered to the non-snow-covered areas.

4.4 DYNAMIC RANGE

A knowledge of the total dynamic range of the received signal level expected for each particular region is important for system design. These values are obtained from the constant range scans given in Figures 21 through 28 and are summarized in Table 25 for the Beaufort Sea sites. It is seen from the data in Table 25 that the dynamic range of received power is greatest on the X-band channels from area 2 (multi-year region) at shallow incidence angles. These values compare favorably with results obtained with the CCRS 13.3 GHz scatterometer during the same period from the same general area in the Beaufort [6]. The dynamic range of both areas 1 and 2 on the X-band channels decreases for a steep incidence angle; on the L-band channels, the values are independent of incidence angle. In addition, it was observed that the dynamic range measured will be a function of resolution.

In the selection of an operating frequency for a radar dedicated to ice surveillance, it is clearly desirable to take advantage of the largest dynamic range response possible. For the measurements made, this would be X-band HH (or HV) at shallow incidence angle. It should be pointed out, again, that a very limited set of parameters could be included for analysis within the scope of this effort and that additional similar measurements should be made at other viewing angles.

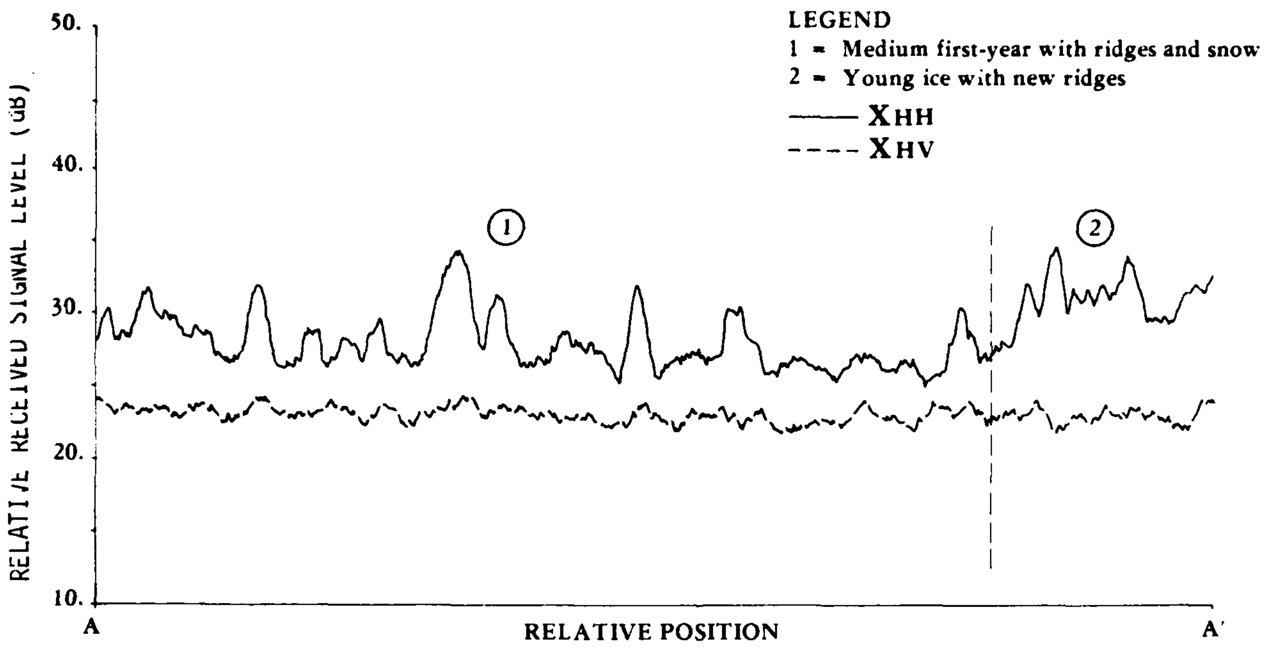

FIGURE 31. ANNOTATED X-BAND (SHALLOW) CONSTANT-RANGE TRANSECTS OF BEAUFORT AREA 1.

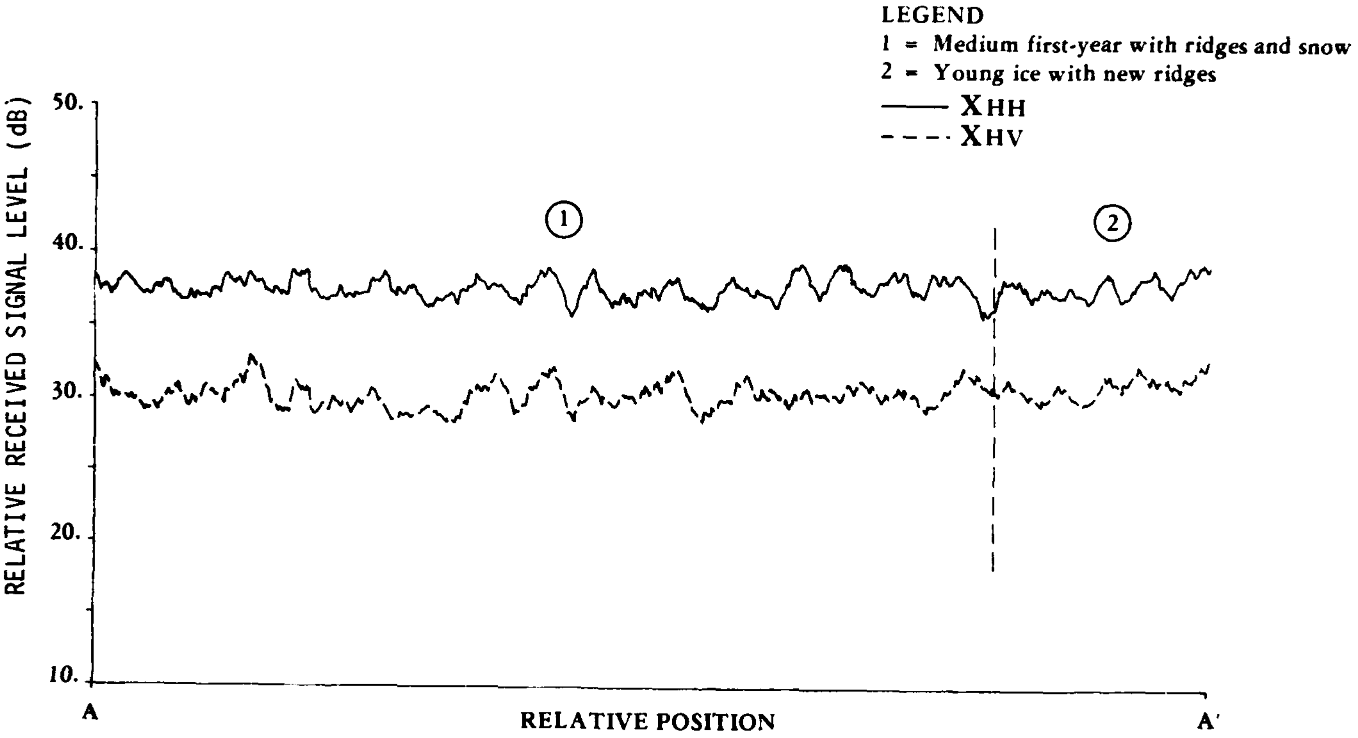

FIGURE 32. ANNOTATED X-BAND (STEEP) CONSTANT-RANGE TRANSECTS OF BEAUFORT AREA 1.

TABLE 25
DYNAMIC RANGE OF RECEIVED SIGNAL (IN dB) FOR BEAUFORT TEST SITES

Steep

	X		L	
	HH	HV	HH	HV
Site 1	3	4	9	3
Site 2	11	15	10	8

Shallow

	X		L	
	HH	HV	HH	HV
Site 1	9	3	9	3
Site 2	15	16	10	8

4.5 RELATIVE BACKSCATTER VALUES

The relative values of radar backscatter, P_{rec}, were obtained from the line-scan data for several different ice types. These measured differences,Δ,in backscatter values are given in Table 26 and compared therein with differences Δ in quantitative values of σ_0 measured for similar ice types. Note that these differences compare very well. These results are significant in that they demonstrate that quantitative σ_0 values obtained using ground-based instrumentation [7, 8, 9] will give the same differential values of σ_0 as data measured with airborne SAR instrumentation.

A particular data set was selected (area 1, Beaufort Sea) to obtain relative values of σ_0 as a function of incidence angle. This required that an estimate of the antenna response be made in order to normalize the data. The error in these estimates is several dB or more, but the general trend is shown in Figure 33. Corrections made for differences in slant range are accurate because the range can be measured from the radar data fairly precisely. For these particular cases, the "no snow" sites have greater σ_0 values. Note that the ice thicknesses are different between the snow and no-snow sites.

4.6 HISTOGRAM ANALYSIS

The ice clutter data considered in this report have been digitized in such a way that a numerical value describing a given pixel of clutter is proportional to its field strength, or the square root of its power. The data in a given scene of interest (see Tables 3 through 21 for numbers of samples) are then formed into a histogram (shown in the figures of this section and in Appendix C as dashed lines) for which the mean μ and standard deviation σ are computed. The density functions for three well-known distributions (normal, lognormal, and gamma) are then constructed using these μ and σ values and superimposed on the histograms for comparison.

TABLE 26
RELATIVE VALUES OF BACKSCATTER FOR VARIOUS BEAUFORT SITES

Shallow Area		SAR Measurements P_{rec}	SAR Measurements Δ	Scatterometer Measurements [9] σ°	Scatterometer Measurements [9] Δ
B1-C	First year	507	6.4 dB	-24 dBm	6 dBm
B2-F	Multi-year	2209		-18 dB	
Steep					
B2-I	Multi-year	8800		-5 dBm	
B2-E	Multi-year	9200	12.0 dB		11 dBm
B2-G	Smooth	729		-16 dBm	

d	$\sigma°$ Young Ice	$\sigma°$ Thick FY Ice
Ref. [7]		
60°	-13 dB	-15 dB
30°	~-21 dB	~-22 dB
Ref. [9]		
60°	-10 dB	-12 dB
30°	-24 dB	-26 dB

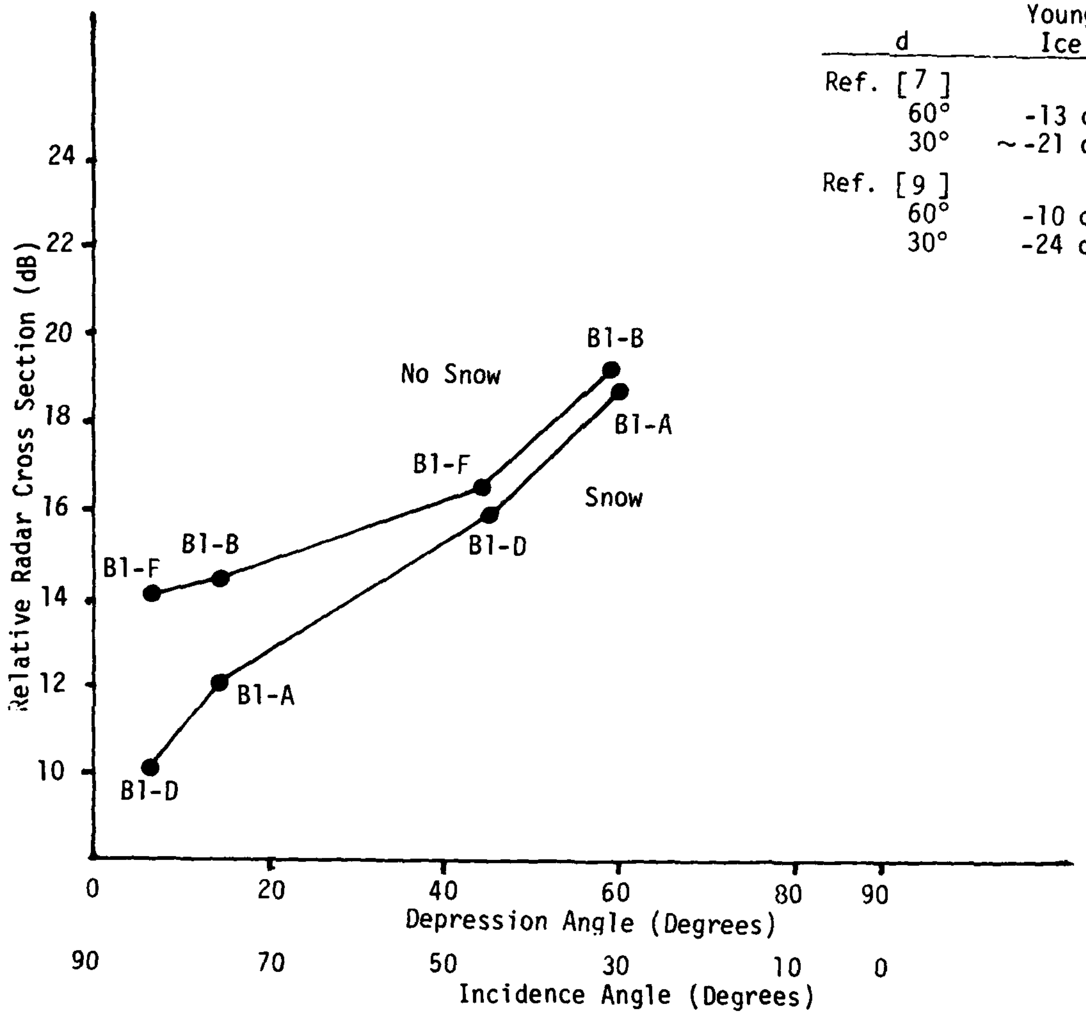

FIGURE 33. RELATIVE VALUES OF BACKSCATTER CROSS SECTION--X_{HH}.

The lognormal and gamma distributions are two distributions much-used for theoretical discussions of clutter data. The gamma distribution contains the chi-square distribution as a special case, and in turn the chi-square distribution contains the Rayleigh distribution as a special case. A brief word concerning their form as used in this application is in order.

The gamma density function is given by

$$\begin{aligned} g_{\alpha,\nu} &= \frac{A}{(\nu)} \alpha^{\nu} x^{\nu-1} e^{-\alpha x}, \ \alpha,\nu > 0, \ x \geq 0, \\ &= 0, \ x < 0. \end{aligned}$$

The mean and variance of this distribution are

$$\mu = \nu/\alpha, \ \sigma^2 = \nu^2/\alpha^2$$

and so, since the parameters α and ν can be uniquely expressed in terms of mean μ and standard deviation σ, the gamma distribution can be completely characterized in terms of its mean and standard deviation. (The mode of the gamma distribution is $x_m = (\nu - 1)/\alpha$. So, an alternative characterization of the gamma distribution is in terms of any two of μ, σ, or x_m.) The parameter A denotes the area under the histogram for a particular scene. If $\nu = 1$, the gamma density becomes a Rayleigh density, with $\mu = \sigma$,

$$\begin{aligned} g_{1/\sigma,1}(x) &= \frac{A}{\sigma} e^{-x/\sigma}, \ x \geq 0, \\ &= 0, \ x < 0 \end{aligned}$$

The lognormal density function can be obtained by taking 20 log x, where x ranges over the data set, as the independent variable of a normal distribution. An additional modification must be made for the mean and standard deviation of the distribution by taking them to be the mean and standard deviation of 20 log of the data.* The

---

*The choice of the operator 20 lg has been made so as to deal with data expressed in dB relative to some power level.

special notation $\mu_{20\ lg}$ and $\sigma_{20\ lg}$ is used to emphasize this modification, where lg (and log) refer to the common, or base 10, logarithm. The resulting lognormal density function may then be written as

$$L(x) = \frac{\frac{20}{\ln 10} A}{\sqrt{2\pi}\ \sigma_{20lg}} e^{-[20 \log x -_{20lg}]/2\sigma^2_{20lg}}, \quad x > 0,$$

$$= 0, \quad x \leq 0.$$

Since tne mean and standard deviation describe the peak region of the histogram, the characteristics of the "tails" of the distributions may, in some situations, be indicative of unique ice types. Therefore, in addition to the utilization of the mean and standard deviation for classification, the complete histogram was also considered.

A comparison of histograms for different ice types within the same area reveals the ability to discern multi-year ice from first-year, and also points up a problem in differentiating first-year from young ice. For example, a comparison of the histograms for areas B2-F (Figure 34) and B2-G (Figure 35), which contain multi-year ice with ridging and smooth first-year ice, respectively, illustrate the differences that are clear from the standard deviation and mean values. On the other hand, the areas B1-A (Figure 36) and B1-B (Figure 37), which contain first-year ice with snow and young ice without snow, respectively, have nearly identical distributions.

For the cases considered in this investigation, there was not a single example of classification based on the histogram alone. However, previous data [10] show that this approach is feasible and should be considered in future studies; therefore, the histogram should continue to be analyzed as a possible classifier of ice types.

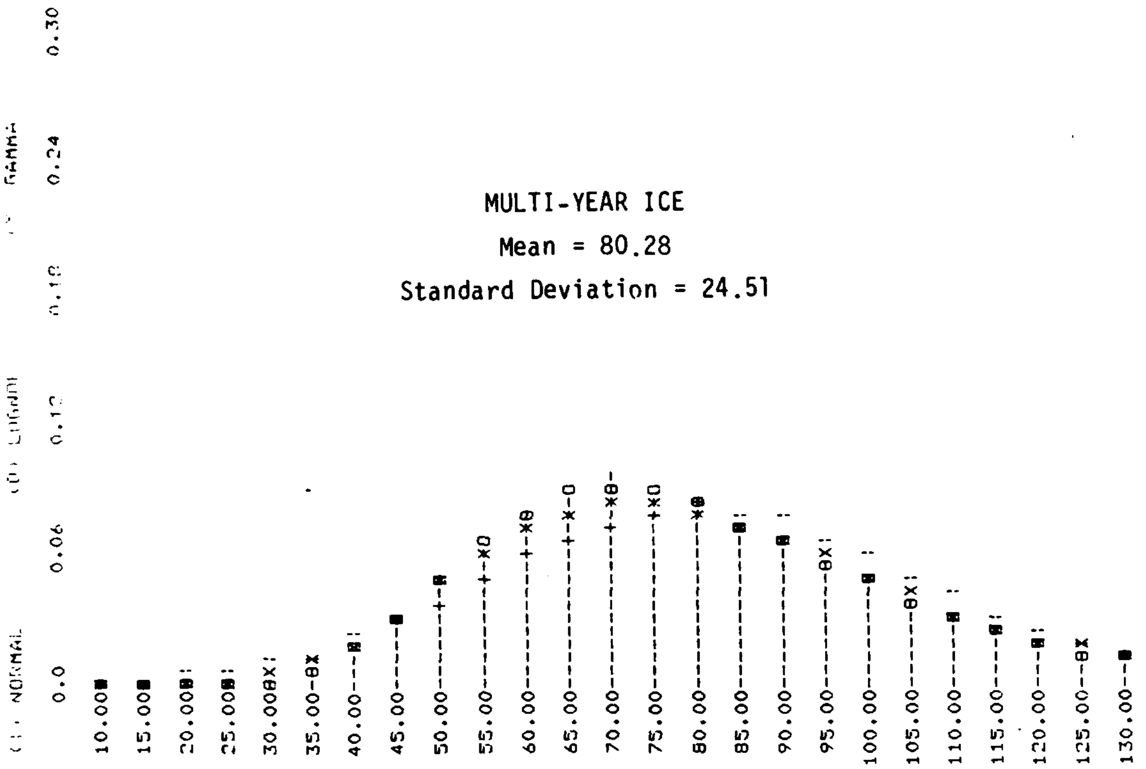

MULTI-YEAR ICE

Mean = 80.28

Standard Deviation = 24.51

FIGURE 34. HISTOGRAM OF SITE B2-F X_{HV} (STEEP).

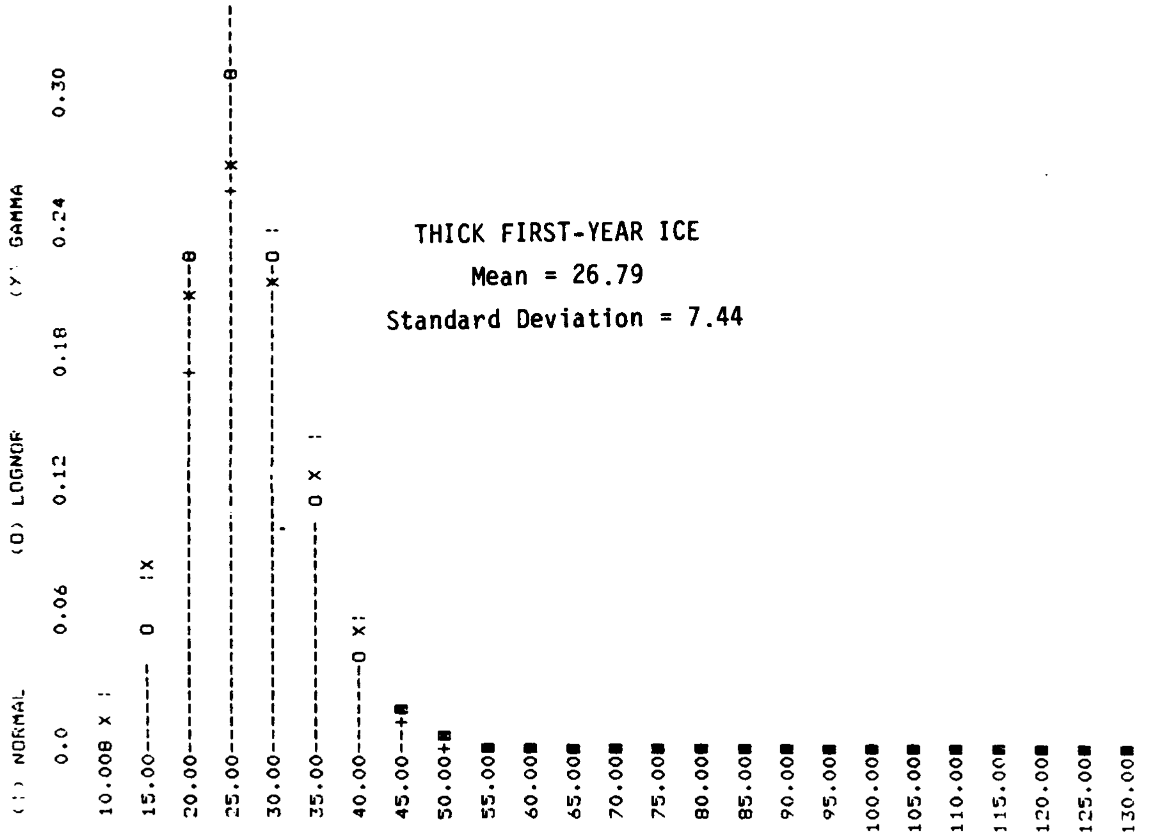

FIGURE 35. HISTOGRAM OF SITE B2-G X_{HV} (STEEP).

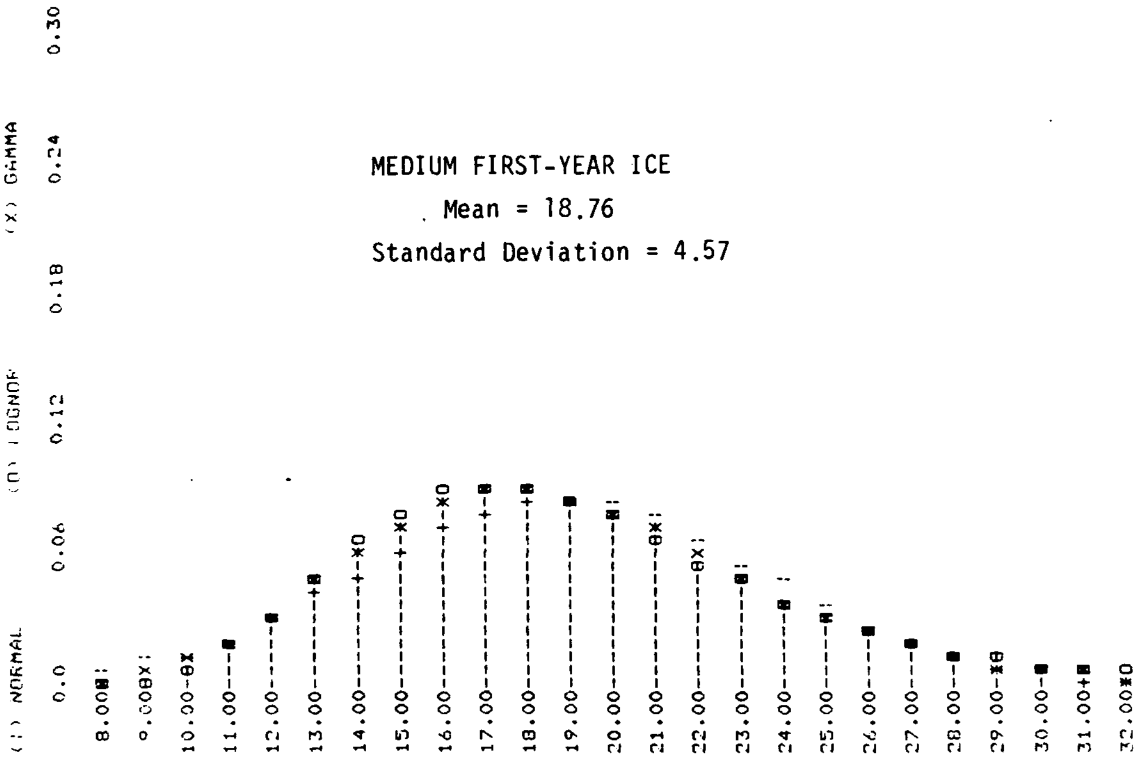

MEDIUM FIRST-YEAR ICE
Mean = 18.76
Standard Deviation = 4.57

FIGURE 36. HISTOGRAM OF SITE B1-A X_{HV} (STEEP).

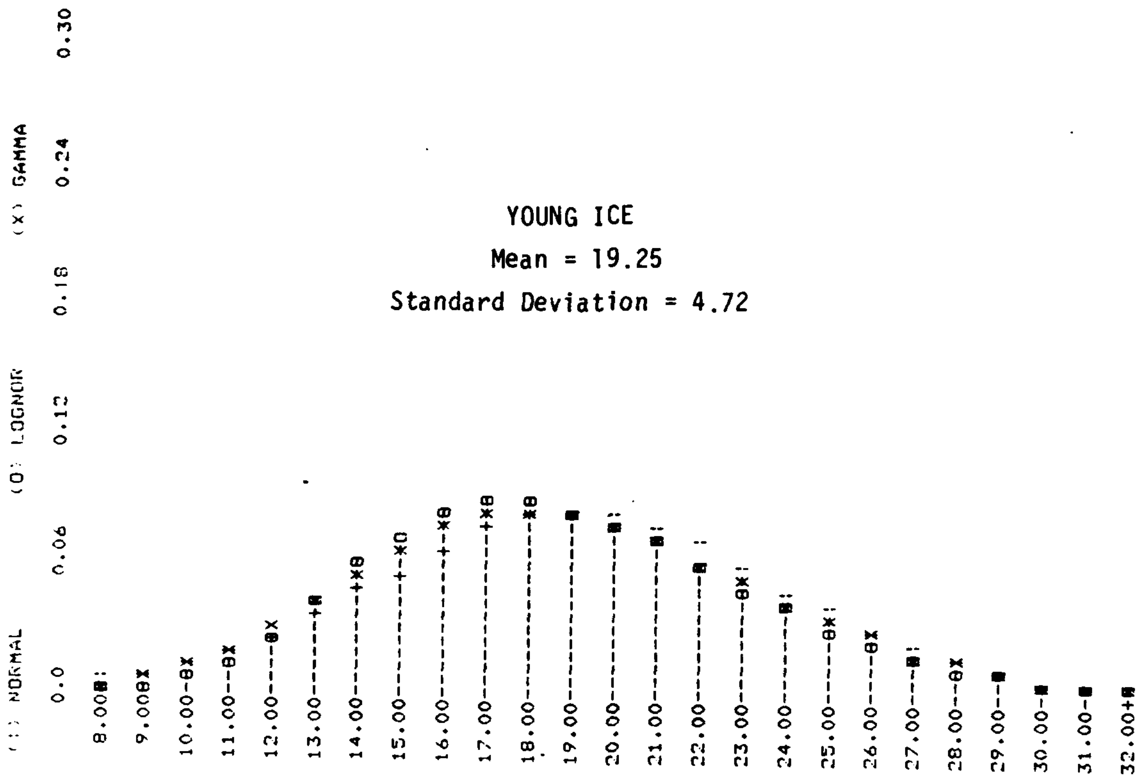

YOUNG ICE

Mean = 19.25

Standard Deviation = 4.72

FIGURE 37. HISTOGRAM OF SITE B1-B X_{HV} (STEEP).

AD-A097 341 ENVIRONMENTAL RESEARCH INST OF MICHIGAN ANN ARBOR RA--ETC F/G 17/9
DETERMINATION OF BACKSCATTER CHARACTERISTICS OF SEA ICE USING S--ETC(U)
MAR 81 R W LARSON, J D LYDEN, R A SHUCHMAN N00014-79-C-0690
UNCLASSIFIED ERIM-142600-1-F NL

2 OF 3
AD
A097341

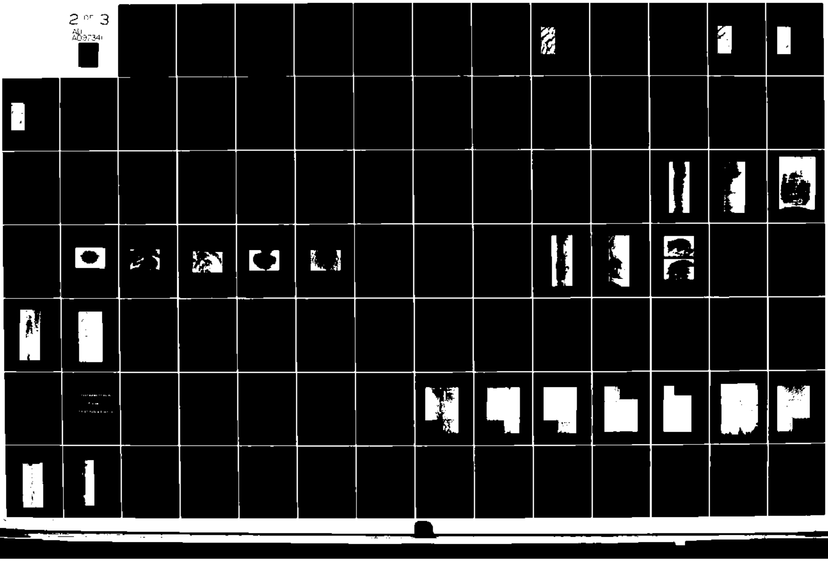

4.7 POLARIZATION RATIOS

As listed in Section 3.4, two multi-parameter measures utilizing polarization ratios were investigated for the classification of ice types. These measures are: (1) the ratio of the mean values obtained for like and cross polarization for each wavelength and (2) the ratio of the coefficients of deviation for the like and cross-polarization channels. These values have been calculated for the four ice types from area 2 (considered previously in Section 4.2) and are listed in Table 27.

The polarization ratio of mean values for the X-band channel, steep incidence angle data set progressively decreases in value for the four ice types, as shown in the table. This may be explained qualitatively as follows: Based on ground truth data, the ice included in these test areas became progressively rougher from the top to the bottom of the list; increased depolarization should occur for increasing roughness (at least up to some roughness scale). Further, volume scattering becomes significant for multi-year ice, again resulting in depolarization which may account for the rather sharp change in the mean depolarization ratio between first year and multi-year ice.

A comparison of the polarization ratio of the coefficient of deviation for steep and shallow incidence angles at X-band shows a change in response for the four ice types listed in Table 27. The reason for this is not now known; however, the fact that this parameter is sensitive to variations in incidence angle would indicate a potential application for classification when the interaction phenomenon is understood.

For the analysis of the polarization ratio for all ice types in area 2, the calculated ratios have been plotted in monotonically-decreasing order. These data are given in Figure 38 for X-band and in Figure 39 for L-band. Since measurements of surface roughness

TABLE 27. POLARIZATION RATIOS FOR FOUR SITES IN AREA B2.

		$\frac{\text{mean}_{X_{HH}}}{\text{mean}_{X_{HV}}}$		$\frac{\text{mean}_{L_{HH}}}{\text{mean}_{L_{HV}}}$		$\frac{\left[\frac{\alpha}{\mu}\right]_{X_{HH}}}{\left[\frac{\alpha}{\mu}\right]_{X_{HV}}}$		$\frac{\left[\frac{\alpha}{\mu}\right]_{L_{HH}}}{\left[\frac{\alpha}{\mu}\right]_{L_{HV}}}$	
Site	Ice Type	Steep	Shallow	Steep	Shallow	Steep	Shallow	Steep	Shallow
B2-G	First year	2.84	1.4	1.38	0.86	1.0	0.84	1.54	1.05
B2-D	First year; ridges	2.56	1.9	1.9	1.0	0.85	2.0	1.44	1.7
B2-F	Multi-year	1.2	2.2	2.1	1.0	0.93	1.05	1.3	1.1
B2-E	Multi-year; ridges	1.1	1.4	1.5	1.3	0.83	0.9	0.93	1.16

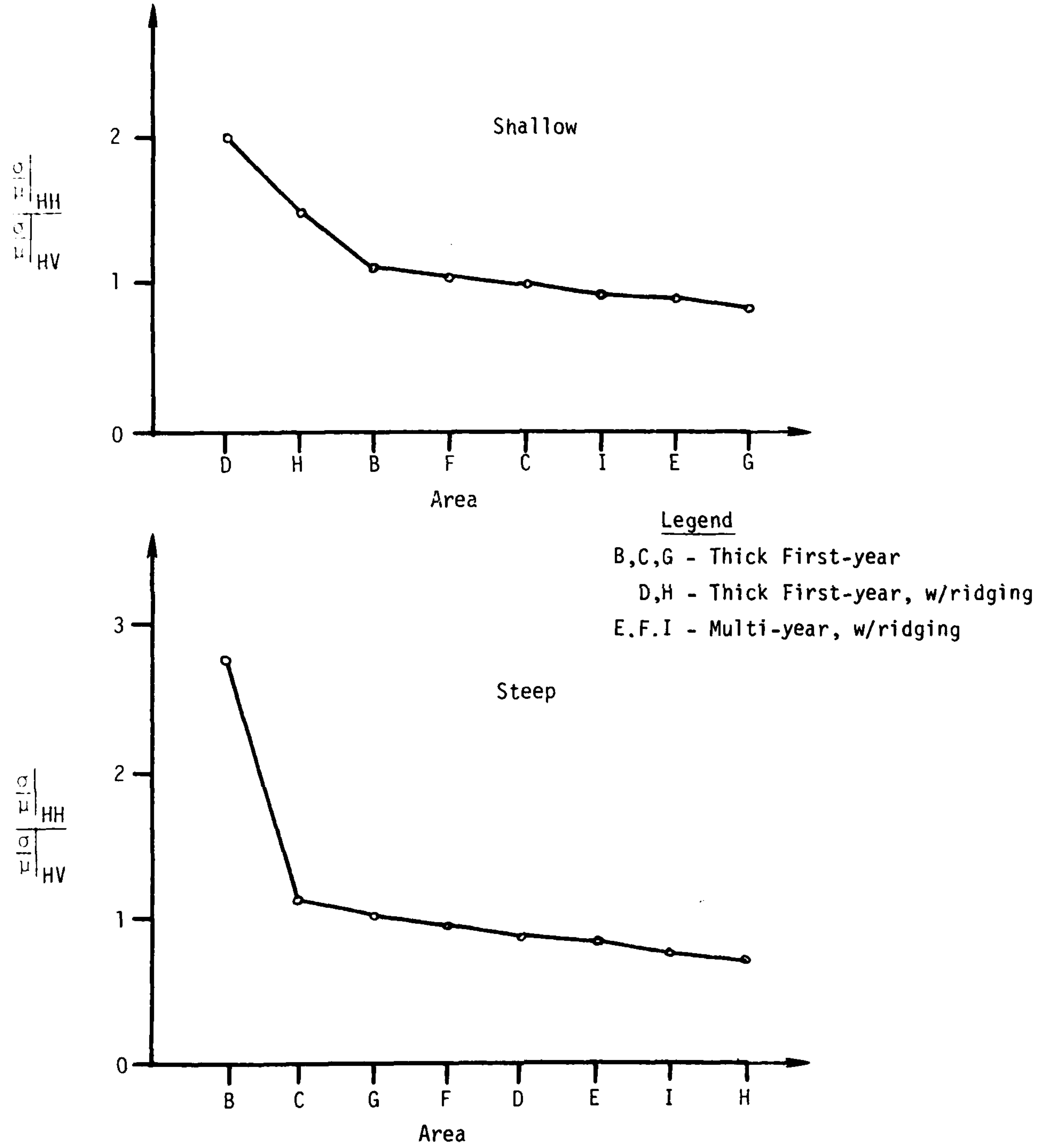

FIGURE 38. POLARIZATION RATIO OF COEFFICIENT OF DEVIATION VS. ICE TYPE, AREA B2, X-BAND.

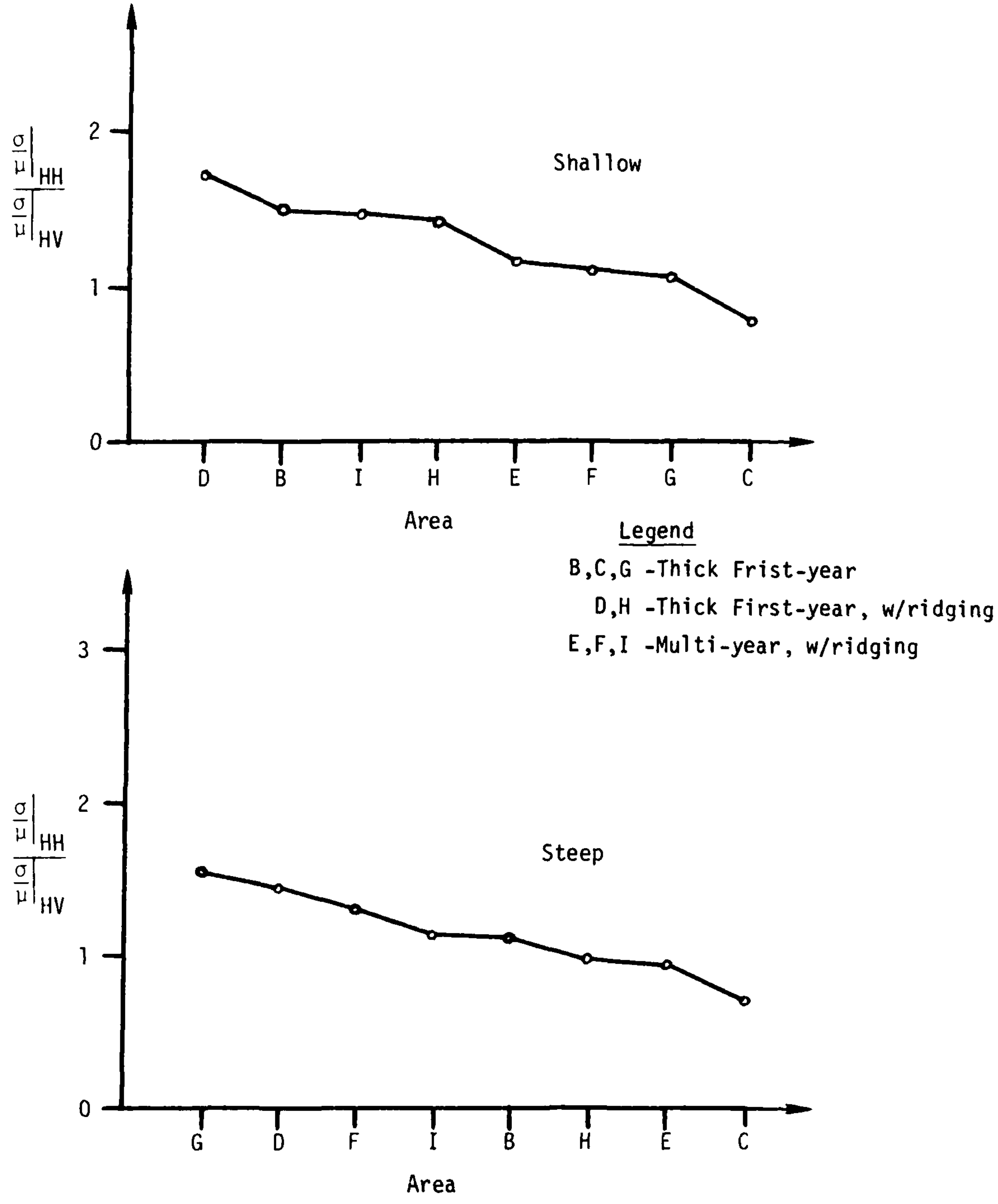

FIGURE 39. POLARIZATION RATIO OF COEFFICIENT OF DEVIATION VS. ICE TYPE, AREA B2, L-BAND.

TABLE 28
VALUES OF THE POLARIZATION RATIO FOR THE COEFFICIENT OF DEVIATION FOR AREA B1

$\frac{\left[\frac{\alpha}{\mu}\right]_{X_{HH}}}{\left[\frac{\alpha}{\mu}\right]_{X_{HV}}}$				$\frac{\left[\frac{\alpha}{\mu}\right]_{L_{HH}}}{\left[\frac{\alpha}{\mu}\right]_{L_{HV}}}$			
Site	Shallow	Site	Steep	Site	Shallow	Site	Steep
B1-D	1.48	B1-A	1.5	B1-F	1.9	B1-C	2.75
B1-C	1.40	B1-B	1.5	B1-D	1.76	B1-A	1.2
B1-E	1.3	B1-C	1.3	B1-A	1.73	B1-B	1.08
B1-F	1.25	B1-E	1.15	B1-B	1.53	B1-D	1.08
B1-A	1.13	B1-F	1.07	B1-E	1.0	B1-E	0.96
B1-B	1.12	B1-D	1.0	B1-C	0.9	B1-F	0.96

scales and electrical properties are not available, it would be difficult to use these results to model the ice. However, this approach should be included in future analysis efforts.

Calculated values of the polarization ratio for the coefficient of deviation for the nearshore site test areas are given in Table 28. The values for each data set are arranged according to decreasing value of the ratio. Note that the ratio for snow-covered first-year ice (area B1-D) is greater than that for no-snow young ice (area B1-F) for the shallow (θ_{inc} ~ 82.5°) X-band data; however the reverse is true for shallow L-band data. Values calculated from the other snow and no snow sites (θ_{inc} ~ 77.5°) show the ratio for the two to be about equal using both L- and X-band data. For steep incidence angles, both the X- and L-band data have similar ratio values for the six sites.

Although the trends and relationships of the polarization ratios calculated from these data are very interesting to contemplate, it is clear that additional examples must be analyzed before any signatures can be verified.

4.8 SIGNAL-TO-CLUTTER RATIOS

As previously mentioned in Section 3.4, signal-to-clutter ratios were calculated for both a ship and icebergs surrounded by ice, and (for comparative purposes) a ship surrounded by water. These results are summarized in Table 29. It can be seen that (generally) cross-polarized X-band discriminates the ship in ice and the iceberg the best. In fact, the iceberg could not be located on either L-band channel.

Probability of detection values were calculated using the values from Table 29 and the curve in Figure 40; these values are summarized in Table 30.

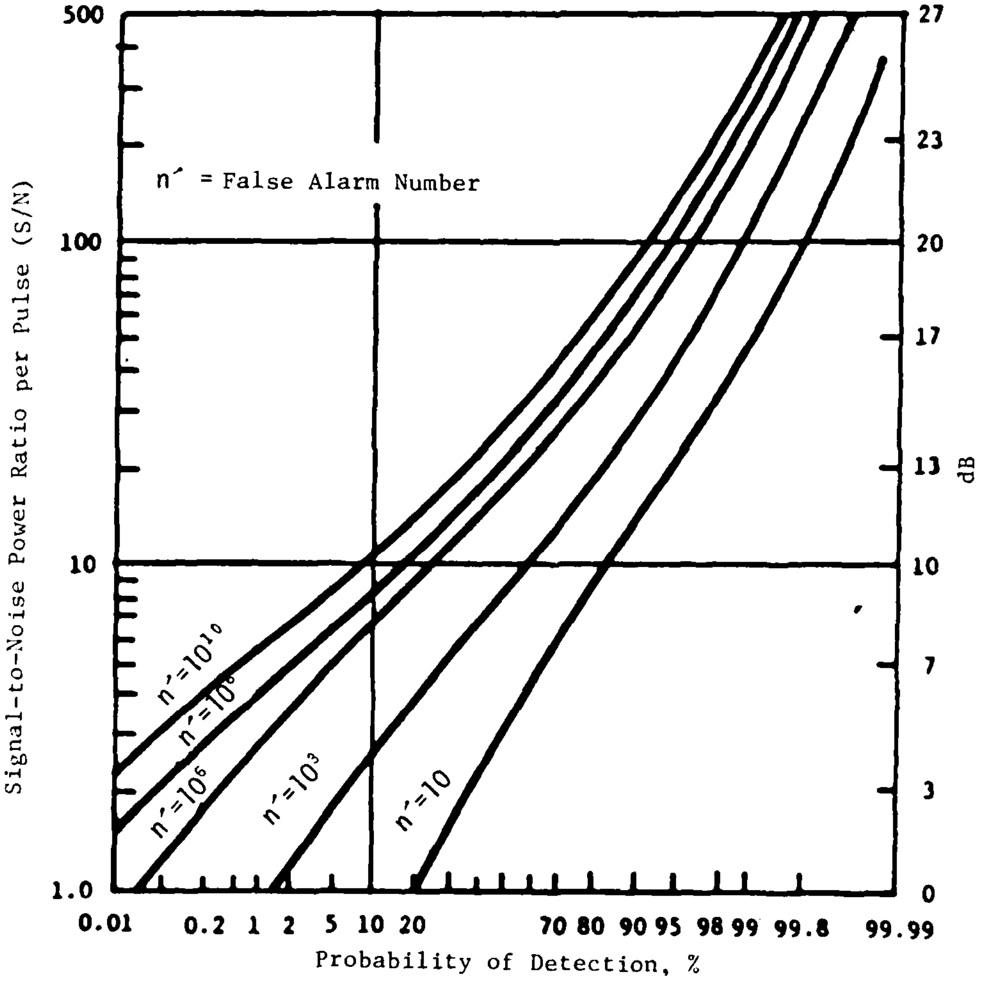

FIGURE 40. PROBABILITY OF DETECTION VS. SIGNAL-TO-NOISE RATIO.

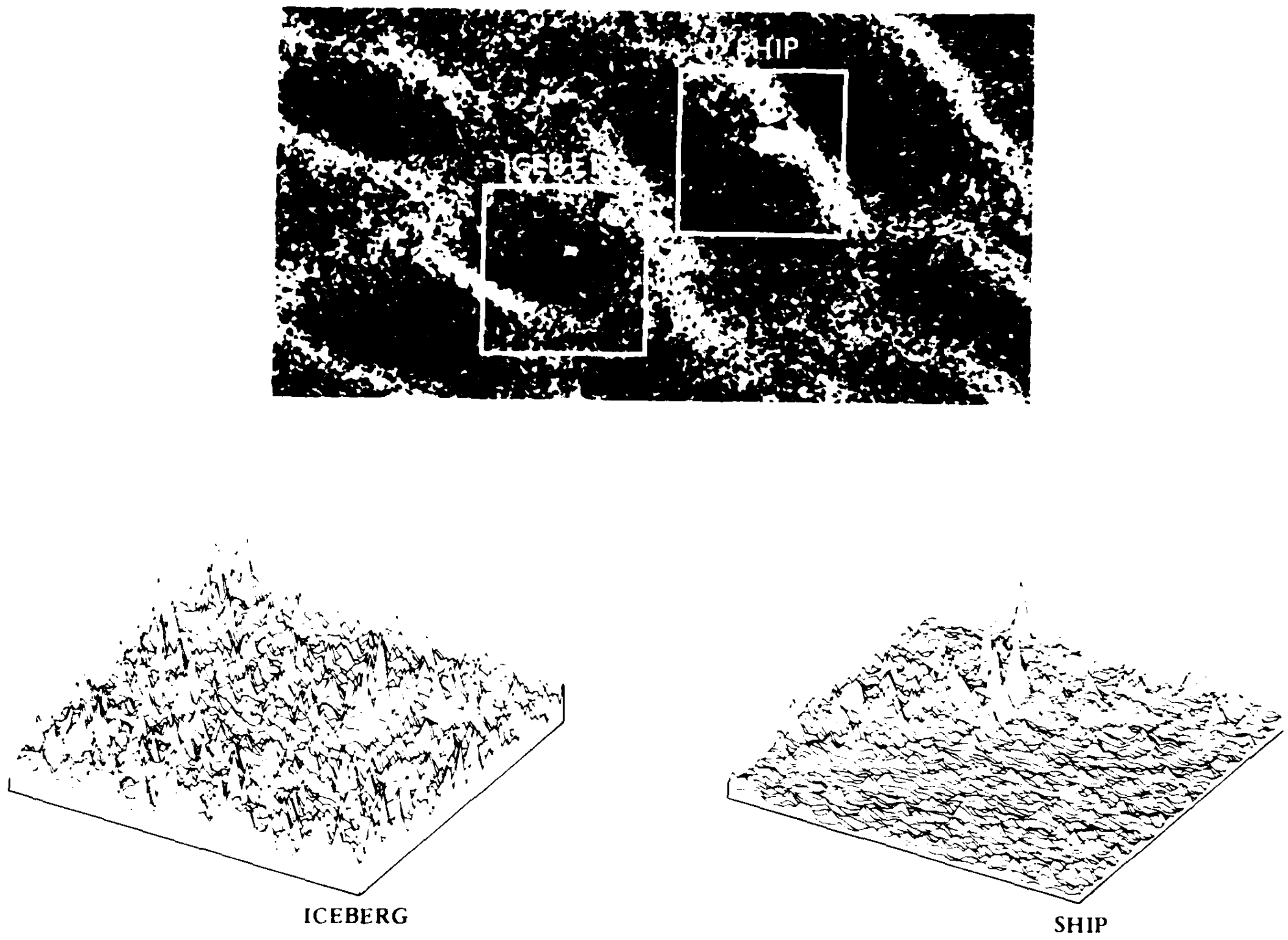

FIGURE 41. X-BAND (HH) PERSPECTIVE PLOTS OF SHIP AND ICEBERG LOCATION.

TABLE 29. SIGNAL-TO-CLUTTER (SURROUNDING ICE) RATIO TABLE
(Values in dB)

Target and Location	Signal-to-Clutter Ratio			
	X-band HH	X-band HV	L-band HH	L-band HV
Ship in ice[1]	18.16	19.77	16.82	12.25
Iceberg	10.40	16.07	*	*
Iceberg[2]	19.80	18.50	14.32	10.90
Ship in water[3]	31.66	**	**	33.72

---

* Not able to locate iceberg on digital image.

** Data not available.

[1] The ship was the M/V Arctic Explorer, a small (50 m) ice-classed vessel.

[2] Data from Ref. 12; these values are signal-to-noise ratios (noise defined as the shadow of an iceberg).

[3] The ship was the Sejwal (see Ref. 11), an 87m fish factory trawler.

TABLE 30. PROBABILITY OF DETECTION OF SHIPS AND ICEBERGS
(False Alarm of 10^{-6} Assumed)

Target and Location	Probability of Detection			
	X-band HH	X-band HV	L-band HH	L-band HV
Ship in ice[1]	93.0%	98%	87%	50.0%
Iceberg	28.0%	82%	*	*
Iceberg[2]	98%	94%	70%	30%
Ship in water[3]	>99.8%	*	*	>99.8%

---

* Data not available.

[1] The ship was the M/V Arctic Explorer, a small (50 m) ice-classed vessel.

[2] Data from Ref. 12; these probabilities were derived from signal-to-noise ratios.

[3] The ship was the Sejwal, an 87 m fish factory trawler.

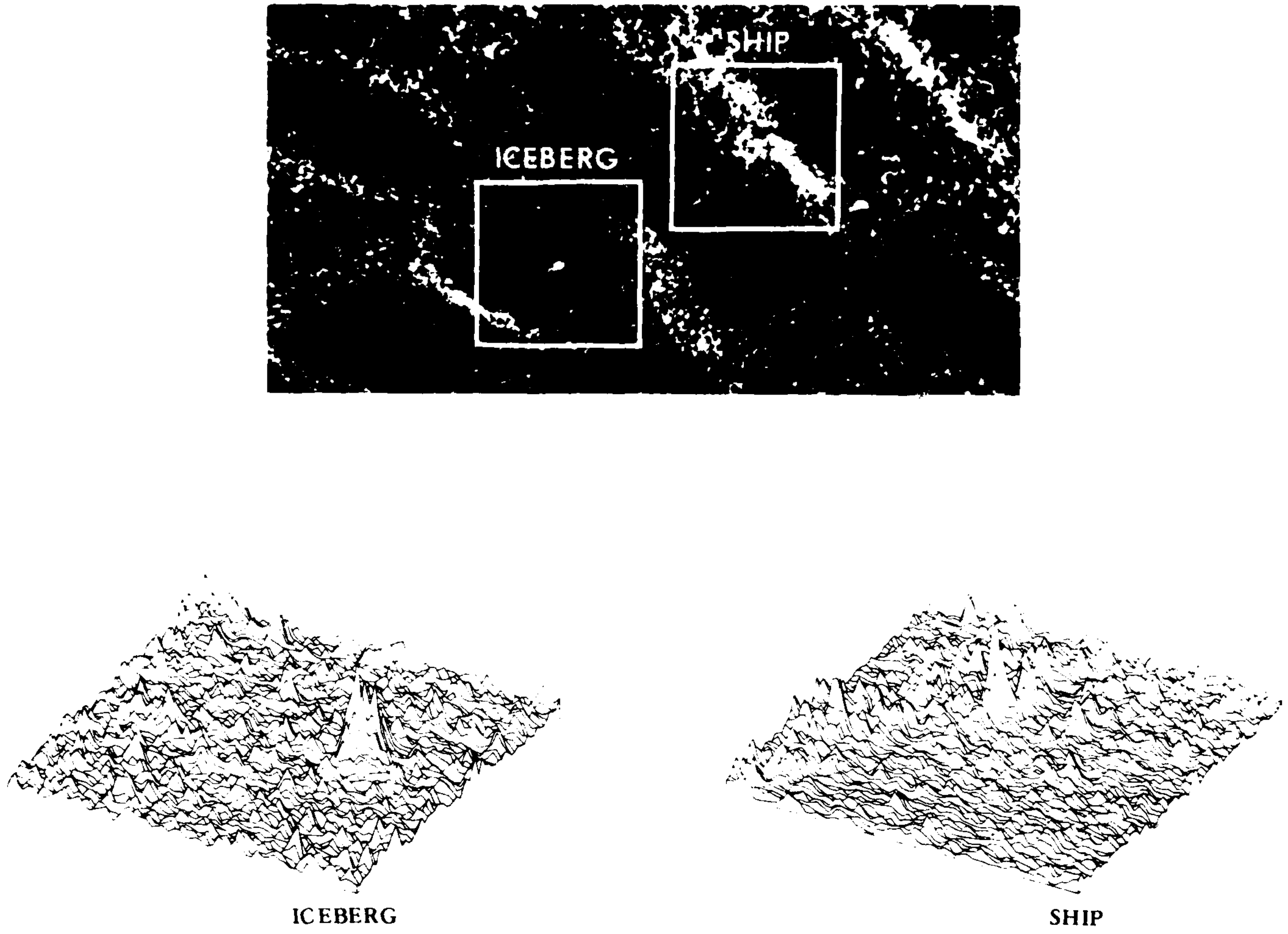

FIGURE 42. X-BAND (HV) PERSPECTIVE PLOTS OF SHIP AND ICEBERG LOCATION.

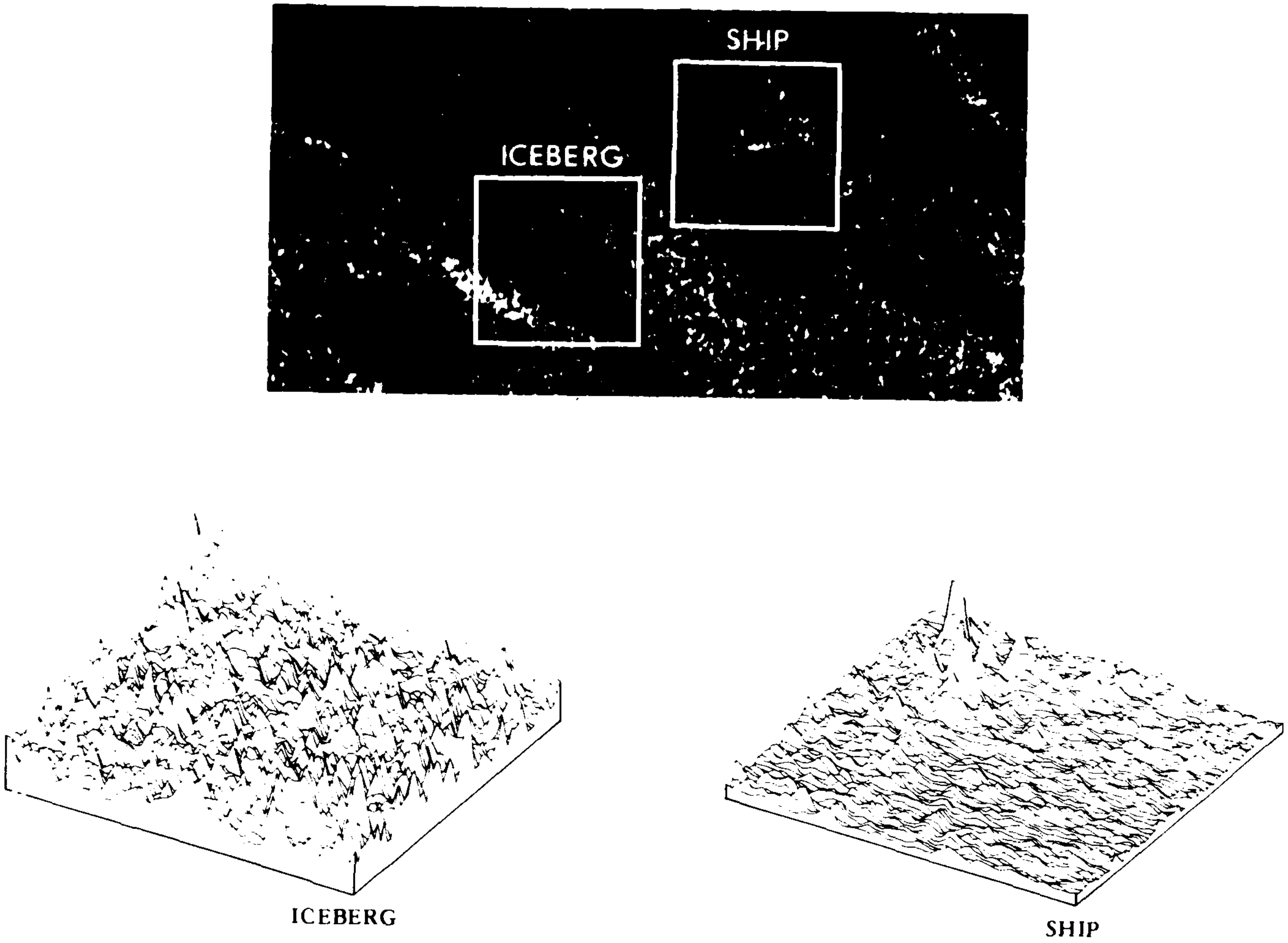

FIGURE 43. L-BAND (HH) PERSPECTIVE PLOTS OF SHIP AND ICEBERG LOCATION.

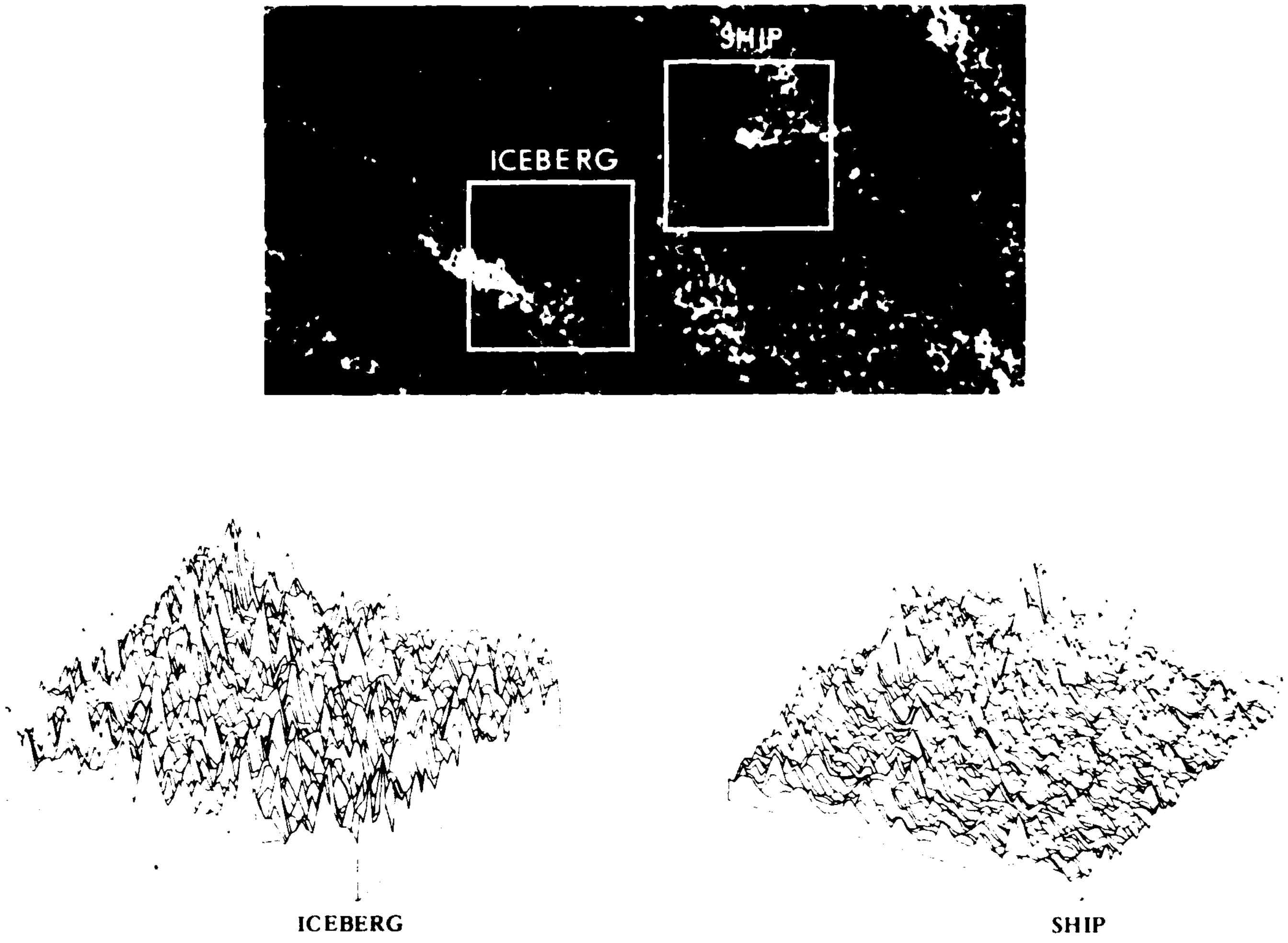

FIGURE 44. L-BAND (HV) PERSPECTIVE PLOTS OF SHIP AND ICEBERG LOCATION.

4.9 GRAPHIC DISPLAY

Perspective plots of ship and iceberg location along with the corresponding optically-produced images are shown in Figures 41 through 44 for each of the four channels. These results are consistent with the previous analysis. The ship is easily discriminated in both X-band channels and also with like-polarized L-band. The iceberg however, is discriminated only with cross-polarized X-band.

During the time of the overflight, surface conditions near the ship were characterized by ice floes, 5-10 meters in diameter, with broken slush between them, giving the visual appearance of complete ice cover. A swell was running through the ice with a period of about 12 seconds (185 m wavelength) and an amplitude (crest-to-trough) of approximately 2 m.

One interesting note: At the time of this overflight, there was 100 percent cloud cover with a ceiling of approximately 1000 ft, thus curtailing any aerial photography. This is an excellent example of radar's all-weather capability.

5
CONCLUSIONS AND RECOMMENDATIONS

As stated in the objectives, SAR imagery of sea ice was studied to determine signatures for classification of ice types. Emphasis in this study was placed on the analysis and evaluation of quantitative measurements and parameters obtained from the SAR data sets utilized. There are many results published [9, 13, 14, 15, 16, 17, 18, 19] from excellent research and study programs that have emphasized the photogrammetry interpretation approach to radar imagery of sea ice. This approach is used in operational SLAR ice reconnaissance systems today. Considerable information is collected from the study of shapes, edges, linear structure, and tonal variations in radar imagery. The long-term goal of this study is the realization of a fine-resolution system with automatic classification of key sea ice types. The general extent of the ice can be determined with coarse-resolution SLAR systems. When it becomes important to detect and to recognize small pieces of multi-year ice, small icebergs, and bergy bits as well as to estimate ridge height, then fine resolution systems with (perhaps) a multi-channel (polarization and/or wavelength) capability need to be considered. Also, it is hoped that signatures can be determined which can classify ridging and rafting (from which ice thickness can be inferred).

Results obtained from this study, thus far, would suggest the selection of 3 cm for the wavelength of an operational sea ice surveillance SAR. Also, the utilization of cross-polarization (transmitting horizontal polarization, receiving vertical), particularly for steep incidence angles (such as were employed with the SEASAT SAR) seems to be indicated. Data from the 3 cm channel provided the best discrimination for the various ice types used; multi-year ice with ridges, multi-year, first-year with ridges, and first-year ice areas were separable (having decreasing values of received power).

Comparisons of the measured values of dynamic range for the received signal, as a function of wavelength and polarization, show the X_{HV} and X_{HH} channels to have the largest dynamic range for the ice types included in this work. The use of vertical transmitted polarization should be investigated further.

Based on a comparison of the relative values of backscatter power from particular ice types as measured using the SAR data with the relative values obtained using scatterometer data, both airborne and ground-based sensors show very similar values for the same areas .

The mean values of the received power from the test sites corresponded to the ice roughness (i.e., ridging, no ridging, etc.) with the largest mean value from the most rough ice (as determined from ground truth data). Similarly, the largest standard deviation measured was from the roughest ice site.

Results from analysis of the L-band channel (23 cm wavelength) data have not provided any support for using this wavelength for ice classification systems. However, there is a situation regarding the Hopedale data where wet first-year ice provides strong signal returns at 3 cm, but low returns at 23 cm. This effect has been observed by others [18] and may constitute a signature with which to distinguish this type from multi-year ice.

To fully exploit the four channels of data available in the current data set, different analysis procedures should be investigated. Perhaps the same sort of analysis procedure used to develop multispectral scanner classification routines could be used on the multichannel SAR ice data. These routines could be employed to analyze the SAR returns in the four-dimensional vector space of observations, on an ice type-by-ice type basis. This would be accomplished through scatter plots, statistical measures of covariance, and multivariate measures of class separability. We would also try to characterize the underlying multivariate distributions of the SAR returns.

Finally, development of a discrimination procedure for digitally mapping ice types, based solely upon the dual-band/dual-polarization returns themselves, would be initiated.

It is anticipated that a future SAR system could include (1) wide-swath capability for large-area search, (2) fine-resolution capability for a detailed study of particular sea-ice areas, and (3) a digital-ice type classification capability, in addition to (4) a real-time digital image processor. In order to realize such a system, considerably more work needs to be accomplished in order to determine and verify the sea-ice type-classification SAR signatures. The technology, both digital and SAR, appears to be available now.

REFERENCES

1. Sivertson, E. and R. Larson, "Space Shuttle Search and Rescue Experiment Using Synthetic Aperture Radar," WESCON, September 1976, Los Angeles, Calif.

2. Luther, C.A. and R.A. Shuchman, "Sea Ice Detectability as a Function of Resolution and Mixed Integration," To be published in the Proceedings of the SURSAT Workshop (held in Toronto, June 1980).

3. Ausherman, D.A., W.D. Hall, J.N. Latta, and J.S. Zelenka, "Radar Data Processing and Exploitation Facility," Proceedings IEEE International Radar Conference, Washington, D.C., 1975.

4. Rawson, R.F., et al., Digitization of SAR 77 Image Data, ERIM Technical Report No. 303400-1-F, October 1978.

5. Blanchard, A.J. and J.W. Rause, Jr., "Depolarization of Electromagnetic Waves Scattered From Inhomogeneous Half Space Bounded by a Rough Surface," Radio Science, Vol. 15, No. 4, pp. 773-779, July-August 1980.

6. Hawkins, R.K., et al., "Single and Multiple Parameter Microwave Signatures of Sea Ice," Sixth Canadian Symposium on Remote Sensing, Halifax, May 1980 (to be published).

7. Deeker, C.V., R.G. Onstatt, and R.K. Moore, Radar Scatterometer Measurements of Sea Ice, Remote Sensing Laboratory Center for Research Inc., The University of Kansas, RSL Technical Report No. TR 331-17, August 1980.

8. Gray, A.L., R.O. Ramsier, and W.J. Campbell, "Scatterometer and SLAR Results Obtained Over Arctic Sea-Ice and Their Relevance to the Problems of Arctic Ice Reconnaissance," Fourth Canadian Symposium on Remote Sensing, Quebec City, pp. 424-443, May 1977.

9. Onstott, R.G., et al., Radar Backscatter Study of Sea Ice, Remote Sensing Laboratory Center for Research, Inc., The University of Kansas, RSL Technical Report No. RSL-TR-331-14, February 1980.

10. Onstott, R.G., R.K. Moore and W.F. Weeks, "Surface-Based Scatterometer Results of Arctic Sea Ice," IEEE Transactions on Geoscience Electronics, Vol. GE-17, No. 3, pp. 78-85, July 1979.

11. Liskow, C., A. Klooster, R. Rawson, R. Shuchman, and H. Wagner, Analysis of Georges Bank Radar Imagery, ERIM Technical Report No. 120800-6-F, 1977.

12. Larson, R.W., et al., "The Use of SAR Systems for Iceberg Detection and Characterization," Proceedings of the Twelfth International Symposium on Remote Sensing of Environment, ERIM, Ann Arbor, pp. 1127-1148, 1978.

13. Dunbar, M., "Interpretation of SLAR Imagery of Sea Ice," Journal of Glaciology, Vol. 15, No. 73, pp. 193-213, 1975.

14. Ketchum, R.D. and S.G. Tooma, "Analysis and Interpretation of Airborne Multi-Frequency Side-Looking Radar Sea Ice Imagery," Journal of Geophysical Research, Vol. 78, No. 3, pp. 520-538, 1973.

15. Glushkov, V.M. and V.B. Komarov, "Side-Looking Imaging Radar System TOROS and Its Application to the Study of Ice Conditions and Geological Explorations," Proceedings of the Seventh International Symposium on Remote Sensing of Environment, University of Michigan, Ann Arbor, 1971.

16. Rouse, J.W., Jr., "Arctic Ice Type Identification by Radar," Proceedings IEEE, Vol. 57, pp. 605-614, 1969.

17. Anderson, V.H., "High Altitude Side-Looking Radar Images of Sea Ice in the Arctic," Proceedings of the Fourth International Symposium on Remote Sensing of Environment, University of Michigan, Ann Arbor, pp. 845-857, 1966.

18. Ketchum, R.B., An Evaluation of ERIM X-L Band Airborne Synthetic Aperture Radar Imagery of Sea Ice, (NORDA Technical Note 28.

19. Rawson, R.F. and A.L. Maffett, et al., L-Band Radar Clutter Statistics for Terrain and Ice, ERIM Technical Report No. 128900-9-F, February 1978.

APPENDIX A

GROUND TRUTH FROM BEAUFORT SEA TEST SITES

Dr. Raymond Lowry
INTERA
Ottawa, Ontario, Canada

BEAUFORT SEA SAR DATA TEST SITE DESCRIPTIONS

The Final Report
of an analysis of three selected sites,
and the SURSAT SAR data collected
over those sites in March 1979.
Prepared for the
Environmental Research Institute of Michigan
by
Intera Environmental Consultants Ltd.

Intera Report 908-81-1 January 1981

intera

PREFACE

This Final Report summarizes work done on behalf of the Environmental Research Institute of Michigan (ERIM) by Intera Environmental Consultants Ltd. (INTERA). The work took place between October 1979 and January 1981, under Contract Number N00014 79 C 0698.

INTERA would like to acknowledge the support of the Surveillance Satellite (SURSAT) Project for collection of the original data set, and for support on some analysis referred to in this report. In addition, some of the digital data discussed in this report was generated under the SURSAT Program.

R.T. Lowry

ABSTRACT

The SAR data, collected by the SURSAT Project in the Beaufort Sea in March 1979, represented the first high-resolution, 4-channel SAR data ever collected over multi-year and first year sea ice. Several sites were selected for detailed analysis, and the prime purpose of this report is to describe in detail three test sites.

The first site is on smooth ice, in a shorefast zone near the Tuktoyaktuk Peninsula. The second is in the rather turbulent transition zone, about 100 km north of the first site. The third is in the multi-year pack ice, some 150 km farther north. All three sites show the range of ice conditions typical of their zones.

In addition to detailed surface descriptions, both hand-held, 35-mm and vertical 9"-by-9" photography has been collected for the sites. The 9"-by-9" photography has been attached in the appendices.

An analysis of the digital data from the multi-year site has been conducted. This includes some observations made directly on the digital data, using the CCRS Image Analysis System. Most, however, are based on the data generated by ERIM, using corrected tapes.

This analysis confirms the general distinctions that have been made between the scattering mechanisms of first year and multi-year sea ice at steep angles. The primary interaction in multi-year ice seems to be volume scattering, whereas in first year ice, it is a surface scattering effect. At very shallow depression angles (7°), this distinction seems to be breaking down. More work is needed to quantify these effects.

TABLE OF CONTENTS

Page

PREFACE A-i

ABSTRACT A-ii

LIST OF TABLES A-iv

LIST OF FIGURES A-v

1. INTRODUCTION A-1

2. THE ICE REGIME OF THE BEAUFORT SEA A-4

3. THE TEST SITES A-8
3.1 The Shorefast Zone: Site "A" A-8
3.2 The Transition Zone: Site "Anomalous" A-8
3.3 The Permanent Pack Zone: Site "II" A-9

4. DETAILED SITE DESCRIPTIONS A-10
4.1 Shorefast Ice Zone A-10
4.2 Transition Zone A-22
4.3 Permanent Pack: Site "II" A-27

5. AVERAGE RADAR CROSS-SECTION STUDY A-31

6. CONCLUSIONS A-39

7. REFERENCES A-40

8. APPENDICES A-41
8.1 Appendix 1 A-41
8.2 Appendix 2 A-41

LIST OF TABLES

		Page
A-1	Site "A" Salinity Samples	A-20
A-2	CIAS Data for Four Classes, Shallow Depression	A-32
A-3	CIAS Data for Four Classes of Various Resolutions for Shallow Depression	A-33
A-4	a) ERIM X-band Data for Four Classes of both Shallow (7°) and Steep (50°) Depression Angles b) The Ratio of Reflected to Scattered X-band data for Both Steep and Shallow Depression Angles	A-35
A-5	Reflected and Scattered Power Ratios for Steep and Shallow Data	A-38

LIST OF FIGURES

		Page
A-1	SURSAT Sea-Ice Reconaissance Flight Line Over Fletchers Island (T3), March 1979	A-2
A-2	Site "A", 16 March 1979, X-HH Steep Depression	A-11
A-3	Site "A", 18 March 1979, X-HV Shallow Depression	A-12
A-4	9"-by-9" Format Vertical Photography from 7000' AS	A-13
A-5	Site "A" Reflectors	A-14
A-6	Radar Reflectors at Site "A", 79-3-4	A-15
A-7	Typical Snow Cover on Shorefast Ice, 79-3-4	A-16
A-8	Ice Surface of Typical Shorefast, Undeformed Ice	A-17
A-9	Photograph Taken 79-3-14, Looking SSE from N of 'New' Lead	A-18
A-10	Snow Flowers that Have Formed on Ice, Approximately Seven Days Old	A-19
A-11	X-HH, 16-3-79, Steep Depression - Anomalous Site	A-23
A-12	X-HV, 18-3-79, Shallow Depression - Anomalous Site	A-24
A-13	Photography Taken While Standing on the Ice, Using a 35-mm Camera, with a 50-mm Lens	A-25

A-14 X-HV, 16-3-79, Steep Depression, Site II A-28

A-15 L-HH, 18-3-79, Shallow Depression, Site II A-29

INTRODUCTION

In March of 1979, a major field program was undertaken through the SURSAT office, aimed at better understanding of the use of microwave remote sensing for sea-ice reconnaissance. Numerous Canadian and American companies, and governmental agencies were involved in this work, with aircraft based in Alaska, Inuvik and Yellowknife, and a large field party, which primarily operated out of the Polar Continental Shelf Project (PCSP) camp at Tuktoyaktuk. The prime sensor was the SAR-580 system, which consists of the ERIM 4-channel Synthetic Aperture Radar (SAR) aboard the CCRS Convair 580 (Inkster et al., 1979).

In addition to the SAR-580, both the NASA Lewis and the AES APS-94 SLAR systems were used to collect radar imagery. The SAR-580 also collected scatterometer and radiometer data, with coincident RC-10 photography. The test line covered by all sensors was located on the meridian 132° W, and went from the Tuktoyaktuk Peninsula to approximately 73° N. An additional short line was flown by some of the sensor combinations, over Fletcher's Ice Island (T3), which was drifting by the 132°-E line at approximately 72 1/2° N, heading east to west (see Figure 1).

The SAR-580 imagery represented a unique data set, for several reasons. It was the first time very high-resolution, X- and L-band imagery (HH and HV) had been collected over sea ice with large amounts of multi-year ice present. The ancillary data set was exceptionally fine, consisting of (1) digital SLAR data from the NASA Lewis APS-94D, (2) CCRS Radiometer/scatterometer data, (3) Numerous 9"-by-9" stereo camera flights, and of most importance, (4) considerable on-ice data, collected by several experienced groups.

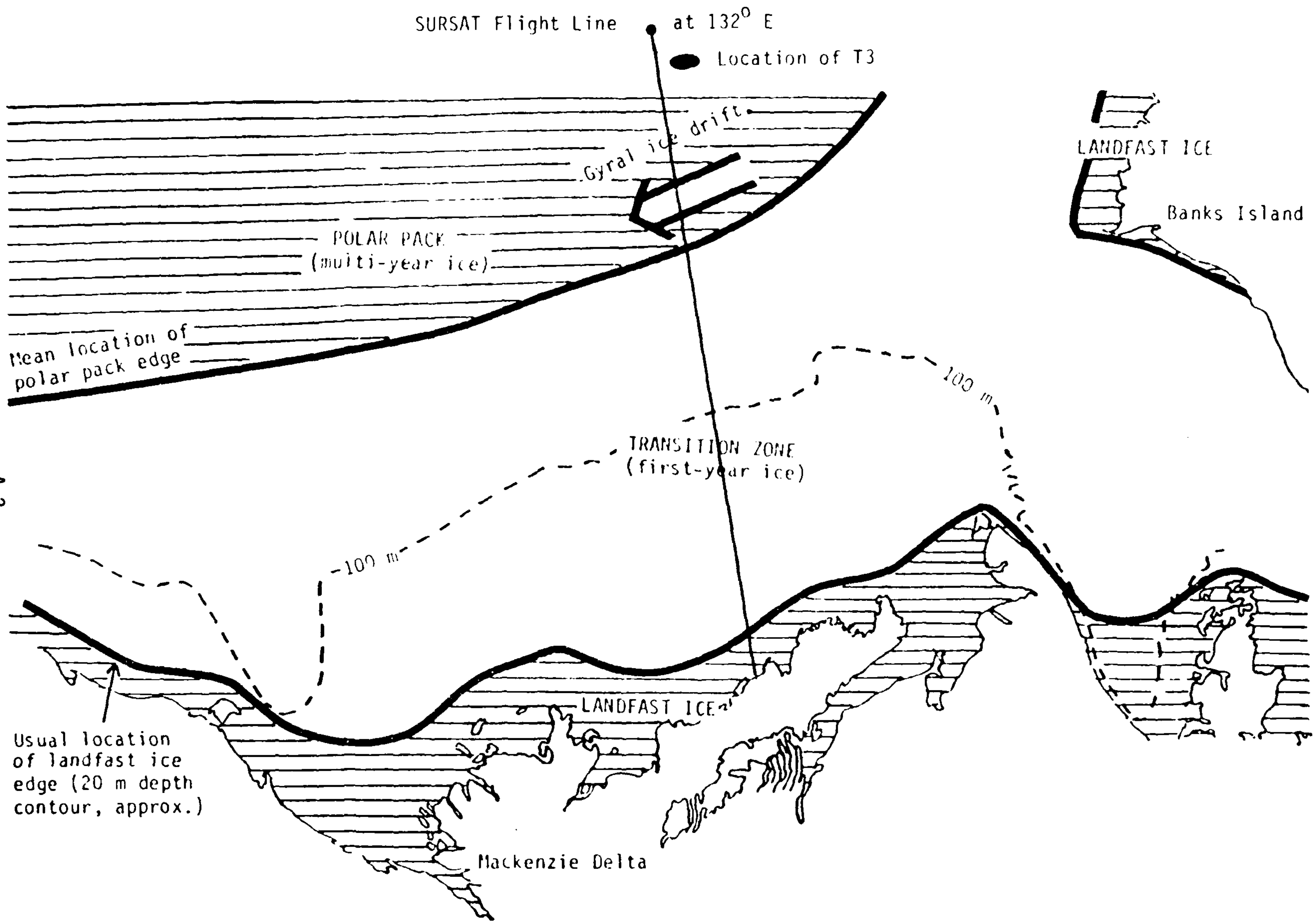

Figure A-1 SURSAT sea-ice reconnaissance flight line over Fletchers Island (T3), March 1979.

Three SAR flights took place, on 12, 16 and 18 March 1979, all following the line 132° E, and heading due north. On March 12th, the X-HH, wide swath antenna was used. An aircraft APU malfunction resulted in the loss of the first third of the data on the main test line. Imagery was collected on the T3 line, however, and scatterometer, radiometer and photography data were collected on the return trip. The 4-channel antenna was flown on March 16th and 18th, in "steep" and "super-shallow" modes respectively. The T3 line was flown on the 16th, but due to the low altitude used on the 18th, this line had to be abandoned to save fuel. Some additional data were collected over the MacKenzie Delta on March 16th.

2. THE ICE REGIME OF THE BEAUFORT SEA

The ice domain of the Beaufort exhibits widely diverse characteristics. Intrinsic properties and surface appearance are seasonally dependent, and the notable features can vary from year to year. This section describes some of the characteristics of the ice domain, especially as they relate to remote sensing. A number of more detailed reviews are available (e.g., Kovacs and Mellor, 1974; Wadhams, 1975).

Typically, the southern Beaufort is ice-covered for about nine months annually, although for about one year in ten, the ice cover may remain throughout the year. The ice, during the late winter at least, is characterized by three zones, as illustrated in Figure 1.

The landfast zone extends outward from the coast to about the 20-m bathymetric contour. Stabilized against movement by the presence of grounded ridge keels out to this depth, the landfast zone annually grows to a thickness of about 2 m. During the early summer, it weakens, fragments, and the resulting floes either melt in the warm southern waters, or join the permanent Arctic Pack ice further offshore.

The permanent pack mainly consists of ice which has survived previous summer melting cycles. The multi-year ice which has thus evolved is characteristically 3 to 5 m thick, in floes which range in size from ten metres to (rarely) tens of kilometers. Normally, the multi-year ice appears in a matrix of first year ice, often heavily ridged. The major characteristic of the permanent pack ice found in the Beaufort Gyre is its large-scale motion. On average, the ice exhibits a clockwise circulation pattern (see Figure 1) and together with the smaller-scale motions superimposed on it, is responsible for creation of the third region of interest, the transition zone.

The transition zone exists as an interface between the stable landfast ice and the circulating pack ice of the Beaufort Gyre. This zone (see Figure 1) encompasses areas where most of the hydrocarbon deposits are believed to be situated. It is also the zone of maximum dynamic ice interaction.

Through the winter, the ice in the transition zone is being transported and transformed. Open water leads are formed under divergent stress conditions, to be rapidly refrozen in the -20° C to -40° C temperatures. Convergent stresses produce ridging and rafting, particularly in the newly refrozen leads, which are thinner and hence, more susceptible to buckling forces. Thus, a particular region will probably contain a range of ice conditions, and thickness and surface characteristics.

Into this region, multi-year ice from the permanent pack may intrude. Intrinsically characterized by greater thickness and lower brine content than first year ice, these floes often contain multi-year ridges, hummocks, and sometimes, hummock fields. In contrast to their first year counterparts, which are partly composed of unconsolidated blocks of ice, these have evolved to a fully consolidated (i.e., solid) state and, therefore, represent a greater challenge to future operational capability.

The three zones described above are representative of the period from December through May. During the freeze-up period of early winter, the landfast ice normally has not developed the thickness and strength to resist the forces imposed upon it, so the whole region participates in the dynamic transformations occurring at this time.

The formation of new ice normally commences by mid-October in the southern Beaufort. Freeze-up occurs first in the shallower near-shore regions, and its evolution is governed by a number of factors, including the heat budget of the water column, the fresh water flow of the MacKenzie River and, more spectacularly, by the dynamic effects of the winds and currents. This early evolutionary history determines the surface properties of the ice, and seems fundamental to the appearance of the ice in X-band radar imagery.

As the ice grows, perhaps to a 30-cm thickness by early November, the dynamic effects produce rafting and subsequently, ridging of the ice. Because of the low tensile strength and the susceptibility to fracture, a range of thickness and surface conditions is produced (including specular smoothness, microscale roughness and macroscale roughness) and distributed on scales of tens of metres to several kilometers. By mid-December, the dynamic evolution is restricted to the transition zone, although even in the landfast zone, the surface characteristics continue to evolve through the mechanisims of brine migration and snow coverage.

The appearance of the ice in the transition zone, therefore, is characterized by a range of roughness scales (from millimeters to metres, and distributed over dimensions of tens of metres to kilometers), and by a range of thicknesses and geometries. Sometimes, superimposed upon this scene will be multi-year ice, which is typified by its low, rolling appearance and smoothed ridges.

The winter of 1978-79 was not an especially hard winter for sea ice in the southern Beaufort Sea. The pack had remained relatively far north for the last two summers, and no multi-year ice was seen south of 72° N. Satellite imagery shows the ice formed normally but consolidated slowly, due to the effect of the so-called "trans-arctic" high-pressure ridge. For a substantial portion of the winter, ice was being swept to the northwest by winds. There was, therefore, no consistent onshore wind bringing in the heavy pack. In addition, the ice formed in the Amundsen Gulf was being carried out into the southern

Beaufort Sea. By February, the ice in the Amundsen Gulf had consolidated, as had that in the southern Beaufort. While there was still movement in the southern Beaufort, it was much more constrained and, on average, tracked the Beaufort Gyre, with winds providing the higher-frequency movements.

3. THE TEST SITES

Four test sites were initially selected for analysis, based on a combination of SAR data availability and quality, intrinsic interest of the ice, and quality of ancillary information. Later, this was narrowed to three sites, for ease of analysis. The T3 test site was dropped, for lack of the shallow-depression SAR imagery. The three remaining test sites were chosen so that one site was in each of the three major zones described in the previous section.

3.1 THE SHOREFAST ZONE: SITE "A"

The plan for the SURSAT experiment was to deploy a series of radar reflections at a number of sites along the test line. The first of these sites, called Site "A", was established at 70° N, 132° W (using the helicopter navigation system). Subsequent sites were not established, due to excessive ice motion. Site "A" was located on what had been an old, and very wide shore lead. The site was approximately 35 km north of the shore, on ice that was about 1 m thick.

It is not known exactly when the ice formed, but the estimate is that this was a shore lead that opened early in the winter (November - December). It appears to have consolidated very rapidly, so the air temperature must have been quite low at the time. It has somewhat less snow cover than ice further south or north, which is again consistent with this theory.

3.2 THE TRANSITION ZONE: SITE "ANOMALOUS"

This site, less than 100 km north of Site "A", was covered with first year ice that was very rough. It was selected for investigation because on the SLAR imagery it appeared to be much more reflective than normal first year ice, and was thought to be multi-year ice. Investigation revealed that this was some of the ice from the Amundsen Gulf, which had been broken up by wind and wave action when it was 20 to 30 cm thick. The surface truth is 35-mm photography from the ground and from a helicopter, plus field notes of the SURSAT party. Its significance is that it demonstrates the range of signals that can result from first year ice in this zone.

3.3 THE PERMANENT PACK ZONE: SITE "II"

This site was selected, in spite of there being no surface-truth data, because the airborne data set was complete, and because the ice presented many very interesting features. Located at the southern edge of the permanent pack, it showed a rather well-defined edge, which is illusionary. There was a considerable quantity of multi-year ice just south of this area, and both large, multi-year floes and very small, multi-year fragments in the scene, shown on low-level, 9"-by-9" photography. It was, therefore, particularly suited for obtaining signatures of all the different ice types, as well as studying the detectability of small, multi-year pieces in a first year matrix.

4. DETAILED SITE DESCRIPTIONS

4.1 SHOREFAST ICE ZONE

The Site "A" reflectors (see Figure 5) show very clearly on the SAR imagery, and mark the location exactly, as can be seen on both Figure 2 (X-HH, 16-3-79) and Figure 3 (X-HV, 18-3-79). The effect of depression angle is quite marked, particularly for angles of 45° or more and 5° or less. At steep angles, the surface of the ice, which is relatively smooth and uniform on the 9"-by-9" photography (see Figure 4), shows tonal variations that are related to the way the ice originally started to form. The slight snow cover, which is stuck to the ice surface because of salt migrating up into the snow, shows very definite texture (see Figure 6). Typically, the ice will have such a surface layer, later covered by snow which will be blown about by the wind (see Figures 7 and 8).

The salinity of the ice normally will be in the range of 5 to 10 ppt, depending to a large extent on how fast the ice freezes. The surface layer will be very much more saline (100 ppt or more), and will be covered in frost flowers before snow covers it.

Figures 9 and 10 show the new lead that opened after the 9"-by-9" photography was taken, but before the SAR was flown. Optically, it appears quite light, due to these frost flowers. It also scatters strongly at X-band, but not at all at L-band. As soon as snow falls on this ice, salt migrates up into the snow. Core samples, with the snow layer intact, were taken at Site "A". A typical salinity profile is shown in Table 1, with the snow having salinities almost three times higher than the ice below it.

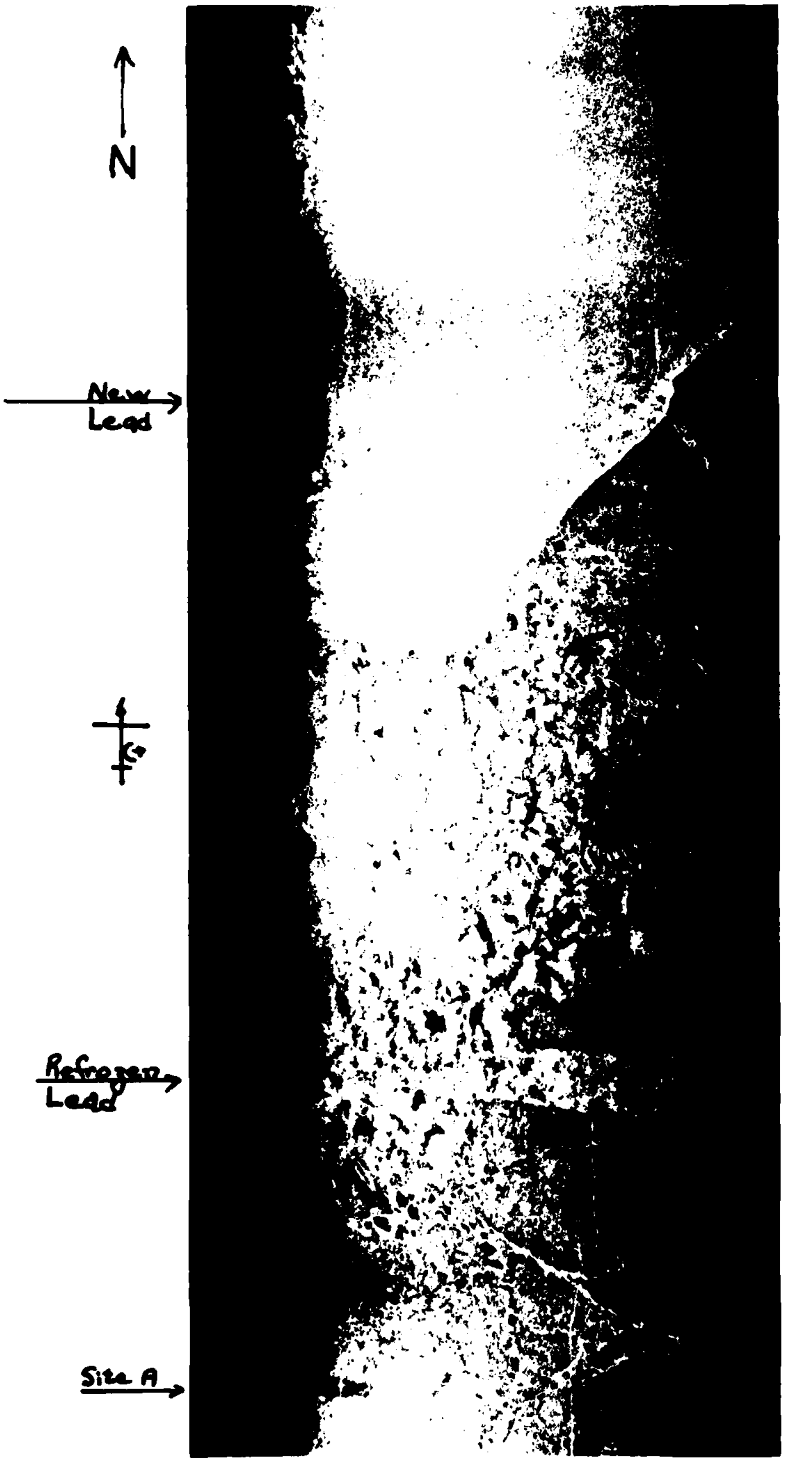

Figure A-2 Site 'A' 16 March 1979 X-HH Steep Depression.

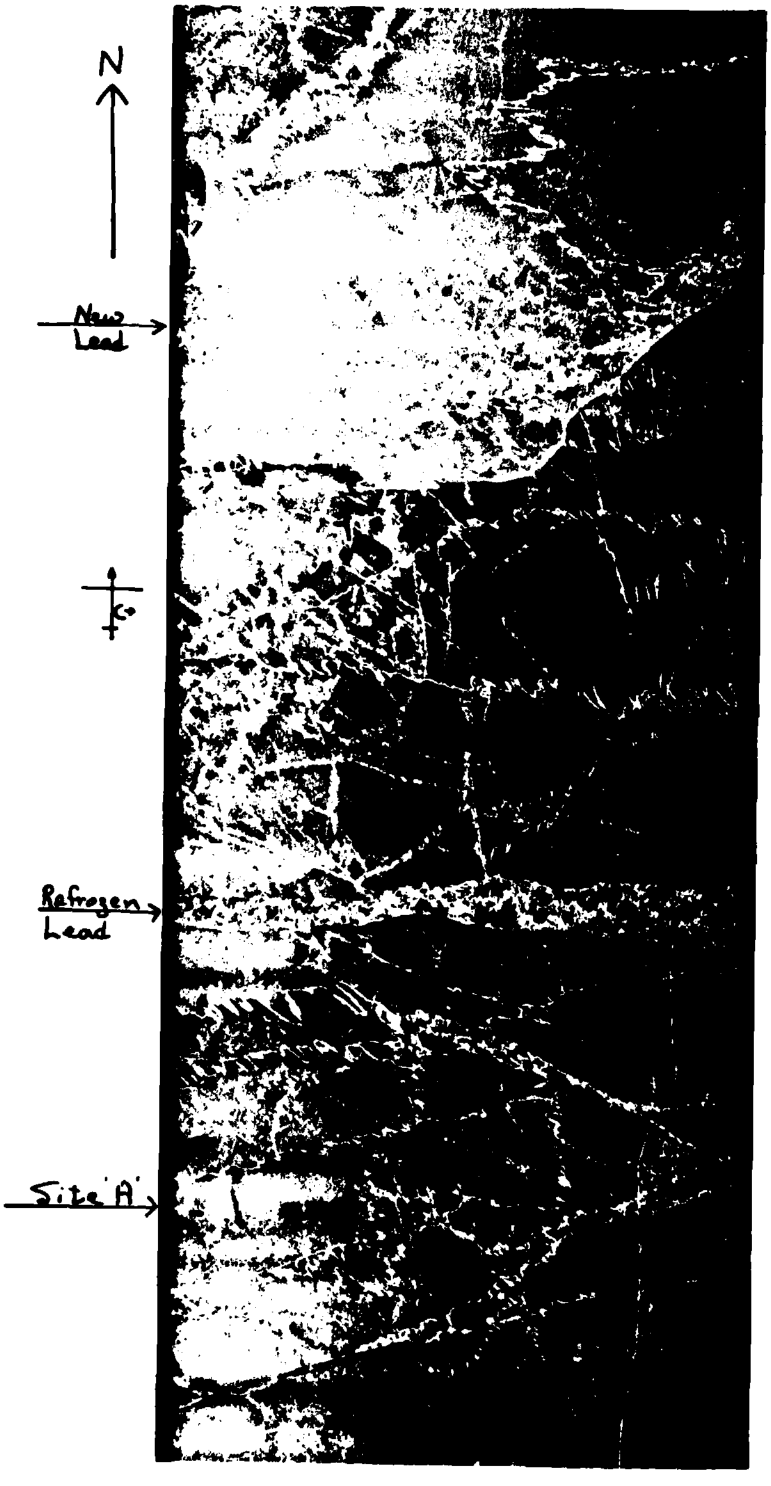

Figure A-3 Site A 18 March 1979 X-HV Shallow Depression

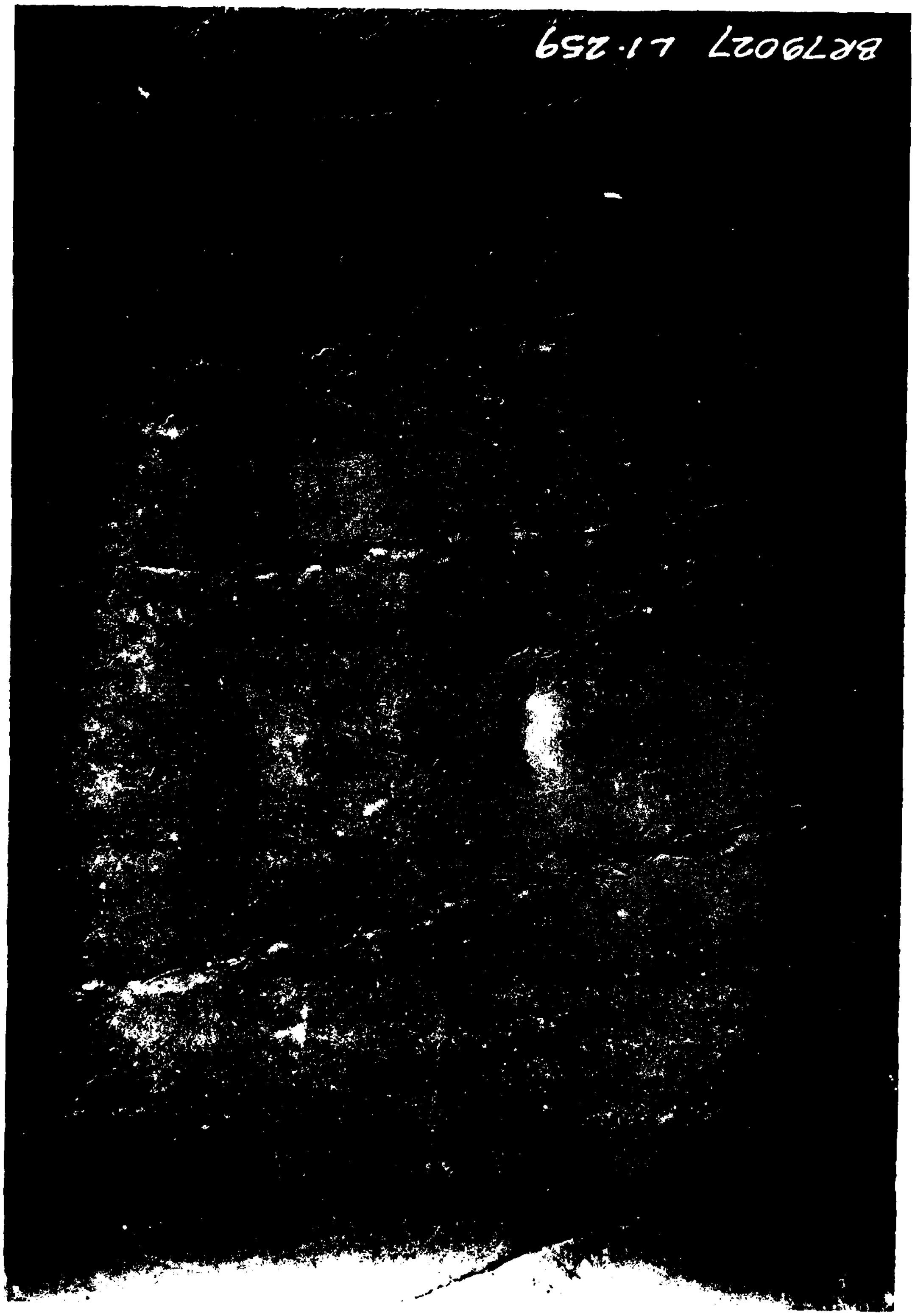

Figure A-4 9"-by-9" format vertical photography from 7000' AS. Scale is 1:14 000, showing the Site "A" reflector array, and the refrozen lead.

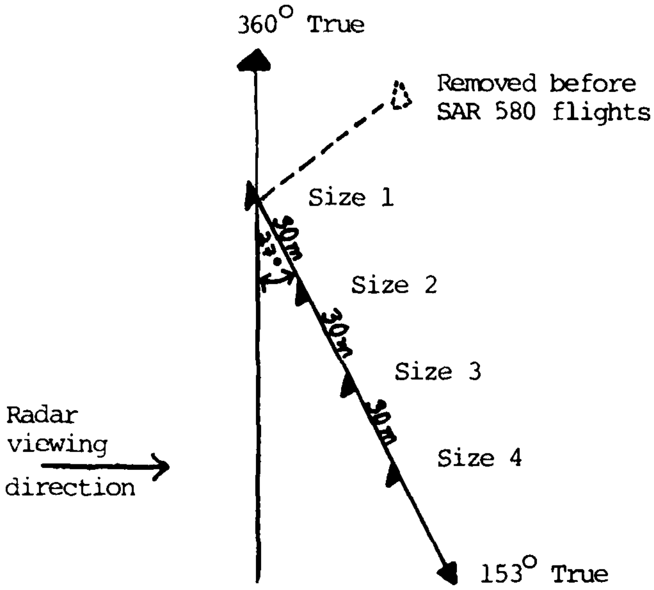

All reflectors are level on the ice, and aligned to be viewed from the 360° True flight line.

Reflector Size	Diagonal Dimension	Edge Dimension
1	1.66 m	1.17 m
2	1.07 m	0.76 m
3	0.715 m	0.51 m
4	0.535 m	0.38 m

Figure A-5 Site "A" reflectors.

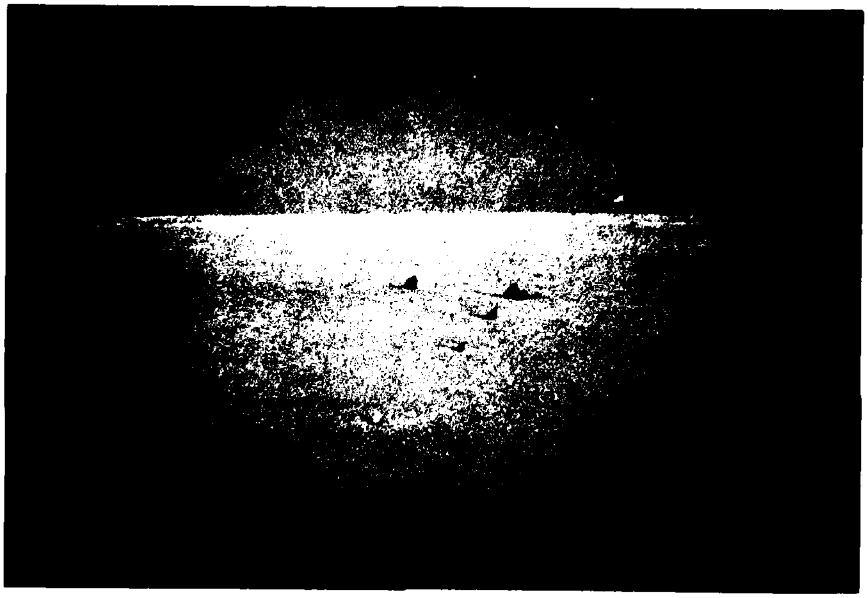

Figure A-6 Radar reflectors at Site "A", 79-3-4. Shadows indicate N. The reflectors were moved, and one large reflector was removed on 79-3-6, to the locations shown in Figure 5.

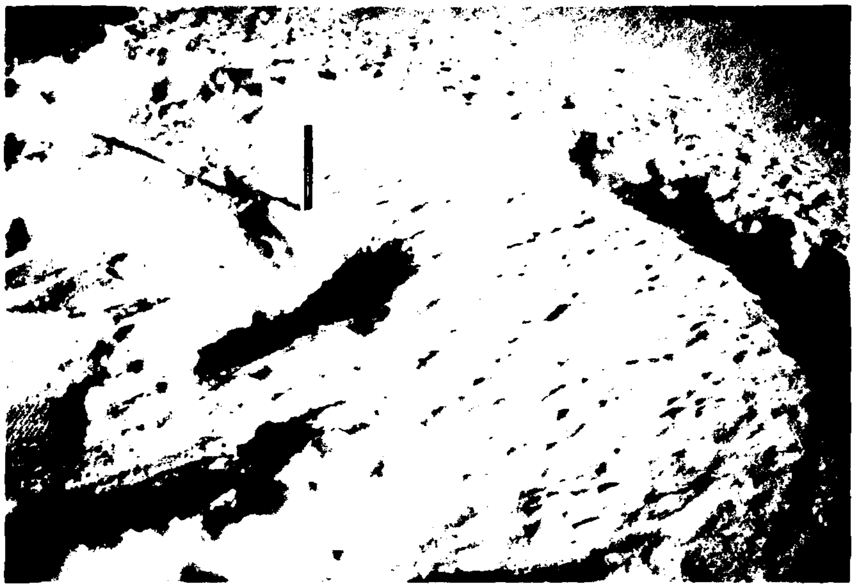

Figure A-7 Typical snow cover on shorefast ice, 79-3-4. Fluff layer is quite dry, has no salt content, and is very cold. It later blew away.

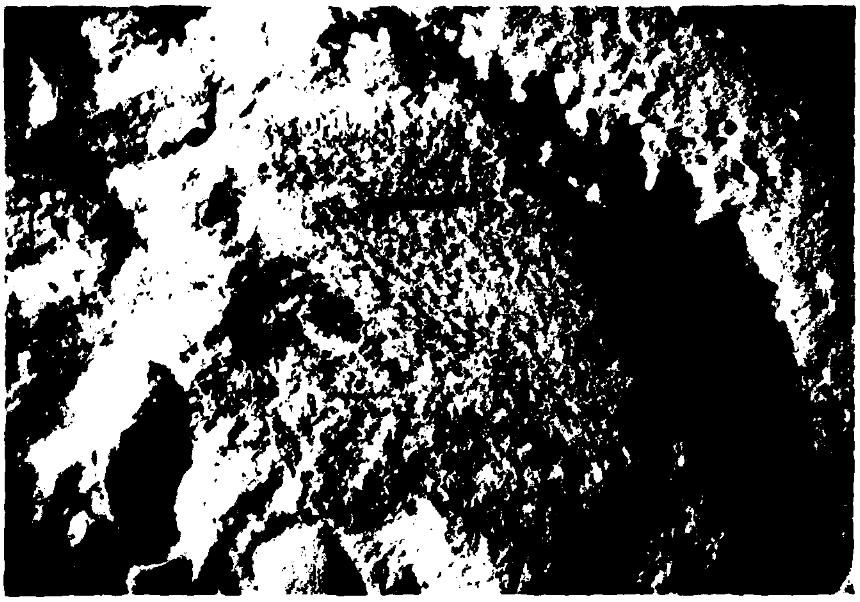

Figure A-8 Ice surface of typical shorefast, undeformed ice.

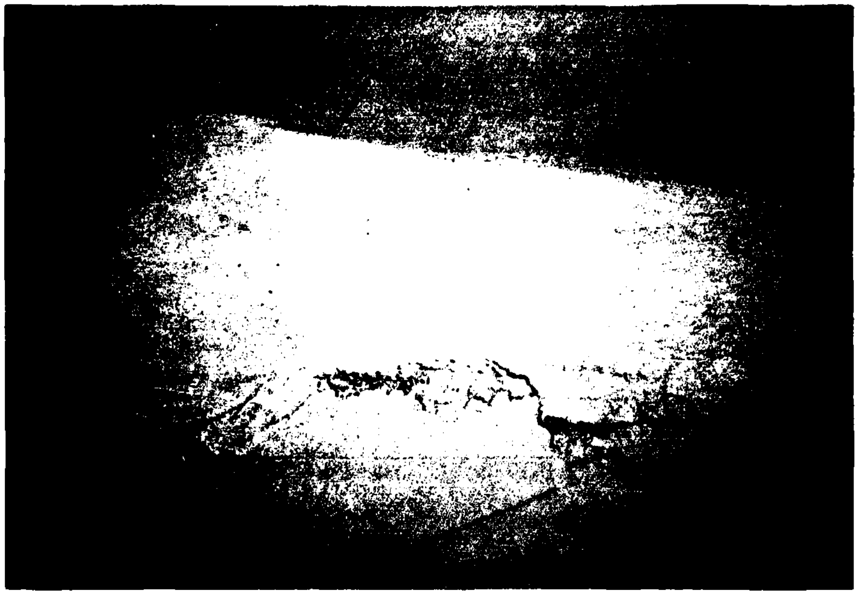

Figure A-9 Photograph taken 79-3-14, looking SSE from N of 'new' lead. The lead is covered with "snow flowers".

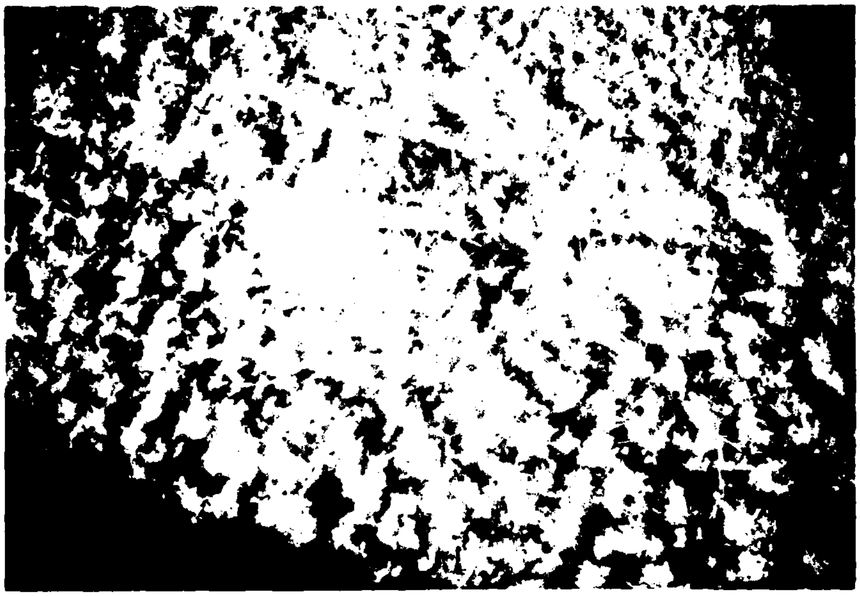

Figure A-10 Snow flowers that have formed on ice, approximately seven days old. There is no snow cover, and the air temperatures have been below -25° C the entire time. The ice surface is covered in a layer of slush (salinities of 100 ppt), and is at about -100° C. The scale is approximate, since it was taken from 1 m, with a hand-held, 35-mm camera.

Table A-1 Site "A" salinity samples.

#	Depth (cm)	Salinity PPT
ss. 1	-3 1.5	9.2
ss. 2	-1.5 0	26.2
1	0-2	28.2
2	4	9.5
3	6	8.5
4	8	6.8
5	10	7.0
6	12	7.0
7	14	8.5
8	16	8.7
9	18	10.0
10	20	9.9
11	22	leaked
12	24	8.8
13	26	8.9
14	28	9.4
15	30	8.8
16	32	8.7
17	34	8.1
18	36	8.2
19	38	8.3
(to 75 cm exists)		

Ice depth was approximately 100 cm on 79-3-6, and was growing at about 4 cm/week.

The snow also forms an insulating layer, which generally means that the surface of the ice is warmer than the air. It is unusual, therefore, to find the surface temperature below the eutectic temperature for a brine solution. This means there will always be brine in the snow-ice interface, so that little or no radar energy will be returned from the ice itself, but rather from the snow-ice interface. This is distinctly different from multi-year ice, where the brine has been leached out.

Comparing Figures 2 and 3 (SAR) with Figure 5 (vertical photography) shows that the SAR distinguishes all the salient features on the ice. Typical is the refrozen lead just north of "A". The rubble associated with this feature was built up when the ice fractured along this line and began to work back and forth.

4.2 TRANSITION ZONE

This site was selected for detailed investigation by the SURSAT ground-truth team, based on an analysis of the data collected by the NASA Lewis SLAR. A particular ice floe was noted as having a signature very near that of multi-year ice. The main helicopter, (a 206) was not capable of reaching the main multi-year pack, but could fly to this feature, so an investigation was launched. It was found not to be multi-year ice at all, but merely very rough, first year ice. This serves to illustrate that classification based on tone alone is very dangerous. The higher-resolution SAR imagery was very clear, and based on texture and tone, a correct identification was made. The anomalously high return gave this site its name.

Between the 16th and 18th of March, the multi-year pack had shifted, and the flight lines were different, due to navigational system drift. For whatever reason, the image swaths are not identical. Figures 11 and 12 show the site imaged on the 16th and 18th respectively. To aid in correlating the images, a point "A" has been shown on both. The field party landed, and made on-site observations at approximately the point shown on Figure 12. This area is not properly imaged on the March 16th pass. Figures 13a and 13b are typical images, taken from a position on the ice, using a 35-mm camera with a 50-mm lens. The general rough texture of the surface can be seen. It should be noted that the ice was 20 to 30 cm thick when the rubble was created, but the general thickness was greater than 1 m (the length of drill carried) and it was fully consolidated. This can be demonstrated by observing that the ridge, noted as "B" on Figure 12, cuts right across ice features of very different tonal character. This ridge formed when the ice had consolidated as a sheet.

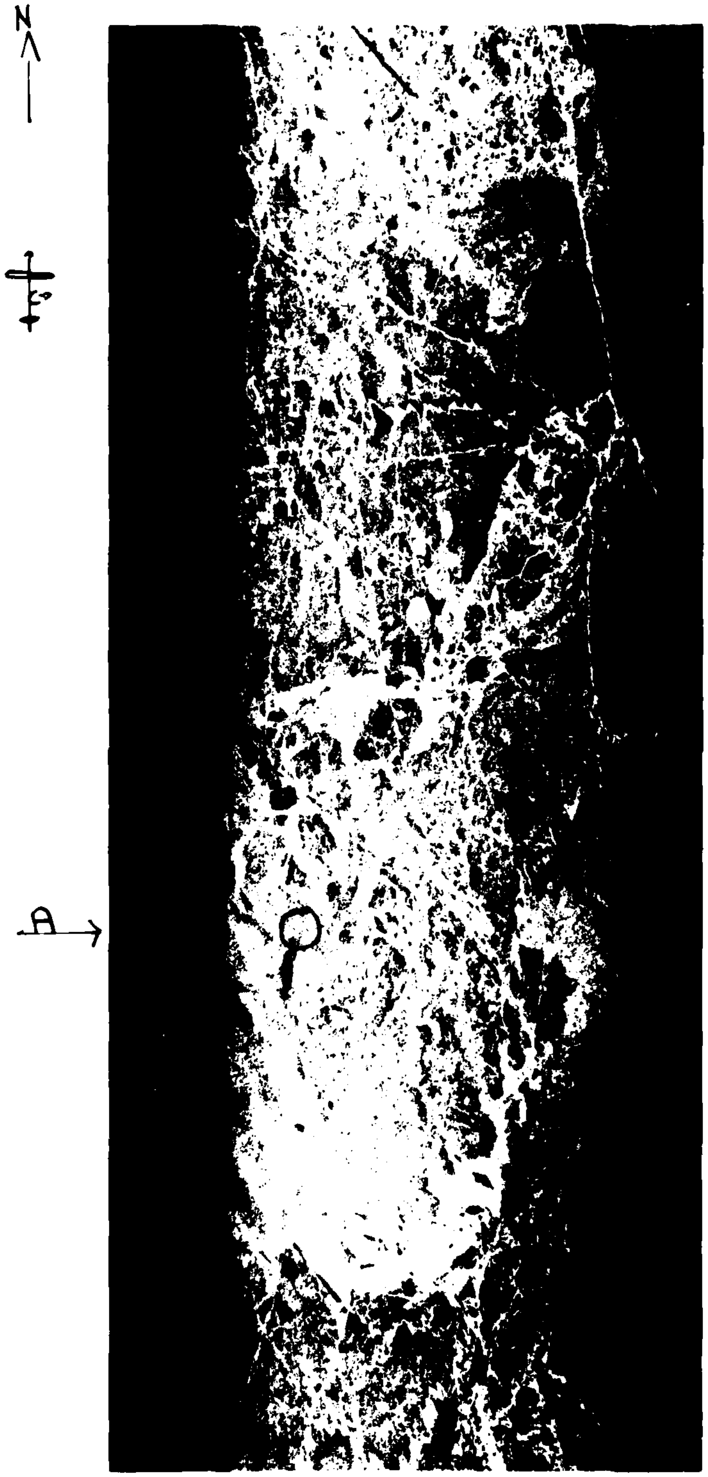

Figure A-11 X-## 16-3-'79 Steep Depression Anomalous Site

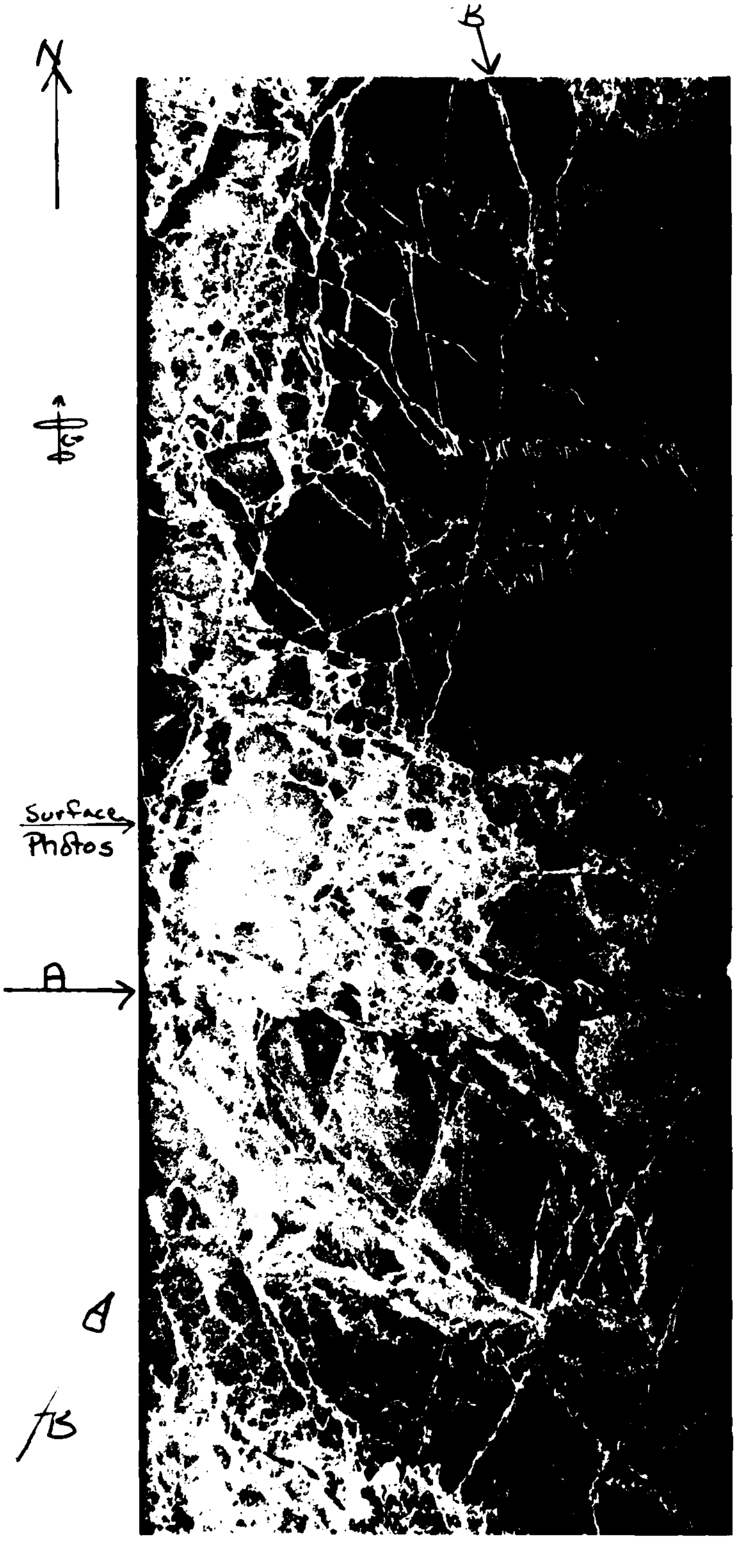

Figure A-12 XHV 10-3-79 Shallow Depression - Anomalous Site

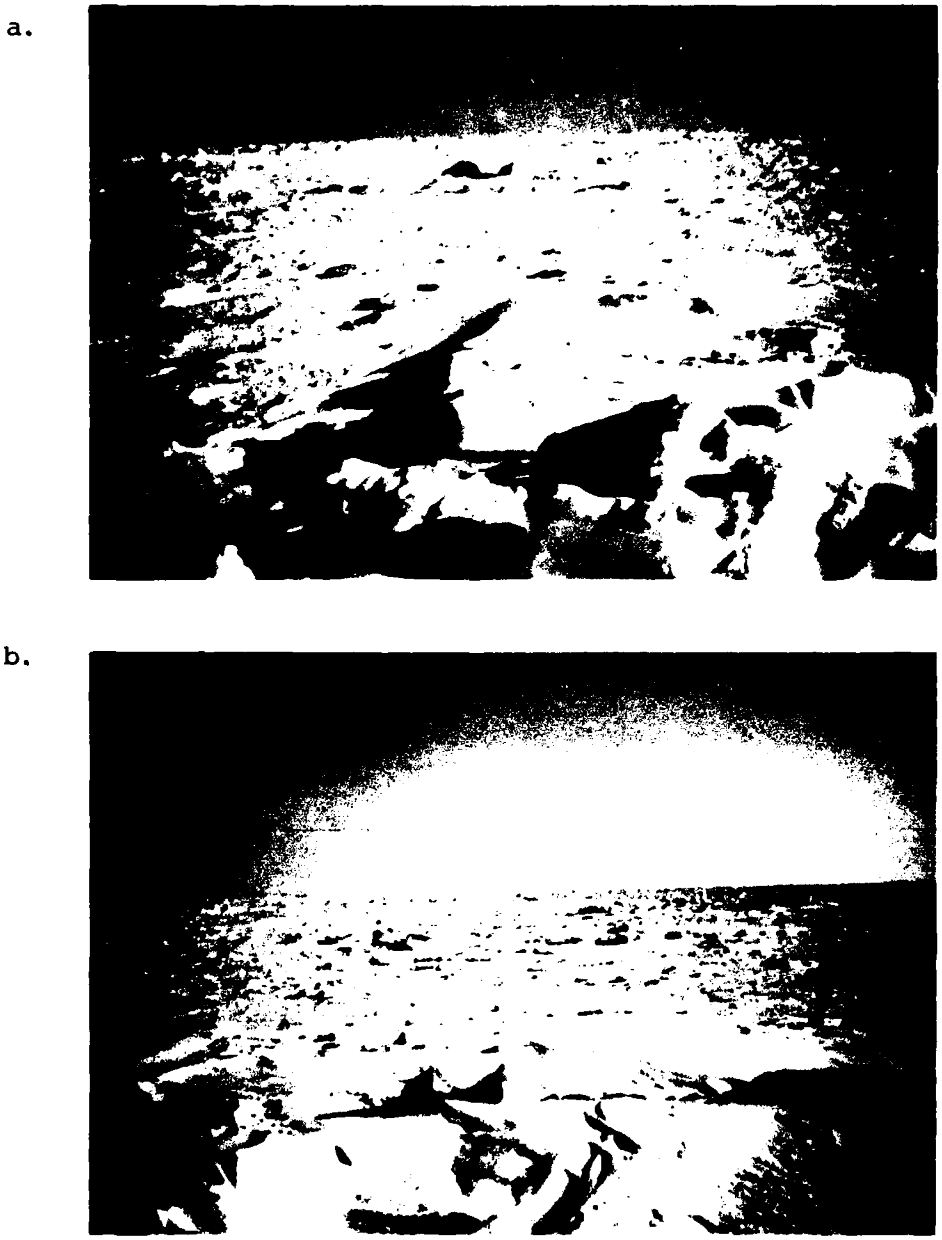

Figure A-13 (a & b). Photography taken while standing on the ice, using a 35-mm camera, with a 50-mm lens. Note the continuously rough surface, composed of rubble thrown up when the ice was 20 to 30 cm thick.

The importance of this site is that it demonstrates the widely varying surface texture that can be found, even in highly consolidated, first year ice. If it is further noted that ice, dating from freeze-up to the most recent moment, can be found at almost any time in the transition zone, the need for skilled interpreters and high-resolution imagery is demonstrated.

4.3 PERMANENT PACK: SITE "II"

During the summer season, the multi-year ice becomes largely desalinated. In particular, the surface layer of high salinity, typical of first year ice, disappears entirely. The effect of this is to allow much more penetration of radar energy and, particularly with X-band, this results in a strong, volume scattering effect. The effect is very pronounced in Figure 14, which shows the X-HV return. The large, multi-year floe noted has considerable surface texture, which is related to the pattern of melt ponds and drainage patterns set up during the summer. Rubble created by grinding against multi-year ice is even brighter than first year rubble, at X-HV.

Line "A", parallel to the SAR flight line on Figure 14, marks the photography flight path followed by the SAR-580 on March 16th. This low-level photography constitutes a suitable ground-truth record for all but the most unusual ice features. Unfortunately, the imagery from March 18th is shifted west, so the photography only covers the very edge of the scene. Figure 15 shows the location of the photography line at "A-A", on the very edge of the coverage.

A comparison of X- and L-band shows why L-band is very unpopular for ice reconnaissance; no tonal information on undeformed ice is seen. It is assumed that the scale size of the granularity in multi-year ice is such that no volume scattering takes place at L-band. The large, multi-year floe noted can be distinguished only by its peripheral ridges on the L-band. In the same manner, small, multi-year bits, seen clearly on X-band, are poorly distinguished on L-band, unless they are accompanied by a large ridge or rubble pile.

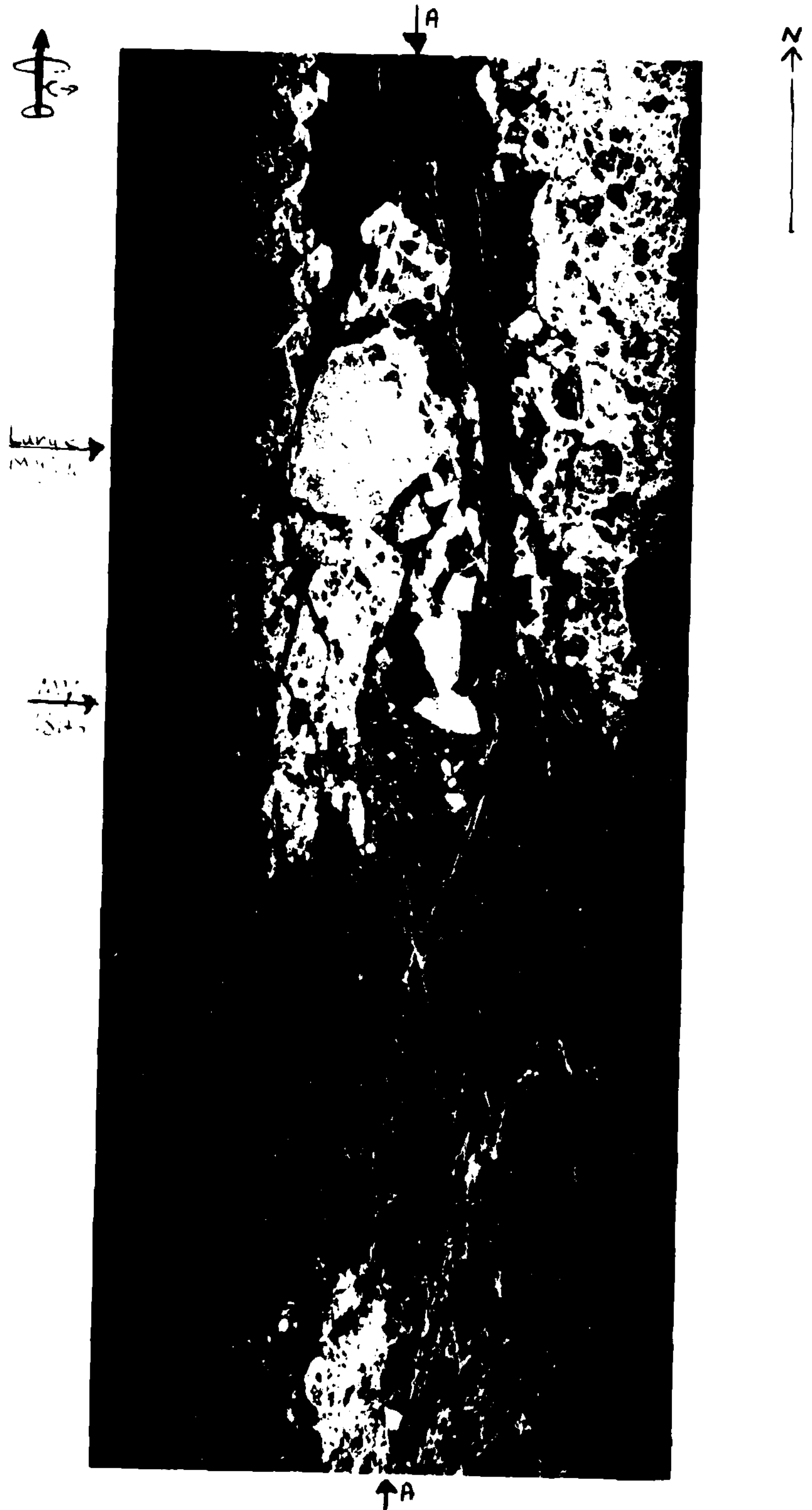

Figure A-14 X-HV [illegible] Steep [illegible] Site [illegible]

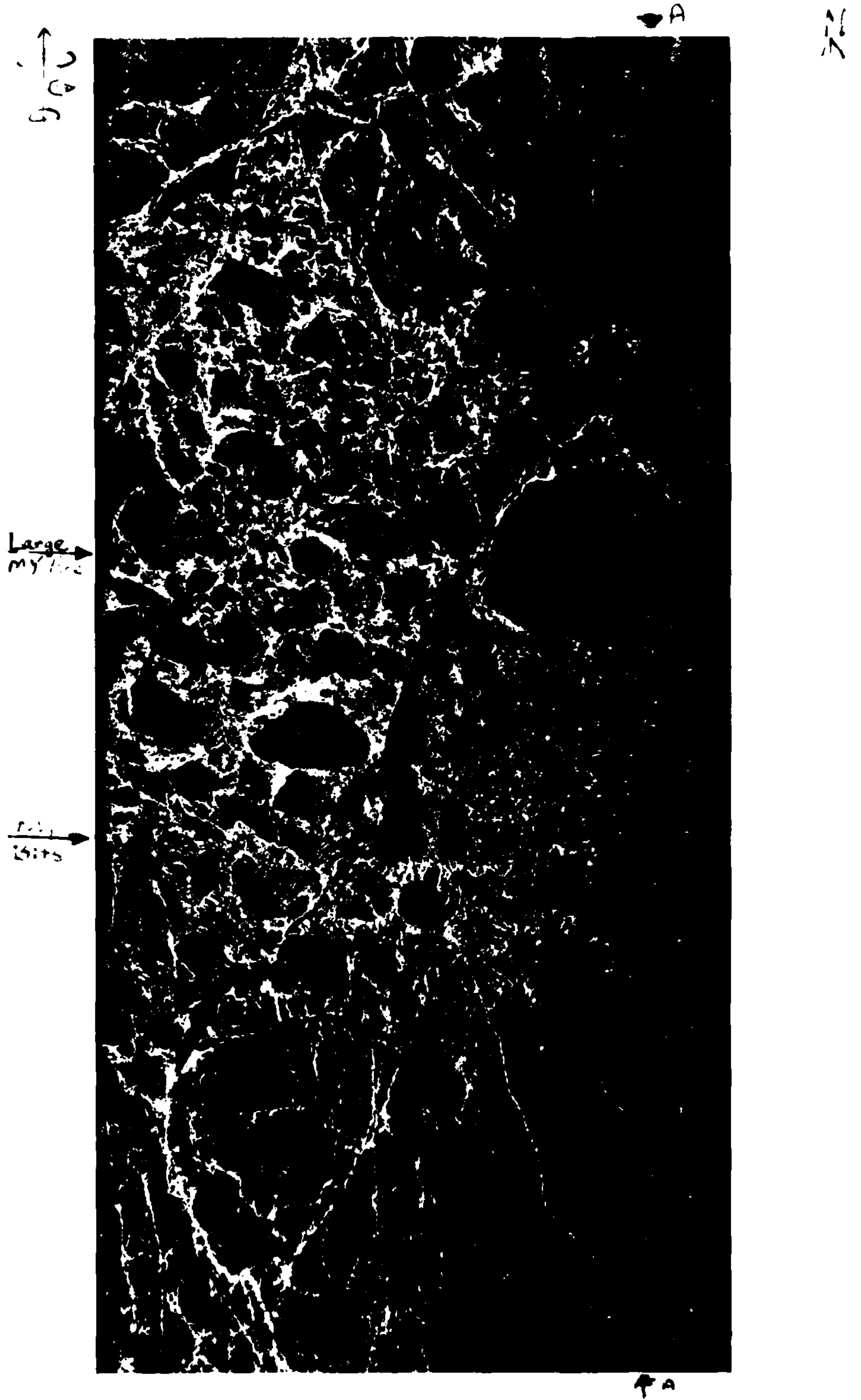

Figure A-15 L-WH 10-3-79 Shallow Depression Site II

This site is very important because it allows a detailed assessment of the ability of SAR to distinguish ice of different ages. In general, L-band gives no useful information that is not present in the X-band (4-channel registered scenes have been made to verify this). X-HV has a more expanded dynamic range than does X-HH, which better distinguishes the different classes of ice. This may not be an advantage, as the separation is adequate at X-HH, but the dynamic range is already too large for photographic prints. X-HV is, therefore, even more difficult to print adequately.

5. AVERAGE RADAR CROSS-SECTION STUDY

A simple study was undertaken, on the shallow-depression data from 18 March 1979, to provide corroboration for the more detailed work being conducted at ERIM. The analysis was conducted, using the CCRS Image Analysis System (CIAS) Radar Analysis package (Lowry et al., 1978). First, the data from all four channels were registered, then, using the cursor, average and standard error (SE) values were calculated for the cursored pixels. No attempt was made to radiometrically correct the data, and all were left in the square root form in which they were generated. The analysis was conducted, using the data at the approximate centre of the image (approximately 7° depression angle) to minimize radiometric variations.

The majority of the data presented here were generated, using data at the provided resolution (3 m). As a validity check, however, on both the technique and the basis data, similar tests were done on files which had been reduced in size by a factor of 3 by 3 (9 looks), or 6 by 6 (36 looks), by multi-looking (see Lowry et al., 1978) in the geometric correction routine. The 36-look data were also median filtered and the tests repeated.

Four classes of ice were selected by an experienced ice observer. These were smooth and deformed first year ice, and smooth and deformed multi-year ice. It was felt that further division into more categories was not justified with these data. The results of this analysis are tabulated in Tables 2 and 3. Comparison with the more complete results generated by ERIM, using the hybrid system, shows that the results are very similar. This is most reassuring.

Table A-2 CIAS data for four classes, shallow depression.

Class 1 Undeformed First-Year Ice Mean (S.E.)

	Site 1	Site 2	Site 3	Site 4	Average
XHH	27.2 (8.4)	21.4 (7.3)	25.3 (7.5)	23.6 (6.7)	24.4 (7.5)
XHV	16.0 (4.4)	14.9 (4.5)	16.8 (4.4)	15.7 (4.1)	15.9 (4.4)
LHH	13.9 (4.4)	11.8 (4.0)	14.4 (4.4)	13.6 (3.9)	13.4 (4.2)
LHV	14.0 (3.8)	13.7 (3.3)	14.0 (7.5)	13.3 (3.2)	13.8 (3.5)

Class 2 Deformed First-Year Ice Mean (S.E.)

	Site 1	Site 2	Site 3	Site 4	Average
XHH	64.6 (34.6)	68.9 (39.4)	71.4 (33.1)	67.9 (35.7)	69.7 (39.7)
XHV	28.3 (11.3)	26.8 (10.9)	55.7 (24.1)	42.5 (23.7)	38.3 (17.5)
LHH	30.1 (15.7)	31.0 (16.8)	32.5 (18.1)	24.2 (17.0)	29.5 (16.9)
LHV	19.5 (7.4)	19.7 (6.7)	26.4 (10.9)	20.9 (11.4)	21.6 (9.7)

Class 3 Undeformed Multi-Year Ice Mean (S.E.)

	Site 1	Site 2	Average
XHH	48.6 (34.6)	46.6 (39.4)	47.6 (20.5)
XHV	23.5 (8.4)	22.2 (7.9)	22.9 (8.2)
LHH	12.9 (4.3)	13.7 (4.7)	13.3 (4.5)
LHV	13.6 (4.1)	13.7 (3.8)	13.7 (4.0)

Class 4 Deformed Multi-Year Ice Mean (S.E.)

	Site 1	Site 2	Site 3	Site 4	Average
XHH	94.3 (47.9)	89.3 (42.8)	98.9 (49.6)	64.9 (39.1)	86.9 (44.9)
XHV	70.6 (35.6)	73.0 (40.0)	60.4 (32.6)	43.4 (26.3)	61.9 (33.6)
LHH	44.0 (24.5)	56.3 (34.9)	45.9 (24.3)	22.8 (14.2)	42.3 (24.5)
LHV	28.9 (14.7)	35.7 (20.3)	34.8 (20.5)	18.5 (7.7)	29.5 (15.8)

Table A-3 CIAS data for four classes of various resolutions for shallow depression.

Multi-Year Ice Undeformed

	1 Average of 3x3m, 1 look	2 9x9m, 9 look	3 18x18m, 36 look	4 18x18m, 36 look Median Filtered
XHH	47.6 (20.5)	45.2 (13.7)	46.8 (9.5)	44.1 (5.1)
XHV	22.9 (8.2)	21.2 (5.8)	21.7 (3.9)	20.6 (2.3)
LHH	13.3 (4.5)	12.9 (3.0)	13.3 (2.1)	12.6 (1.7)
LHV	13.7 (4.0)	13.0 (2.3)	12.9 (1.5)	12.7 (0.8)

G6II Files

	1 Multi-Year Deformed	2 Multi-Year Undeformed	3 First-Year Deformed	4 First-Year Deformed	5 First-Year Undeformed
XHH	61.5 (20.7)	46.8 (9.5)	36.3 (16.4)	35.2 (14.4)	23.7 (3.7)
XHV	44.1 (17.0)	21.7 (3.9)	16.1 (3.9)	14.7 (2.7)	14.0 (1.8)
LHH	22.9 (8.5)	13.3 (2.1)	14.5 (5.5)	14.7 (4.8)	13.4 (1.8)
LHV	19.4 (6.7)	12.9 (1.5)	3.9 (5.2)	6.4 (6.1)	13.2 (1.6)

An analysis of the data from Site "I1", taken on the ERIM hybrid optical-digital processor, has been done. Four sites were selected to represent the four categories that have been outlined above. These are sites G, D, F and E, all on file B2. The results are re-tabulated in Table 4a for both steep (approximately 50°) and shallow (approximately 7°) depression angle data.

Examination of the data in Table 4a shows that all single-channel data increase in magnitude from first year undeformed, to first year deformed, to multi-year undeformed, to multi-year deformed ice. At shallow angles, the contrast between the types is not greatly different on the two channels. At steep angles, however, the cross-polarized channel shows much greater separation of the classes than does the like-polarized. This has been a constant result of work with steep depression-angle scatterometer data. It is clear that the scatterometer data do not extrapolate easily to shallow angles. The contrast stretch of the cross-polarized channel, compared to the like-polarized channel, is a good example of this point.

A simple analysis of the depolarization effect has been conducted. By assuming that the cross-polarized channel represents isotropically scattered data, and that the like-polarized term is the sum of a reflected and isotropically scattered term, a reflected term can be calculated by subtracting the cross-polarized from the like-polarized term. We can thus examine the ratio of reflected-to-scattered power. This is meaningful, both from the point of view of understanding the mechanisms of radar returns from ice, and designing a classifier for ice. L-band data have been discarded because they are not anticipated to be available in the future, due to their limited utility.

Table A-4 a) ERIM X-band data for four classes of both shallow (7°) and steep (50°) depression angles.

Site	X-HH Shallow	X-HV Shallow	X-HH Steep	X-HV Steep
G	14.9	10.5	54.4	18.9
D	22.2	11.5	56.0	21.6
F	33.1	15.1	67.1	56.8
E	43.5	31.5	68.8	62.0

Table A-4 b) The ratio of reflected to scattered X-band data for both steep and shallow depression angles.

Site	R/S Shallow (7°)	R/S Steep (50°)
G	0.42	1.9
D	0.93	1.6
F	1.19	0.18
E	0.38	0.11

SITE LEGEND

G	Undeformed first year ice
D	Deformed first year ice
F	Undeformed multi-year ice
E	Deformed multi-year ice

Table 4b shows the results of calculating the mean reflected-to-scattered power ratio for the four classes under study. Obviously, the absolute values of these numbers are subject to considerable error, as these are not calibrated data. Considerable care, however, has been taken at ERIM to ensure that the relative values are meaningful. In this respect, the CIAS data cross check is again very reassuring.

The steep-depression data are easily interpreted. In first year ice, the surface reflections dominate, even when there are considerable numbers of ridges present. The ridges, if viewed separately, using the screen on the CIAS, show these numbers to be correct. That is to say, at steep depression, the undeformed first year ice shows contrast similar to deformed first year ice on both like-polarized and cross-polarized channels. The very strong response of the multi-year ice, both deformed and undeformed at steep depression angles, is largely due to the scattered return. This is in line with current thinking, which says that the return from multi-year ice is largely associated with a volume scattering mechanism at X-band.

In contrast to the highly saline first year ice, multi-year ice is very permeable. The structure is very non-uniform, both in air content (dielectric constant) and brine content (loss tangent). It is for these reasons that this theory is widely accepted, and it seems quite applicable for the steep-depression data. For undeformed ice, scattered energy dominates. This is consistent with the return being due to small features, of the order of the wavelength (by the sine of the angle), which scatter largely. It is acceptable, if a little surprising, that this is the process.

The rough first year ice shows equal response of the two mechanisms, which seems very reasonable. First year rubble has a great many sharp corners, but a great many flat facets as well. What are surprising are the shallow-depression ratios of R/S for multi-year ice.

For undeformed ice at shallow angles, the dominant effect is reflection. At this time, the author can put forward no good explanation for this. The surfaces of old floes, as represented here, are covered in gently rolling hummocks of about 1/2 to 1 m in height, and some 5 to 20 m in scale. Typically, they do not have facets protruding sharply from the surface, and have low salinities. One can only assume that these undulations must be clearly visible, even at 7° depression angle, and that they reflect strongly from the surface of the ice. Little energy returns to the radar via refraction from sharp edges or from volume scattering.

The cross-polarized ratio for deformed multi-year ice, when compared to deformed first year ice, shows the greater importance of scattering effects in multi-year rubble. Again, this can be ascribed to greater volume scattering.

A comparison of the reflected data for steep and shallow angles is shown in Table 5. The difference between first year and multi-year ice is striking in the reflected component. Except for the undeformed multi-year ice, however, no change is seen for the scattered ratio. Again, this emphasizes the relative stability of signatures in the scattered channels, and the rather odd response of undeformed multi-year ice at very shallow angles.

Table A-5 Reflected and scattered power ratios for steep and shallow data.

Site	R Shallow/R Steep	S Shallow/S Steep
G	0.12	0.56
D	0.28	0.53
F	1.75	0.27
E	1.76	0.51

6. CONCLUSIONS

A ground-truth report for the three selected sites has been prepared, and some analysis has been conducted. The sites show the remarkable range of radar reflectivity that can be observed in new ice. Both the reflection and scattering mechanisms are variable for first-year ice. Multi-year ice shows a tremendous signature variation as well, but is relatively more stable than first year ice. It is also easy to distinguish multi-year ice from first year ice if both X-HH and X-HV data are available.

The analyzed data set, while very exciting, is incomplete. Firstly, the range of temperatures over which data were collected is very narrow. Secondly, the range of depression angles over which coincident data are available is limited to the two extremes. With the limitations noted, the results are nonetheless very exciting, and may well lead to further work.

7. REFERENCES

Inkster, D.R., R.K. Raney, and R.F. Rawson. 1979. State of the art in airborne imaging radar. Proceedings of the 13th International Symposium of Remote Sensing of Environment. 361-381.

Kovacs, A., and M. Mellor. 1974. Sea ice morphology and ice as a geologic agent in the Beaufort Sea. Ed. J.C. Reed and J.E. Sater. Arctic Institute of North America, Arlington, Virginia. 113-161.

Lowry, R.T., S. Shlien, and D.G. Goodenough. 1978. Proceedings of the 5th Canadian Symposium on Remote Sensing. Victoria, British Columbia. 363-372.

Wadhams, P. 1975. Sea ice morphology in the Beaufort Sea. Technical Report No. 36, Beaufort Sea Project, Department of the Environment. Victoria, British Columbia.

8. APPENDICES

Appended to this report are two sets of photographs. They are described below.

8.1 APPENDIX 1

This series of 9"-by-9" vertical photography was taken on 7-4-79 by Gulf Canada Ltd. The reflectors at Site "A" are shown.

8.2 APPENDIX 2

This series of 9"-by-9" vertical photography was taken from the Convair 580 on 16 March 1980. The ice at Site "II" is shown.

APPENDIX B

INTERPRETATION OF SAR '77 DIGITIZED ICE DATA

Mr. Richard Worsfold
REMOTEC Applications, Inc.
St. John's, Newfoundland, Canada

REMOTEC
Remotec Applications Inc.

INTERPRETATION

OF SAR '77

DIGITIZED ICE DATA

Remotec Applications Inc., Telephone (709) 364-1779, -2032, -2033, Telex 016-4939
Mailing Address: P. O. Box 5547, St. John's, Newfoundland, Canada, A1C 5W4
Business Address: K-Mart Plaza, Topsail Road, Suite 202

SUMMARY

The interpretation of the digitized ice regions of the SAR "77" imagery was done using transparencies provided by C-CORE. The analysis was carried out on all four bands for each digitized area using a comparator as an aid. Ground truth information from the Hopedale and Ship in the Ice reports was used as an aid where possible.

In the near shore sites where there was actual ground-information collected the interpretation was based on this data. However, in the offshore areas, where there was no ground information other than oblique air photos (Fig 31 A), the interpretation was based on experience in ice feature recognition and general observations taken from the reports. The only exception to this was the ship area which has recorded ground information during the overpass.

Three basic ice types were identified within the digitized areas. These were new ice, first year ice and ice ridges. (Multi-year ice can be identified on SAR imagery however there are no pieces evident within the digitized areas).

Fast, first year ice with ridging predominates the digitized areas which are close to shore (sites 3,4, and 7 and site between 7 and 15). Offshore regions contain floes, pancake ice, large leads and show evidence of swell action.

In certain areas such as the strip between site 7 and 15, the poor quality of the imagery prevents any detailed analysis. (Fig 23). In sites 3,4 and 7 the digitized areas on the X-band do not correlate exactly with those on the L-band imagery as shown in Fig I. Ridges and hummocking can be identified by the high return areas (speckle pattern). Finger rafting on new ice can be identified easily within area "C" Fig 15. The zig-zag pattern on the smooth surface is the clue for identifying this feature.

Dynamic ice is evident in Area "B" Fig 11 as is shown by the fracturing in the large floe. In area "C" the ice shows definite patterns in ridging. This is due to compression of the ice. The low return areas are areas of low compression whereas those areas which show considerable ridging are highly compressed. In Fig 31 the ice shows swell patterns. Areas where swell pattern is suppressed are areas where the ice is closely packed (compressed) as is shown in the area just ouside the upper left boundary of the digitized region.

The relevant ground truth data is recorded in Table I and the details of interpretation are lisited by area in Table II.

Table B-1

	GROUND TRUTH DATA
SHIP AREA	-Sea Cakes -Small floes-2-20m -Ocean swell & pulp ice -first year fast ice -iceberg
SITE 3	-first year fast ice -Snow covered
SITE 4	-first year, fast ice -young ice -rafted & ridged ice
SITE 7	-first year fast ice -new ice
SITE BETWEEN 7 & 15	-Transition zone between fast ice & open water

Table B-2

SITE	DETAILS OF INTERPRETATION
A (FIG 7)	-first year ice -new ice -unconsolidated floes -leads -speckle pattern on image indicated ridging or hummocking -the small leads show formation of new ice
A (FIG 6)	-first year ice -unconsolidated floes -freshly refrozen floes
B (FIG 11)	-first year ice -the large lead is what was once a large floe the solid line indicated the boundary between the large floe and consolidated small floes this area of small floes is spotted with polynyas.
C(FIG 15)	-first year ice -ridges -rafting on the new ice -the darker areas on the left of the image are areas of much less ridging -first year floes
ICEBERG	-unconsolidated first year floes -3 large leads -one iceberg -sea swell is also evident
SHIP AREA	-first year unconsolidated floes -ocean swell evident -iceberg in area -ice cakes
3	-this is an area of fast, first year ice -the speckle pattern is the result of ridging -snow covered
4	-first year fast ice, floes -minor ridging -new ice
7	-first year fast ice with ridges -new ice
Site between 7 & 15	-first year -small leads -transition zone between fast ice & open water

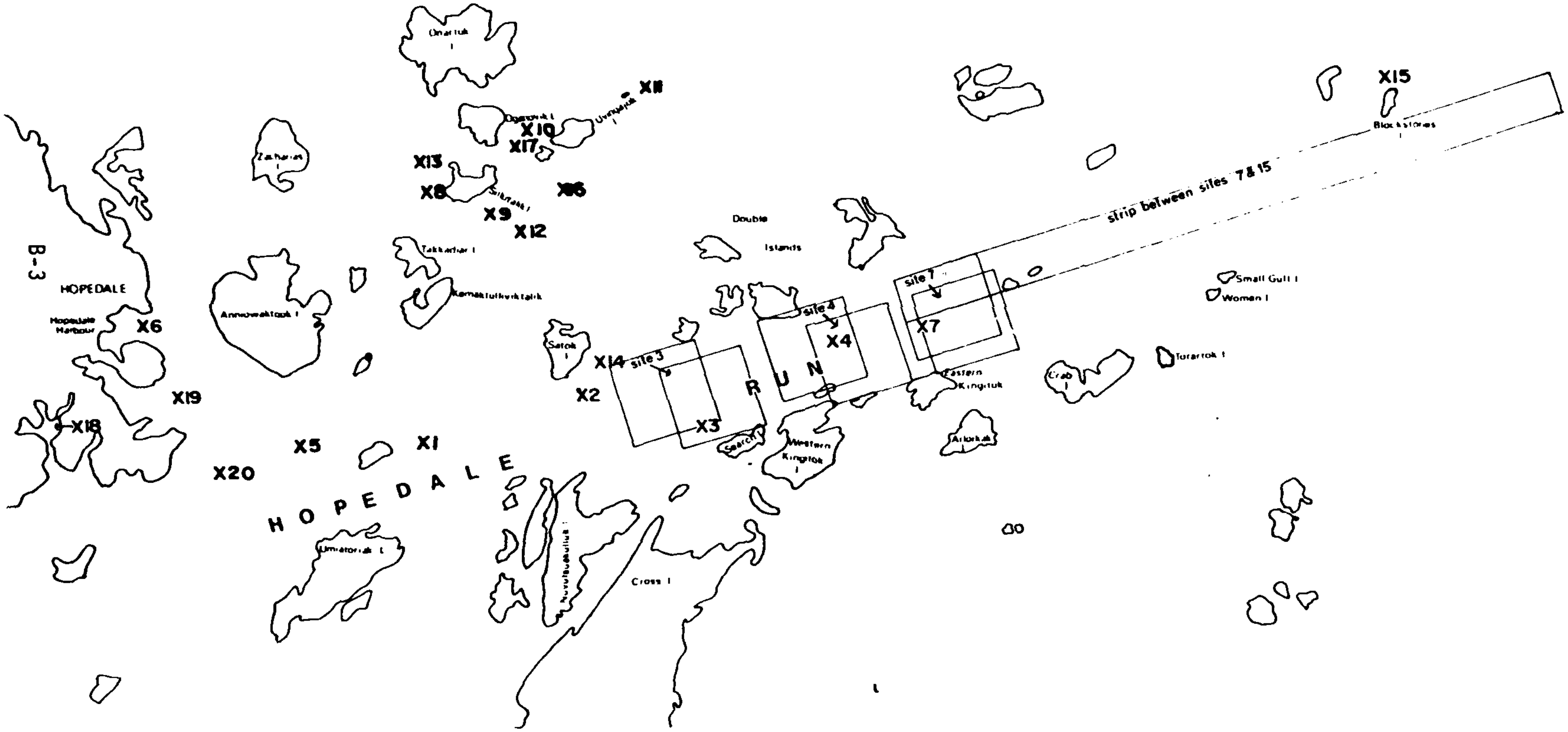

Figure B-1

GROUND TRUTH — HOPEDALE

DIGITIZED AREAS 3, 4, & 7

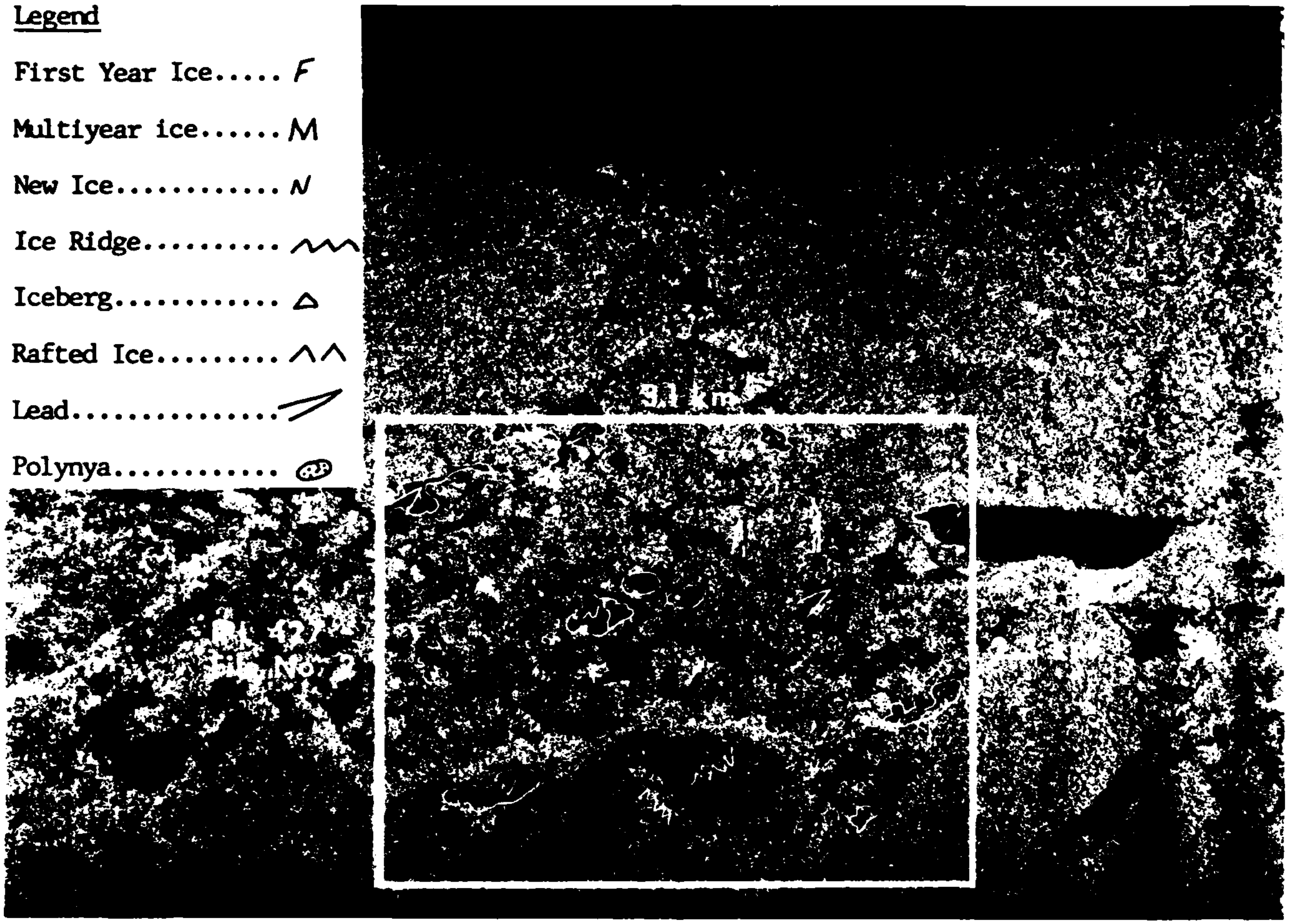

FIGURE 7. IMAGERY OF AREA A SHOWING DIGITIZED REGION (X-Band, HH Polarization)

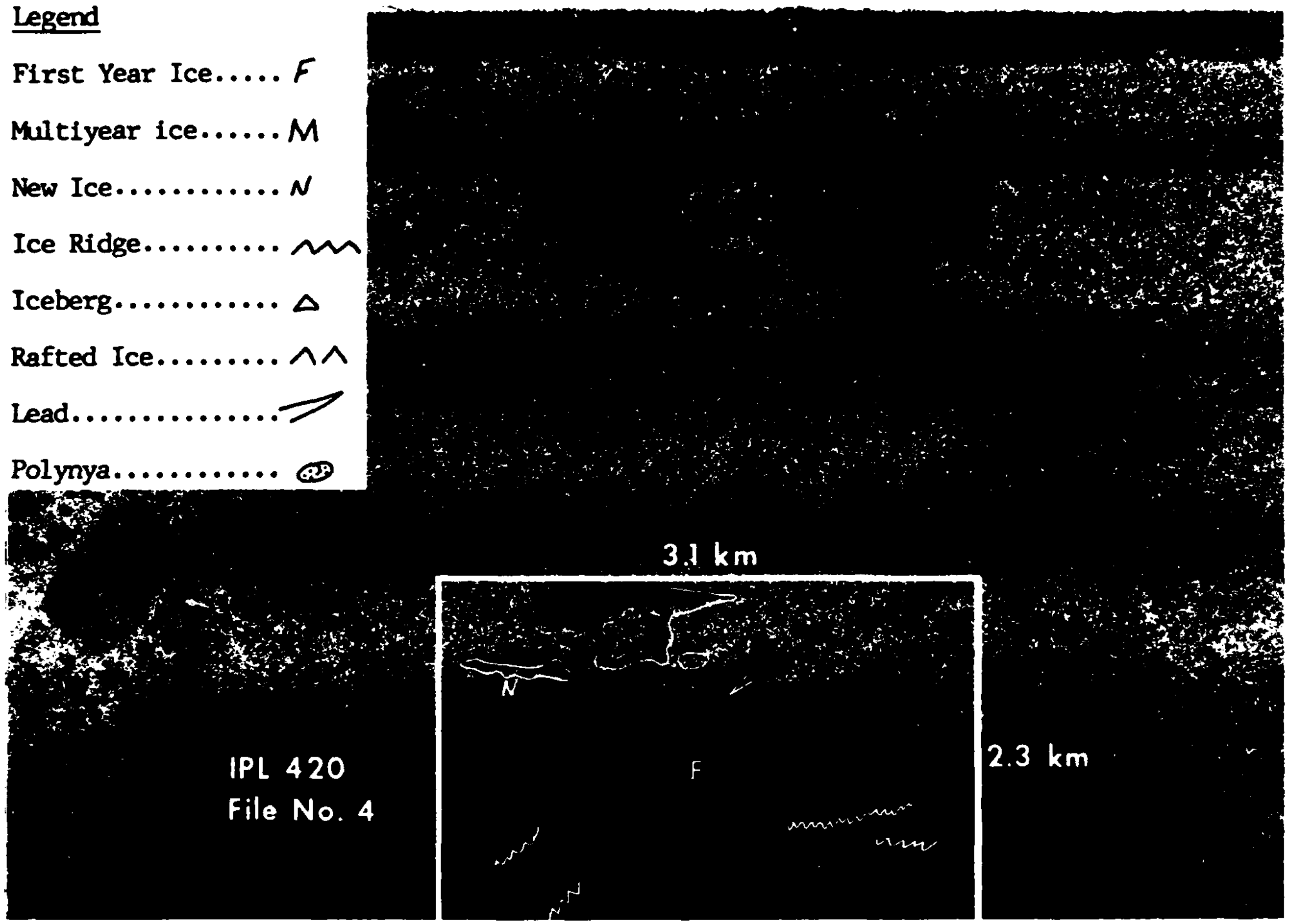

FIGURE 6. IMAGERY OF AREA A SHOWING DIGITIZED REGION (L-Band, HV Polarization)

Legend

First Year Ice.....	F
Multiyear ice......	M
New Ice............	N
Ice Ridge..........	∿∿
Iceberg............	△
Rafted Ice.........	∧∧
Lead...............	⟋
Polynya............	⬭

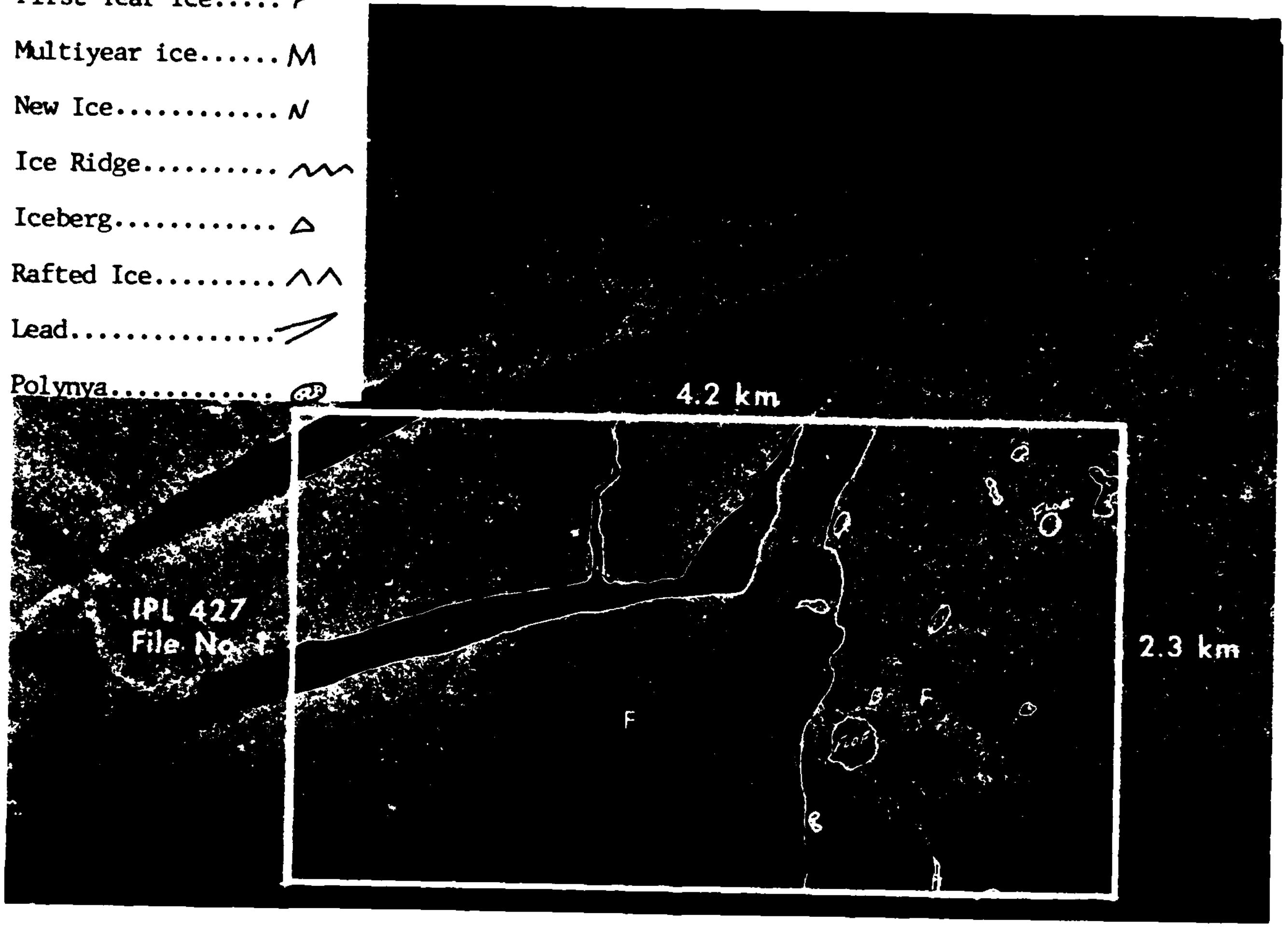

FIGURE 11. IMAGERY OF AREA B SHOWING DIGITIZED REGION (X-Band, HH Polarization)

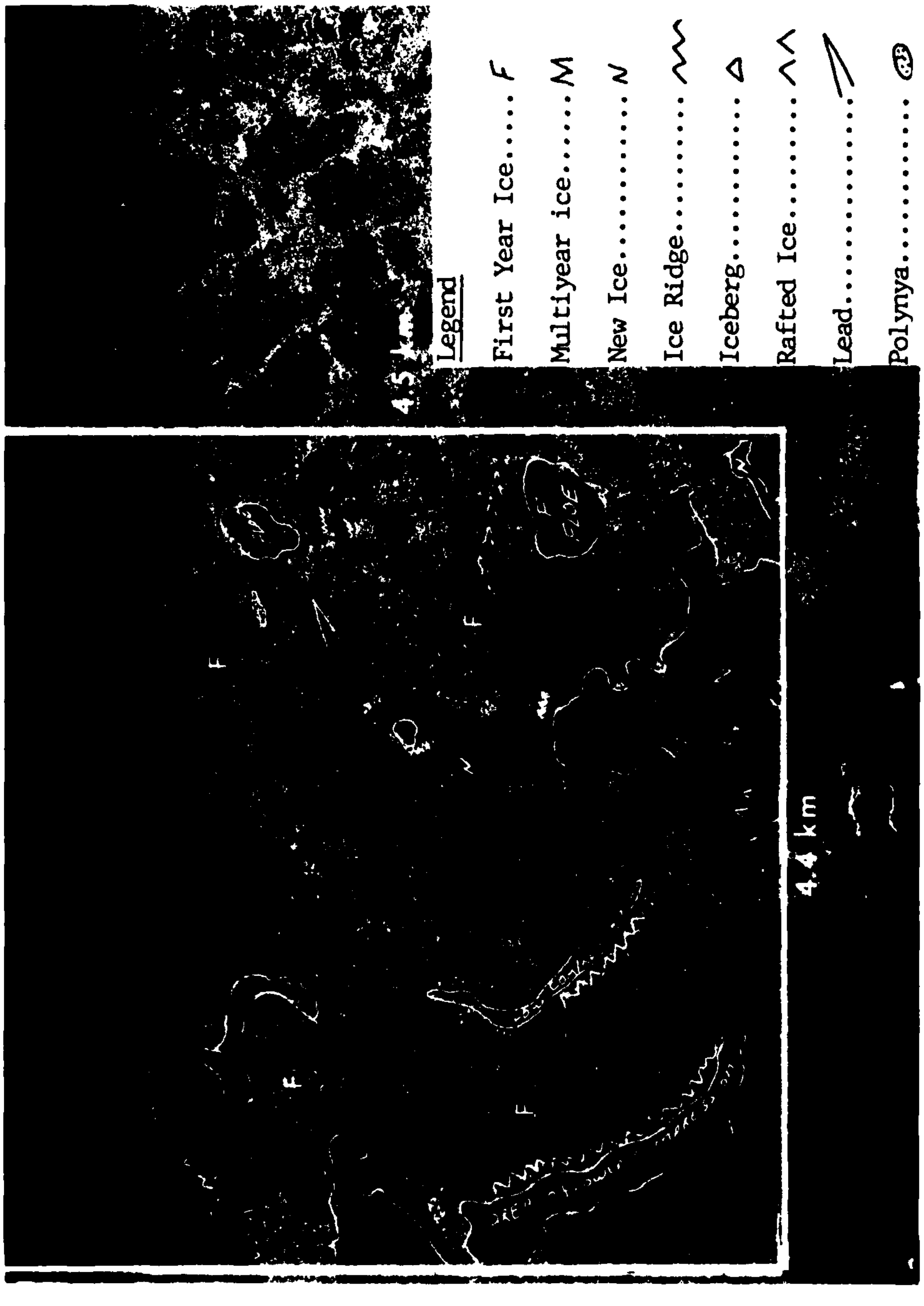

FIGURE 15. IMAGERY OF AREA C SHOWING DIGITIZED REGION (X-Band, HH Polarization)

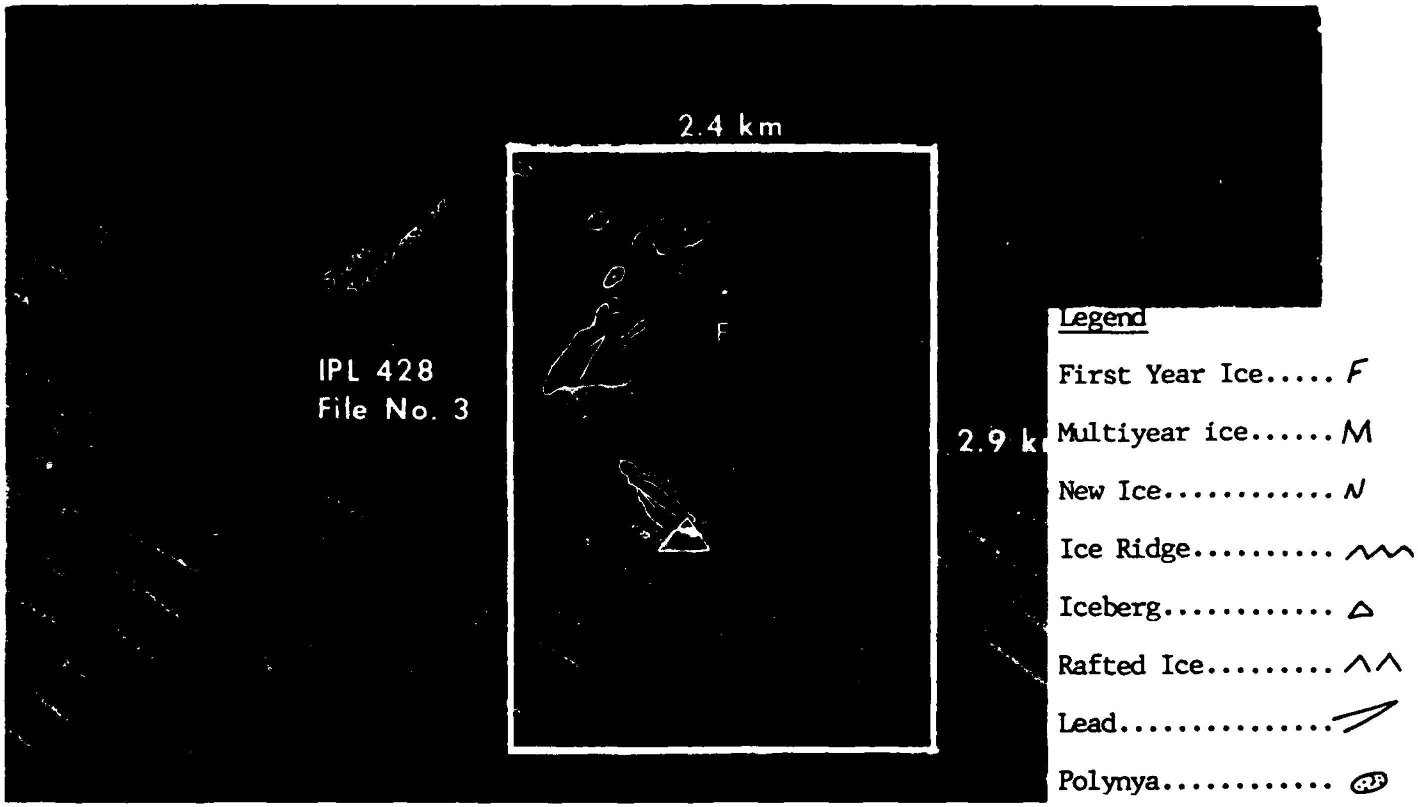

FIGURE 31. IMAGERY OF ICEBERG SHOWING DIGITIZED REGION (X-Band, HH Polarization)

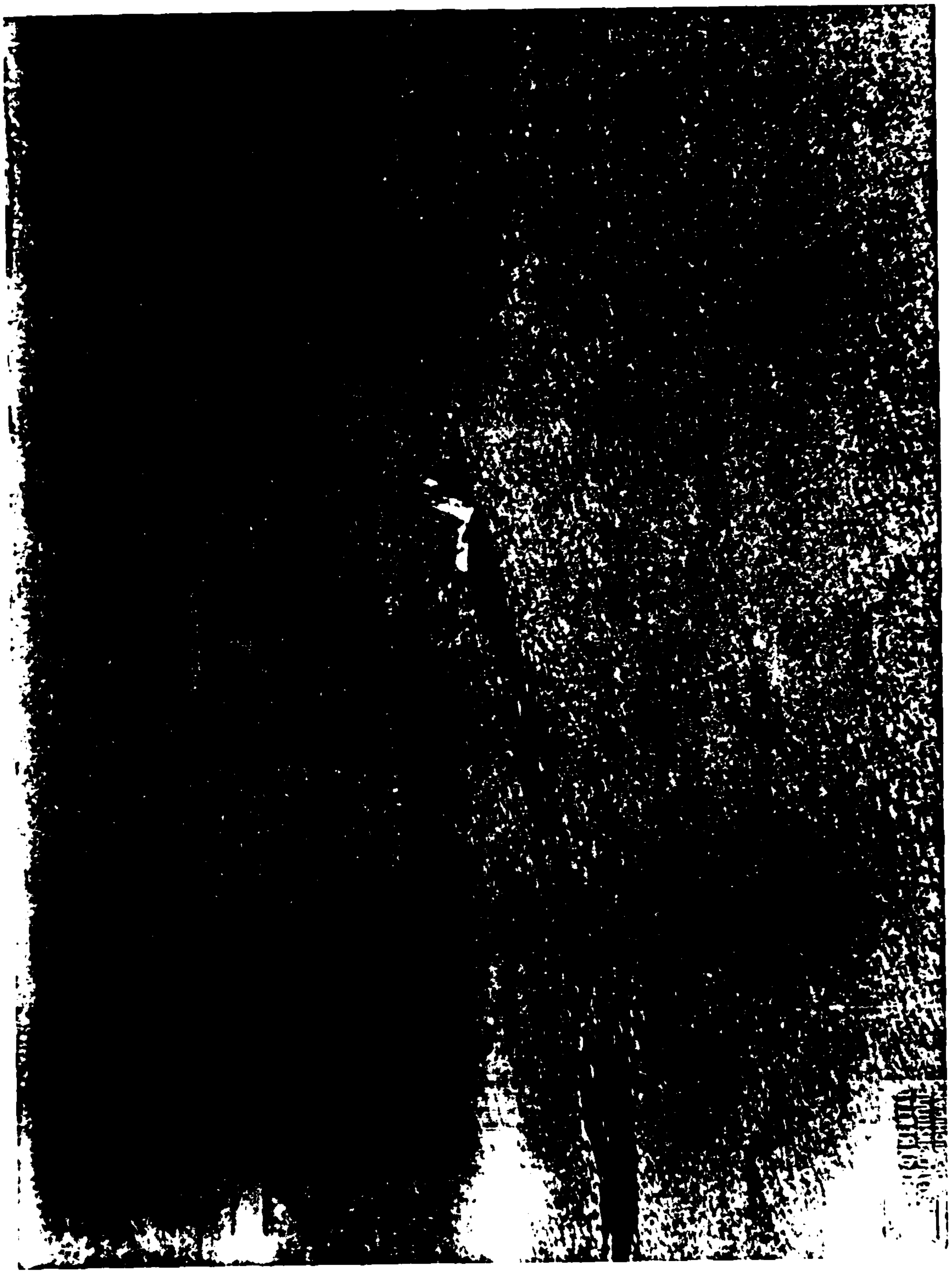

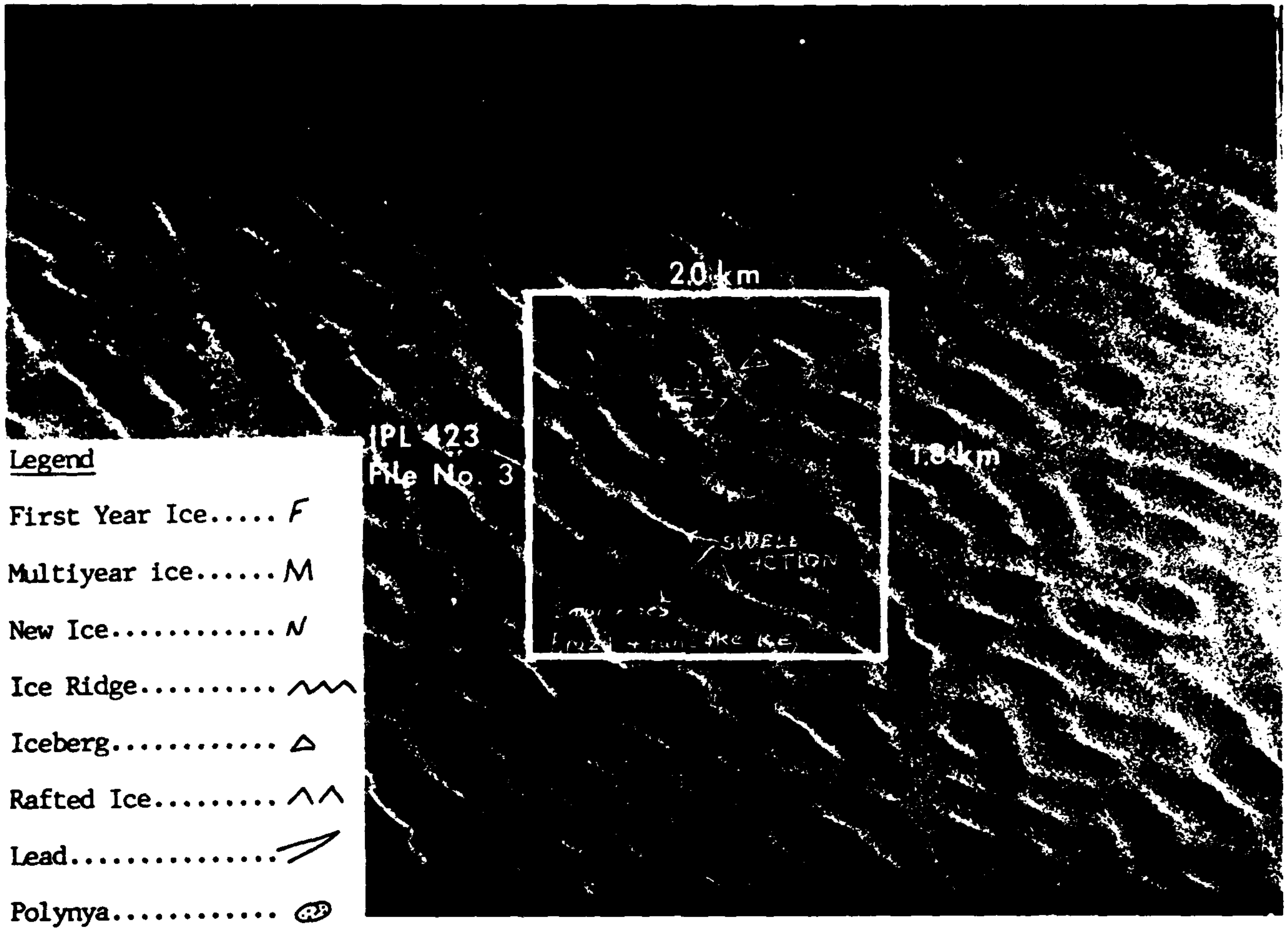

FIGURE 29. IMAGERY OF SHIP AREA SHOWING DIGITIZED REGION (X-Band, HH Polarization)

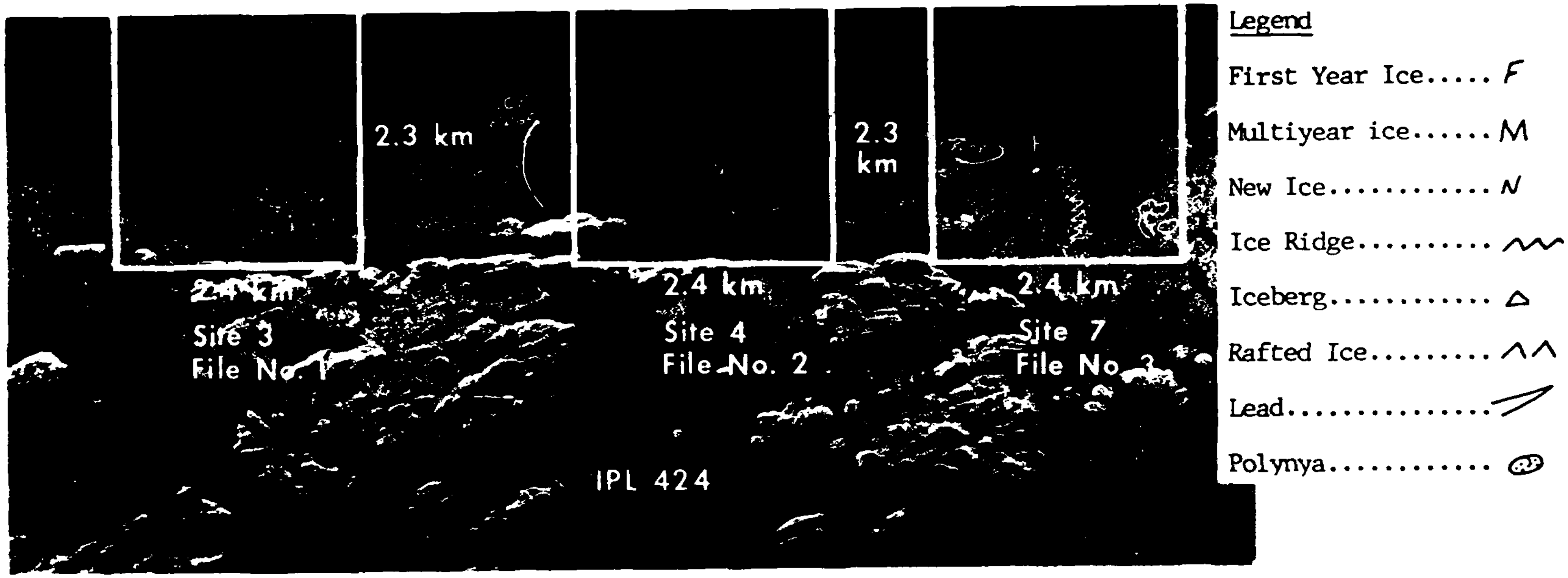

FIGURE 20. IMAGERY OF SITES 3.4, and 7 SHOWING DIGITIZED REGIONS (X-Band, HH Polarization, IPL 424)

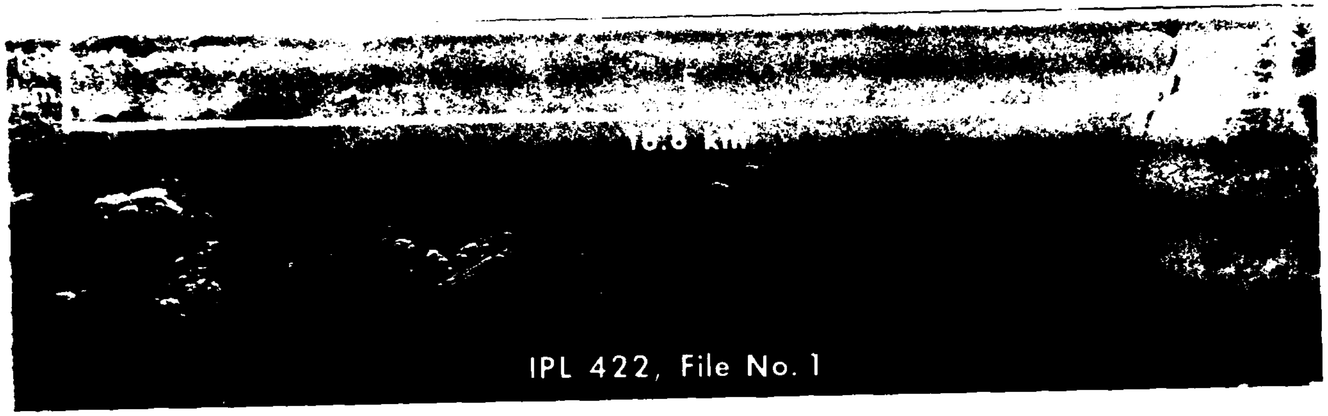

Figure B-23 IMAGERY SHOWING NARROW STRIP BETWEEN SITES 7 and 15 WHICH WAS DIGITIZED (L-Band, HH Polarization)

Legend

First Year Ice..... F

Multiyear ice...... M

New Ice............ N

Ice Ridge.......... 〰

Iceberg............ △

Rafted Ice......... ΛΛ

Lead.............. /

Polynya........... ∞

APPENDIX C

HISTOGRAMS FROM BEAUFORT SEA DATA

APPENDIX C
HISTOGRAMS FROM BEAUFORT SEA ICE DATA

A number of histograms showing the distribution of received signal amplitude for several ice types are included in this Appendix. Each histogram is a graph of the percent of total samples versus received signal amplitude. Histograms from each of the four channels of the X-L SAR are given for each ice type. Three distributions (normal, lognormal, and gamma) are given on each histogram as best fits to the distribution based on the empirical data. The symbols used in each figure for the various distributions are: normal (:), log-normal (O), and gamma (X).

Several sets of histograms are given for each of the following ice types:

Site	Ice Type	Page	
		Shallow	Steep
B1-A, B1-D	Medium first-year with ridging	C-2, C-6	C-3, C-7
B1-B, B1-F	Young ice with ridging	C-4, C-8	C-5, C-9
B2-A, B2-F	Multi-year with ridging	C-10, C-13	C-14
B2-E	Multi-year pieces with hummocking	C-11	C-12
B2-I	Multi-year with hummocking	C-15	C-16
B2-A	Multi-year with ridging and effects of resolution	C-17	---

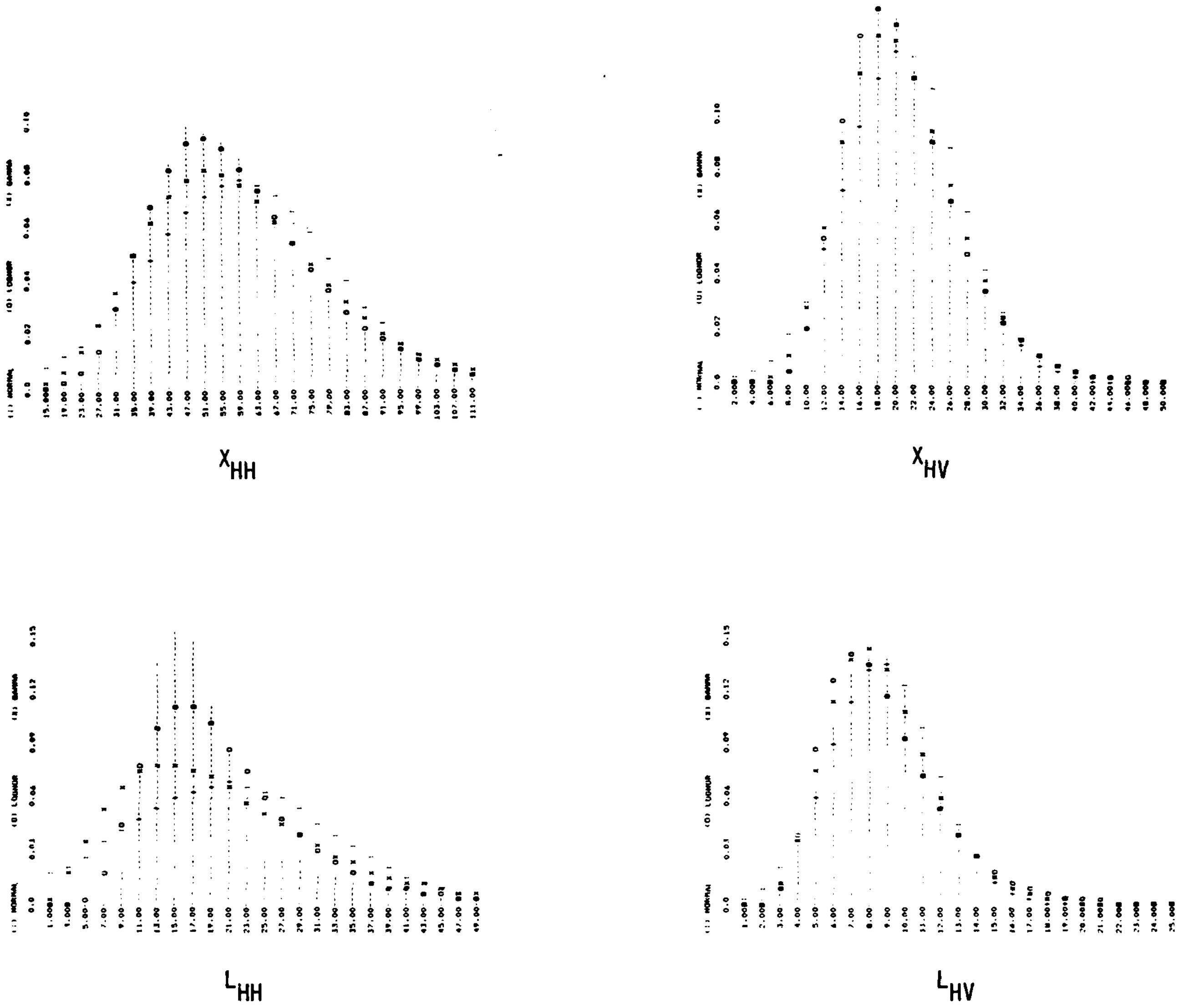

Figure C-1. HISTOGRAMS OF SITE B1-A/SHALLOW
(Medium first-year ice with ridging)

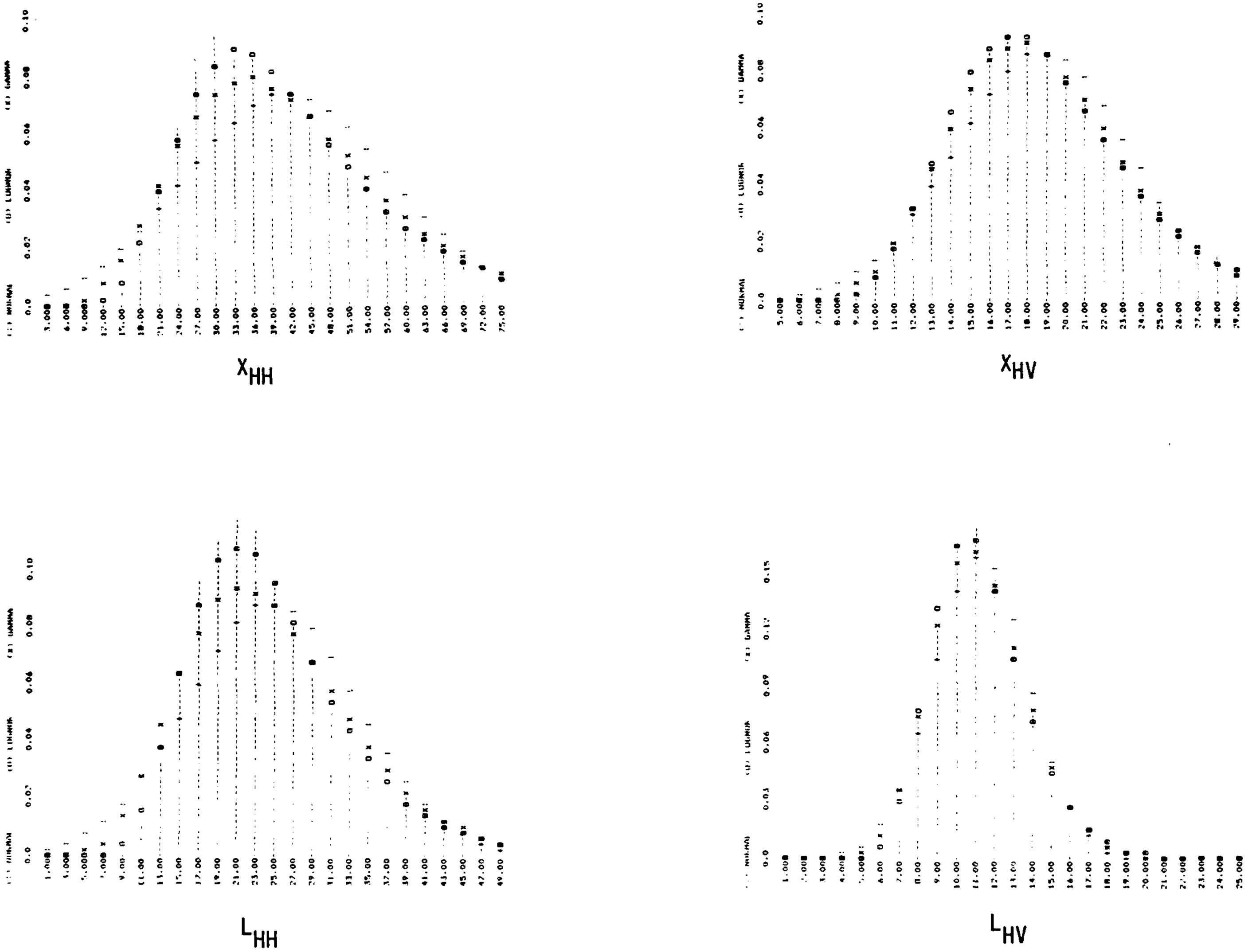

Figure C-2. HISTOGRAMS OF SITE B1-A/STEEP
(Medium first-year ice with ridging)

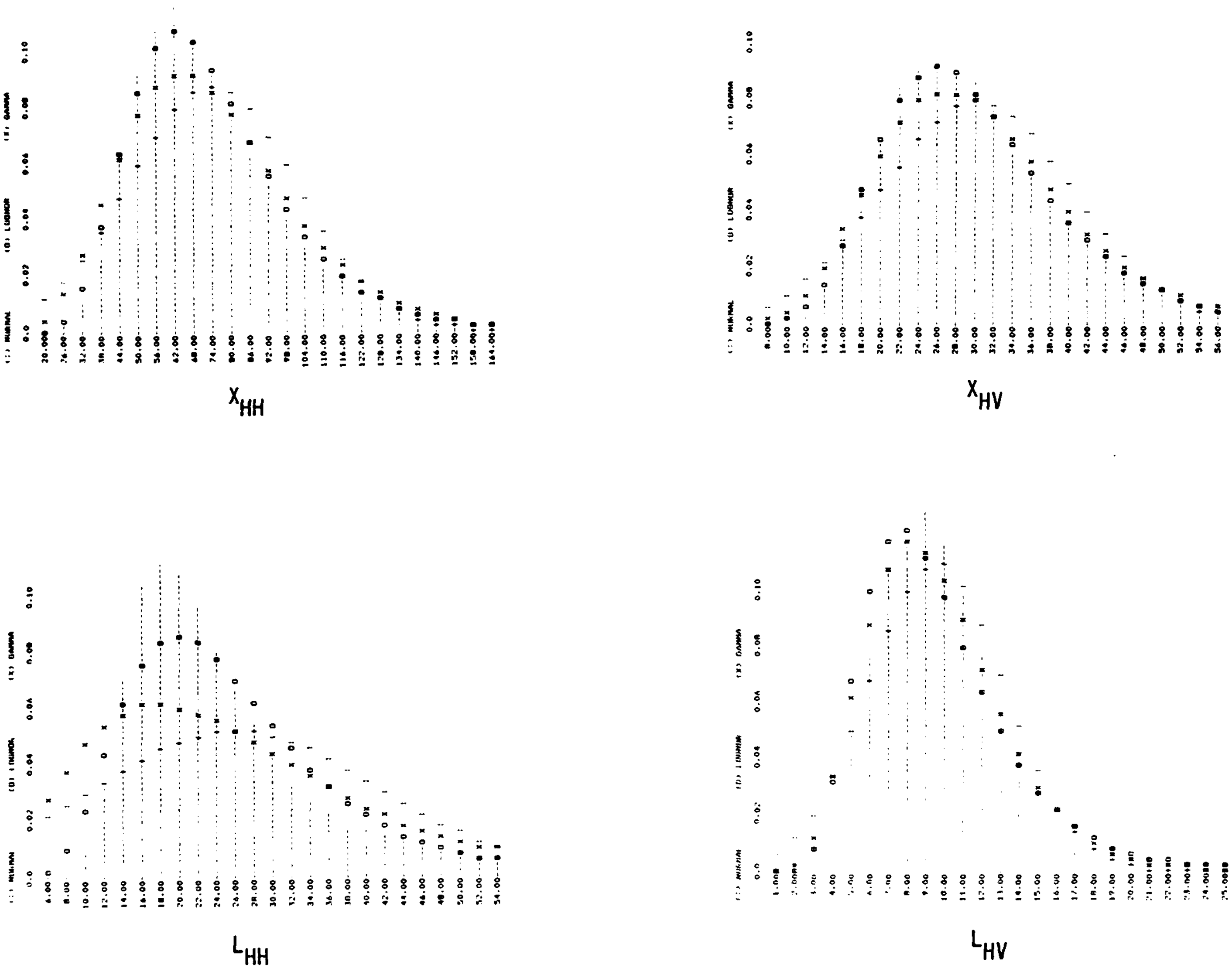

Figure C-3. HISTOGRAMS OF SITE B1-B/SHALLOW
(Young ice with ridging)

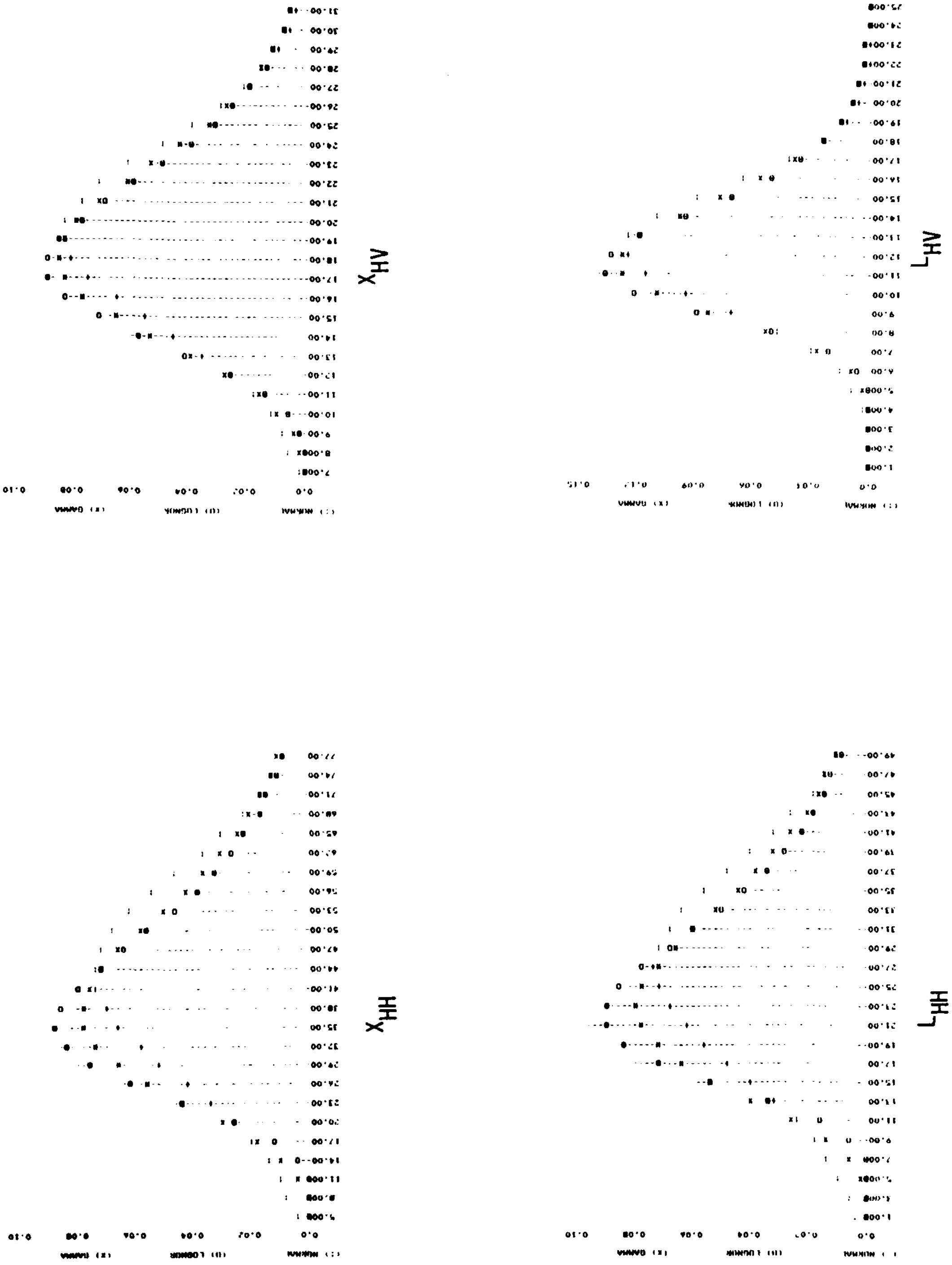

Figure C-4. HISTOGRAMS OF SITE B1-B/STEEP
(Young ice with ridging)

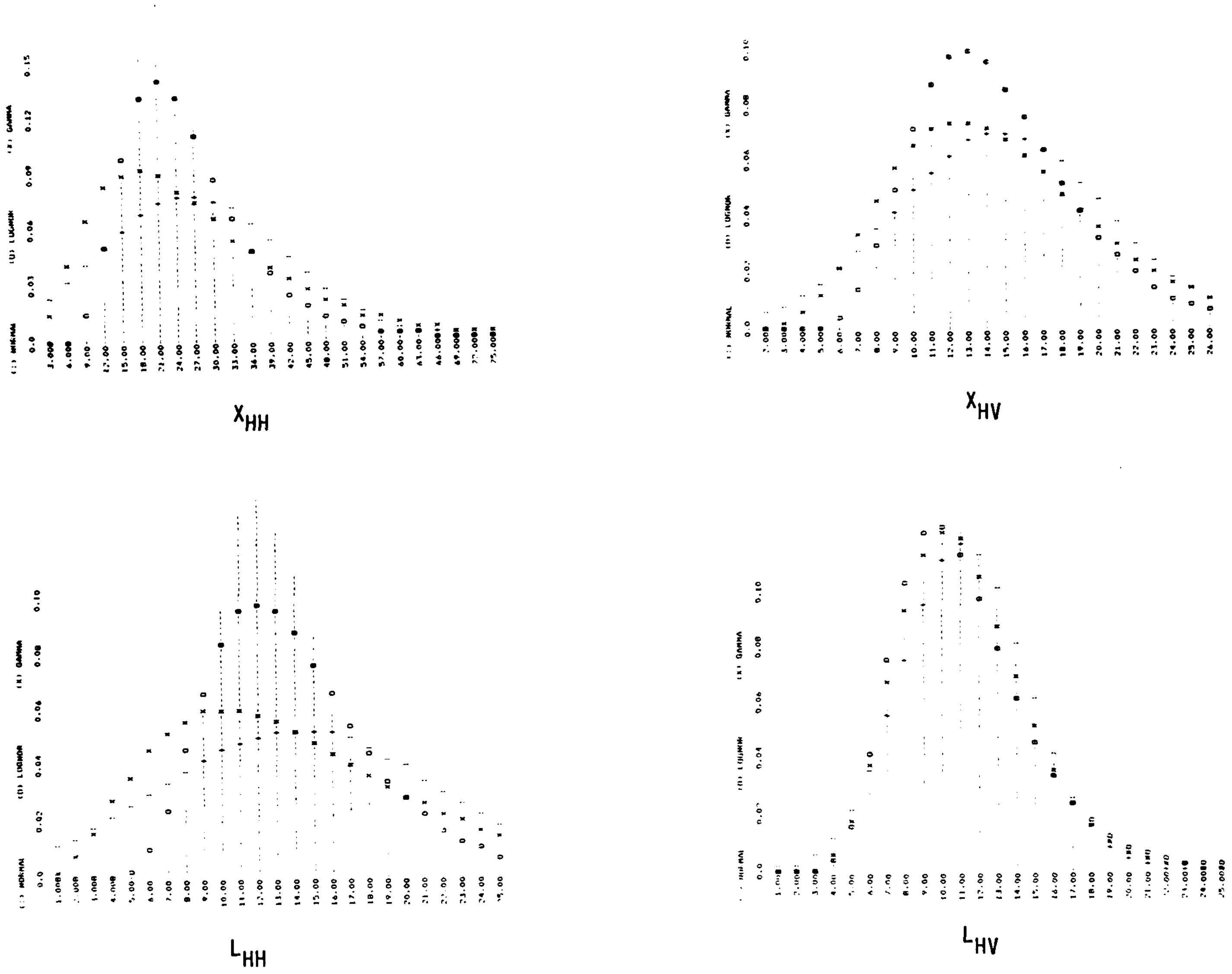

Figure C-5. HISTOGRAMS OF SITE B1-D/SHALLOW
(Medium first-year ice with ridging)

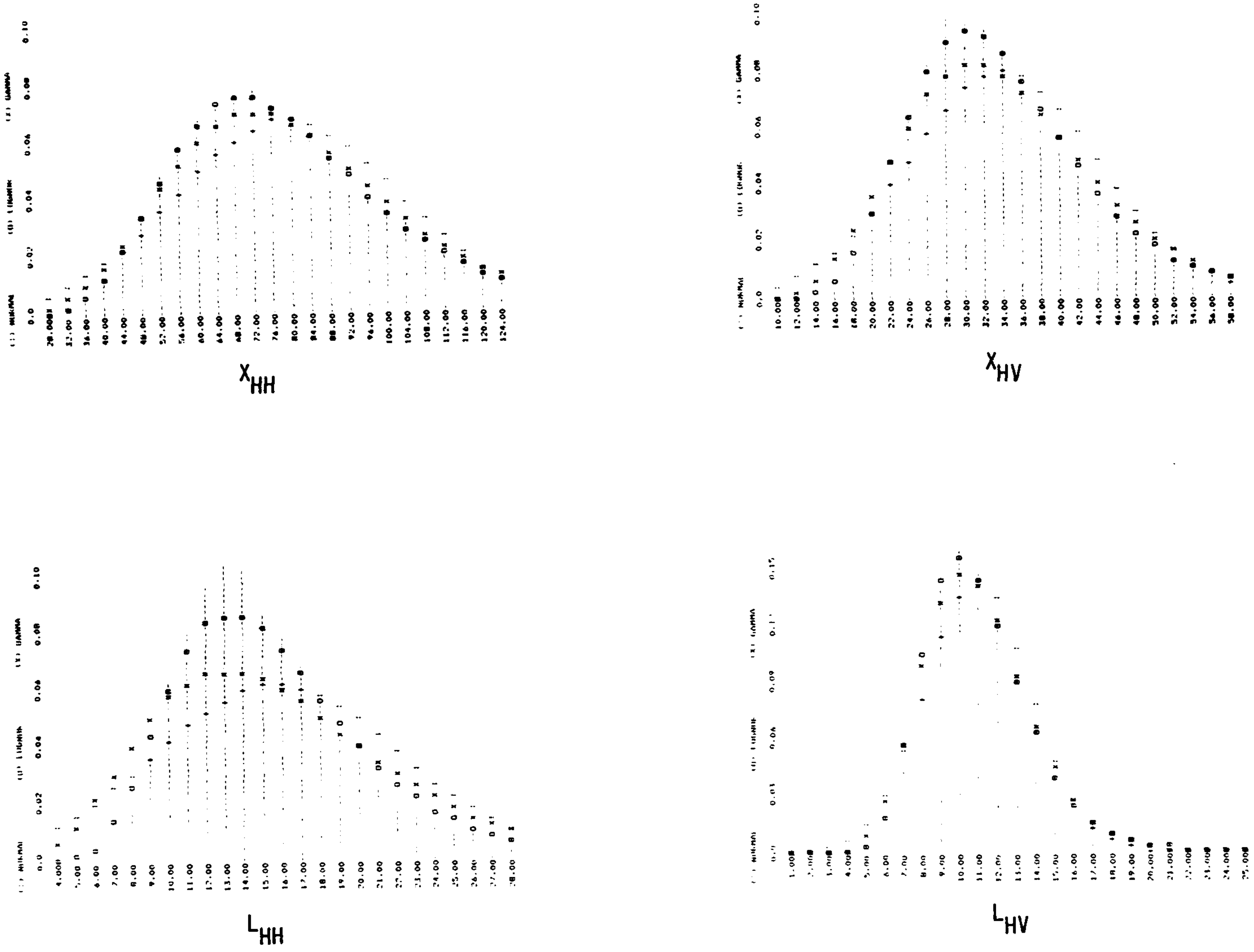

Figure C-6. HISTOGRAMS OF SITE B1-D/STEEP
(Medium first-year ice with ridging)

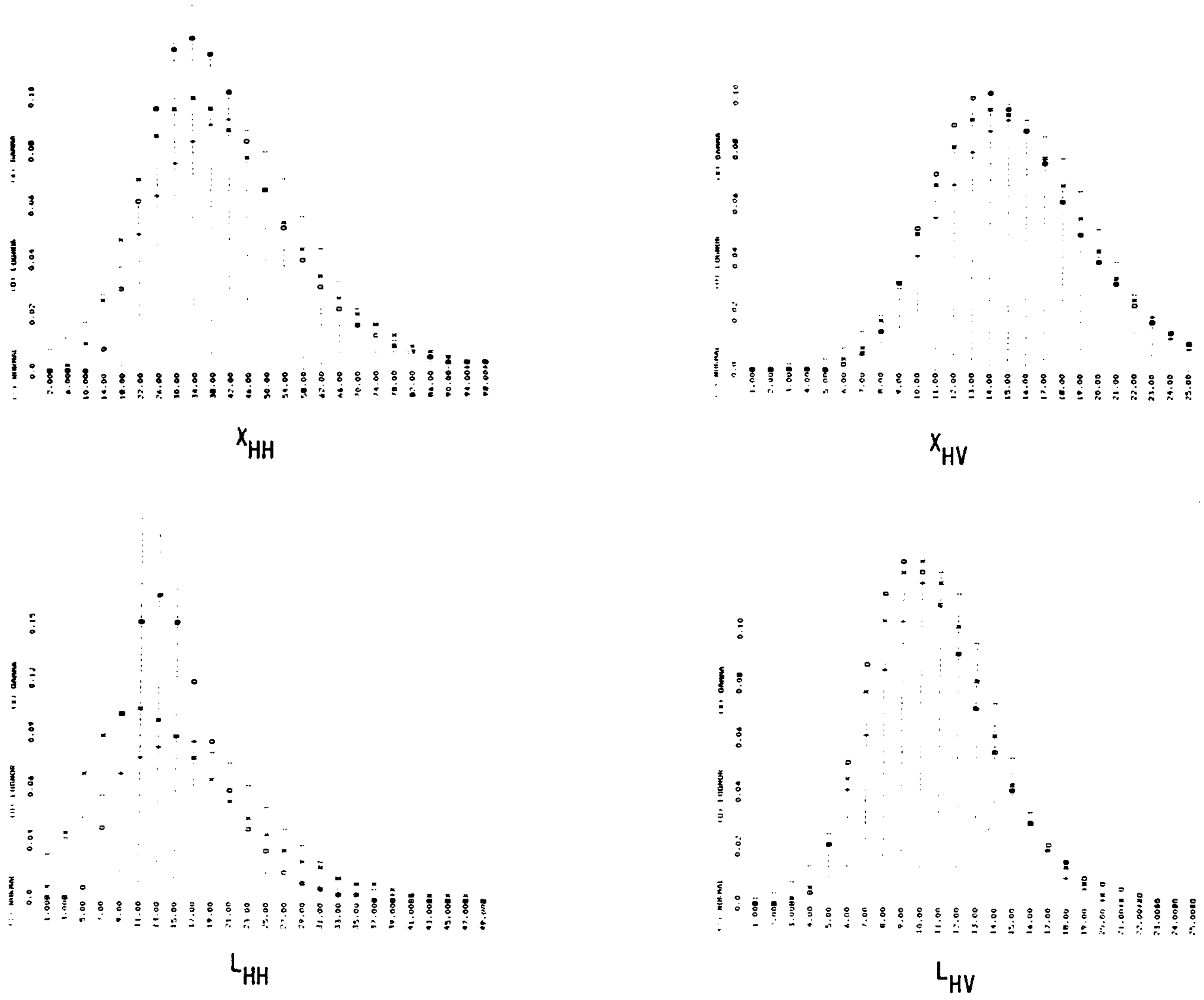

Figure C-7. HISTOGRAMS OF SITE B1-F/SHALLOW
(Young ice with ridging)

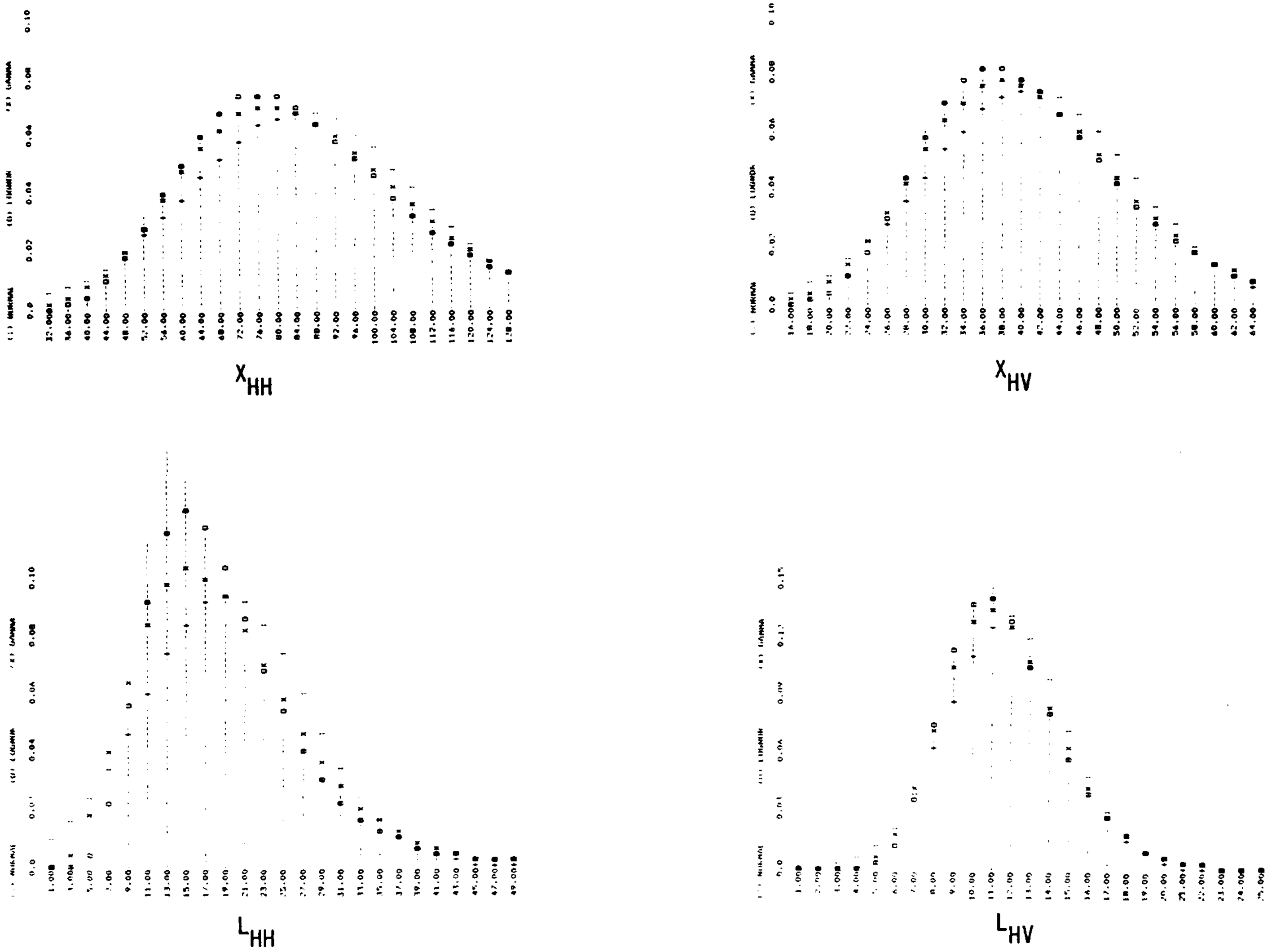

Figure C-8. HISTOGRAMS OF SITE B1-F/STEEP
(Young ice with ridging)

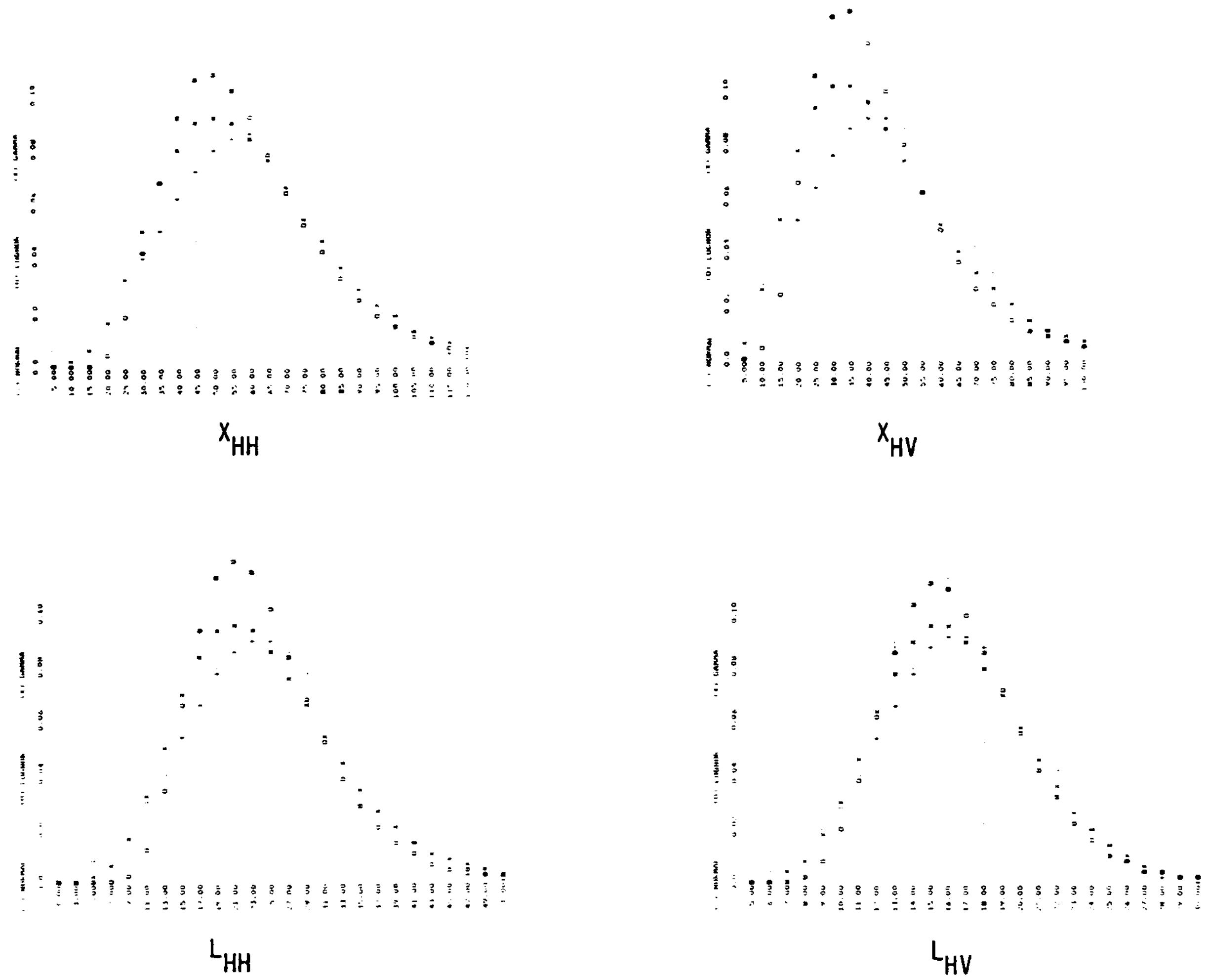

X_{HH} X_{HV}

L_{HH} L_{HV}

Figure C-9. HISTOGRAMS OF SITE B2-A/SHALLOW
(Multi-year ice with ridging)

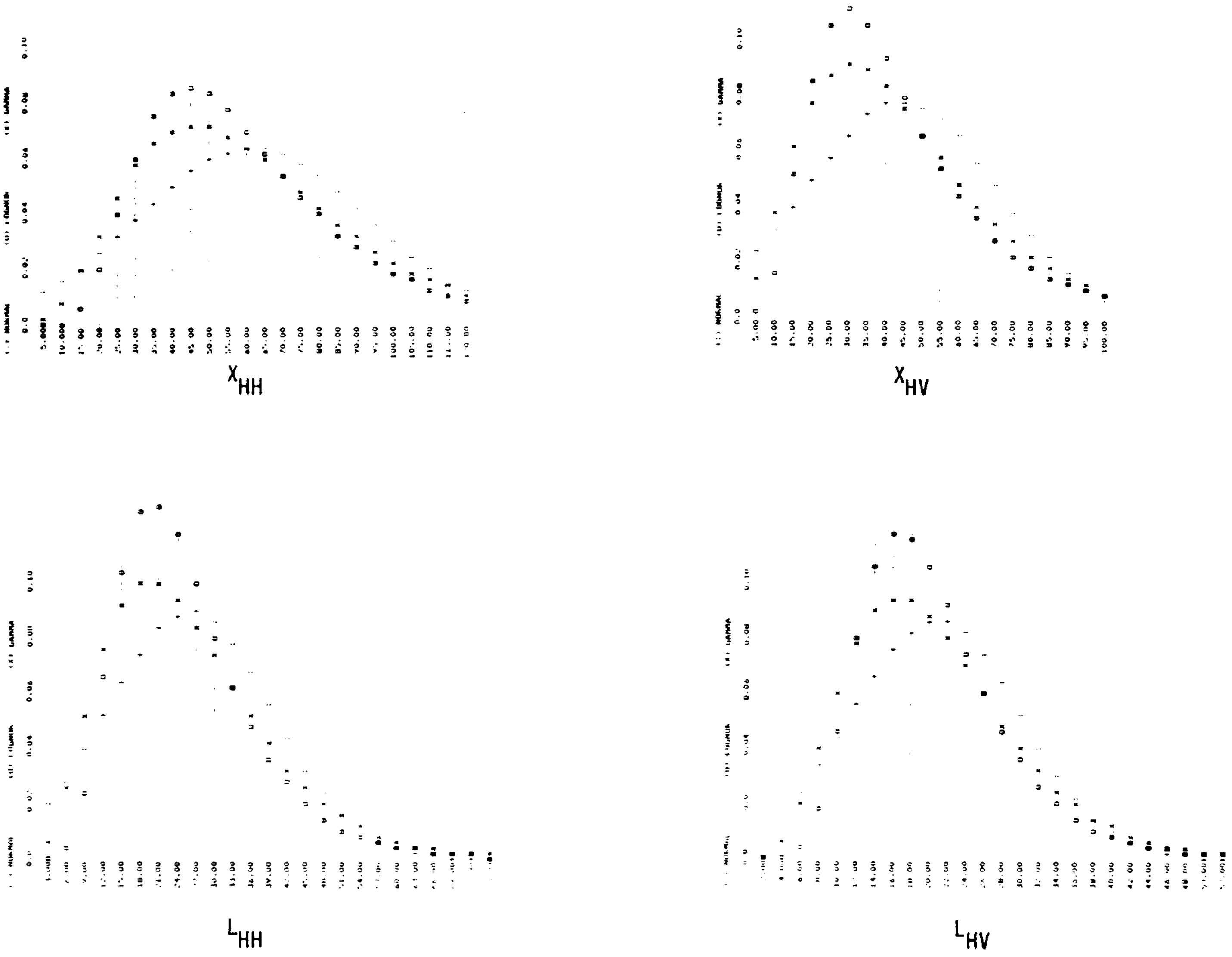

Figure C-10. HISTOGRAMS OF SITE B2-E/SHALLOW
(Multi-year pieces with hummocking)

AD-A097 341 ENVIRONMENTAL RESEARCH INST OF MICHIGAN ANN ARBOR RA--ETC F/G 17/9
DETERMINATION OF BACKSCATTER CHARACTERISTICS OF SEA ICE USING S--ETC(U)
MAR 81 R W LARSON, J D LYDEN, R A SHUCHMAN N00014-79-C-0690
UNCLASSIFIED ERIM-142600-1-F NL

3 OF 3
AD
A097341

END
DATE
FILMED
5 81
DTIC

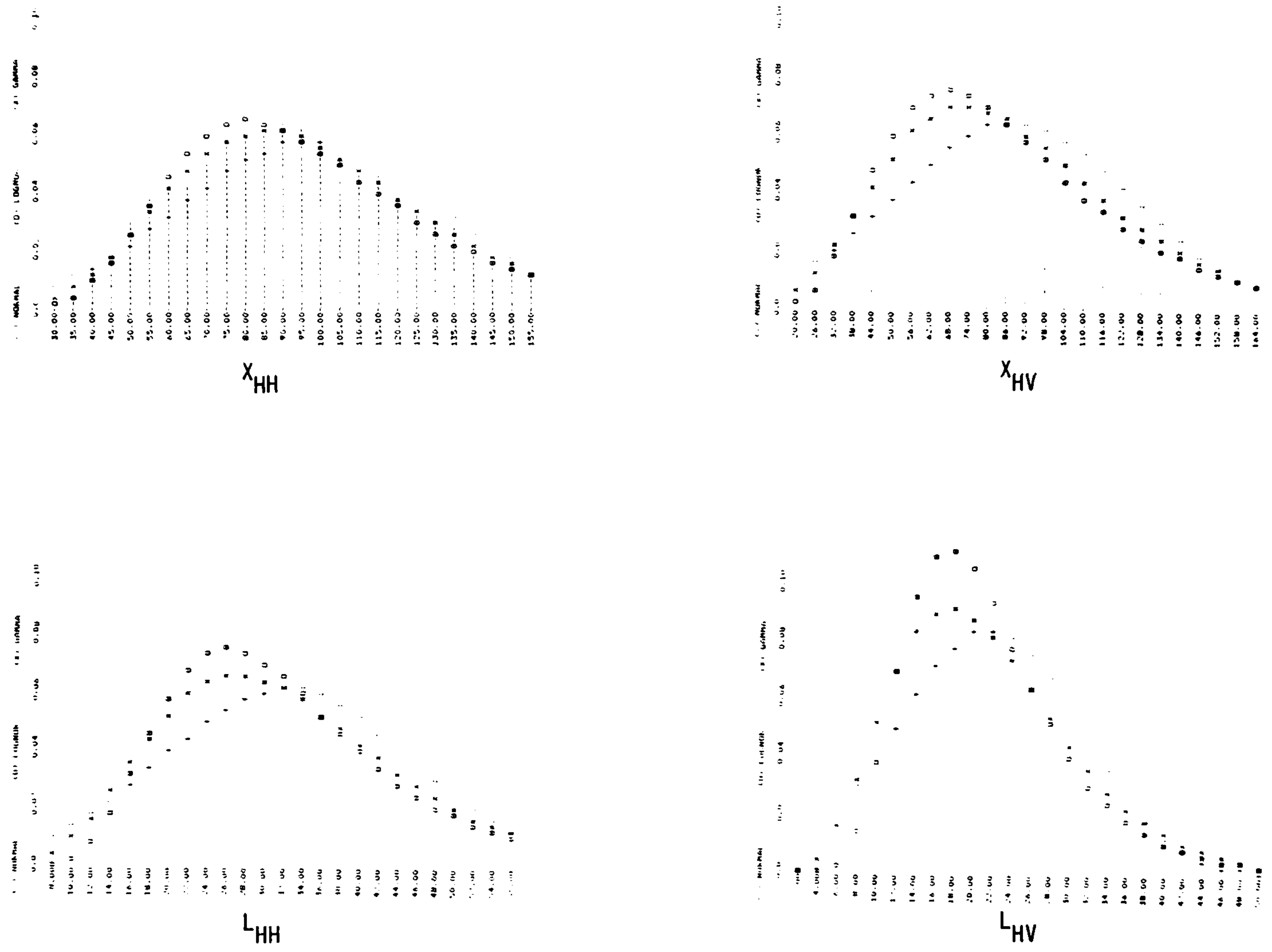

Figure C-11. HISTOGRAMS OF SITE B2-E/STEEP
(Multi-year pieces with hummocking)

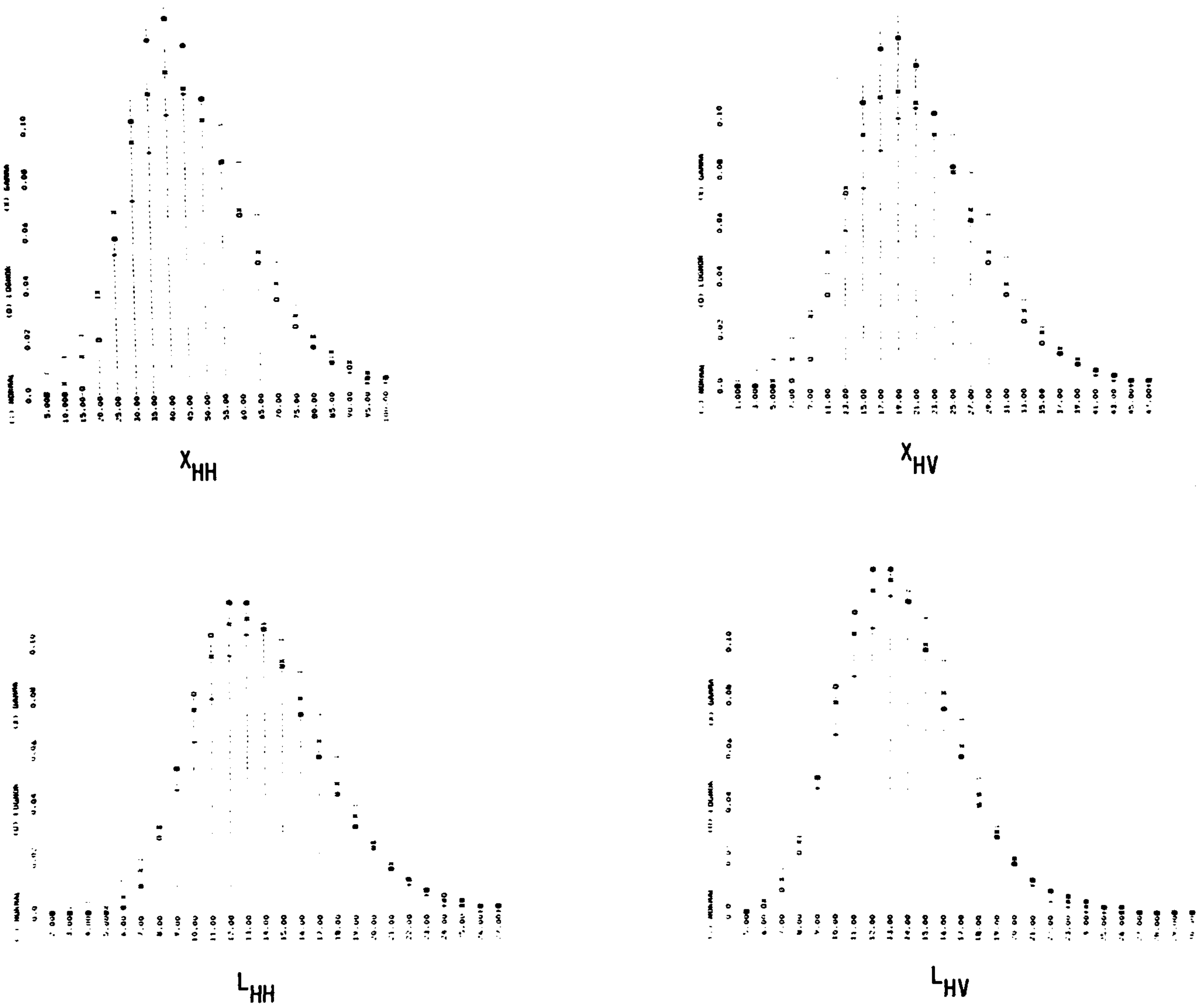

Figure C-12. HISTOGRAMS OF SITE B2-F/SHALLOW (Multi-year ice with ridging)

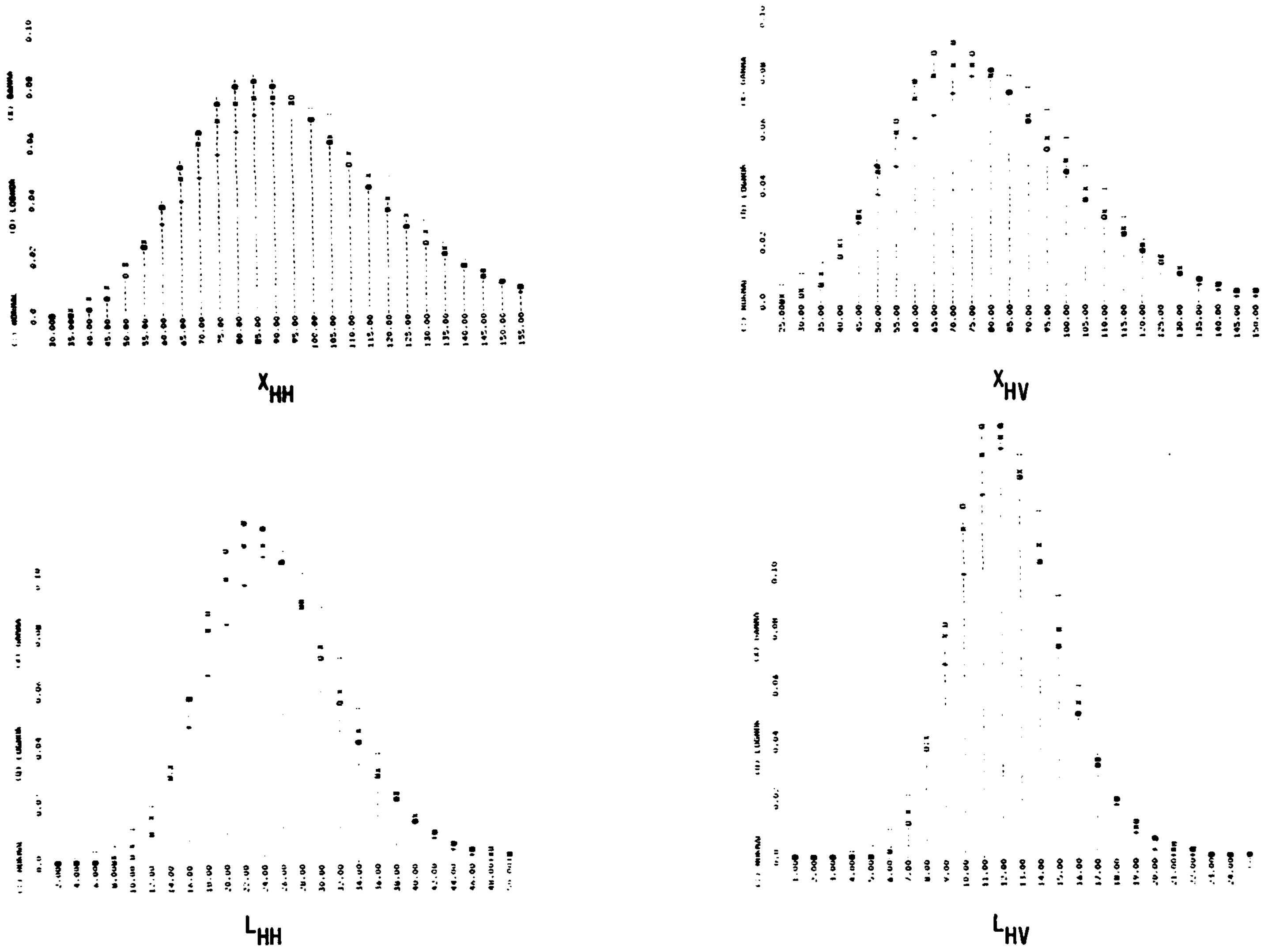

Figure C-13. HISTOGRAMS OF SITE B2-F/STEEP
(Multi-year ice with ridging)

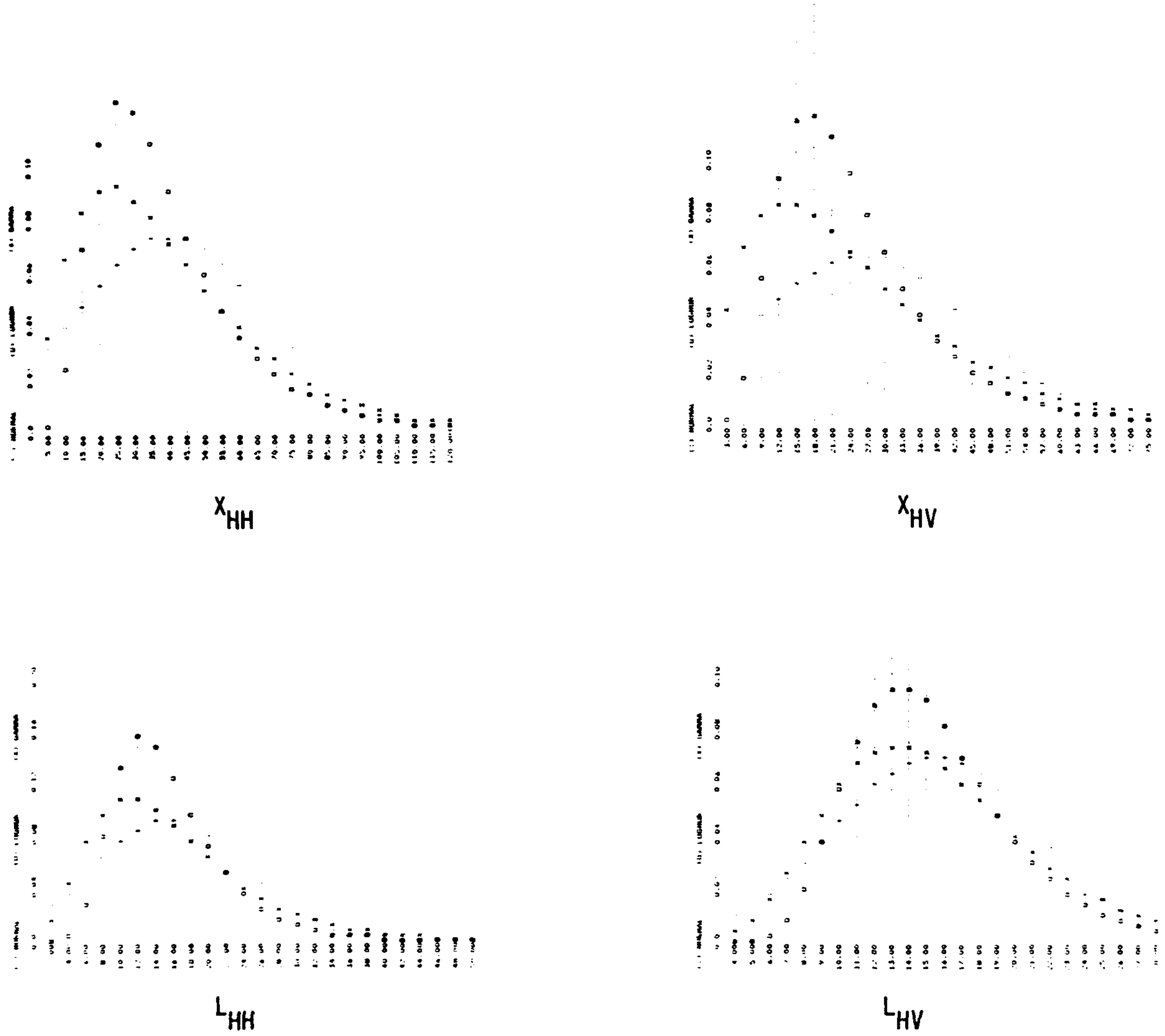

Figure C-14. HISTOGRAMS OF SITE B2-I/SHALLOW
(Multi-year ice with hummocking)

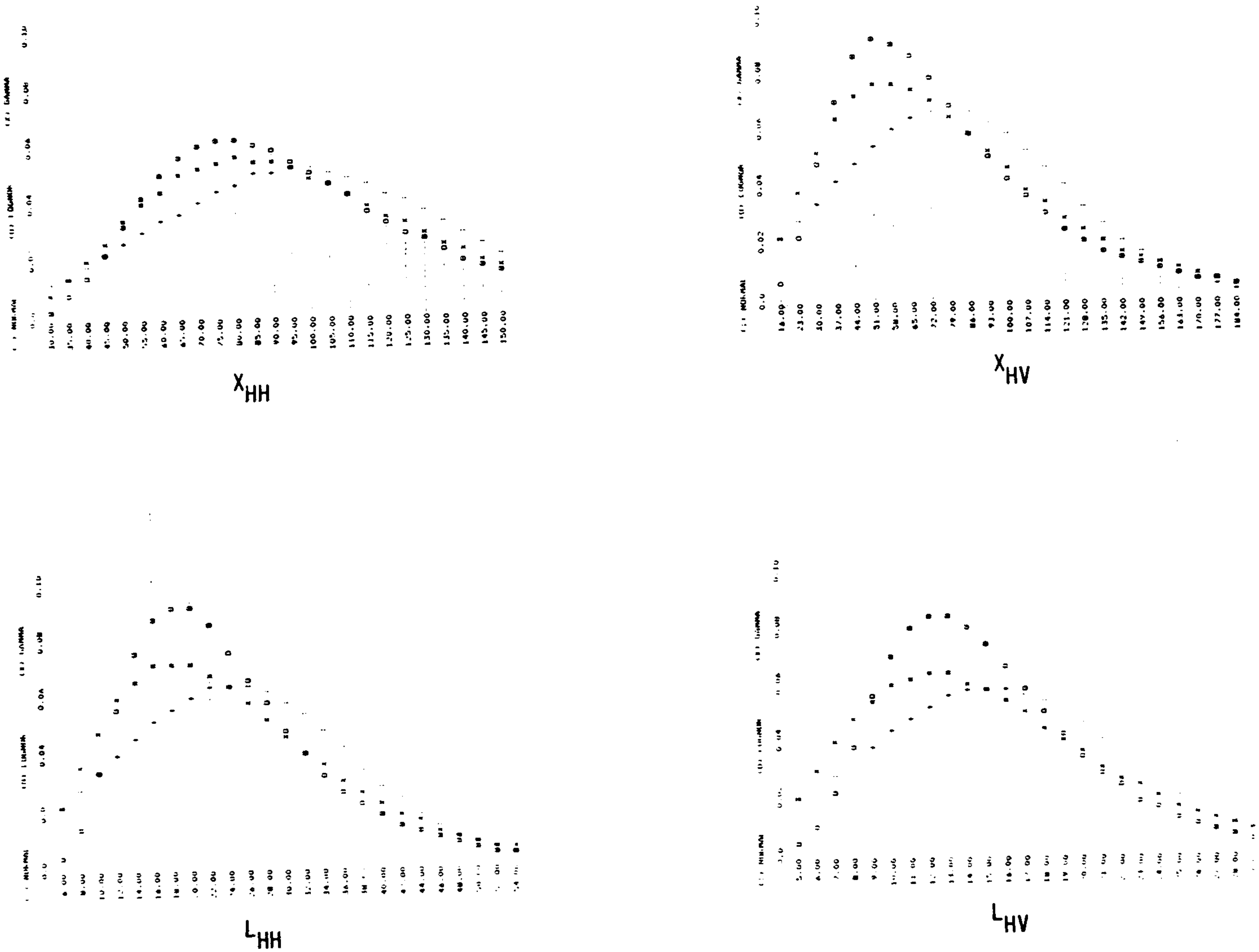

Figure C-15. HISTOGRAMS OF SITE B2-I/STEEP
(Multi-year ice with hummocking)

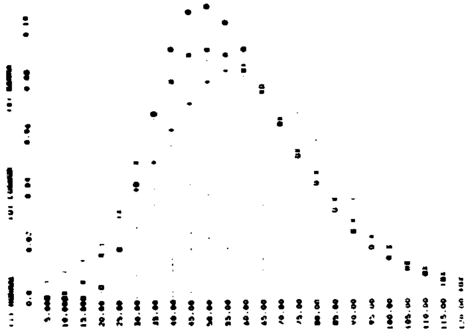

6 m x 6 m

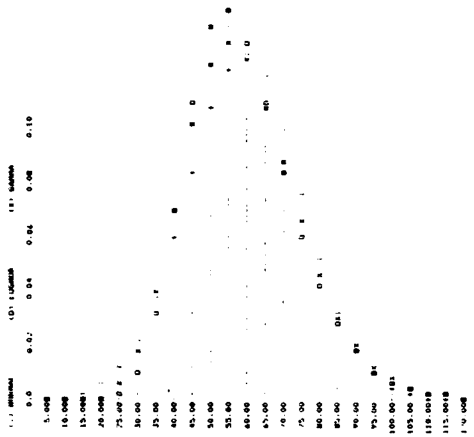

18 m x 18 m

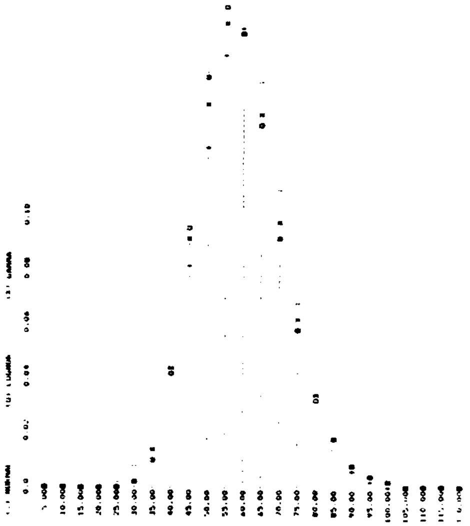

30 m x 30 m

Figure C-16. HISTOGRAMS SHOWING EFFECT OF VARYING RESOLUTION